IntechOpen

Earthquakes
Recent Advances, New Perspectives and Applications

Edited by Walter Salazar

Earthquakes - Recent Advances, New Perspectives and Applications

Edited by Walter Salazar

Contributors

Shutian Ma, Dariush Motazedian, Tse-Shan Hsu, Jamal Alomari, Vadim Bogdanov, Aleksey Pavlov, Walter Salazar, Nikola Solarić, Miljenko Solarić, Ivan Němec, Miroslav Trcala, Adéla Gálová, Kerimcan Apak

Notice

Statements and opinions expressed in the chapters are these of the individual contributors and not necessarily those of the editors or publisher. No responsibility is accepted for the accuracy of information contained in the published chapters. The publisher assumes no responsibility for any damage or injury to persons or property arising out of the use of any materials, instructions, methods or ideas contained in the book.

We are IntechOpen,
the world's leading publisher of
Open Access books
Built by scientists, for scientists

6,300+
Open access books available

171,000+
International authors and editors

190M+
Downloads

156
Countries delivered to

Our authors are among the
Top 1%
most cited scientists

12.2%
Contributors from top 500 universities

BOOK CITATION INDEX
CLARIVATE ANALYTICS
INDEXED

WEB OF SCIENCE™

Selection of our books indexed in the Book Citation Index
in Web of Science™ Core Collection (BKCI)

Interested in publishing with us?
Contact book.department@intechopen.com

Meet the editor

Dr. Walter Salazar is a structural civil engineer who obtained a doctoral degree in Engineering Seismology from the Interdisciplinary Graduate School of Science and Engineering, Tokyo Institute of Technology, Japan, in 2004. Dr. Salazar has been active in site effects and seismic hazard research, producing several peer-reviewed maps for El Salvador, Jamaica, and the Eastern Caribbean. He has published about sixty articles in peer-reviewed journals, books, and international conferences. In 2011, he received a Distinguished Salvadoran National Award. He is a peer reviewer for several scientific journals. Dr. Salazar is a Professor of Structural Engineering at the Catholic University of El Salvador.

Contents

Preface

The catastrophic earthquake sequence in Türkiye and Syria in February 2023 is a reminder that many aspects of earthquake science need further multidisciplinary research. Scientists and engineers must understand the fault's rupture and estimate the earthquake's ground motion and its consequences on building performance. In other words, a new educational curriculum must merge the seismology, geotechnical, and structural engineering fields to fulfill research trends and demand practices. This book attempts to start to do so.

Earthquakes - Recent Advances, New Perspectives and Applications results from the tireless effort of thirteen distinguished scholars from eight countries and is organized into four sections containing nine chapters.

Section 1, "Tectonics and Seismicity", includes Chapters 1–4. In Chapter 1, Motazedian and Ma study the June 23, 2014, M 7.9 Rat Islands Alaska earthquake by applying a full moment tensor inversion and a source rupture model accompanied by hypocenter relocations of aftershocks. The chapter can be used to teach how to perform inversions at universities and research centers for engineers and seismologists. In Chapter 2, Bogdanov and Pavlov construct probabilistic models that make it possible to trace self-consistent changes in space, time, and energy for background earthquakes preceding a strong event (e.g., M > 7.0) by employing wavelet decomposition methods, including depth uncertainty, in the analysis. The authors use the earthquake catalog for the Kamchatka regional network of the Russian Academy of Sciences during the period 1994–1997. In Chapter 3, Salazar presents a methodology to test the Weibull and Poisson probability distribution of earthquakes, employing a clustered and declustered catalog based on subduction events in El Salvador; magnitude conditional probabilities are computed for a time-dependent seismic hazard assessment. In Chapter 4, Motazedian and Ma recalculate the original parameters of the intraplate 1982 Miramichi earthquake and aftershocks using a master-event location method combined with regional depth-phase modeling.

Section 2, "Earthquake Forecasting", includes Chapter 5 in which N. Solarić and M. Solarić present a prominent application of GPS satellites for earthquake forecasting, analyzing the distance changes amongst different Earth stations before and after an earthquake occurrence.

Section 3, "Geotechnical Engineering", includes Chapter 6, in which Hsu presents an improvement of the classical methodologies to calculate the bearing capacity on soils considering the strain softening and asymmetric shear failures under the finite element analysis. It also presents new findings on Coulomb's earth pressures and slope stability analysis.

Section 4, "Building Structures", includes Chapters 7–9. Chapter 7 by Apak summarizes the morphology of the vernacular structures in Türkiye at Adana City and presents a qualitative analysis of these heritage buildings due to vertical, seismic, and wind loadings, including out-of-plane behavior. Chapter 8 by Alomari describes the risks associated with modifying the structural systems of buildings. It also shows remedial measures locating special devices to reduce the earthquake response of the structures. Chapter 9 by Trcala, Němec, and Gálová explains several structural dynamics techniques employing accelerograms as input excitation of buildings in the nonlinear range behavior.

Walter Salazar, Ph.D.
Professor,
Faculty of Engineering and Architecture,
Catholic University of El Salvador UNICAES,
Santa Ana, El Salvador

Section 1

Tectoncis and Seismicity

Studies on the Source Parameters of the 23 June 2014 Rat Islands, Alaska, M_W 7.9 Earthquake Sequence

Dariush Motazedian and Shutian Ma

Abstract

On 23 June 2014, an M_W 7.9 earthquake occurred in the Rat Islands region, Alaska, United States. We inverted the full moment tensor for the mainshock, and found the shallow-dip nodal plane (P1) is: strike 207.4°, dip 27.1°, slip −12.7°; the steep-dip plane (P2) is: strike 308.7°, dip 84.2°, slip −116.5°. The larger aftershocks that have depth phase records were relocated and found the majority were distributed along a moderate dipping trend. The steep-dip plane was selected as the causative plane. Using the steep-dip plane as the rupture plane, source rupture process inversions were performed. The obtained maximum slip was about 3.5 m. The optimal rupture velocity V_R was about 2.0 km/s. The shallow-dip plane was also used as a rupture plane to perform rupture inversion trials. Curiously the overall waveform fit between the observed and the synthetic seismograms is slightly better than that when the steep-dip plane was used. The catalogue hypocenters of the aftershocks with magnitude ≥ 4.0 were used to simulate a spatial plane. The simulated plane is moderate dipping towards north-west. When the simulated plane was used as the rupture plane, the overall waveform fit was poor. The moderate dipping plane was not the causative plane.

Keywords: the 23 June 2014 Rat Islands M_W 7.9 earthquake, source rupture model, aftershocks, master-event relocation, depth phase

1. Introduction

On June 23, 2014, an M_W 7.9 earthquake occurred in the central Aleutians near the Rat Islands, Alaska (**Figure 1**). This earthquake was one of the largest seismic events along the boundary between the Pacific and the North American plates in a century. The focal depth of this earthquake was about 100 km; it is an intermediate-depth event. In most cases, intermediate-depth events are not followed by many aftershocks [1]. However, this mainshock was followed by a large number of aftershocks. The Alaska Earthquake Centre (AEC) located more than 1800 aftershocks within 1 month after the mainshock, and more than 40 of them were larger than magnitude 4 [2].

Figure 1.
The location of the 23 June 2014 M_W 7.9 earthquake and the study region in the global setting. The red solid circle at the center shows the epicenter. The trapezoid shows the study region. The triangles show the positions of the seismic stations, at which the recorded mantle Rayleigh-wave seismograms were selected for the moment tensor inversion. The cross sign shows the location of the north pole.

Intermediate-depth earthquakes with $M_W \geq 7.5$ are rare. The Global Centroid Moment Tensor (G-CMT) catalog lists only 14 with magnitude $M_W \geq 7.5$, which occurred between depths of 70–200 km [2]. The occurrence of this large earthquake with many aftershocks is a very rare case.

The mainshock caused an intention to the seismological society. Some seismologists studied it and published papers on or related to this Rat Islands earthquake sequence.

Ye et al. [3] modeled the source ruptures using both nodal planes. They found the shallow-dip fault plane with strike azimuth Az 205.9° and dip angle 23.6° toward the northwest provides better matches to *P* waveforms at azimuths from 300° to 340° than does the steep-dip fault plane (strike azimuth Az 308° and dip angle 84°). However, the overall waveform mismatch is comparable between the two models, and some signals are better fit using the steep-dip fault plane, so their preference for selecting the shallow-dip plane as the rupture plane is mild. In another word, for this M_W 7.9 earthquake, its causative plane cannot be 100% determined using the fit

between the observed and the synthetic waveforms. The maximum slip they obtained is 10.3 m; the average slip is 3.9 m. The rupture velocity they used is 1.5 km/s.

Macpherson and Ruppert [2] relocated the aftershocks. To attempt to determine the correct rupture plane, they plotted cross-sections parallel to the dipping directions of the nodal planes as determined by the Global Centroid Moment Tensor (gCMT) project. The gCMT solutions found one nodal plane with subvertical dip (84°) and a strike of 308° and the other with a moderate dip of 26° and strike of 207°. They found that the seismicity is dipping at a moderate angle to the northwest and does not align well with the dips from either of the gCMT nodal planes. They also found the shallow-dip plane does align well with the mainshock hypocenter and a group of unusual oceanic mantle seismicity to the south of the mainshock. They interpret that alignment as delineating the mainshock fault plane, and thus, they prefer the moderately dipping nodal plane as the rupture plane of the M_W 7.9 mainshock. They used the double-difference relocation method [4], and the catalog travel time picks from 29 Broadband and short-period stations to relocate over 2500 earthquakes, which occurred from June 23, 2014, to the end of the year in the mainshock epicenter region (50°N–53°N; 176°E–178°W). As those smaller aftershocks were included; the catalog travel time picks for smaller earthquakes may not be accurate, and the relocation results may or may not be reliable.

Twardzik and Ji [5] first performed a set of finite-fault inversions to invert the slip history of the M_W 7.9 earthquake. They found they cannot identify the causative fault plane by comparing the misfits between observed and the synthetic seismograms. As such, they relocated aftershocks and used the relocated hypocenters to determine the causative plane. They used the Joint hypocenter determination (JHD) method and the arrival times of seismic phases (P, S, pP, sP, PcP, and ScP) reported by the International Seismological Centre (ISC). They selected a dataset, including 19 earthquakes with $m_b \geq 4$; 17 earthquakes with ($3 \leq m_b \leq 4$), occurred from June 23 to September 23, 2014, within 60 km from the epicenter of the mainshock. The mean horizontal error of those JHD locations is 6.2 km; the mean vertical error is 19.8 km. They found that most relocated aftershocks distribute along a 40 km long linear segment orienting northeast and that coincides with the width of the surface projection of the steep-dip fault plane. Vertically, the relocated aftershocks span a depth range from 70 km to 150 km. It is noteworthy that the depth extension of the relocated aftershock distribution is nearly double of its horizontal extension. They concluded that the relocated aftershocks tend to align preferentially along with the fault plane that has a dip of 87° and a strike of 308°. Since the mean vertical error is 19.8 km in the relocated aftershocks, the hypocenter distribution may have some uncertainties. The maximum slip they obtained is about 3.5 m; the rupture velocity V_R is about 2.0 km/s.

Miyazawa [6] studied the remote and dynamic earthquake triggering phenomena caused by global transient stress changes generated from seismic waves' propagation of other large earthquakes at a great distance. The author calculated the dynamic changes beneath station ADK and AMKA in the Coulomb Failure Function (ΔCFF) for the M_W 7.9 mainshock. The focal mechanism from the Global CMT (strike 207°, dip 26°, and rake/slip −13°) and focal depth 109 km were used. It was found that the ΔCFF varies within roughly 10 Pa when the Lame's parameters, λ and μ, are 66 GPa and the effective friction coefficient μ′ is assumed to be 0.4 at the depth. The stress changes varying within at most 10 Pa at the hypocenter region probably caused a reduction in the fault's strength by cyclic fatigue and eventually triggered the fault failure and released energy in the form of an M_W 7.9 earthquake. Unfortunately, the author did not provide the results from the steep-dip plane.

Florez and Prieto [7] introduced a relative earthquake depth determination algorithm using depth phases. They applied their method to determine focal depths for 17 larger aftershocks of the M_W 7.9 earthquake. They projected their relocated hypocenters onto two vertical planes. One is parallel to the steep-dipping direction; the other to the shallow-dipping direction. They found that their results are not consistent with a shallow-dip nodal plane. Therefore, they can confidently assign the causative fault plane to the steep-dip plane. It seems that the catalog epicenters were used when projections of the hypocenters were plotted. It is noticed that their hypocenter projections on the vertical plane that is parallel to the steep-dipping direction did not form a linear trend along with the 84° dipping. The majority are along with about 60° dipping (their Figure 2c).

The above authors made contributions to the studies of this M_W 7.9 sequence. For example, they found that the causative plane of the mainshock cannot be determined using the misfit between observed and synthetic waveforms. Some phenomena related to the mainshock are still not very well emphasized. Such as, the majority of the aftershocks were distributed along with a moderate-dipping trend neither along with the shallow dip nor the steep-dip nodal plane. We have been studying this very rare event from its occurrence; we want to present our results and confirm some phenomena we found. We organized a chapter, which covers parts of our results.

1. The seismic activity features obtained using catalog data for earthquakes with magnitude ≥ 4.0, occurred before and after seven and half years from the mainshock;

2. introduction to some of the methods used in our studies;

3. full moment tensor solution for the mainshock; the double-couple solution retrieved is:

   - nodal plane 1, $P1$: strike 207.4°, dip 27.1°, rake/slip -12.7°, dipping at Az 297.4° (shallow-dip);

   - nodal plane 2, $P2$: strike 308.7°, dip 84.2°, rake/slip -116.5°, dipping at Az 38.7° (steep-dip).

4. hypocenter relocations for larger aftershocks which have depths obtained using a depth phase method;

5. source rupture process modeling results;

6. discussions of some issues.

2. Several types of data used in our work

The catalog data: We retrieved the catalog of earthquakes with magnitude ≥ 4, which occurred between 2007-0101 and 2022-0220 in the M_W 7.9 source region and its vicinity from IRIS (the Incorporated Research Institutions for Seismology), and made up a computer program to process the catalog for plotting various hypocenter distribution figures. The data duration covers about seven and a half years before and after the occurrence of the mainshock.

Seismogram data: When we perform a moment tensor inversion, and model source rupture process for an earthquake, we need waveform records. Usually, we retrieve waveform records from IRIS. For this M_W 7.9 earthquake:

1. the Broadband records at tele-stations (some seismic arrays) were retrieved for measuring the time differences between the tele-depth phase pP and the direct P phase to calculate focal depths.

2. the Broadband records at regional stations were retrieved for measuring the arrival times of P and S phases to relocate those larger aftershocks that have focal depth solutions obtained using a tele-depth phase.

3. the Broadband records at tele-stations around the epicenter of the mainshock were retrieved for modeling source rupture processes.

4. the long period mantle wave records at tele-stations globally were retrieved for moment tensor inversion.

An earth velocity model is required for relocations of the aftershocks. We used the velocity model provided by Macpherson and Ruppert [2], to replace the crustal part in the Preliminary Reference Earth Model (PREM; [8]). This revised model was used for aftershock relocations and the source rupture modeling.

3. The geological background and seismic activities in the source region and its vicinity

The M_W 7.9 Rat Islands earthquake ruptured beneath the Rat Islands in the western Aleutians Islands, Alaska. **Figure 2** shows its geographic location and the seismicity in the epicenter region and its vicinity. This Mw 7.9 event happened within the subducting Pacific slab in a region where the Bowers Ridge and the Aleutian Trench (subduction zone) meet. The Aleutian Trench is the boundary between the Pacific Plate and the America Plate. In the Aleutian Trench region, the Pacific Plate is moving relative to the North American plate, which is relatively stationary, at a rate of about 7.5 cm/year [e.g., [9]].

The Aleutian trench is, along the Alaska-Aleutian arc, one of the largest active tectonic margins in the world, spanning nearly 4000 km from the Gulf of Alaska to the Kamchatka Peninsula, Russia. The arc is formed by a convergent plate boundary where the Pacific plate is subducted beneath the North American plate at a rate that varies between 5.4 cm/yr in the east to 7.8 cm/yr in the far west [9]. The Aleutian trench zone is very seismically active. In the Rat Islands region, there are 10 earthquakes with a magnitude ≥ 7 occurred since 1960 (IRIS earthquake catalog). The June 23, 2014 M_W 7.9 earthquake occurred at a depth of about 100 km. It is often called an intermediate-depth event. In the following paragraphs, we analyze the seismicity that occurred about seven and a half years before and after the M_W 7.9 earthquake in the source region and its vicinity.

Figure 3 shows the epicenter distribution of earthquakes with magnitudes ≥ 4.0, which occurred about seven and half years before and after the Mw 7.9 mainshock in the mainshock region and its vicinity. A solid circle shows the epicenter of an earthquake. It was color-coded with focal depth; its size is proportional to the magnitude.
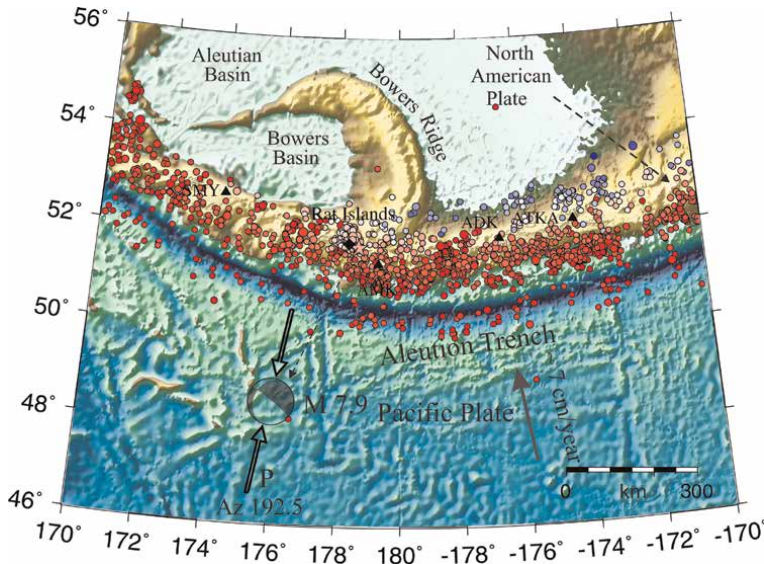
Figure 2.
The seismicity and the geological background in the vicinity of the 23 June 2014 Rat Islands, Alaska, M_W 7.9 earthquake sequence. A color-coded solid circle shows an epicenter. A deeper color shows a deeper focal depth. The catalog, retrieved from the IRIS, cont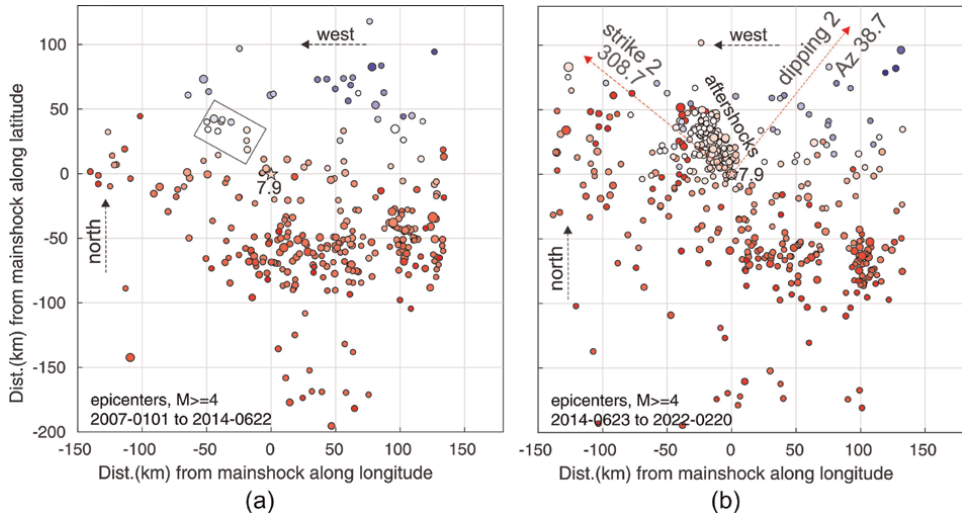ains the earthquakes with magnitude ≥ 4, which occurred from 2014-0101 to 2022-0220. The star shows the epicenter of the M_W 7.9 mainshock; the diamond approximately shows the location of the Rat Islands (the new name is Hawadax Islands); the triangles show the locations of the four seismic stations used in the aftershock relocation; the headed-on arrows show the compressive force directions. The earthquake sequence occurred in the region where the Bowers Ridge and the Aleutian Trench (subduction zone) meet.

The left panel (a) shows the earthquakes that occurred seven and half years before the occurrence of the Mw 7.9. The events within the rectangular are those that occurred in the source region. The right panel (b) shows the earthquakes that occurred after the occurrence of M_W 7.9. The aftershocks formed a trend in the northwest direction.

To analyze the seismicity along the vertical direction, we simulated a spatial plane using the hypocenters of 90 earthquakes with magnitudes ≥ 4.0, which occurred below the depth of 80 km from 2007-0101 to 2014-0622. The simulated strike is Az 276.8°; the dip angle is 47.7°. The plane dips at Az 6.8°. Then we projected the hypocenters of earthquakes onto a vertical plane that is parallel to the dipping direction. **Figure 4** shows the hypocenter projection comparison for the same earthquakes in **Figure 3**. The left panel (a) shows that the hypocenter projections beneath about 90 km are along with a dipping of 47.7° direction. Coincidently the hypocenter distribution trend of the aftershocks in the right panel (b) is also approximately along this dipping direction. The trend is neither in the dipping direction of the steep-dip plane nor in the dipping direction of the shallow-dip plane.

To observe the spatial distribution features of the aftershocks of the M_W 7.9, we simulated a spatial plane using the hypocenters of 184 aftershocks, of which the magnitudes ≥ 4.0. The simulated strike is 201.7°; the dip angle is 39.4°. The plane dips at Az 291.7° (from north to west 68.3°). These parameter values are close to those of the nodal plane P1 (strike Az 207.4°, dip angle 27.1°, dips at 297.4°; **Table 1**). **Figure 5** shows the hypocenter projections onto a vertical plane, which is perpendicular to the strike of the simulated plane. It is found that the hypocenters of the aftershocks were distributed approximately along the simulated dipping direction (39.4°).

Figure 3.
The epicenter comparison for earthquakes with magnitudes ≥ 4.0, occurred about 7 and half years before and after the Mw 7.9 mainshock, in the mainshock region and its vicinity. (a) the earthquakes occurred 7 and half years before the occurrence of the Mw 7.9 (between 2007-0101 and 2014-0622). (b) the earthquakes occurred after the occurrence of the Mw 7.9 (between 2014-0623 and 2022-0220). The earthquakes in the rectangle of the left panel are in the source region of the mainshocks. The star with the number 7.9 shows the initial location of the M_W 7.9 mainshock. The catalog was retrieved from IRIS.
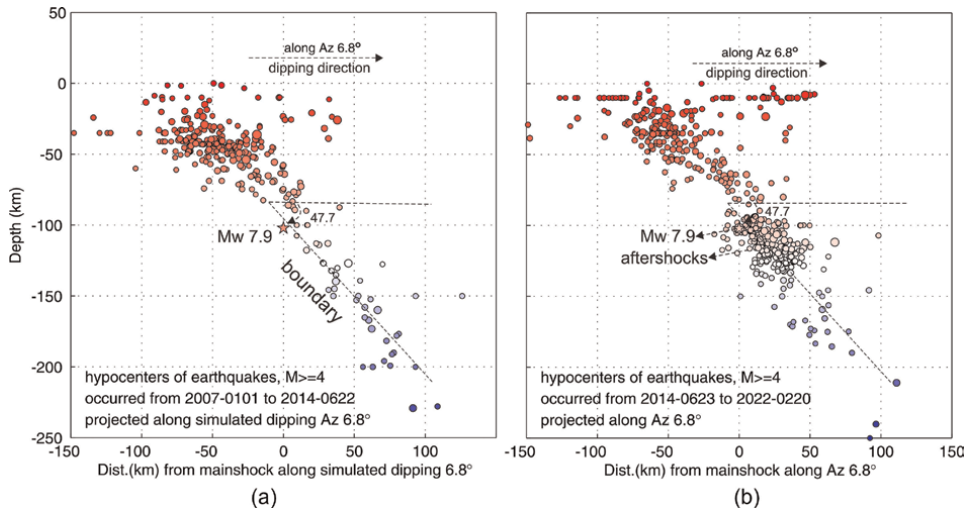
Figure 4.
*The hypocenter projection comparison for the same earthquakes in **Figure 3**. (a) The hypocenter projections show the seismic activity along the dipping direction of a simulated spatial plane. The simulation was performed using the hypocenters of 90 earthquakes with magnitudes ≥ 4.0, which occurred below the depth of 80 km from 2007-0101 to 2014-0622. The simulated strike is Az 276.8°; the dip angle is 47.7°. The plane dips at Az 6.8°. The relatively narrow seismicity belt below the red star may be assumed to be close to the boundary between the Pacific Plate and the North American plate beneath the Rat Islands region. The red star shows the initial location of the mainshock. (b) The hypocenter projections of earthquakes occurred between 2014-0623 and 2022-0220.*

To further observe the spatial distribution trend of the aftershocks, we projected the hypocenters onto two vertical planes. The left panel of **Figure 6** a shows the hypocenters projected onto a vertical plane at a steep-dipping direction. The tilted

Major double couple: moment = 9.16						Prin. val.	Dev. part	Azimuth	Plunge
P1:	strike	dip	slip	dipping at 297.4 (shallow-dip)	P	−8.895	−9.159	192.50	44.47
	207.4	27.1	−12.7						
P2:	strike	dip	slip	dipping at 38.7 (steep-dip)	T	9.088	8.825	61.10	33.97
	308.7	84.2	−116.5						
Minor double couple: moment = 0.33					N	0.597	0.334	311.60	26.36
P1:	strike	dip	slip		Isotropic part: moment = 0.26 (trace = 0.78)				
	93.2	44.8	−6.6						
P2:	strike	dip	slip						
	187.9	85.3	−134.7						

Note: prin. val. refers to the principal axis value ($10^{20}Nm$); dev. part refers to the deviatoric part ($10^{20}Nm$); P, T, and N mean the compressional, tensional, and null components. P1 and P2 mean nodal planes 1 and 2. The unit for the strike, dip, slip, and dipping is the degree (°), and for the moment is $10^{20}Nm$. Compared to the scalar moment of the major double couple, the isotropic part (ISO) is 2.88%, and the minor double couple is 3.64%. The inversion was performed using a depth of 105 km.

Table 1.
A full moment tensor solution for the Rat Islands M_W 7.9 mainshock.
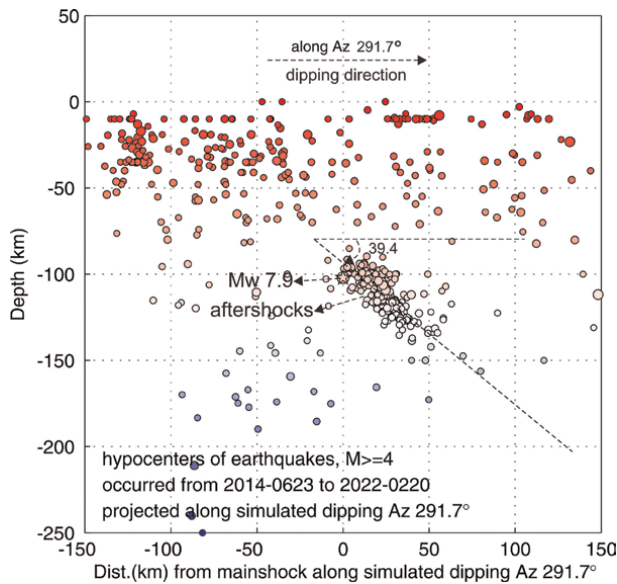
Figure 5.
*Hypocenter projections onto a vertical plane, perpendicular to the simulated spatial plane using the hypocenters of 184 aftershocks, of which the magnitudes ≥ 4.0. The red star shows the initial location of the mainshock. The simulated strike is 201.7°; the dip angle is 39.4°. The plane dips at Az 291.7° (from north to west 68.3°). These parameter values are close to those of the nodal plane P1: strike Az 207.4°, dip angle 27.1°, dips at 297.4° (**Table 1**).*

dashed line indicated with the P2 projection shows the projection of the steep-dip plane (P2). Generally, those aftershocks should form a linear trend around that tilted line, if the plane P2 is the real rupture plane. The right panel (b) shows the hypocenters on a vertical plane in a shallow-dipping direction. In the same sense, those aftershocks should form a linear trend around that tilted line indicated with P1
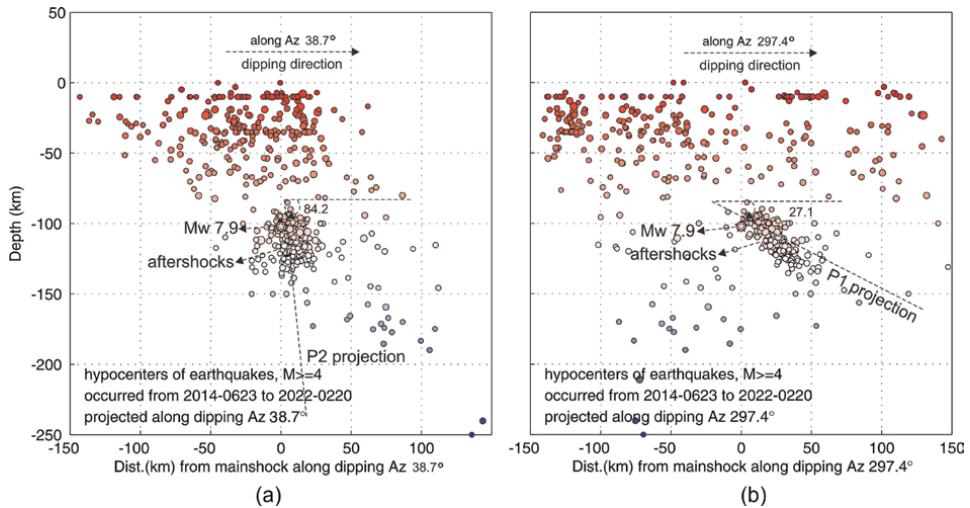
Figure 6.
*The comparison between hypocenters projected onto dipping planes for the same earthquakes is in **Figure 3** (b). (a) The hypocenter projections on a vertical plane at a steep-dipping direction. The tilted dashed line indicated with the P2 projection shows the projection of the steep-dipping plane (P2). Ideally, those aftershocks should be approximately aligned around that tilted line, if the plane P2 is the rupture plane. (b) The hypocenter projections on a vertical plane at a shallow-dipping direction. The tilted dashed line indicated with the P1 projection shows the projection of the shallow-dip plane (P1). The trend of the belt formed by the aftershocks is not consistent with the P1 projection; the trend has a moderate dipping. Both panels show that most aftershock activities were from a depth of about 80 km to 150 km.*

projection, if P1 is the real rupture plane. The trend of the belt formed by the aftershocks in (a) or (b) is not consistent with the P2 projection or P1 projection.

4. Method introduction

To perform source parameters studies on the M_W 7.9 mainshock and its larger aftershocks we used several advanced methods. These methods are introduced briefly in this section.

4.1 Method used to obtain a full moment tensor

An earthquake source can be described using a seismic moment tensor. The moment tensor can be decomposed into three parts: an isotropic (ISO), double-couple (DC), and compensated linear vector dipole (CLVD) part (e.g., [10]). It can also be decomposed into an isotropic (ISO), a major double-couple, and a minor double-couple part (e.g., [11]). The seismic moment is a 3 × 3 matrices. In linear algebra, a complex matrix can be expressed by the summation of several simple, independent matrices. Applying this principle, Kikuchi and Kanamori [12] expressed an arbitrary moment tensor by summing six different constant moment tensors. Given an earthquake hypocenter and earth model, each of the constant tensors is used to generate Green's functions and obtain three-component synthetic seismograms at a given seismic station.

There are several ways to generate Green's functions depending on the wave type used. As the M_W 7.9 Rat Islands earthquake was large, we used a long-period Rayleigh

wave fitting method to obtain its moment tensor. Green's functions were generated using the normal modes summation method [13].

Once Green's functions are obtained, synthetic seismograms are calculated using a set of coefficients. A moment tensor inversion is to search for a set of the coefficients used to generate synthetic seismograms, which should be as similar as possible to the observed seismograms in shapes and amplitudes. To do this, two functions are often separately used. One function is to calculate the correlation between the synthetic and the observed seismograms using:

$$e_j = 1 - \frac{\sum_i X_j(t_i) \bullet O_j(t_i)}{\sqrt{\sum_i X_j^2(t_i) \bullet \sum_i O_j^2(t_i)}} \tag{1}$$

where the subscript j is an ordinal number of the digital recording; i is the data time point index in the observed or the synthetic seismograms. $O_j(t_i)$ is a segment of a digital record; $X_j(t_i)$ is a segment of a synthetic seismogram corresponding to $O_j(t_i)$.

The second function is to calculate the amplitude differences between the synthetic and the observed seismograms:

$$e_j = \sqrt{\frac{\sum_i \left[X_j(t_i) \times a_0 - O_j(t_i)\right]^2}{N_j}} \tag{2}$$

The factor a_0 is a constant, determined using the following function:

$$a_0 = \frac{1}{N} \sum_{j=1}^{N} \frac{O_j(t)_{\max}}{X_j(t)_{\max}} \times 10^{20} \, dyne \bullet cm \tag{3}$$

where N is the number of records used in the inversion.

We, first, use function (1) to obtain a preliminary moment tensor solution, then use (3) to obtain a_0, and use (2) to obtain a solution. The procedure is repeated many times to find a target set of coefficients when function (2) is at its minimum. Then the moment tensor is calculated using the target set of coefficients. We used the procedures developed by Ma and Adams [14] for simultaneous waveform shape and amplitude inversion.

4.2 The method to determine focal depth using arrival time difference pP-P

Crotwell, et al. [15] developed a Taup Toolkit, called "Flexible Seismic Travel-Time and Raypath Utilities." Using this tool, the travel times for many seismic phases can be calculated.

We developed a procedure [16] using the relationship that the time duration between the tele-depth phase pP and its reference phase P is roughly positively proportional to the focal depth, to determine focal depths for the larger aftershocks of the Rat Islands, M_W 7.9 earthquake.

1. For a given station, we pick out the station distance from the SAC record at the station;

2. We select a possible depth range;

3. Using the station distance and a range of depth, with the Taup tool we calculate several time durations between the tele-depth phase pP and its reference P;

4. Using Matlab, we plot a line determined by the focal depths and the corresponding calculated time durations pP-P, and obtain a linear formula;

5. Put the measured time duration pP-P at the selected station in the formula, the calculated focal depth for the aftershock is obtained;

6. For several stations at which the time durations pP-P are measured, several focal depth solutions are obtained, and the average is used as the final solution for the earthquake.

4.3 Earthquake locating method

Earthquake hypocenter parameters are fundamental information for studying earthquakes, as such many people have contributed to earthquake locating methods and computer programs. The hypocenter locating program that we used is a part of a computer program package called SEISAN. The SEISAN (seismic analysis system) is a complete set of programs for analyzing earthquakes. With SEISAN it is possible to locate events, determine spectral parameters, seismic moments, and so on. The hypocenter locating program used in this article in the SEISAN package is a modified version of HYPOCENTER [17–19].

4.4 The method to set up a source rupture model

The commonly used procedure to set up an earthquake rupture model is described below. One of the nodal planes obtained from a seismic moment tensor is used as the earthquake rupture plane. Usually, the x-axis is along the strike direction, and the y-axis is along the dip direction. The selected rupture plane is divided into $M \times N$ sub-faults with lengths of dx and dy. Each sub-fault is treated as a point source and the synthetic seismogram at each seismic station is the summation of the synthetic seismograms generated by all of the sub-faults. The source time function of a sub-fault is usually depicted as overlapped triangles. The layout of the source rupture model can be found in Hartzell and Heaton [20].

A unit constant rupture slip vector for each sub-fault is divided into two orthogonal vector components (one aligned along the strike and the other aligned along the dipping direction). Any slip vector on the sub-fault is obtained by multiplying the two constant vector components with appropriate coefficients. The goal of the inversion method is to obtain the coefficients of all of the sub-faults. The slip function (source time function) of each sub-fault is depicted by overlapped L triangles with a rise time τ, which is half the length of the bottom side of the triangle. The initial constant unit slip direction (slip0) of each sub-fault is the slip of the selected nodal plane. The initial slip is separated into two components in the directions of (slip0 + 45°) and (slip0 - 45°). This breakdown is convenient for Green's functions calculations.

If we assume that on a sub-fault mn ($m = 1, \cdots, M; n = 1, \cdots, N$) at the kth component direction ($k = 1, 2$), the slip corresponding to the lth triangle is X_{mnlk} and the vertical component of the Green's functions generated at station j is g_{mnkj}, at the same station the vertical component of the synthetic seismogram, W_j, generated by all sub-faults at the time point t_i, is expressed as:

$$W_j(t_i) = \sum_{mnlk} X_{mnlk} g_{mnkj}(t_i - (l-1)\tau - T_{mn} - dl_{mn})$$

(4)

where T_{mn} is the rupture start time at the mn^{th} sub-fault and dl_{mn} is a time delay generated by the different travel path lengths between the P-waves generated by the mn^{th} sub-fault and the rupture start sub-fault m_0n_0 (hypocenter). The set of X_{mnlk} that can generate a W_j, which is most similar to the observed seismogram at station j, is the best fitting rupture model for the earthquake.

In this study, two methods were used to determine the rupture slip distribution—the non-negative least squares (NNLS) method [21] and the simulated annealing (SA) method [22]. For most trial inversions, we used the NNLS method, while the SA method was used at the final step to confirm the solution obtained with NNLS.

The smoothness constraint of the total spatial slip distribution was implemented by a Laplacian differential operator to stabilize the slip solution [23]. To calculate the time delay dl_{mn} in function (5), a rupture velocity is required. To calculate Green's functions, we need an initial focal depth, which is also required to obtain a reasonable slip distribution.

5. The source parameters obtained using the methods introduced above

Using the methods introduced above we studied the source parameters for the mainshocks and relocated its larger aftershocks that occurred about 20 days following the mainshock. In this section, we present those results.

5.1 Full moment tensor inversion for the M_W 7.9 Earthquake

Using the method outlined above, we performed the full moment tensor inversions for the Rat Islands earthquake using a range of focal depths and provided the moment tensor solution obtained using a focal depth of 105 km.

5.1.1 Rayleigh wave records

Since the Rat Islands M_W **7.9** earthquake was very large, it generated very strong Rayleigh waves, recorded at stations throughout the world. Hundreds of these wave-form records were on the LHZ (long period, high gain, and vertical component) channel. We selected vertical records from 57 stations, filtered those records with a band-pass filter of 135 s to 500 s, and decimated the sampling interval from 1 s to 10 s. When the velocity of the mantle waves is assumed to be on the order of 3 km/s, the shortest wavelength is on the order of 400 km, which was approximately seven times of the rupture length of this M_W 7.9 earthquake. For such long-period mantle waves, the earthquake source can be treated as a point source.

5.1.2 Full moment tensor inversions

We conducted the following tests using a depth range from 80 km to 120 km with a depth increment of 5 km. For each focal depth, (1) we calculated the Green's functions, (2) took the same length for the observed Rayleigh wave record aligned with the synthetic seismogram, calculated at the focal depth, and (3) performed a full moment tensor inversion. The used source time function was three overlapping tri-angles. The time length of each bottom side was 20 s. **Table 1** lists the obtained

parameters for the full moment tensor solution using our preferred focal depth of 105 km. Compared to the scalar moment of the major DC in **Table 1**, the isotropic (ISO) is 2.88%. At all other depths from 80 km to 120 km (not listed), the ISO as a percentage of the total seismic moment was less than 6%. The smallest ISO occurred at the depth of 95 km.

The trace (trace = 3 × ISO; e.g., [11]) obtained in our inversions was small. As the trace quantifies a volume change in the source region (e.g., [11]), the small trace implied that the change of the earth's material volume in the source region was small. Compared to the major DC moment in **Table 1**, the minor DC moment was only 3.64%. The small minor DC and small ISO moments imply that the Rat Islands mainshock was dominated by a major DC event.

To evaluate the creditability of the solutions we need to compare the synthetic seismograms with those of the observed ones. **Figure 7** shows the moment tensor projection and the waveform comparison for the first four pairs of seismograms. The similarities between the synthetic and observed seismograms in both the waveform shapes and the maximum amplitude ratios were good. Other pairs at the remaining 53 stations had a similar quality. The good waveform fit implies that the moment tensor solution obtained is reasonable.
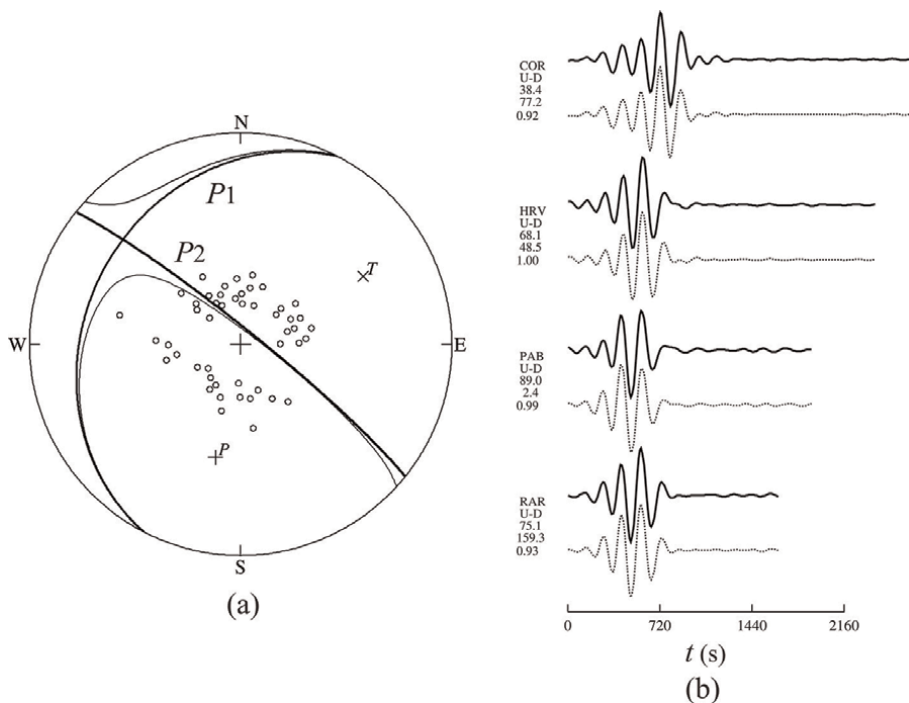
Figure 7.
(a) The lower hemispherical projection of the moment tensor solution obtained using a depth of 105 km. (b) Comparison between the first 4 observed and synthetic seismograms used in the inversion. For each pair, the upper trace is the observed (solid line), and the lower trace is the synthetic (dashed-line), generated with the solution displayed in panel (a). Both the observed and synthetic waveforms were filtered with a band-pass filter in the range of 135 s to 500 s. The symbols and numbers on the left side of each pair from the top to the bottom indicate the station name, vertical component, station distance in degree, station azimuth in degree, and the ratio between the observed and synthetic maximum amplitudes. The waveform shape similarity and the small bias of the ratios from an ideal case (ratio = 1) show that the fit is good.

5.2 Relocation of aftershocks with magnitude ≥ 4.5

There are two nodal plane solutions in **Table 1**. One nodal plane is close to the rupture plane of the M_W 7.9 mainshock. The hypocentral distribution of the aftershocks could help us to identify which nodal plane is close to the rupture plane. The requirement is that the errors in the hypocenters should be small. To obtain a distribution of hypocenters with small error, the aftershocks with magnitude ≥ 4.5 were relocated.

The error in the focal depth obtained using a conventional method may be large. The reason is that the travel times of the P and S phases are dominated by the station distance, not the focal depth. We used a combined procedure to relocate the aftershocks.

We searched tele-depth phase pP from the vertical component (BHZ) of teleseismic P-wave records retrieved from IRIS for 23 aftershocks that occurred

No	Date	Time	Lat.	Lon.	Depth	m	t-err	lat-err	lon-err
1	**2014-6-23**	**21:11:39.4**	**51.867**	**178.451**	**110.4**	**6.0**	0.40	6.1	2.7
2	**2014-6-23**	**21:30:44.7**	**51.850**	**178.363**	**110.3**	**6.0**	0.31	4.9	2.1
3	2014-6-23	22:03:27.1	52.064	178.471	126.7	5.1	0.52	7.8	3.6
4	2014-6-23	22:18:35.8	52.066	178.323	137.2	4.8	0.48	7.6	3.4
5	**2014-6-23**	**22:29:50.4**	**51.949**	**178.593**	**113.5**	**6.0**	0.45	6.5	3.1
6	2014-6-23	22:47:51.7	52.012	178.421	128.5	4.8	0.33	5.1	2.3
7	2014-6-23	23:33:51.4	51.923	178.391	109.2	4.5	0.33	5.0	2.3
8	2014-6-23	23:39:31.5	51.972	178.525	122.4	4.7	0.48	7.2	3.3
9	**2014-6-24**	**00:52:27.0**	**51.889**	**178.418**	**110.0**	**5.8**	0.34	5.1	2.3
10	2014-6-24	01:20:11.2	51.821	178.584	108.2	4.7	0.28	4.2	1.9
11	2014-6-24	04:33:04.8	52.029	178.444	131.1	4.5	0.47	7.2	3.3
12	2014-6-24	06:20:21.0	52.048	178.384	127.4	5.2	0.26	3.9	1.8
13	2014-6-24	06:55:29.2	52.001	178.446	123.6	4.9	0.43	6.5	3.0
14	2014-6-24	15:15:03.1	51.963	178.445	118.3	4.6	0.45	6.7	3.1
15	2014-6-25	00:03:03.9	51.983	178.452	121.9	5.1	0.32	4.9	2.2
16	2014-6-27	14:24:47.2	52.025	178.430	125.7	4.5	0.34	5.2	2.4
17	2014-6-28	16:24:35.0	52.020	178.393	122.8	4.6	0.29	4.4	2.0
18	2014-6-29	08:54:44.4	51.806	178.528	92.3	4.8	0.59	8.5	4.0
19	2014-7-03	04:43:40.7	51.929	178.571	118.3	5.0	0.47	6.4	2.7
20	**2014-7-03**	**19:06:47.2**	**52.020**	**178.428**	**124.7**	**5.8**	0.30	4.2	1.8
21	2014-7-04	13:57:38.1	51.978	178.477	119.4	4.5	0.48	7.2	3.3
22	2014-7-08	14:43:31.3	52.056	178.455	116.2	5.3	0.35	5.0	2.4
23	2014-7-11	05:53:25.6	51.847	178.508	101.0	4.7	0.58	8.6	4.0

*Note: lat. means latitude (°); lon., longitude (°); depth in km; m, magnitude; t-err, error in the origin time (s); lat-err, error in latitude (km); lon-err, error in longitude (km). The magnitude values are from the IRIS database. The bold text shows the 5 larger aftershocks.*

Table 2.
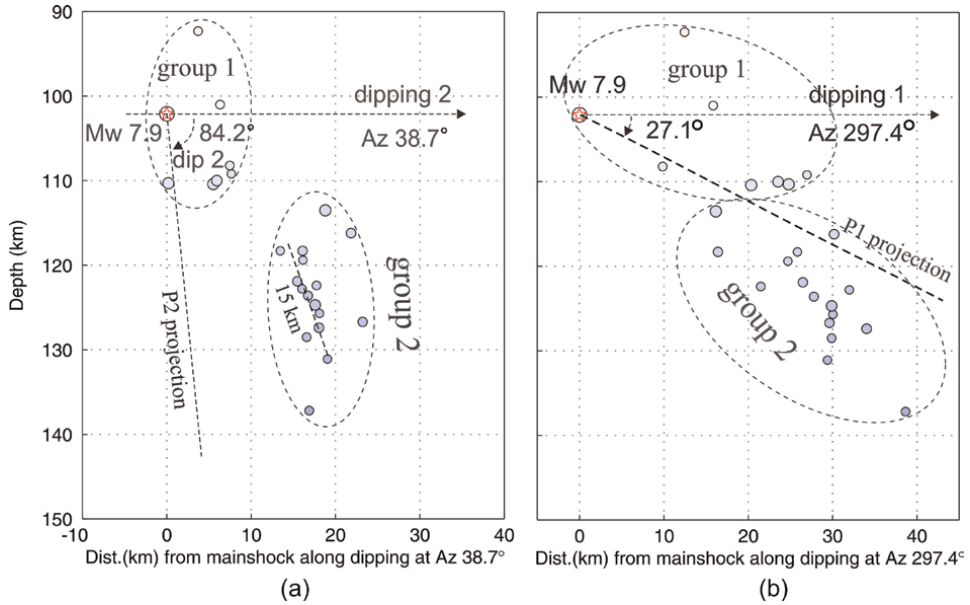*Catalog of the 23 relocated aftershocks.*

between June 23 and July 11, 2014, with magnitude ≥ 4.5, and determined focal depths for these 23 aftershocks using depth phase pP [16]. Then the arrival times of the recorded P and S phases at the same four regional stations for these 23 aftershocks were carefully measured, and the SEISAN [24, 25] was used to locate the epicenters at the focal depth obtained using the depth phase pP. The re-located 23 aftershocks were listed in **Table 2**.

The bird-view distribution of the obtained 23 hypocenters in **Figure 8** shows that the hypocenters are separated into two groups. Group 1 was formed by the hypocenters with the lighter color, while group 2 was formed by the hypocenters with the deeper color. **Figure 9a** shows the hypocenter projection onto a vertical plane perpendicular to the steep-dip plane (nodal plane 2). Eleven (11) aftershocks in group 2 formed a linear trend in the steep-dipping direction. The other hypocenters are scattered. **Figure 9b** shows the hypocenter projection onto a vertical plane, perpendicular to the shallow-dip plane, indicated with P1 projection (nodal plane 1). No linear trend was formed by the hypocenters at the dipping (27.1°) direction of the shallow-dip plane.

In order to observe a spatial trend, we simulated a plane using the hypocenters of the 23 well relocated aftershocks. **Figure 10** shows the simulated spatial plane. Its strike is at Az 258.2°; its dip angle is 44.8°. To clearly observe the dipping of the simulated plane we projected the hypocenters of the mainshock and the 23 aftershocks onto a vertical plane which is along the simulated dipping direction. **Figure 11** shows that most hypocenters were distributed along the tilted line, the projection of the simulated plane, at dip angle 44.8°. This angle is close to the one (47.7° in Figure 4a)
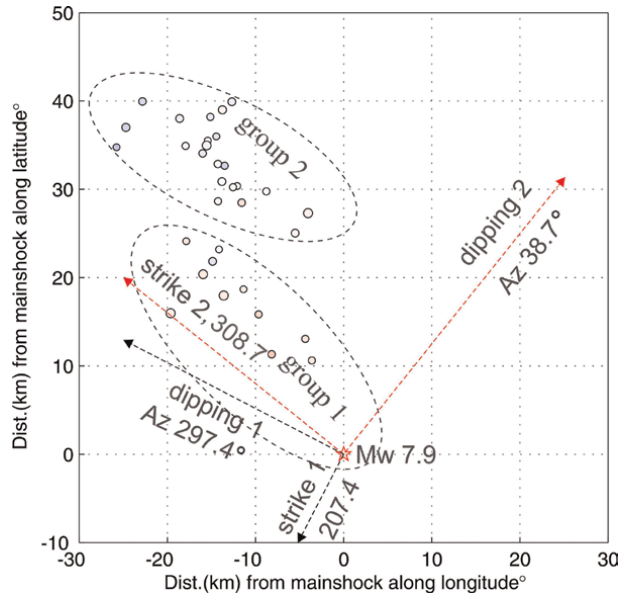
Figure 8.
Distribution of the epicenters for the mainshock and the 23 relocated aftershocks. Each solid circle shows an epicenter. It was color-coded with focal depth. A deeper color shows a deeper depth. The size of each circle is proportional to the magnitude. The epicenters are separated into a shallower group (group 1) and a deeper group (group 2). The strike and the dipping directions of two nodal planes of the mainshock were indicated with strike 1 and dipping 1 (shallow-dip plane); strike 2 and dipping 2 (steep-dip plane), respectively. The latitude and longitude of each epicenter were converted to a Cartesian coordinate system for distance comparison. The star with Mw 7.9 shows the epicenter of the mainshock.

Figure 9.
Hypocenter projections. (a) The hypocenters of the mainshock and the 23 relocated aftershocks projected onto a vertical plane that is perpendicular to the steep-dip nodal plane (P2). The tilted dashed line indicated with 84.2° is the projection of the steep-dip plane. The number 84.2 is the dip angle. Eleven (11) aftershocks in group 2 formed an about 15 km linear trend along the steep-dip plane. (b) The hypocenters of the mainshock and the 23 relocated aftershocks are projected onto a vertical plane that is perpendicular to the shallow-dip plane (P1). The tilted dashed line indicated with 27.1° is the projection of the shallow-dip plane. It was found that no linear trend was formed along a nodal plane (P1).
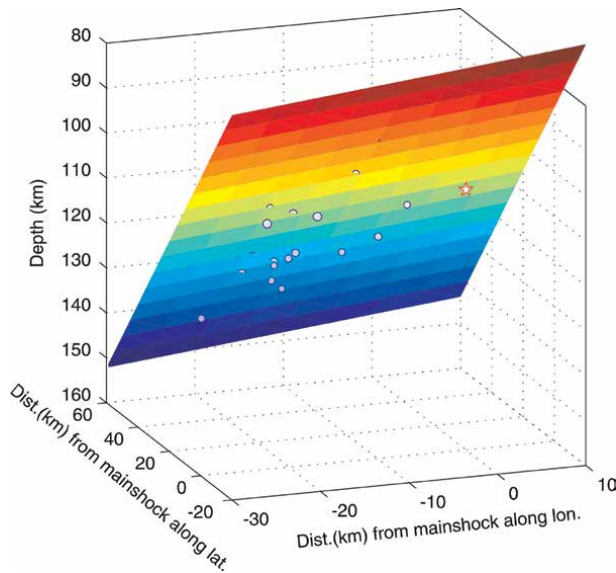
Figure 10.
*The simulated spatial plane uses the hypocenters of the 23 well-relocated aftershocks (**Table 2**). The simulated strike is Az 258.2°; the dip angle is 44.8°. The plane dips at Az 348.2° (from north to west 11.8°). The red star shows the initial location of the mainshock.*
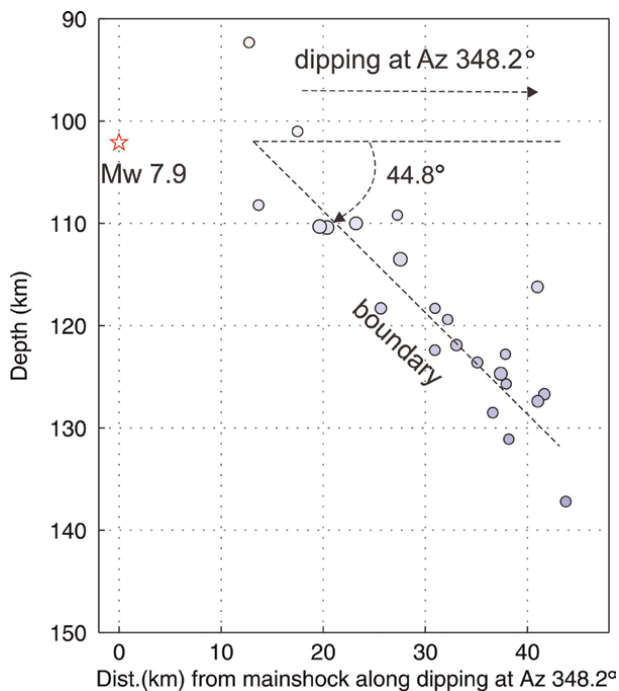
Figure 11.
The hypocenters of the mainshock and the 23 relocated aftershocks are projected onto a vertical plane that is along the simulated dipping direction (perpendicular to the simulated spatial plane. The tilted dashed line indicated with 44.8° (dip angle) is the projection of the simulated plane. The red star shows the initial location of the mainshock. The relatively narrow seismicity belt may be assumed to be close to the boundary between the Pacific Plate and the North American plate beneath the Rat Islands region.

obtained by simulating hypocenters of the earthquakes occurred before the mainshock. They are neither close to the steep-dip angle 84.2° nor the shallow-dip angle 27.1°. The trend may be close to the boundary between the Pacific plate and the north America plate beneath the Rat Islands region.

5.3 Source rupture inversions for the Rat Islands M_W 7.9 earthquake

We performed the source rupture inversions for the Rat Islands earthquake using the procedure outlined above and the inversion code developed by Kikuchi and Kanamori, provided by Lingling Ye (personal communication) with a subroutine we revised to speed up the calculations of the Green's functions.

5.3.1 Initial depth selection for the rupture model

For the Rat Islands mainshock, the focal depth published online by ISC is 102.1 km; the centroid depth calculated by the G-CMT group is 104.3 km. The shallowest focal depth for the 23 aftershocks we relocated is 92.3 km. From the consideration that 104.3 km is the centroid depth, the mainshock is a large one with normal faulting, the rupture initial point may be shallower than the centroid depth by tens of kilometers; therefore, we took 92 km as the initial rupture depth. This value is close to that (95 km) used by Ye et al. [3].

*5.3.2 Source rupture inversion results using the steep-dip nodal plane*

In the rupture inversion procedure, the nodal plane 2 of the full moment tensor solution obtained using a depth of 105 km, was used as the rupture plane (**Table 1**; strike 308.7°, dip 84.2° and slip -116.5°). The epicenter (51.7028°N; 178.6428°E) used in the inversion was retrieved from the IRIS website. The fault model dimensions are 270 km × 210 km, while the size of each sub-fault is 15 km × 15 km. The total number of sub-faults is 252.

To perform the source rupture inversion, we needed a rupture propagation velocity (V_R). The rupture velocity (V_R) is often assumed to be a fraction of the shear wave velocity (β). For example, Stein and Wysession [26] assumed a formula $V_R = 0.7\beta$. To obtain a proper rupture velocity, we performed trial inversion tests using a V_R from 1.3 km/s to 2.6 km/s with an increment of 0.1 km/s. **Figure 12** shows the variance (the misfit between the observed and the synthetic waveforms) change with rupture velocity when the initial rupture depth was taken 92 km. The minimum variance (0.1570) occurred at a V_R = 2.0 km/s.

Figure 13 shows the source time function and the final slip distribution obtained using an initial depth of 92 km and a V_R = 2.0 km/s. The initial point is indicated by a star sign *. The largest slip (3.52 m) occurred at a depth of about 120 km. The rupture area is about 60×60 km^2. **Figure 14** shows a waveform comparison between the observed and synthetic seismograms. The fit in each pair between the observed (upper) and synthetic (bottom) traces was generally good, except that at station AAK. This station is in the strike direction of the steep-dip nodal plane.

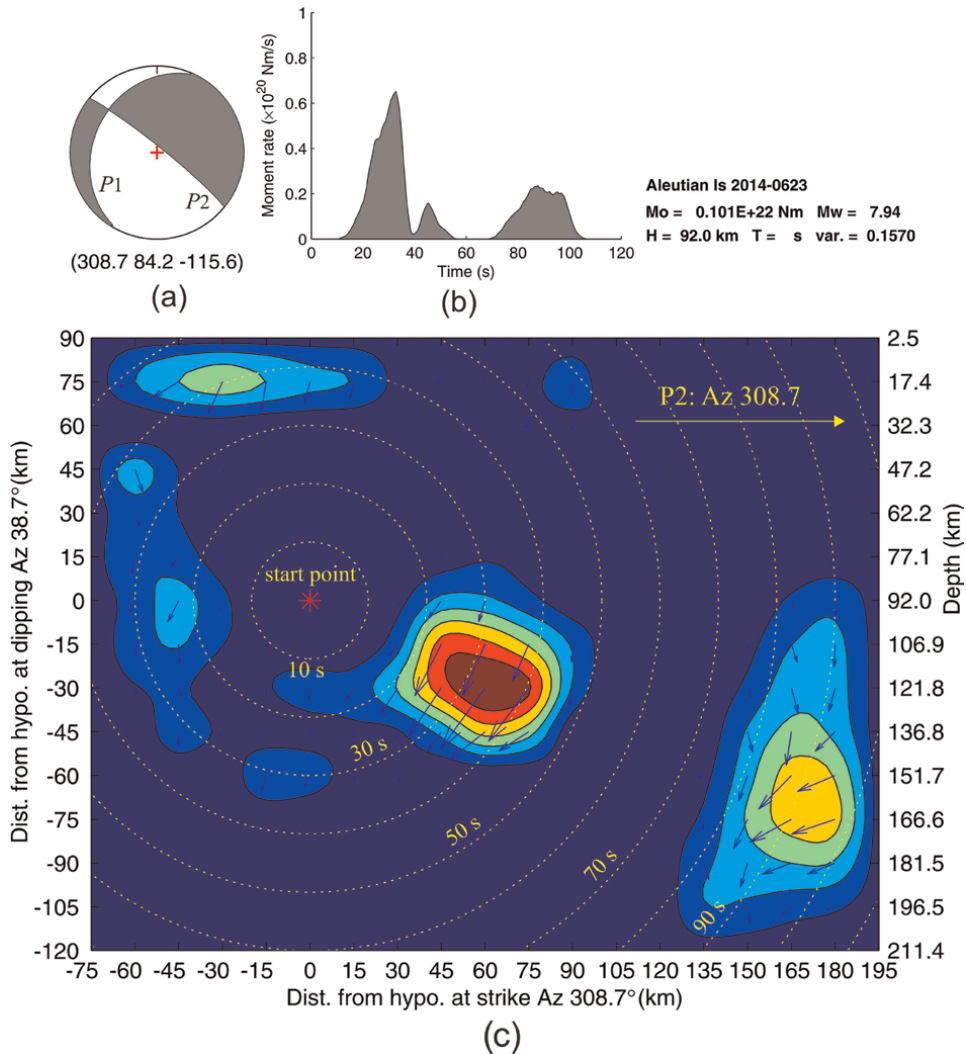*5.3.3 Source rupture inversion results using the shallow-dip nodal plane*

Based on the well-relocated hypocenter trend, we used the steep-dip plane as the rupture plane. This was the same as that by Twardzik and Ji [5]. However, Ye et al. [3]
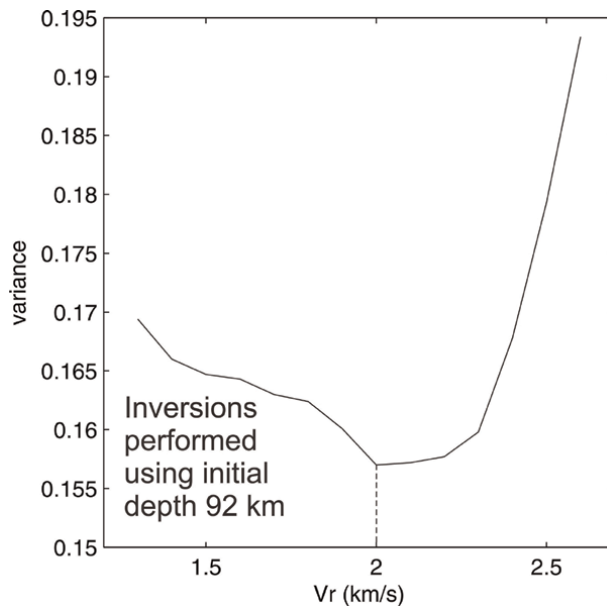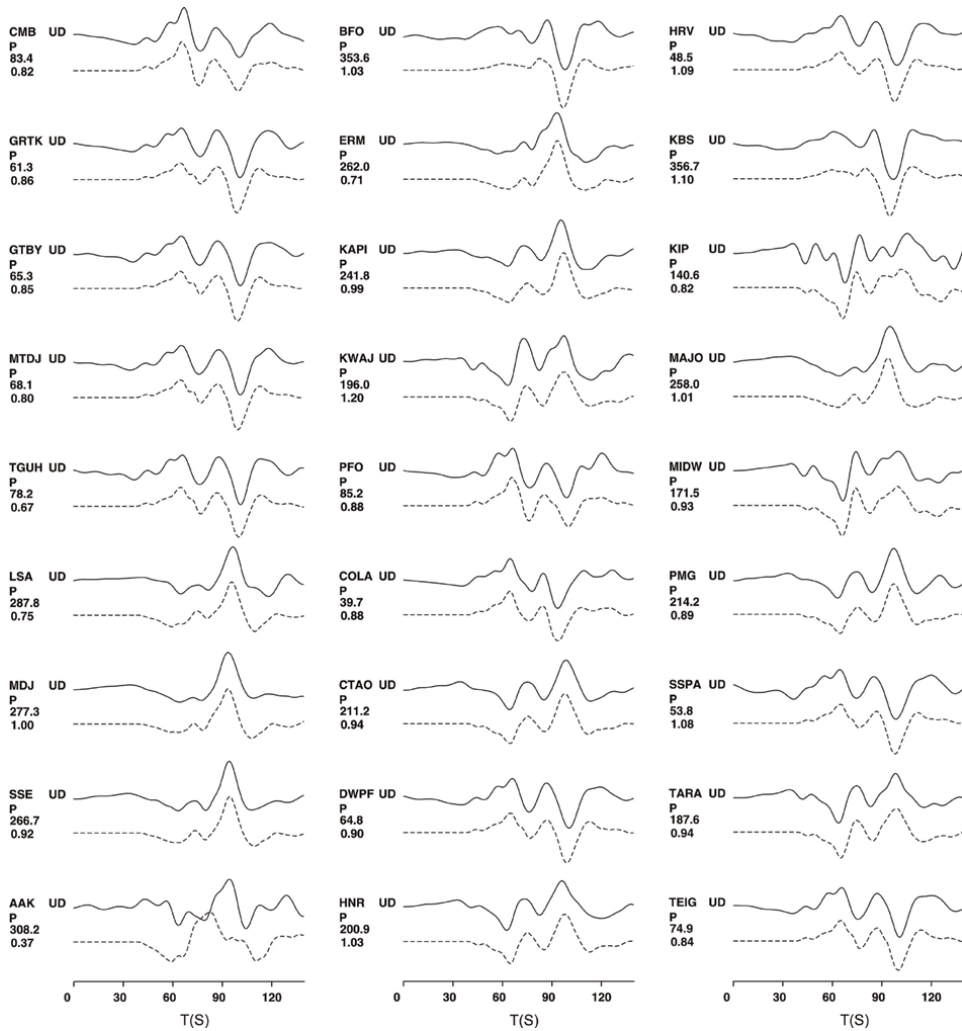

Figure 12.
The variance changes with rupture velocity. The minimum variance occurred at a rupture velocity of 2.0 km/s.

Figure 13.
*(a) Lower hemispherical projection of the double couple focal mechanism (**Table 1**). (b) Source time function. (c) Distribution of the slip on the steep-dip nodal plane (**Table 1**). The star sign * with "start point" shows the location of the initial rupture. The arrow at a sub-fault shows the direction and the amount of the slip. The maximum slip was about 3.52 m and occurred at a depth of about 120 km. The used rupture velocity V_R = 2.0 km/s, at which the variance reached the minimum (**Figure 12**). The dashed circles show the rupture propagation.*

found that the back-projection images were more straightforwardly reconciled with the shallow-dip plane. They also found their waveform misfits were comparable when the steep-dip plane or the shallow-dip plane was used as the causative plane, and some signals were better fitted using the steep-dip plane. As a result, their preference for the shallow-dip plane was mild. We also performed trial inversion with the key parameters used by Ye et al. [3], V_R = 1.5 km/s, and the initial depth = 95 km. **Figure 15** shows the rupture distribution we obtained. The largest slip (3.33 m) occurred at a depth of about 115 km within the largest patch. **Figure 16** shows a waveform comparison between the observed and synthetic seismograms. The fit in each pair between the observed (upper) and synthetic (bottom) traces was also good.

Figure 14.
Comparison between the 27 observed and synthetic seismograms. For each pair of waveforms, the upper trace is the observed (solid line), and the lower trace is the synthetic (dashed-line), generated with the slip distribution in **Figure 13c**. *Both the observed and synthetic waveforms were filtered with a band-pass filter in the range of 0.01 Hz to 0.1 Hz. The symbols and numbers on the left side of each pair from the top to the bottom indicate the station name, P-wave vertical component, station azimuth in degrees, and the ratio between the observed and synthetic maximum amplitudes. As shown, the observed and the synthetic seismograms have a good fit in shape, except at station AAK. The average variance is 0.1570. All the ratios between the maximum amplitudes are close to 1 (the ideal case), except at station AAK. This station is in the strike direction of the steep-dip plane.*

To observe the misfit between the observed and the synthetic seismograms, we found the fit at station AAK (Az 308°) was better in **Figure 16** than that in **Figure 14**. Ye et al. [3] found that the shallow-dip fault plane toward the northwest provides better matches to P waveforms at azimuths from 300° to 340° (their Figure S2) than does the steep-dip fault plane solution (their Figures S3 and S4). This result is exactly the same as that we obtained.

To confirm that the record at AAK does not have a problem, we retrieved the records in the station AAK region, plotted the seismograms, and found the waveform shapes are similar (**Figure 17**). This implies that the recording quality at AAK does not
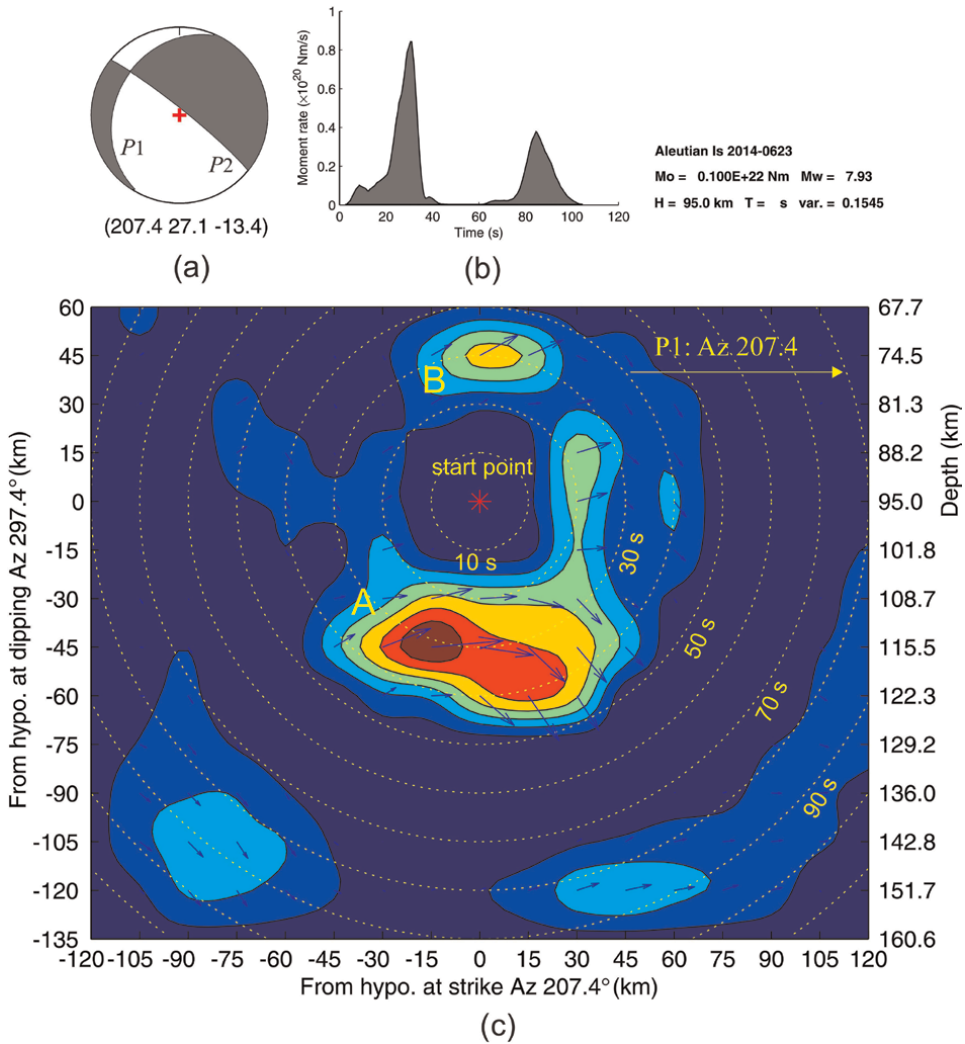
Figure 15.
*(a) Lower hemispherical projection of the double couple focal mechanism (**Table 1**). (b) Source time function. (c) Distribution of the slip on the shallow-dip nodal plane 1 (**Table 1**). The star sign * with "start point" shows the assigned location of the initial rupture. The arrow at a sub-fault shows the direction and the amount of the slip. The obtained maximum slip is about 3.33 m, occurred at about a depth of 115 km. The used rupture velocity V_R = 1.5 km/s. The dashed circles show the rupture propagation.*

have a problem, so the better waveform fit at AAK support to select the shallow-dip plane as the rupture plane.

5.3.4 Source rupture inversion results using the simulated plane

Based on the simulated spatial plane obtained using the well-relocated hypocenters, we found the majority of the hypocenters distributed around a mild dipping plane (**Figure 11**; dip 44.8°). We may assume that the mainshock ruptured on that plane. We performed trial inversions with the values of input parameters, rupture velocity V_R = 1.5 km/s, and the initial depth = 95 km. **Figure 18** shows the rupture distribution obtained. **Figure 19** shows a waveform comparison between the observed
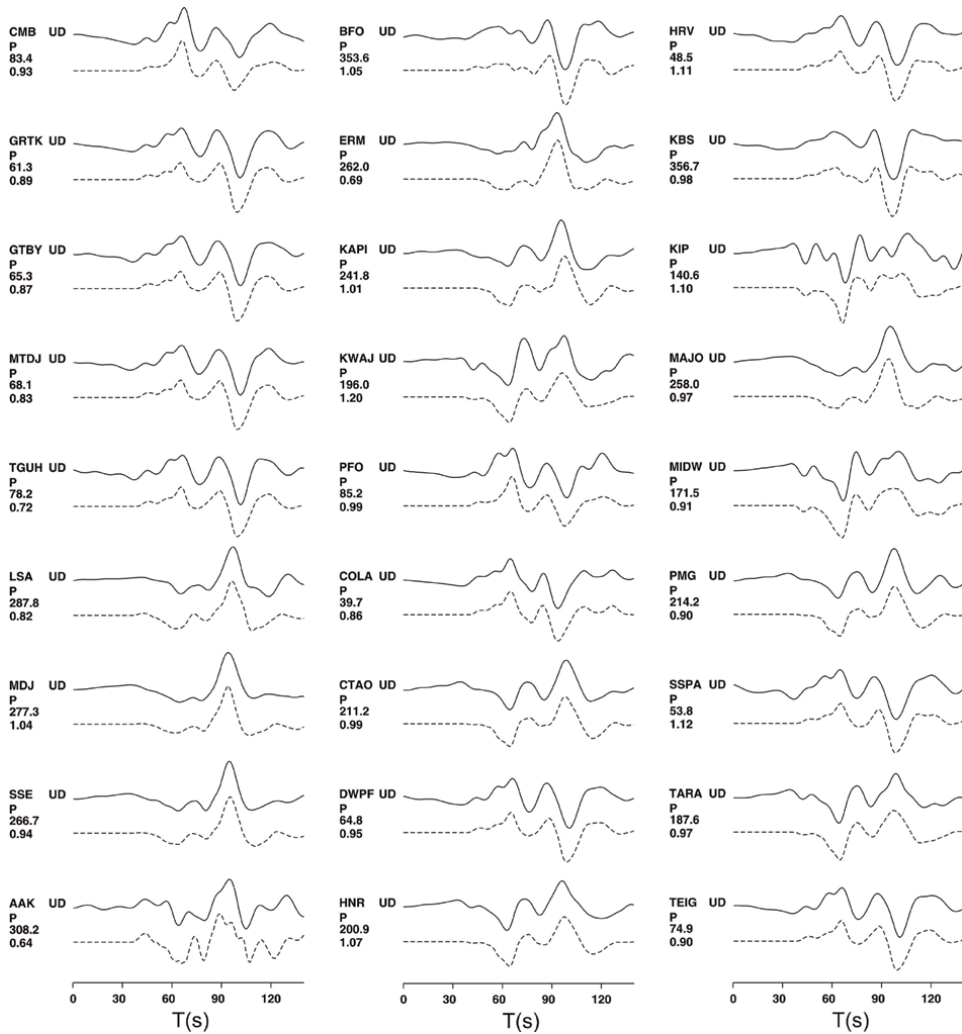
Figure 16.
*Comparison between the 27 observed and synthetic seismograms. For each pair of waveforms, the upper trace is the observed (solid-line); the lower trace is the synthetic (dashed-line), generated with the slip distribution in **Figure 15c**. The observed waveforms are exactly the same as those in **Figure 14**. The overall fit between the observed and the synthetic seismograms is also good. The fit at station AAK is better than that, and the average variance (0.1545) is slightly smaller than that, in **Figure 14**.*

and synthetic seismograms. The observed waveforms are exactly the same as those in **Figure 16**. The fits at stations AAK, KIP, and MIDW are not good; the ratio of the maximum amplitudes at several stations is not close to 1 (the ideal ratio is 1). The average variance (0.2720) is larger than those in **Figures 14** and **16**. The obtained maximum slip is about 3.36 m, which occurred at about a depth of 70 km within a smaller patch. Logically the maximum slip should occur at a depth below the initial depth (95 km), owing to the normal faulting. Since the misfit at several stations is not good, the ratio between the observed and synthetic maximum amplitudes at several stations is far from the ideal value, and the maximum slip occurred at a too shallow depth, the simulated plane is not acceptable to be the rupture plane.
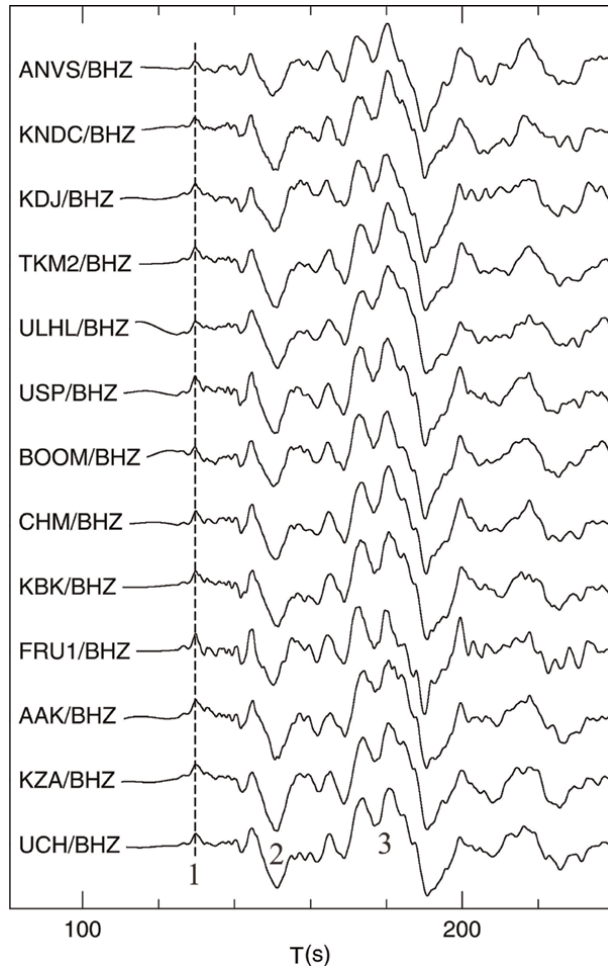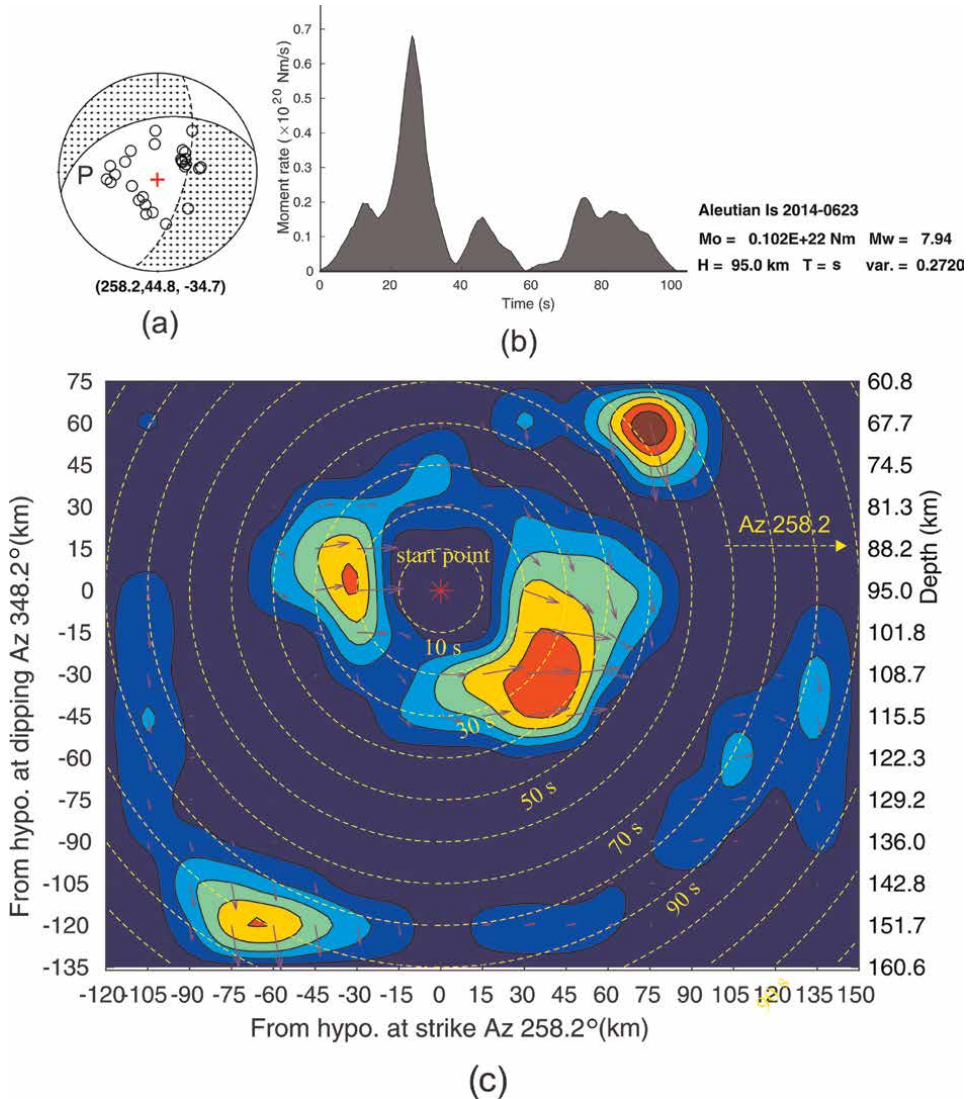
Figure 17.
Vertical P-wave displacement records in station AAK region (63°N–66°N; 50°W–54°W). It is clear that the shapes of these waveform records are similar, showing that the record at AAK does not have a problem. Along the bottom trace, UCH/BHZ three ruptures are indicated. The first one is small, the second one is larger, and the third is a combination of at least two large ruptures. The station (UCH) distance is 7300 km.

6. Discussion and conclusion

This M_W 7.9 event intrigued scientific interests and generated issues. In this section, we discuss some issues and provide some conclusions.

Beneath the Rat Islands at a depth of 100 km, the shear wave velocity is about 4.5 km/s. Using the PREM earth model and the assumed rupture velocity formula $V_R = 0.7\beta$, $V_R = 0.7 \times 4.5 = \sim 3.1$ km/s. This value is much larger than what was obtained using the back-projection method (1.5 km/s) by Ye et al. [3]. The average rupture velocity obtained by Twardzik and Ji [5] was 2.4 km/s from modeling the steep-dip plane and 2.3 km/s from the shallow-dip plane. The optimal rupture velocity we obtained from trial inversion tests at the initial depth of 92 km was 2.0 km/s. For the trial tests with an initial depth of 84 km, the optimal rupture velocity was 1.8 km/s, and 2.1 km/s at the initial depth of 105 km. Therefore, the rupture velocities of around 2.0 km/s may be reasonable for the Rat Islands M_W 7.9 earthquake.

Figure 18.
*(a) Lower hemispherical projection of the simulated focal mechanism. (b) Source time function. (c) Distribution of the slip on the simulated plane. The star sign * with "start point" shows the assigned location of the initial rupture. The arrow at a sub-fault shows the direction and the amount of the slip. The obtained maximum slip is about 3.36 m, occurred at about a depth of 70 km. The used rupture velocity V_R = 1.5 km/s. The dashed circles show the rupture propagation.*

Two nodal planes can be retrieved from an earthquake moment tensor solution. One of them is assumed to be close to the rupture plane and used for establishing a rupture slip model. Ye et al. [3] preferred the shallow-dip plane for rupture modeling. Twardzik and Ji [5] relocated larger aftershocks. Based on the relocated hypocenters they selected the steep-dip plane as the rupture plane. When Miyazawa [6] calculated the dynamic changes in the Coulomb Failure Function for the M_W 7.9 mainshock, the shallow-dip plane of the G-CMT was used. Macpherson and Ruppert [2] relocated the aftershocks. They found that the seismicity is dipping at a moderate angle to the northwest and does not align well with any dip. They also found the shallow-dip plane
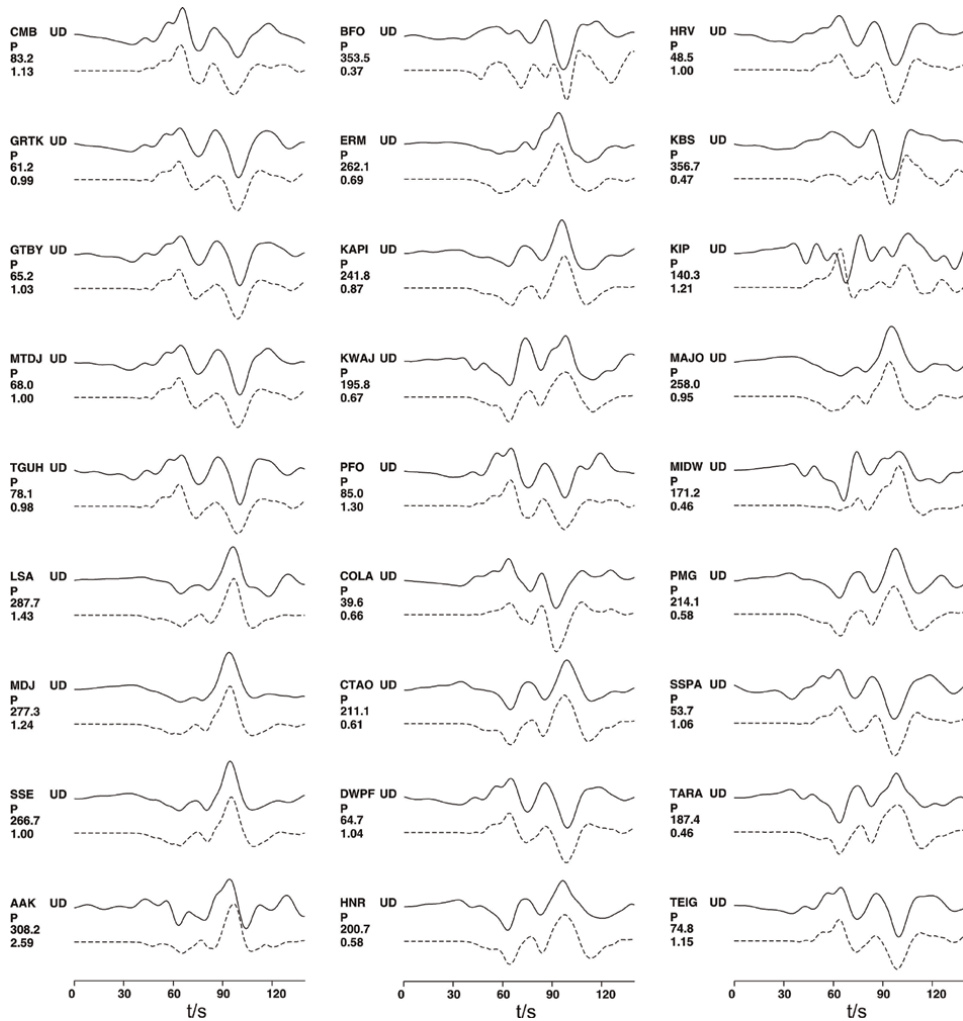
Figure 19.
Comparison between the 27 observed and synthetic seismograms. For each pair of waveforms, the upper trace is the observed (solid-line); the lower trace is the synthetic (dashed-line), generated with the slip distribution in **Figure 18c**. *The observed waveforms are exactly the same as those in* **Figure 16**. *The fits at stations AAK, KIP, and MIDW are not good; the maximum amplitudes ratio at several stations is not close to 1 (AAK 2.58; BFO 0.37; KBS 0.47; MIDW 0.46; TARA 0.46). All these numbers are far from the ideal ratio (1). The average variance (0.2720) is also larger than those in* **Figure 14** *(0.1570) and* **Figure 16** *(0.1545).*

does align well with the mainshock hypocenter, so they preferred the moderately dipping nodal plane as the rupture plane of the M_W 7.9 mainshock. Florez and Prieto [7] recalculated the focal depths for a subset of 17 $M_W > 4.9$ aftershocks using the time difference between a tele-depth phase pP and direct P phase. Based on their results they confidently assigned the causative fault plane to the steep one. To identify which nodal plane is close to the rupture plane we also relocated the larger aftershocks. We carefully recalculated the focal depths using pP-P times and relocated the epicenters at the recalculated depths for 23 aftershocks with mb > 4.5, which occurred within 20 days after the mainshock. We found a linear segment about 15 km long formed by 11 aftershocks in the deeper group (**Figure 9a**) is approximately parallel to the dipping of

the steep-dip plane, but no linear segment along the dipping of the shallow-dip plane was formed (**Figure 9b**). Based on the above features we deduced that the steep-dip nodal plane is close to the rupture plane of the mainshock.

When the steep-dip plane was used as the rupture plane, the major rupture patch we retrieved was distributed in a depth range from about 80 km to 140 km (**Figure 13**, the largest patch). The maximum slip we obtained was about 3.5 m, which was well consistent with that (3.7 m) obtained by Twardzik and Ji [5].

We also performed trial inversion using the shallow-dip plane as the rupture plane and found the average variance (0.1545) is almost the same as that (0.1570) obtained using the steep-dip plane. This implies that the rupture plane indeed cannot be identified using the mismatch between the observed and synthetic seismograms.

Since the majority of aftershocks are distributed along a moderate-dipping plane, it may be thought that the mainshock ruptured along the moderate-dipping plane. Test inversions using the simulated plane as the rupture plane were performed. It was found that the waveform fits at stations AAK, KIP, and MIDW are not good; and the ratio of the maximum amplitudes at several stations is far from the ideal ratio. The average variance (0.2720) is much larger than those in **Figures 14** and **16**; so, the simulated moderate-dipping plane was denied to be the rupture plane of the mainshock.

Based on the assumption that the immediate aftershocks occurred on the rupture plane of the mainshock or near the edges of the rupture [27], aftershock distributions are often used to select the rupture plane from the two nodal planes. When Kikuchi and Kanamori [28] studied the 1994 Shikotan M_W 8.2 earthquake, they found the aftershocks seem to favor the steep nodal plane as the fault plane. The steep-fault model resulted in a better waveform match than the shallow-dip fault model. Delouis and Legrand [29] found that the aftershocks of an intermediate-depth large earthquake delineate a low angle plane, and the low angle fault model provides a much better fit for the strong-motion waveforms. However, for this M_W 7.9 earthquake, the majority of aftershocks were distributed neither along the steep-dip, nor the shallow-dip nodal plane. The waveform fits for both nodal planes are almost the same.

A hypothesis may be able to explain that the majority of aftershocks occurred along a moderate-dipping plane, which may be close to the boundary between the Pacific plate and North American plate beneath the Rat Islands region—most parts of the huge rupture fault were immediately locked under a tremendous pressure blow about 80 km of the depth after the occurrence of the mainshock, the stress in the source region was re-distributed, and migrated to the boundary region beneath the Rat Islands region, so most aftershocks distributed along that boundary, rather than the rupture plane of the mainshock.

This huge earthquake is very unique. For example, it had a vigorous aftershock sequence; other intermediate-depth earthquakes were usually followed by few or no aftershocks [1]. Solve the mysteries behind the observed phenomena requires more studies.

Acknowledgements

Planetary Sciences, University of California, Santa Cruz, California provided a version of the source rupture modeling program. We are grateful for her help.

Data sources

Author details

Dariush Motazedian and Shutian Ma*
Department of Earth Sciences, Carleton University, Ottawa, Ontario, Canada

*Address all correspondence to: shutian33@yahoo.ca

IntechOpen

References

[1] Pavlis GL, Hamburger MW. Aftershock sequences of intermediate-depth earthquakes in the Pamir-Hindu Kush seismic zone. Journal of Geophysical Research. 1991;**96**(B11): 18,107-18,117. DOI: 10.1029/91JB 01510

[2] Macpherson KA, Ruppert NA. Evidence of Wadati-Benioff zone triggering following the M_w 7.9 Little Sitkin, Alaska intermediate depth earthquake of 23 June 2014. Geophysical Research Letters. 2015;**42**:6269-6277. DOI: 10.1002/2015GL065023

[3] Ye L, Lay T, Kanamori H. The 23 June 2014 M_w 7.9 Rat Islands archipelago, Alaska, intermediate depth earthquake. Geophysical Research Letters. 2014;**41**: 6389-6395

[4] Waldhauser F, Ellsworth WL. A double-difference earthquake location algorithm: method and application to the northern Hayward fault, California. Bulletin of the Seismological Society of America. 2000;**90**(6):1353-1368

[5] Twardzik C, Ji C. The M_W7.9 2014 intraplate intermediate-depth Rat Islands earthquake and its relation to regional tectonics, Earth Planet. Science Letters. 2015;**431**:26-35. DOI: 10.1016/j. epsl.2015.08.033

[6] Miyazawa M. Seismic fatigue failure may have triggered the 2014 M_w7.9 Rat Islands earthquake. Geophysical Research Letters. 2015;**42**:2196-2203. DOI: 10.1002/2015GL063036

[7] Florez MA, Prieto GA. Precise relative earthquake depth determination using array processing techniques. Journal of Geophysical Research Solid Earth. 2017; **122**:4559-4571. DOI: 10.1002/2017 JB014132

[8] Dziewonski A, Anderson D. Preliminary reference earth model. Physics of the Earth and Planetary Interiors. 1981;**25**:297-356

[9] DeMets C, Gordon RG, Argus DF. Geologically current plate motions. Geophysical Journal International. 2010; **181**(1):1-80. DOI: 10.1111/j.1365-246X.2009.04491.x

[10] Vavrycuk V. Moment Tensors: Decomposition and Visualization, in book: Encyclopedia of Earthquake Engineering. Berlin, Heidelberg: Springer; 2015. DOI: 10.1007/978-3-642-36197-5_288-1

[11] Jost ML, Herrmann RB. A Student's guide to and review of moment tensors. Seismological Research Letters. 1989;**60**: 37-57

[12] Kikuchi M, Kanamori H. Inversion of complex body waves-III. Bulletin of the Seismological Society of America. 1991; **81**(6):2335-2350

[13] Gilbert F, Masters G. Low-Frequency Seismology. San Diego, USA: University of California; 1989

[14] Ma S, Adams J. Estimation of moment tensor for moderate earthquakes in eastern Canada and its vicinity by modeling surface waveforms (open file draft to Natural Resources Canada, 110 pages). 2002

[15] Crotwell HP, Owens TJ, Ritsema J. The TauP Toolkit: Flexible seismic travel-time and ray-path utilities. Seismological Research Letters. 1999;**70**: 154-160

[16] Motazedian D, Ma S. Source parameter studies on the 8 January 2017

Resolute, Nunavut, Canada M_W 6.1 earthquake. Seismological Research Letters. 2018;**89**:1030-1039

[17] Lienert BRE, Berg E, Frazer LN. Hypocenter: An earthquake location method using centered, scaled, and adaptively least squares. Bulletin of the Seismological Society of America. 1986; **76**:771-783

[18] Lienert BRE. Report on Modifications Made to Hypocenter. Technical Report, Institute of Solid Earth Physics, University of Bergen, Bergen, Norway; 1991

[19] Lienert BRE, Havskov J. A computer program for locating earthquakes both locally and globally. Seismological Research Letters. 1995;**66**: 26-36

[20] Hartzell SH, Heaton TH. Inversion of strong ground motion and teleseismic waveform data for the fault rupture history of the 1979 Imperial Valley, California, earthquake. Bulletin of the Seismological Society of America. 1983; **73**:1553-1585

[21] Lawson C, Hanson R. Solving Least Squares Problems. Philadelphia, PA: Society for Industrial and Applied Mathematics; 1995

[22] Goffe WL, Ferrier GD, Rogers J. Global optimization of statistical functions with simulated annealing. Journal of Econometrics. 1994;**60**:65-99

[23] Yagi Y, Mikumo T, Pacheco J, Reyes G, G. Source rupture process of the Tecomán, Colima, Mexico earthquake of 22 January 2003, determined by joint inversion of teleseismic body-wave and near-source data. Bulletin of the Seismological Society of America. 2004; **94**(5):1795-1807. DOI: 10.1785/ 012003095

[24] Havskov J, Ottemöller L. SeisAn earthquake analysis software. Seismological Research Letters. 1999; **70**:5

[25] Havskov, J., L. Ottemöller, and P. Voss (2014). SEISAN tutorial (online).

[26] Stein S, Wysession M. An Introduction to Seismology, Earthquake, and Earth Structure. Malden, MA: Blackwell Publishing; 2003

[27] Mendoza C, Hartzell SH. Aftershock patterns and main shock faulting. Seismological Society of America. 1988; **78**:1438-1449

[28] Kikuchi M, Kanamori H. The Shikotan earthquake of October 4, 1994: Lithospheric earthquake. Geophysical Research Letters. 1995;**22**:1025-1028

[29] Delouis B, Legrand D. Mw 7.8 Tarapaca intermediate depth earthquake of 13 June 2005 (northern Chile): Fault plane identification and slip distribution by waveform inversion. Geophysical Research Letters. 2007;**34**(1). Article No. L01304

Chapter 2

Investigation of the Dynamics of the Seismic Regime in the Kamchatka Region Based on the Combination of Methods of Nonequilibrium Thermodynamics and the Axiomatic Method of Kolmogorov A.N.

Vadim Bogdanov and Aleksey Pavlov

Abstract

In the presented chapter, the preparation of an earthquake on the example of the Kronotsky event that occurred on 1997-12-05 with a magnitude Mc = 7.7 is considered from the standpoint of nonequilibrium thermodynamics, in which the evolution of systems is due to self-organization processes. With this approach, the lithosphere is an open nonlinear system in which, due to internal dissipation and the coordinated interaction of its elements, a self-organization process can occur, leading the system to a critical state. In this case, the scales of the connection between different parts of the nonlinear structure change, that is, the scales of temporal and spatial correlation change. However, the methods of seismological monitoring of the stress-strain geoenvironment can be expanded if, for its study, the method of calculating the probability distribution of earthquakes for various random events is used, based on the axiomatic approach of Kolmogorov A.N., applied to the catalog of Kamchatka earthquakes. This makes it possible to follow the dynamics of correlated spatial and temporal changes in the probability distribution of random variables for weak earthquakes preceding a strong event using probabilistic methods.

Keywords: nonequilibrium thermodynamics, open systems, unstable dissipative nonlinear systems, self-organization processes, Kolmogorov's axiomatic method, probability space, random variables and events, earthquake

1. Introduction

The study of the processes that determine the evolution of open physical systems has led scientists to understand the fact that their development is due to unstable dissipative nonlinear systems [1]. Moreover, the instability of open systems is

understood as such that, at characteristic observation times, as a result of the influence of minor external perturbations, it comes to a deviation in its state by an amount comparable to the characteristic values of the quantities that determine this state. In turn, an open nonequilibrium system that is in a stationary state far from thermodynamic equilibrium, which is provided by a balance between energy dissipation within the system itself and the influx of energy coming from outside, is called a dissipative system or a dissipative structure [1]. In addition, in an open system, due to the coordinated interaction of many of its elements through intensive (flow) exchange of matter and energy with the environment in nonequilibrium conditions, an ordering process (spatial, temporal, or spatio-temporal), called self-organization, can occur. In other words, in such systems, the coordinated behavior of subsystems is observed, as a result of which the degree of its ordering increases, i.e. entropy decreases. The conducted research in the field of "dissipative structures" led to the conclusion that the process of "self-organization" occurs much faster in the presence of external and internal disturbances (noise) in the system. Thus, noise phenomena lead to an acceleration of the self-organization process.

It is clear that any real open physical system is continuously under the action of small external and internal perturbations. Based on the most general considerations, it can be assumed that an earthquake is the result of a manifestation of a certain set of processes in the lithosphere, which is a nonlinear unstable system and which is under the action of the background field of external disturbances. A regular process, determined by compression or extension of the lithospheric plate, or other physical and chemical phenomena in a seismically active region on a global scale, is affected by a certain set of external disturbances in a consistent system of geospheres, determined by the system of solar-terrestrial relations. These perturbations excite the development of various instabilities, ultimately leading to local (in the volume of the focus) destruction of the structure, which is in a special limiting (critical) state. This state is characterized by a certain but rather complex balance between fluctuations in the system and its average characteristics, which determine the macroscopic state.

Thus, from the most general considerations, we can consider the preparatory stage of an earthquake as the development of instability that forms in local areas of the lithosphere against the background of external disturbances that arise in the chain "Sun—heliosphere—magnetosphere—ionosphere—neutral atmosphere—lithosphere."

The proposed work uses the catalog of earthquakes recorded by the Kamchatka regional network of seismic stations of the Kamchatka branch of the Geophysical Service of the Russian Academy of Sciences (KB GS RAS). This catalog can be divided into two parts [2]. The first part includes events from 1962 to 2009. By 2010, the approaches and methods for calculating the main parameters have changed, and the conditions for the formation of the catalog in close to real time have developed. This second part of the catalog contains data on earthquakes from 2010 to the present and is formed with a delay of 1–7 days. The Kronotskoe earthquake (1997-12-05) falls into the first part.

It should be noted that the greatest difficulties in processing the parameters of the catalog arise when determining the depth of an event. Each real value of the depth h_{real} is within the corresponding error interval $\pm \Delta h_{mist}$ relative to the depth h_{met} calculated by a certain method. Strictly speaking, the relation $h_{real} \in h_{met} \pm \Delta h_{mist}$ holds. That is, the real depth h_{real} can take any value from the set of values covered by the interval $h_{met} \pm \Delta h_{mist}$. Therefore, in this fuzzy situation, we will be interested not in some undefined value of the depth h_{real}, which falls somewhere in the corresponding error interval, but in the depth value h_{met} itself, calculated according to

a certain method, for which the error interval $\pm \Delta h_{mist}$ is calculated. In this case, the depth value h_{met} is a fixed value and will depend only on the method of its calculation. For a homogeneous catalog, this technique is the same for all calculated depths. In the analysis carried out in this chapter, we will follow the dynamics of the trend, which would indicate a tendency in the distribution of the depths of various "background" earthquakes that form on large spatial scales, to group at the depth of the source of the impending major event. In other words, we will be interested in the question: at what depths h_{met} do "background" events fall on the eve of a strong earthquake. At the same time, we believe that the trend h_{met} reflects the general tendency of the real depth h_{real} of "background" earthquakes to cluster at the source depth of a major event. We will study this trend by probabilistic methods using wavelet decomposition methods [3, 4].

If the error is taken into account and some of its numerical values Δh_{mist} are specified, then in this case, events for which this error is greater than the specified one will be filtered out of all earthquakes in the catalog for the period under consideration. Naturally, in this case, the statistics will be reduced. Moreover, the smaller the given error, the closer the value of the real depth h_{real} to the value h_{met}, the smaller the statistics. In what follows, unless otherwise specified, the event depth will be understood as h_{met}.

2. Probabilistic methods for describing the seismic regime

As noted above, in a seismically active region against the background of external disturbances, conditions are formed for the development of local nonlinear processes, which are described by methods of nonlinear dynamics. The final stage of such instability is its destruction, which is registered on the Earth's surface in the form of an earthquake. Therefore, in order to consistently fulfill an earthquake forecast and answer the questions "where and when" a structure will form in a special state, and "what energy will be released" when it is destroyed, you need to know the trajectory of the unstable system, which describes the evolution of the active structure of the source zone in the phase space with dimension equal to the number of variables describing the behavior of the source zone.

For such a description of earthquakes, it is necessary to create a model that includes the whole complex of phenomena of various nature, and it is also necessary to know the parameters of the macroscopic state of the structure, as well as the boundary conditions. But there is no such model. However, assuming that the structure of the source zone is an unstable nonlinear system, which is under the influence of external perturbations, then, according to the general principles of nonlinear dynamics, it can go into a special limiting state. In this case (purely theoretically), we must calculate various averaged characteristics on the actual trajectories of unstable systems, the dynamics of which has the nature of chaos [5].

The averaging functional is chosen as a certain probability. Consequently, initially nonlinear systems with chaos dynamics are described by probabilistic methods. Therefore, the transition of the system to one or another special state and its destruction itself is of a probabilistic nature. However, it is the destruction of unstable structures in the lithosphere in a seismically active region that is perceived as an earthquake, and this fact, therefore, also has a probabilistic character. Thus, by studying the result of the destruction of the nonlinear structure of the source zone as a random event, we ultimately study the seismic regime by probabilistic methods and,

ultimately, by indirect methods, study the dynamics of the structure of seismically active zones of the lithosphere.

The methods of seismological monitoring of a stress-strain geoenvironment related to the study of changes in the seismic regime can be extended if the method for calculating the probability distribution of earthquakes for various random events proposed in [6] and further developed in [7] is used to study it. This method is based on the axiomatic approach proposed by A.N. Kolmogorov in 1933 [8]. The application of this method to the catalog of Kamchatka earthquakes makes it possible to study the dynamics of the seismic regime using probabilistic methods for various regions both over the entire time period of instrumental observations and over various intervals lasting several years. With this approach, the catalog of seismic phenomena is represented as a probabilistic space of three objects. This allows us to consider each earthquake as a single outcome ω_i in the space of elementary events Ω, the power of which is determined by the number of events n (catalog). In turn, each elementary event ω_i in Ω is characterized by a system of random variables: energy class K_i, latitude φ_i, longitude λ_i, depth h_i, and time t_i. The time of a specific event in this model, as a random variable and having no mathematical expectation, is excluded from this system. In the future, we will consider a certain time interval ΔT, in which random events fall according to the catalog. The seismicity of the entire region or its selected part is considered as a complete group of events and is described in the form of distributions of conditional and unconditional probabilities P having a frequency representation. Random events are defined as combinations of a system of random variables φ, λ, h, and K in the set $\tilde{F}$. This allows us to represent the catalog of seismic events over the observation period as a probability space of three objects $\{\Omega, \tilde{F}, P\}$ and makes it possible to calculate probability distributions for various random events. If the distribution law of a system of random variables is given in analytical form by means of the distribution function $F(\varphi,\lambda,h,K)$ or its density $f(\varphi,\lambda,h,K)$, then the distribution laws of individual variables can be found using standard formulas. In our formulation, the most logical is the reverse representation of the problem: using the laws of distribution of random variables, obtain the distribution law of the system. For continuous values of the probability of hitting random events for some interval, the time interval ΔT within the given intervals in latitude $\Delta\varphi_i$, longitude $\Delta\lambda_j$, depth Δh_m, and class ΔK_n are calculated by the formula:

$$
\begin{aligned}
P\big(\Delta\varphi_i,\ \Delta\lambda_j,\ \Delta h_m,\ \Delta K_n\big) &= F\big(\varphi_i,\ \lambda_j,\ h_m,\ K_n\big) - F\big(\varphi_{i-1},\ \lambda_{j-1},\ h_{m-1},\ K_{n-1}\big) = \\
&= P(\Delta\varphi_i) \cdot P\big(\Delta\lambda_j|\Delta\varphi_i\big) \cdot P\big(\Delta h_m|\Delta\varphi_i,\ \Delta\lambda_j\big) \cdot \\
&\quad P\big(\Delta k_n|\Delta\varphi_i,\ \Delta\lambda_j,\ \Delta h_m\big),
\end{aligned}
\tag{1}
$$

where i, j, m, and n are the indices of the corresponding intervals of random variables. This expression uses the notation: $P(\Delta\varphi_i)$ is the unconditional probability of events falling into the interval $\Delta\varphi_i$; $P(\Delta\lambda_j|\Delta\varphi_i)$ is the probability of occurrence of events in $\Delta\lambda_j$ provided that the latitude of events is $\Delta\varphi_i$; $P(\Delta h_m|\Delta\lambda_j,\Delta\varphi_i)$ is the probability of hitting Δh_m, provided that the latitude and longitude are, respectively, $\Delta\varphi_i$ and $\Delta\lambda_j$; $P(\Delta k_n|\Delta h_m,\Delta\lambda_j,\Delta\varphi_i)$ is the probability of falling into the interval of the energy class ΔK_n, provided that the longitude, latitude, and depth are $\Delta\lambda_j$, $\Delta\varphi_i$, and Δh_m, respectively. Numerical values of $P(\Delta\varphi_i,\ \Delta\lambda_j,\ \Delta h_m,\ \Delta k_n)$ representations are easy to calculate. In a similar way, unconditional distribution laws are calculated for all random variables φ, λ, h, and K, as well as various combinations for conditional distribution laws from these variables. Processing the catalog according to the above

formula makes it possible to calculate the frequencies of seismic events in a given interval of variation of random variables Δ and obtain the values of the distribution function $F(\Delta\varphi_i, \Delta\lambda_j, \Delta h_m, \Delta k_n)$. Let us consider the practical application of this approach to describe the seismic regime using examples of the study of the distribution of the depth of weak events $K_S \geq 8.5$ on the eve of Kronotsky (1997-12-05).

To this end, on the basis of the described approach with the subsequent use of wavelet decomposition methods, we study the dynamics of changes in the probability distributions over the depth of "background" earthquakes that occur several years before strong Kamchatka events with $M \geq 7.0$. This allows us to identify the depth range at which anomalous changes the parameters of this wavelet decomposition. At the same time, according to the findings of nonlinear dynamics, it is known that as the degree of instability of an arbitrary system increases and it approaches the critical state, both the intensity of parameter fluctuations and the time and length of correlations increase [1]. Therefore, the initial local ("microscopic") internal processes develop and acquire the character of coordinated ones, forming already on a global ("macroscopic") scale and capturing large seismically active areas. An increase in the length and amplitude of correlations in a nonequilibrium seismically active system indicates the connection of processes in some local selected area with its other parts. But logically, this should lead, over a certain time interval τ, to the formation of conditions conducive to an increase in the frequency of earthquakes in various parts of this region with less energy than in the main impending shock. Therefore, during the preparation of a strong (catastrophic) earthquake, large volumes of the lithosphere of a seismically active region are involved in the preparation area with a simultaneous increase in the frequency of occurrence of weak (background) events.

Based on the foregoing, it can be assumed that the preparation of an earthquake corresponds to the formation of an unstable nonlinear system, which is under the influence of external disturbance factors and develops according to the scenario of nonlinear dynamics. The interaction of the lithosphere with the environment (the chain "Sun—heliosphere—magnetosphere—ionosphere—neutral atmosphere"), with its nonequilibrium conditions, can be the starting point in the emergence of a new dynamic system, called the dissipative structure [9]. In this case, the scales of the connection between different parts of the nonlinear structure change. In other words, the scales of temporal and spatial correlation change. For example, during the formation of a dissipative structure, which are Benard cells or self-oscillating Belousov-Zhabotinsky reactions, the spatial scales change from intermolecular 10^{-8} cm, which describe the interaction between molecules, to several cm [10, 11]. In turn, the time scales vary from 10^{-15} s, corresponding, for example, to the periods of oscillations of individual molecules, to several seconds, minutes, or even hours [12]. With this in mind, we hypothesize:

During the preparation of the main major event with $M \sim 7.0$ in a certain volume of a seismically active region, which is in an unstable state far from equilibrium, a consistent, correlated increase in seismic activity occurs at the "background" level, which covers areas far from the epicenter of the future event. At the same time, strong foreshocks with subsequent development of aftershock activity are possible in these areas at the depths of an upcoming earthquake. The scales that determine the temporal τ and spatial L correlation during the formation of these earthquakes are several years for τ and hundreds of kilometers for L and depend on the magnitude M of the upcoming main shock.

To test this hypothesis, the Kronotsky earthquake was considered: 1997-12-05 11:26:51 (UT), $\varphi = 54.64°\ N$, $\lambda = 162.55°\ E$, depth $h = 10$ km, depth determination error

2 km, energy class in terms of the amplitude of the S wave, determined by the nomogram of S. A. Fedotov K_S = 15.5, local magnitude of the Kamchatka region (according to Ch. Richter) M_L = 7.0, magnitude by code waves Mc = 7.7.

Figure 1 shows the area along the eastern coast of the Kamchatka Peninsula, which is divided into 12 sectors, defined by intervals of latitude $\Delta\varphi$ = 1° and longitude $\Delta\lambda$ = 1.5°. For these areas, based on the catalog of seismic events provided by the KB GS RAS, on the basis of equation (1) the probability distributions $P(\Delta h)$ (histograms) characterizing the occurrence of seismic events with an energy class $K_S \geq 8.5$ ($M \geq$ 3.5) in the given depth intervals with a step Δh = 1 km will be further calculated up to H = 100 km for two cases—without taking into account the determination of the depth error and taking into account the given error. At the next processing step, the obtained seismic event probability distribution series $P(\Delta h)$ over depth were presented in the form of a continuous wavelet decomposition [4], which makes it possible to smooth the histogram of the probabilistic representation of the earthquake depth distribution:

$$(W_\Psi P)(b, a) := |a|^{-1/2} \int_{-\infty}^{\infty} P(h) \overline{\Psi\left(\frac{h-b}{a}\right)} dt \qquad (2)$$

where Ψ is the basis wavelet, $P(h)$ is the numerical series of probabilities, and coefficients are $a, b \in R$, and $a \neq 0$.

In the process of transformation, orthonormal Daubechies wavelets of the third order were used [4]. The decomposition was carried out up to the 32nd scale level. As an example, **Figure 2a** shows the original probability distribution series calculated for 1996 for the entire area indicated in **Figure 1**. **Figure 2b** shows the results of the wavelet transform of this distribution. Since the wavelet transform coefficients are proportional to the squares of the probabilities and, therefore, give the distribution of the intensity ("energy") of the process over scales [3, 4], the sum of the wavelet coefficients was calculated over all scale levels that characterize the distribution of the
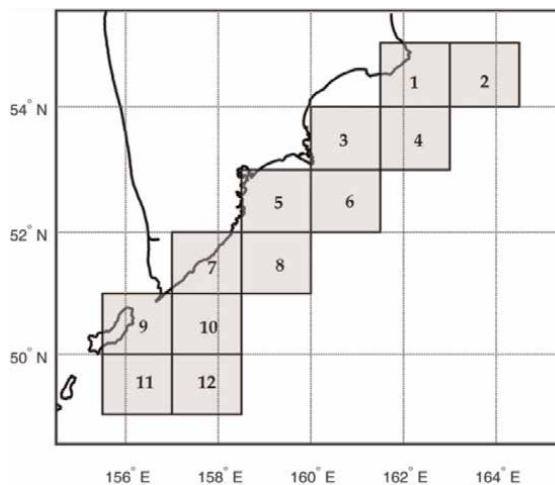
Figure 1.
Location of 12 regions along the eastern coast of Kamchatka with dimensions in latitude and longitude
$S_i = \Delta\varphi \times \Delta\lambda = 1° \times 1.5°$.
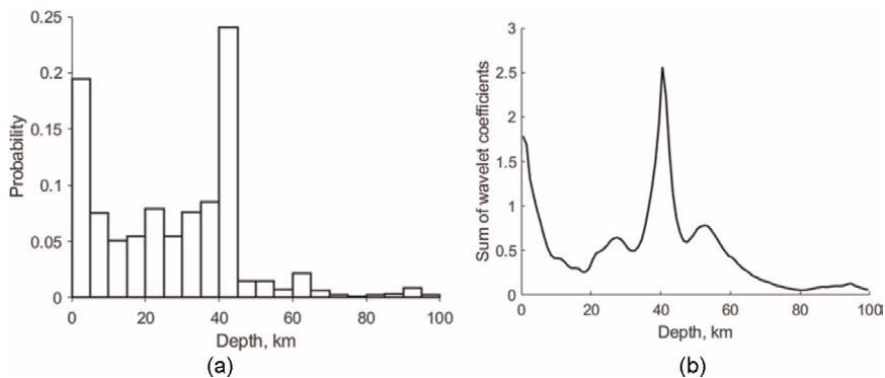
Figure 2.
(a) Probability distribution earthquakes by depth for 1996 and (b) sum of wavelet coefficients for probability distribution earthquakes by depth for 1996.

"energy" of the studied seismic process in depth in a given sector (y-axis in **Figure 2b**):

$$E = \sum_{i=1}^{n} W_{\psi} P_i \tag{3}$$

where n is the number of scale decomposition levels and $W_{\psi} P_i$ is the wavelet coefficient at the ith level of decomposition of the function $P(h)$.

3. Analysis of the Kronotsky earthquake without taking into account the determination of the error in the depth of the event

For the Kronotsky earthquake, four time periods were considered from 1 January to 31 December for 1994, 1995, and 1996 and from 1 January to 4 December, 1997 until the event itself (see **Figures 3** and **4**). The earthquake itself occurred on 1997-12-05 in sector № 1. The consideration was carried out without an error in taking into account the depth of the event.

Figure 3 shows the results of wavelet decompositions for 1994 and 1995 for all the studied sectors. In sector № 1 in 1994, 23 events occurred (N is marked in the legend for the corresponding year and in the corresponding sector) with their concentration at depths of 18 km and 40 km, while the sum of the wavelet coefficients for these depths was respectively $(Coeff)_{18} = 1$ and $(Coeff)_{40} = 1.5$. In 1995, the number of events in this sector increased to 44, and their intensity shifted to depths in the region of 30, 40, and 50 km and $(Coeff)_{30} = 1.1$, $(Coeff)_{40} = 1.6$, $(Coeff)_{50} = 1.1$. In 1996, the number of events increased to 96 with a clear maximum at 40 km ($(Coeff)_{40} = 2.2$) and additional maxima at 12 km ($(Coeff)_{12} = 0.5$), 23 km ($(Coeff)_{23} = 0.9$), and 50 km ($(Coeff)_{50} = 1.1$). In 1997, the number of events decreased to 64 with two intensity maxima at depths of 36 km ($(Coeff)_{36} = 0.6$) and 48 km $(Coeff)_{48} = 0.8$) (see **Figure 4**). Moreover, at a depth of 40 km, there was a clear decrease in seismic activity $(Coeff)_{40} = 0.2$.

Corresponding changes for the period 1994-01-01/1995-12-31 (**Figure 3**) also occurred in each of the studied sectors from 2 to 12, and an increase in the number of
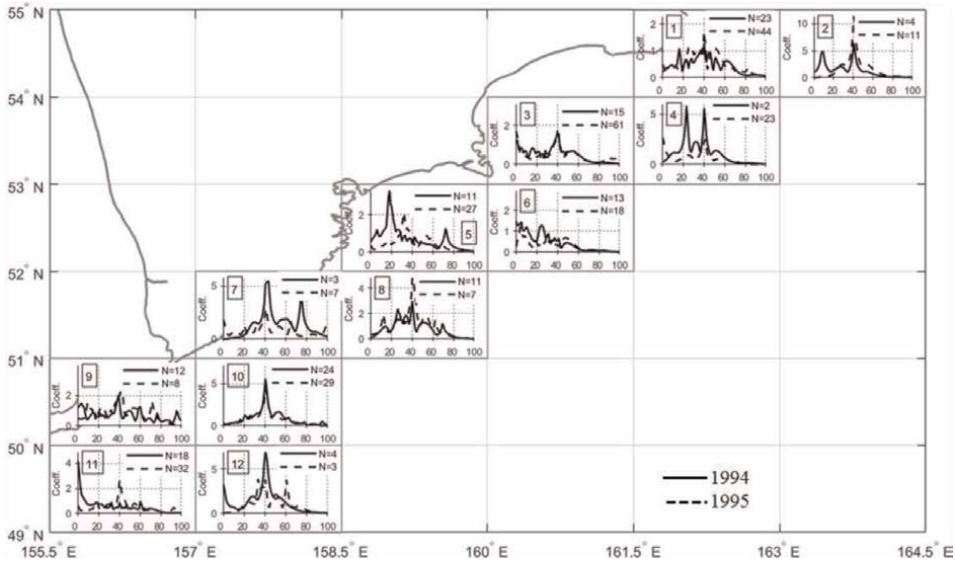
Figure 3.
The summed wavelet coefficients from scale level 1 to 32 for probability distributions P(Δh) of earthquakes with energy class $K_S \geq 8.5$ over depth intervals Δh = 1 km for 1994 and 1995.
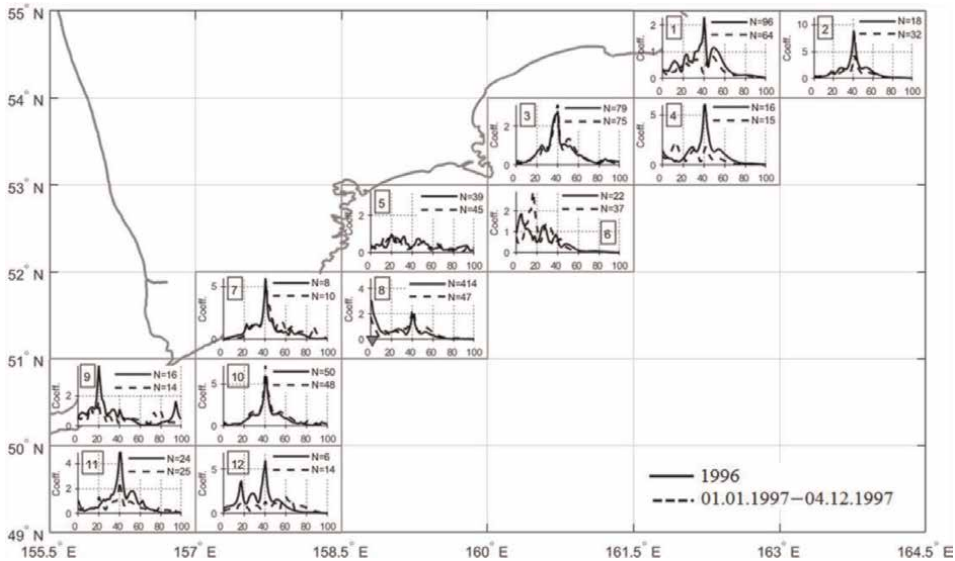
Figure 4.
The summed wavelet coefficients from scale level 1 to 32 for the probability distributions P(Δh) of earthquakes with energy class $K_S \geq 8.5$ over depth intervals Δh = 1 km for 1996 and for the period from 01.01.1997 to 12.04.1997. The triangle in sector № 8 marks two earthquakes on June 21, 1996 and July 18, 1996 (see text).

events is characteristic of all sectors. The exceptions are sectors № 8, № 9, and № 12, for which the number of events decreased from 11, 12, and 4 in 1994 to 7, 8, and 3 in 1995. At the same time, a shift to shallow depths with increasing earthquake intensity occurred in 1995 in sectors № 4 (at zero depths with $(Coeff)_0$ = 2.4) and №. 7 (at zero depths with $(Coeff)_0$ = 1.8). In sector № 6, the intensity of events at shallow depths up

to 20 km in 1994 slightly decreased compared to 1995. In sector 11, the intensity of events in 1994 was located at shallow depths from 0 to 10 km with a maximum at zero depth $((Coeff)_0 = 4)$. In 1995, the intensity of earthquakes dropped sharply with the formation of a maximum at a depth of 40 km with $(Coeff)_0 = 2.2$. It should be noted that for the period 1994-01-01/1995-12-31 at a depth of 40 km, distinct maxima of events of different intensity formed at a depth of 40 km in sectors 2, 3, 4, 7, 8, 10, and 12.

In 1996 (see **Figure 4**), an increase in the intensity of earthquakes at shallow depths up to 20 km clearly manifested itself in sectors № 6 $((Coeff)_5 = 1.9)$ and № 8 $((Coeff)_0 = 3)$. During this period, two earthquakes occurred in sector № 8, followed by aftershock activity with a total number of events $N = 414$:

- 1996-06-21.; $\varphi = 51.27$, $\lambda = 159.63$; $h = 2$ km, $K_S = 13.9$; $M = 6.2$;

- 1996-07-18; $\varphi = 51.22$, $\lambda = 159.82$; $h = 8$ km, $K_S = 13.5$; $M = 6.0$.

From 1996-01-01 to 1996-06-20 (before the earthquake of 1996-06-21), five seismic events with $K_S \geq 8.5$ occurred in sector № 8. From 1996-06-21 to 1996-07-17 (before the earthquake of 1996-07-18), there were 348 earthquakes with $K_S \geq 8.5$ (aftershock activity). After the earthquake of 1996-07-18, the aftershock activity in this sector sharply decreased, and until 1996-12-31, only 61 seismic events with $K_S \geq 8.5$ occurred. Seismic activity at a depth of 40 km decreased in 1997 in sectors № 1, 2, 4, 9, 11, 12.

Graphs of the summed wavelet coefficients calculated from the probability distributions $P(\Delta h)$, calculated for the entire area S_Σ, which includes 12 regions, are shown in **Figure 4**. This figure shows the dynamics of changes in the intensity distributions of seismic events over the years, starting from 1994-01-01 and ending on 1997-12-04 (one day before the Kronotsky event). For comparison, **Figure 4** shows the distribution of seismic events averaged over the period of instrumental observations from 1962-01-01 to 2021-12-31 without taking into account the error in determining the depth of earthquakes. In this figure, for the average intensity plot 1962-01-01/2021-12-31 at a depth of 40 km, the peak of seismic activity for the entire eastern coast is clearly distinguished, which is also distinguished for shorter periods of time (1994-01-01/1997-12-31). In addition, **Figure 4** also shows less intense "petals" of averaged activity at depths of approximately 12, 18, 30, and 55 km, which, to one degree or another, repeat the "petals of activity" for 1994, 1995, 1996, and 1997 with large values of the wavelet expansion coefficients Coeff. This similarity indicates that in the lithosphere, at least along the studied area of the eastern coast of Kamchatka, there is a certain "fine" structure of zones of increased activity [13].

It follows from **Figures 3–5** that for 1994, starting from zero depths, the intensity of seismic events (numerical values of Coeff) decreases with increasing depth and merges with the averaged intensity of 1962-01-01/2021-12-31 obtained over the entire instrumental period of observation. Starting from 30 km, the intensity for 1994 exceeds the average. Over 1995, the intensity at shallow depths (from 0 to 10 km) becomes less than the intensity over 1994. In 1996, due to the earthquakes of 1996-06-21 and 1996-07-18, and aftershock activity, the intensity of seismic events at shallow depths (from 0 to 15 km) exceeds the intensity for 1994 and 1995, remaining similar to the average intensity for the period of instrumental observations from 1962 to 2021-12-31. In 1997, the intensity at shallow depths decreases and practically merges with the intensity from 1994 to 1996 at depths greater than 35 km.
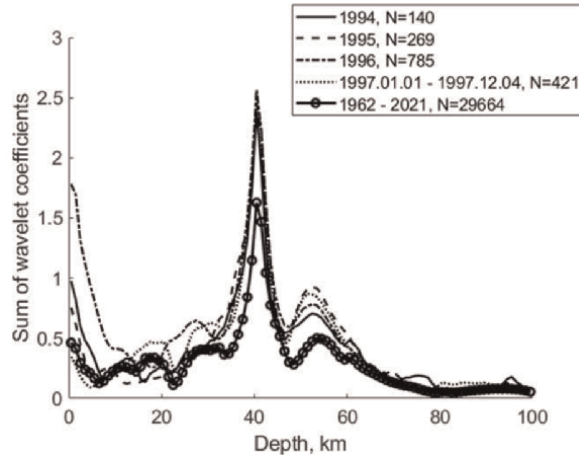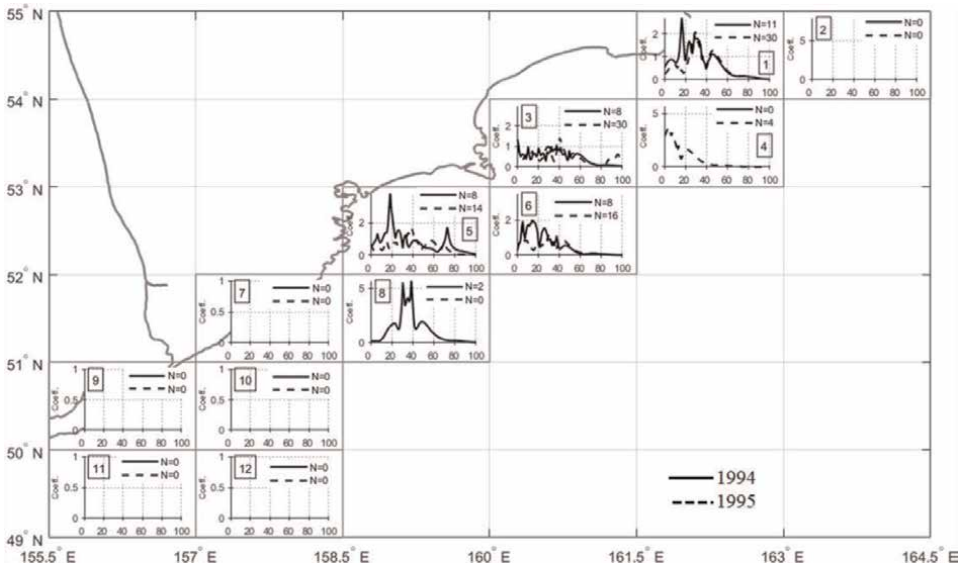
Figure 5.
The summed wavelet coefficients from scale level 1 to 32 for the probability distributions P(Δh) of earthquakes with energy class K$_S$ ≥ 8.5 over depth intervals Δh = 1 km for the S$_\Sigma$ region for the entire period of 1994, 1995, and 1996 and from 01.01.1997 to 04.12.1997. For comparison, the intensity distribution of seismic events for the period of instrumental observations from 01.01.1962 to 31.12.2021 is presented, against which events develop for the considered period of time 1994–1997.

4. Analysis of the Kronotsky earthquake, taking into account the determination of the error in the depth of the event

Let us consider the case when the error in determining the depth of the earthquake hypocenter $\Delta h_{mist} \leq 5$ km is taken into account. **Figures 6** and **7** show the results of wavelet decompositions for 1994, 1995, and 1996 and from 1995-01-01 to 1997-12-04 for all the studied sectors. As can be seen from the figures, taking into account the error in determining the depth of the hypocenter leads to a sharp reduction in statistics. In some sectors, there are no events at all, which, of course, complicates the analysis. **Figures 8** and **9** for the region S_Σ present the summed wavelet coefficients from scale level 1 to 32 for the probability distributions $P(\Delta h)$ of earthquakes with $K_S \geq 8.5$ over depth intervals $\Delta h = 1$ km and the error in determining the depth of hypocenters for. For comparison, **Figures 8** and **9** show the intensity distribution of seismic events over the period of instrumental observations from 1962-01-01 to 2021-12-31, taking into account $\Delta h_{mist} \leq 5$ km, against which events develop over the considered time period 1994–1997. As can be seen from **Figures 8** and **9**, taking into account the error leads to a significant change in the depth distribution of earthquake intensity. So in **Figure 8**, the peak of the maximum seismic activity at 40 km for 1994, which is clearly distinguished in **Figure 5**, is completely absent. Instead of a maximum at this depth, we have a minimum.

In addition, **Figure 8** for 1994 shows several clear intensity peaks in the altitude range of 18–40 km (Coeff ≈ 1.4, Coeff ≈ 1, and Coeff ≈ 1.2), 40–65 km (Coeff ≈ 0.7), and 65–90 km (Coeff ≈ 0.4). In turn, the intensity at shallow depths from 0 to 10 km for 1994-01-01/1995-12-31 slightly exceeds the intensity for the period 1962-01-01/ 2021-12-31. The absence of a maximum at a depth of 40 km in **Figure 8** indicates that the error in determining the depth for 1994 is mostly greater than the selected Δh_{mist} ≤ 5 km, so these earthquakes were not included in the statistics and were sifted out. In turn, in 1996, the accuracy in determining the depth of hypocenters equal to 40 km
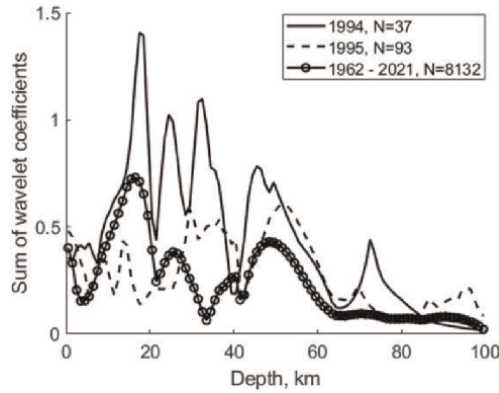
Figure 6.
The summed wavelet coefficients from scale level 1 to 32 for the probability distributions P(Δh) of earthquakes with energy class $K_S \geq 8.5$ over depth intervals Δh = 1 km for 1994 and 1995, taking into account the error in determining the depth $\Delta h_{mist} \leq 5$ km.
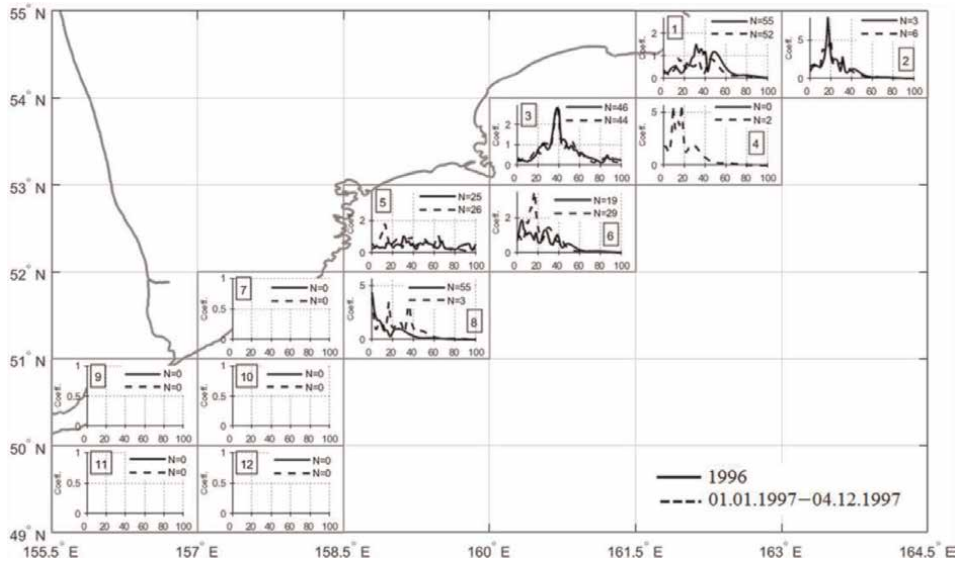
Figure 7.
The summed wavelet coefficients from scale level 1 to 32 for the probability distributions P(Δh) of earthquakes with energy class $K_S \geq 8.5$ over depth intervals Δh = 1 km for 1996 and for the period from 01.01.1997 to 04.12.1997, taking into account the error in determining the depth $\Delta h_{mist} \leq 5$ km.

mostly satisfied the accuracy of $\Delta h_{mist} \leq 5$ km, and as a result, the intensity peak was identified (see **Figure 9**).

It follows from the analysis of **Figure 8** that the intensity of the wavelet coefficients at depths from 0 to 10 km in 1996 increased sharply compared to 1994 and

Figure 8.
The summed wavelet coefficients from 1 to 32 scale decomposition level for the probability distributions P(Δh) of earthquakes with $K_S \geq 8.5$ over depth intervals Δh = 1 km and an error in determining the depth of hypocenters $\Delta h_{mist} \leq 5$ km. The periods under consideration are 1994, 1995, and 1962–2021.
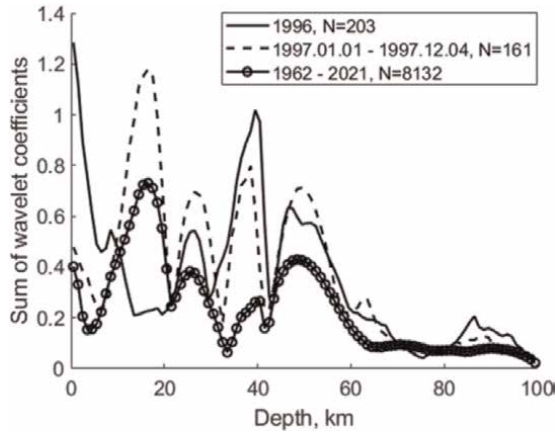

Figure 9.
The summed wavelet coefficients from scale level 1 to 32 for the probability distributions P(Δh) of earthquakes with $K_S \geq 8.5$ over depth intervals Δh = 1 km and an error in determining the depth of hypocenters $\Delta h_{mist} \leq 5$ km. The periods under consideration are 1996, 1997.01.01–1997.12.04, and 1062–2021.

1995. This happened, as we know, as a result of aftershock activity after the earthquake of June 21, 1996.

If we compare **Figure 5** with **Figures 8** and **9**, then the latter show some chaotization in the distribution of wavelet coefficient intensity peaks over depths with similar Coeff values. A similar picture is also observed in the averaged distributions of wavelet coefficients for 1962-01-01/2021-12-31, taking into account the determination of the error in the depth of hypocenters and without taking into account. This suggests that with such a choice of the numerical value of Δh_{mist}, we simply lose information about the intensity of the distribution of events over h.

5. Conclusions

Taking into account the hypothesis stated earlier, we will summarize this section. In sector № 8 in 1996, two earthquakes with magnitudes M ≥ 6 took place at depths

ranging from 0 to 10 km. The first event (1996-06-21) was accompanied by increased aftershock activity (348 earthquakes with $K_S \geq 8.5$ occurred from 1996-06-21 to the second shock on 1996-07-18). After the second shock, the activity decreased sharply, and until 1996-12-31, only 61 seismic events occurred. Considering the dynamics of general seismicity over the years (see **Figures 3** and **4**), we see that in areas far from the main shock, at the depths of the upcoming earthquake, strong events with after-shock activity arose, after which a seismic lull followed and continued until the main event on 1997-12-05 with M_L = 7.0, which occurred at a depth of h = 10 km. The distance from the main shock, which took place in sector 1, to the seismic events preceding it in sector 8 with subsequent intensification of aftershock activity, was more than 400 km. In turn, from 1994 to the main shock on 1997-12-05, seismic activity increased at shallow depths (from 0 to 20 km) in sectors that are mosaically scattered along the eastern coast of Kamchatka, as well as in different time intervals (not simultaneously).

To support this hypothesis, we can note:

- for several years, sectors of the background enhancement of seismic activity at the depths of an impending major event, mosaically scattered along the eastern coast;

- the occurrence of foreshock events far and at the depths of an impending major earthquake.

It is absolutely clear that the consideration of one event as a confirmation of the stated hypothesis is not enough and requires further research on the example of other large earthquakes. In addition, the impossibility of a more accurate determination of the hypocenter depth and its replacement by h_{met}, when the error Δh_{mist} is commen-surate with the depth itself, seems to be somewhat arbitrary. However, the ideology of this approach to the analysis of the depth distributions of earthquake epicenters on the eve of major events based on the application of the general conclusions of nonequilibrium thermodynamics, in our opinion, is promising.

Author details

Vadim Bogdanov* and Aleksey Pavlov
Institute of Cosmophysical Research and Radio Wave Propagation FEB RAS,
Paratunka, Russia

*Address all correspondence to: vbogd@ikir.ru

IntechOpen

References

[1] Nikolis G, Prigozhin I. Poznanie slozhnogo. Editorial URSS; 2003. p. 344

[2] Chebrova A, Matveenko E. Sostojanie okonchatel'nogo kataloga zemletryaseniy Kamchatki i Komodorskikh ostrovov v 2013 godu. In: Problemy kompleksnogo monitoringa Dal'nego Vostoka Rossii; 29 sentjabrja-5 oktjabrja 2013; Petropavlovsk-Kamchatskij. Obninsk: GS RAN; 2013. pp. 122-126

[3] Dobeshi I. Desjat' lekcij o vejvletah. Izhevsk: NIC "Reguljarnaja i haoticheskaja dinamika"; 2001. p. 464

[4] Chui K. Vvedenie v vejvlety. Per. s anglijskogo, M.: Mir2001. p. 412

[5] Zhigulev V. Dinamika neustojchivochtej (Dinanstika): Fizicheskie osnovy nelinejnoj dinamiki. MFTI; 1996. p. 344

[6] Bogdanov V. Verojatnostnaja interpritacija zakona povtorjaemosti zemletrjasenij na primere Kamchatskiz zemletrjasenij. Dokl. AN. 2006;**408**: 393-397

[7] Bogdanom V, Pavlov A, Poljuhova A. A Probabilistic model of seismicity: Kamchatka earthquakes. Journal of Volcanology and Seismology. 2010;**4**: 412-422

[8] Kolmogorov A. Osnovnye ponjatija teorii verojatnostej. Nauka; 1974. p. 120

[9] Prigozhin I, Stengers I. Vremja. Haos. Kvant. M. Editorial URSS; 2001. p. 240

[10] Chandrasekhar S. Hydrodynamic and Hydromagnetic Stability. Oxford, England: Clarendon Press; 1961. p. 652

[11] Merischal M, Malek MM, Puhl A, Kestemont E. Molecular hydrodynamic versus hydrodynamic in two-dimensional Rayleigt-Benard Systems. Physical Review Letter. 1988;**61**:2550

[12] Prigozhin I, Stengers I. Porjadok iz haosa: Novyj dialog cheloveka s prirodoj. Editorial URSS; 2001. p. 312

[13] Boldyrev SA. Otrazhenie struktury i svojstv litosfery v sejsmicheskom pole Kamchatskogo regiona. Fizika zemli. 2002;**6**:5-28

Chapter 3

Perspective Chapter: Testing the Interoccurrence Times Probability Distributions of Earthquakes

Walter Salazar

Abstract

This chapter aims to provide a methodology to test the probability distributions of earthquakes in terms of the interoccurrence times (ITs), namely, the time between consecutive earthquakes of a specific magnitude. First, we compile a new earthquake catalog for the El Salvador subduction zone within moment magnitude M 5.0–8.12 comprising historical and instrumental data for 1609–2019. Secondly, we explain the fundamentals of the Weibull and Poisson distributions and verify the IT probability fits when considering the clustered catalog. We find that the Weibull distribution fits all ITs, while the Poisson distribution fails to explain the natural seismicity patterns for small magnitude bins. Besides, we test the assumption that the declustering process leads to a Poisson probability distribution when removing foreshocks and aftershocks in the earthquake catalog. Finally, the classical Gutenberg–Richter relationship and conditional magnitude probabilities are calculated as an essential input in any seismic hazard assessment.

Keywords: earthquake catalog, Weibull and Poisson probability distribution, subduction zone, interoccurrence times

1. Introduction

1.1 Earthquake data

The subduction zone comprises earthquakes with focal depths down to 300 km in the Central America Isthmus, where the Cocos Plate submerges beneath the Caribbean Plate. Interface subduction earthquakes occur at shallower depths in the two plates' boundary near the trench, characterized by thrust focal mechanisms. Intraplate subduction earthquakes are deeper and characterized mainly by normal focal mechanisms. Outer rise earthquakes occur southwest of the trench due to the initial flexure of the oceanic slab, yielding a shallow normal mechanism. The slab dips an average of 45^0 north-east, with deeper earthquakes away from the subduction trench having offshore and inland epicenters. Correa-Mora et al. [1] suggested employing GPS measurements as a weak coupling between the Cocos and the Caribbean plates with a slip rate of about 7–8 cm/year between the two plates.

The last destructive earthquake in this seismogenic zone occurred on January 13, 2001, with an M 7.7 with its epicenter offshore El Salvador [2]. Large shocks occurred

on December 19, 1862 [3] and September 7, 1915 [4] beneath the western El Salvador territory with M 8.12 and M 7.8, respectively. Ambraseys and Adams [4] reported an event dated August 6, 1942, M 8.12 beneath the western Guatemalan territory. On September 2, 1992, an M 7.6 offshore Nicaragua triggered a local tsunami [5]. On July 29, 1773, an earthquake with M 7.6 struck Guatemala [3].

We updated the homogenized moment magnitude catalog of Salazar et al. [6] using online global information as the International Seismological Centre ISC [7], the Preliminary Determination of Epicenters PDE [8], the Centroid Moment Tensor solutions [9], and detail-oriented studies for earthquake locations of large earthquakes [3, 4, 10–12]. The catalog covers the geographical window between 11 and 16.5^0 N and $85.5–92^0$. The final subduction catalog contains 2764 events covering 1609–2019 within M 5–8.12 (**Figure 1a**). Note that earthquakes from other regional seismogenic sources (e.g., volcanic chain, Guatemalan faults, and Honduran–Guatemalan Grabens) were also compiled; however, this study is devoted to only subduction events. Salazar et al. [6] present the criteria to separate upper-crustal and subduction events based on geological and focal mechanism information. We also applied the Gardner and Knopoff [14] method to extract the main events from the original catalog, eliminating the foreshocks and aftershocks. The final declustered catalog contains 889 main events. Note that the method of Gardner and Knopoff [14] calibrated their method to identify aftershocks; however, it has also been applied to eliminate foreshocks with the same temporal and spatial windows of the former (e.g., [15–17]) and to assure all dependent events are removed from the catalog. About 68% of dependents' events were eliminated in the decluster process (**Figure 1b**). **Figure 2** shows a hypocenter cross-section for El Salvador and the USGS subduction slab 2.0 model [13]. The depth determination in the Central America Isthmus gives significant uncertainty; however, the USGS slab model generally depicts a reasonable top slab geometry when compared with our hypocentral determinations.

It is necessary to investigate the year of completeness for the magnitudes, especially because small events are not listed in the catalog for early years. We present in **Table 1** the year of completeness of the subduction catalog for several magnitude bins after applying the Tinti and Mulargia [18] method for both the clustered and the declustered catalog after applying the Gardner and Knopoff [14] method; **Figure 3** shows an example of completeness analysis for the magnitude bin 5.0–5.5, suggesting that the catalog entirely lists events from the year 1975 to 2019.

Salazar [16] studied the earthquake interoccurrence times and seismic hazards for earthquakes related to another seismogenic zone, namely, the upper-crustal volcanic chain in El Salvador. This work extends the former article by employing data from the overall subduction zone and studying the interoccurrence times based on the Weibull and Poisson cumulative probability distributions.

2. The Weibull and Poisson cumulative distributions

A straightforward way to investigate if a specific probability distribution fits the time seismicity patterns in a seismogenic zone is by applying the cumulative probability distribution based on the interoccurrence times (ITs), namely, the time between consecutive earthquakes of a specific magnitude bin. Salazar [16] studied the ITs matching the Weibull and Poisson cumulative distributions for the upper-crustal
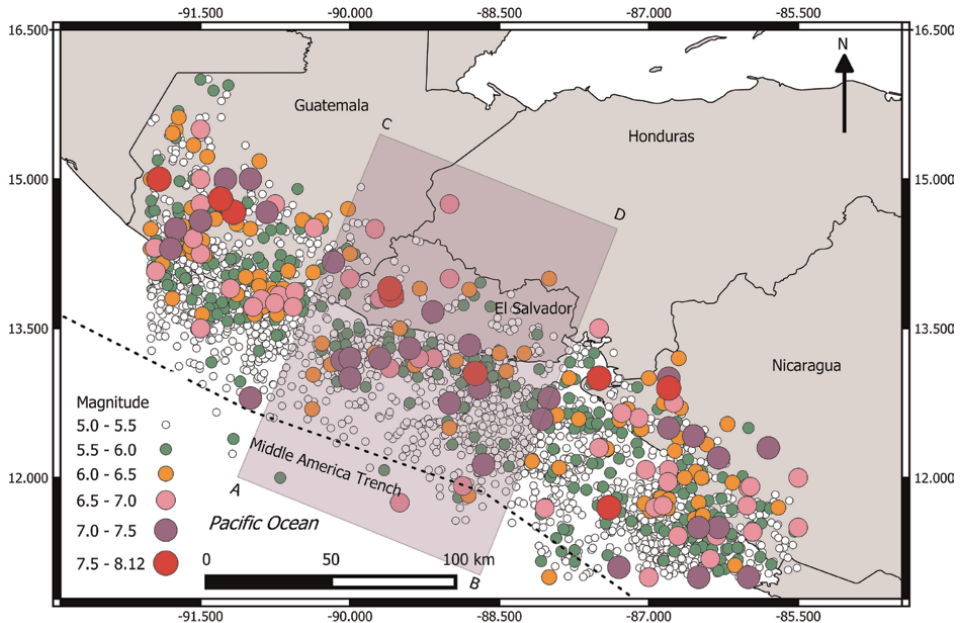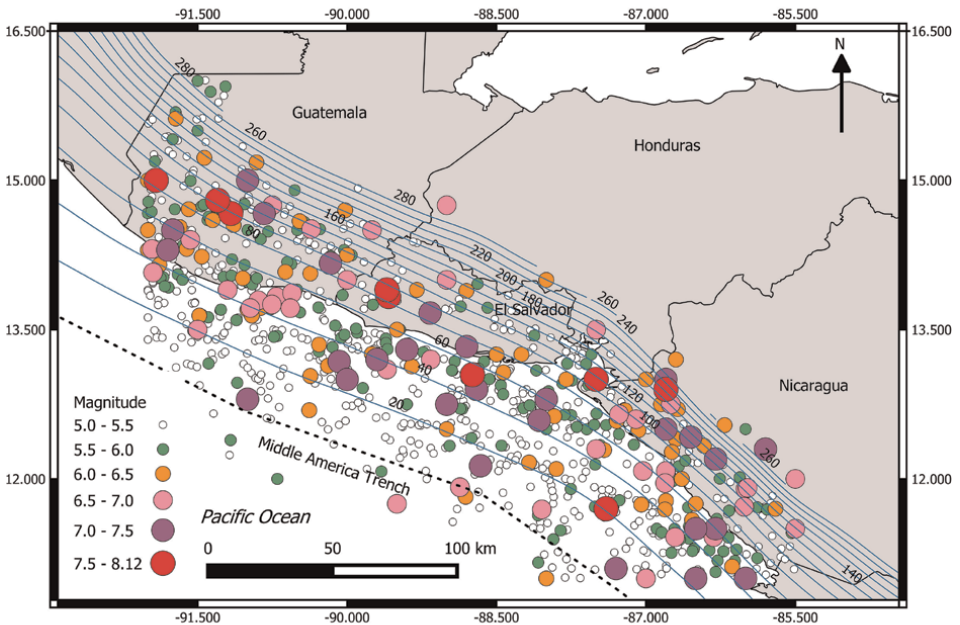
Figure 1.
*Earthquake epicenters (circles) for the subduction zone comprising events with moment magnitude M 5.0–8.12, 1609–2019, and focal depth from 1 to 300 km. a) Clustered catalog (all events); the rectangle depicts the area of the cross-section AB-CD in **Figure 2** b) Declustered catalog (after removing foreshocks and aftershocks). Blue contour lines depict the top Cocos plate depths every 20 km based on the USGS slab 2.0 model [13].*
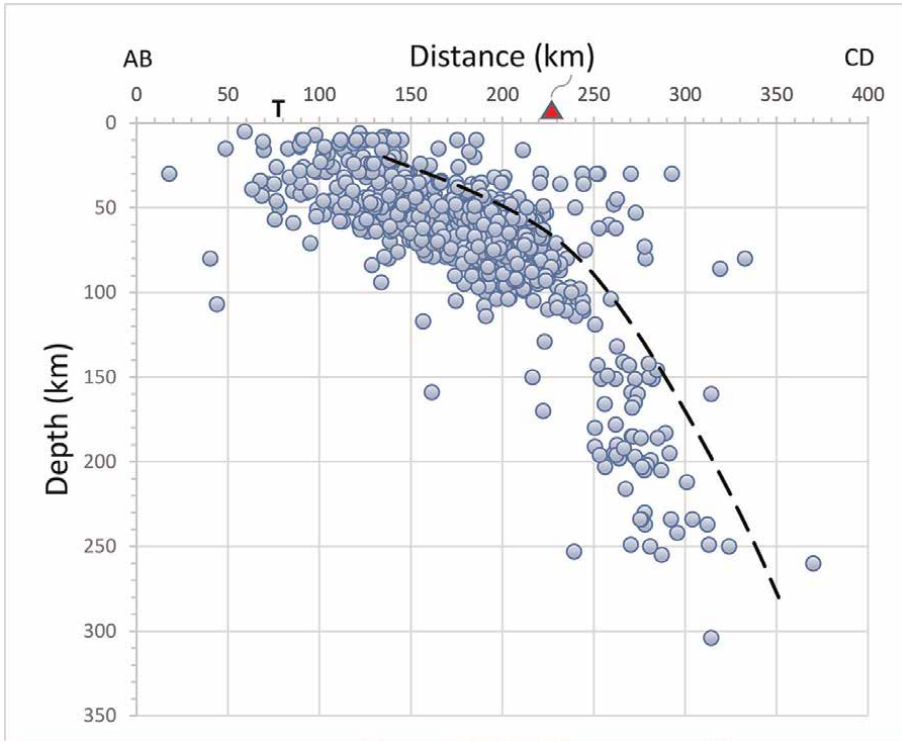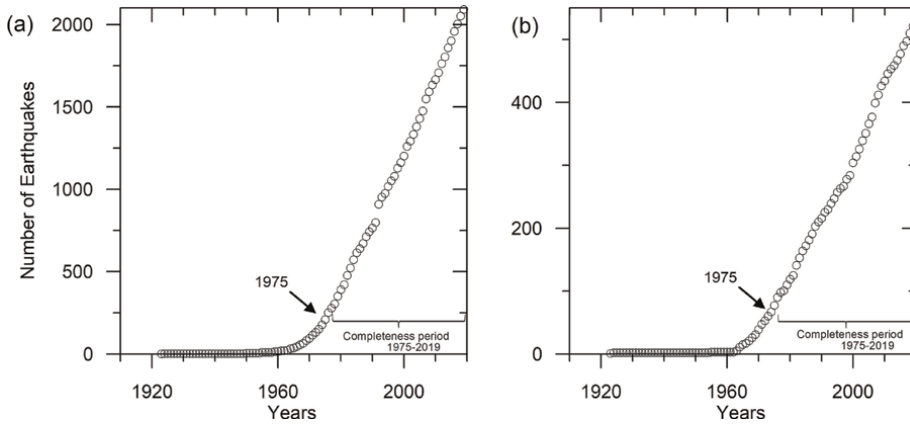
Figure 2.
*El Salvador cross-section illustrates hypocenters for all subduction earthquakes with moment magnitude M 5.0–8.12. Dashed lines depict the top of the Cocos plate based on the USGS slab 2.0 model [13] for the area AB-CD in **Figure 1**. Earthquakes with a fixed depth of 33 km are not plotted. The red triangle indicates the position of the volcanic chain in Central America, and the letter T indicates the position of the trench between the Cocos and the Caribbean plates.*

M	Year
5–5.5	1975
5.5–6	1955
6.0–6.5	1920
6.5–7	1900
7–7.5	1800
7.5–8	1765
8–8.12	1862

Table 1.
*Estimated year of completeness for the subduction zone. We noticed that for all magnitude bins, the year of completeness is the same when employing the clustered and the declustered catalogs (see **Figure 3**).*

volcanic chain earthquakes in El Salvador. Other authors have also studied the ITs in other parts of the globe [19–23]. Note that we count the ITs in a magnitude bin (e.g., 5–5.5, 5.5–6.0) since the final objective is to use the probability of occurrence of events in a seismic hazard assessment.

Figure 3.
*Example of the completeness period for subduction earthquakes within a magnitude bin M 5.0–5.5 employing the a) clustered catalog: Main shocks, foreshocks, and aftershocks; b) declustered catalog: Only main shocks. The catalog is complete for this magnitude interval back to 1975 because the cumulative annual number of earthquakes for this magnitude range is approximately linear back to that date [18]. All other magnitude bins' periods of completeness are presented in **Table 1**.*

The cumulative $F(t)$ Weibull distribution yields [24]:

$$F(t) = 1 - e^{-\alpha t^{\beta}} \quad t > 0, \alpha, \beta > 0 \qquad (1)$$

where t is the earthquake ITs, and α and β are constants found by the non-linear search algorithm of Bean et al. [25]. The Poisson probability cumulative distribution $F(t)$ yields:

$$F(t) = 1 - e^{-\lambda t} \quad t > 0, \lambda > 0 \qquad (2)$$

where λ is the number of earthquakes per unit of time [26], and t must be calculated based on the completeness analysis explained in the previous section. **Table 2** shows the α and β Weibull and the Poisson λ constants for the clustered and

	Weibull clustered catalog					Poisson clustered catalog		Poisson declustered catalog	
M	α	β	RMS	Mean μ years	σ years	λ	RMS	λ	RMS
5–5.5	0.219	0.767	0.010	0.02	0.03	0.116	0.035	0.028	0.030
5.5–6	0.038	0.822	0.017	0.16	0.20	0.017	0.038	0.008	0.020
6–6.5	0.017	0.733	0.023	0.84	1.17	0.003	0.084	0.002	0.028
6.5–7	0.006	0.762	0.028	2.46	3.27	0.001	0.064	8×10^{-4}	0.050
7–7.5	6×10^{-4}	0.964	0.051	6.19	6.44	3.6×10^{-4}	0.079	9×10^{-4}	0.083
7.5–8.12	4×10^{-4}	0.863	0.085	24.91	28.97	1.0×10^{-4}	0.094	1×10^{-4}	0.094

RMS: root mean square; μ: mean

Table 2.
Weibull and Poisson cumulative probability distribution parameters (Eqs. 1 and 2). σ denotes the standard deviation. M: moment magnitude; λ is expressed above as the number of earthquakes per year; however, for the Poisson cumulative probability calculations, the number of earthquakes per day must be used in Eq. (2).

declustered earthquake catalogs and their corresponding mean and standard deviations for several magnitude bins. The mean μ for the Weibull distribution is:

$$\mu = \alpha^{-1/\beta} \Gamma\left(1 + \frac{1}{\beta}\right) \tag{3}$$

and the variance σ^2 gives:

$$\sigma^2 = \alpha^{-2/\beta}\left\{\Gamma\left(1 + \frac{2}{\beta}\right) - \left[\Gamma\left(1 + \frac{1}{\beta}\right)\right]^2\right\} \tag{4}$$

The standard deviation σ is the root square of the variance. Γ is the gamma function; we also listed the fit error in terms of the root mean square (RMS):

$$RMS = \sqrt{\frac{\sum_{i=1}^{N}(Prob\_Obs_i - Prob\_Pred_i)^2}{N}} \tag{5}$$

where N is the number of data, Prob_Obs_i is the observed cumulative probability, and the $Prob\_Pred_i$ is the predicted cumulative probability at the i event.

We infer by comparing the observed and the predicted ITs using the obtained constants that subduction events pose the Weibull cumulative distribution when considering all the events in the subduction catalog, namely, principal, fore, and aftershocks (clustered catalog) for all magnitude bins with low RMS between 0.01 and 0.085 (**Figure 4a, c, e, g, i**, and **k**). Abaimov et al. [19] suggested that the conventional graphs depicting the cumulative probability $F(t)$ vs. the ITs (left panel in **Figure 4**) are not appropriate for judging, in the first instance, the fit between observed and predicted probabilities. Instead, they propose linearizing the cumulative probability, applying -ln (1-$F(t)$). The linearized probability Weibull plots confirm the goodness to fit (**Figure 4b, d, f, h, j**, and **l**) in all cases. However, the Weibull distribution better predicts the probabilities for longer ITs than short ones in one case after 100 days (e.g., M 6.5–7). The α value yields practically zero for M 7.5–8.12 (**Table 2**), arguing a Poisson process tendency for the largest subduction shocks. Indeed, the Poisson and Weibull models predict similar probabilities (see the right panel in **Figure 4j** and **l**). Although the Poisson probability distribution is thought to be applied to independent events only, we also tested the ITs to the clustered catalog to investigate if such distribution fits some magnitude bins under consideration, especially for big events.

The Poisson cumulative distribution does not fit the ITs for smaller events with magnitudes between 5.5 and 7 when using the clustered catalog (all events in the analysis), yielding RMS from 0.035 to 0.064 (**Table 2**). The linearized plots on the right panel in **Figure 4d, f**, and **h** confirm such a statement for M 5.5–6, 6–6.5, and 6.5–7.0, respectively.

However, when applying the Gardner and Knopoff [14] method to remove the foreshocks and aftershocks and conform to the declustered catalog, the Poisson distribution better fits the ITs for M 5.5–6 and 6–6.5 (**Figure 5d** and **f**) but still fail to reproduce the ITs for M 6.5–7.0 (**Figure 5h**), although there are lower RMS yields for
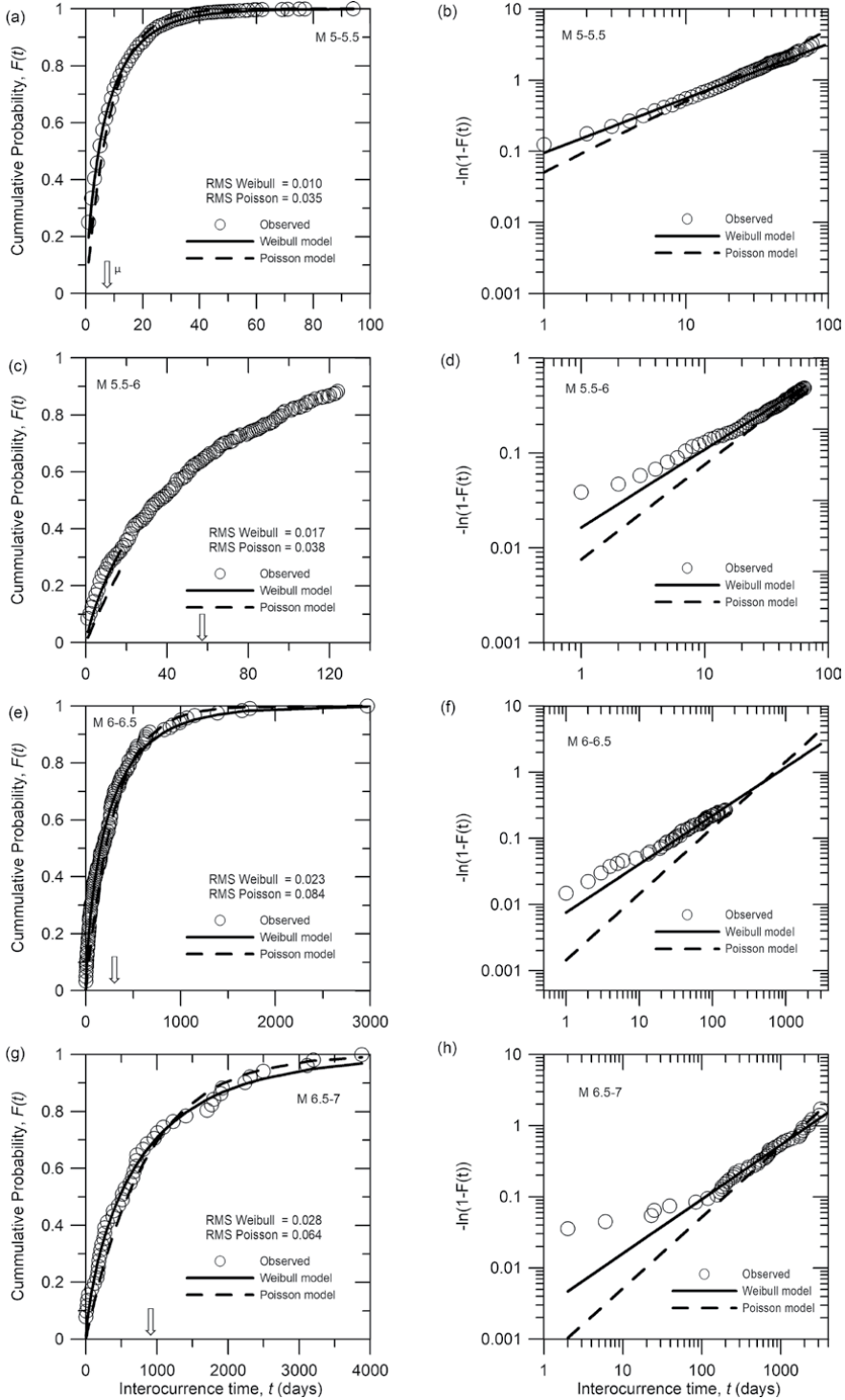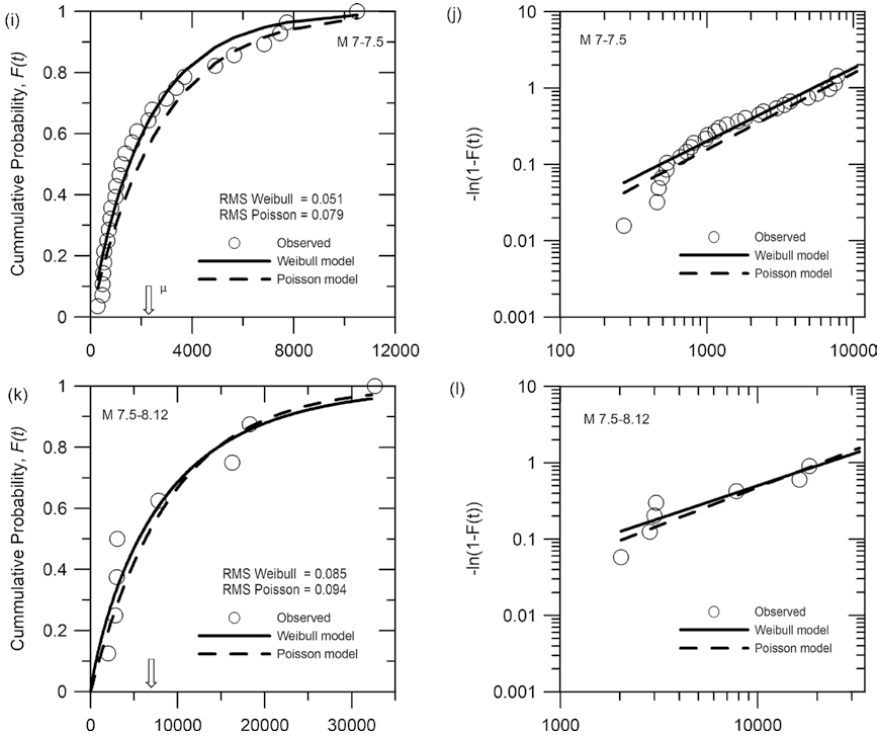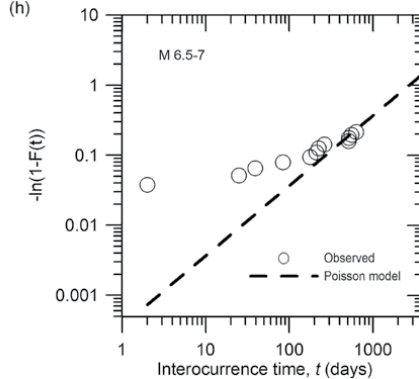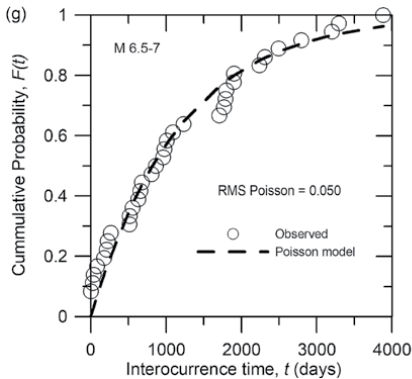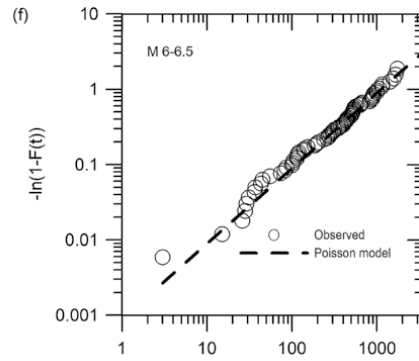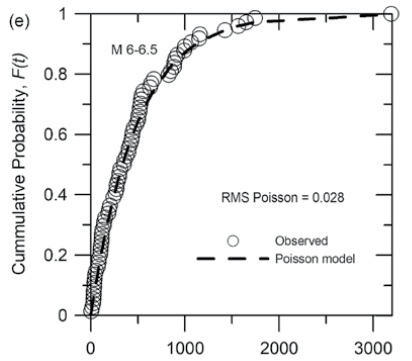
Figure 4.
Interoccurrence times vs. cumulative probabilities for several magnitude bins. (a) M 5–5.5 (c) M 5.5–6 (e) M 6–6.5 (g) M 6.5–7 (i) M 7–7.5 (j) M 7.5–8.12. We compare the observed and the estimated cumulative probability distributions employing the Weibull and Poisson models based on the clustered catalog. The arrow depicts Weibull's mean. The right side (b, d, f, h, j, and k) depicts the linearized probability plots.

these cases (**Table 2**). The linearized probability plots confirm the goodness of the Poisson fit in most of the magnitude bins under analysis, including large shocks above M 7.5 (**Figure 5j** and **l**). We conclude that the Poisson distributions fit the time seismicity patterns once only when the main shocks are considered in the analysis, except for the magnitude bin between 6.5 and 7.0 when ITs are less than 100 days.

3. Seismicity evaluation

Seismicity evaluation is a fundamental part of any seismic hazard assessment where the initial objective is to retrieve the magnitude probability of occurrence. In the case of a time-dependent seismic hazard, once we ensure that the Weibull cumulative distribution fits the subduction seismicity time patterns, we calculate the conditional probability $CP(M)t, \Delta t$ yielding the probability that an earthquake occurs after an elapsed time Δt once an earthquake has happened at time t. Note that time t is the last year in which an earthquake of a specific magnitude M appears in the catalog [27]:

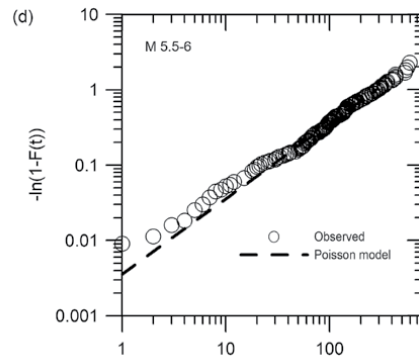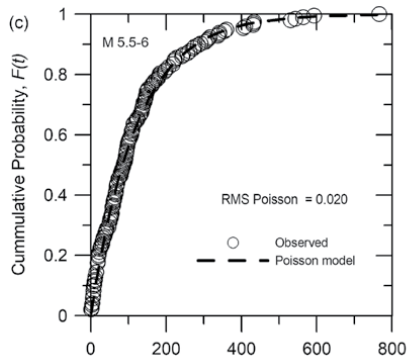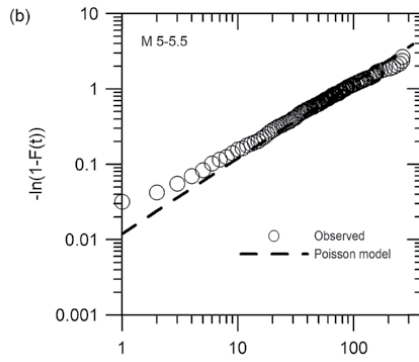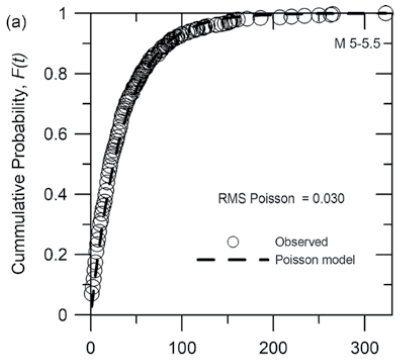$$CP(M)_{t,\Delta t} = \frac{R(t) - R(t + \Delta t)}{R(t)} \qquad (6)$$

Figure 5.
Interoccurrence times vs. cumulative probabilities for several magnitude bins. (a) M 5–5.5 (c) M 5.5–6 (e) M 6–6.5 (i) M 7–7.5 (j) M 7.5–8.12. We compare the observed and the estimated cumulative probability distributions employing the Poisson model based on the declustered catalog. The right side (b, d, f, h, j, and k) depicts the linearized probability plots.
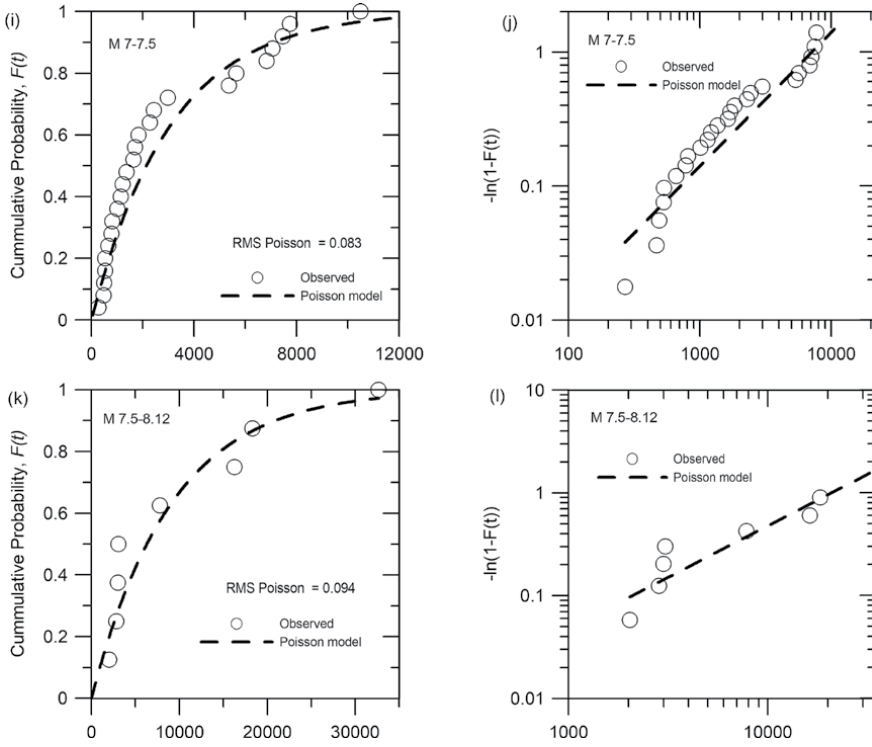
where the reliability function is $R(t) = 1 - F(t)$. **Figure 6** shows the conditional probabilities for each magnitude bin under consideration until 2120. For M 5–5.5 and 5.5–6.0, the conditional probability is practically unity after 2019, while for the rest of the magnitudes, the probabilities increase at a lower rate as the size of the earthquakes increases and time passes. For example, for large shocks with M 7.5–8.12, the probability of occurrence after 2001 (the last destructive earthquake in the region happened that year) yields 0.28, 0.73, and 0.95 for the years 2025, 2050, and 2100, respectively. Such values are suitable for time-dependent seismic hazard assessment [16]. M 6–6.5 and 6.5–7 yield similar conditional probabilities as the elapsed time increases.

We finally test our subduction catalog deriving the classical Gutenberg–Richter (G-R) relationship, yielding:

$$\log N = A - BM \tag{7}$$

where N is the number of earthquakes per year with a magnitude equal to or above M. A and B are constants obtained by regression analysis. Note that the values of N must be taken after the year of completeness analysis (see Section 1 and **Table 2**) to avoid underestimation of seismicity levels in the magnitude bins. The relationships are obtained for the clustered and the declustered catalog (see **Figure 7a**). The G–R relationships yield $\log N = 6.43-1.01$ M, $\sigma = \pm 0.045$ and $\log N = 7.73-1.17$ M, $\sigma = \pm 0.097$ for the declustered and clustered catalogs, respectively. Note that we
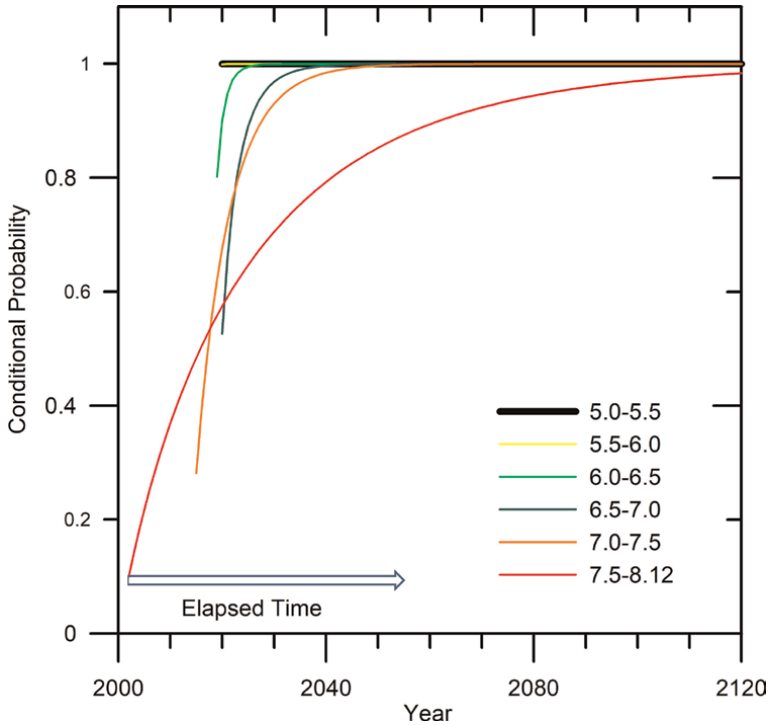
Figure 6.
Weibull conditional probabilities vs. elapsed times (Eq. 6). Note that the probabilities for M 5.5–6 completely overlap the ones from M 5–5.5 since the yield is unity.
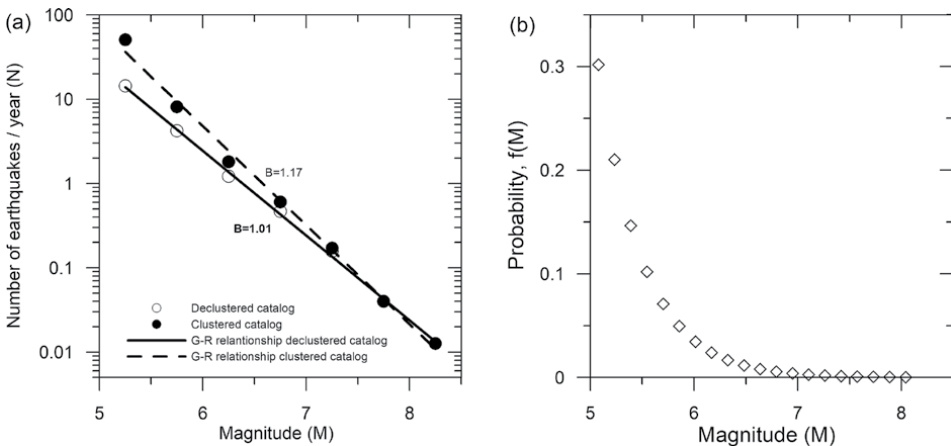
Figure 7.
a) Classical Gutenberg–Richter relationships: The observed number of earthquakes per year N above a specific magnitude M (Eq. 7). The circles represent observed data; the lines represent N's estimation of the G–R relationships after a regression analysis. The G–R yields log N = 6.43–1.01 M, σ = ±0.045 and log N = 7.73–1.17 M, σ = ±0.097 for the declustered and clustered catalogs, respectively; b) discrete probability function for 20 magnitudes between M 5 and 8.12 for the declustered catalog (Eq. 8).

retrieved a *B* value of 1.0 with a very low standard deviation σ for the subduction earthquakes when using only the main events in the analysis, which is a characteristic value of tectonic earthquakes worldwide used in several seismic hazard analyses. Note

that such G–R relationship must be truncated to the maximum possible magnitude when employing it in a seismic hazard assessment. Since we have yet to compute design spectra, we opt to present our results using the classical relationships based on Eq. (7).

For time-independent seismic hazard analysis, the probability that a magnitude will fall within a magnitude *m1* and *m2* is given by:

$$P(M) = \int_{m1}^{m2} f(M)dM \tag{8}$$

where $f(M)$ is the magnitude probability density function based on the constants *A* and *B* in Eq. (7) [28]. We present in **Figure 7b** the magnitude probability for the overall subduction zone suitable for time-independent seismic hazard analysis. The probability of the occurrence of small shocks is higher than the ones of large shocks. The sum of all probabilities is 1.0.

4. Conclusions

We have compiled a new earthquake catalog for historical and instrumental subduction earthquakes in El Salvador and surrounding areas that represent the input data for the ITs analysis and the seismicity evaluation. Subduction seismicity patterns fit the Weibull probability distribution well for all events (including main, foreshocks, and aftershocks). The Poisson probability distribution is not suitable for the natural seismicity for small events in the subduction zone. However, such distribution fits when dependents shocks are removed from the catalog for most of the magnitude range under scrutiny but fails to explain the interoccurrence times less than 100 days for the magnitude bin 6.5–7.0. Such failure might be explained because the Gardner & Knopoff [14] method was calibrated for Southern California crustal events rather than subduction zones. Indeed, each region should have its declustering dynamic window on time and space that belongs to the tectonics of the region under study. We conclude that the catalog declustering process is necessary when employing the classical Cornell seismic hazard assessments on time-independent schemes as previous works have applied for the region [6, 29–31]. In other words, despite the Poisson probability distribution not fitting the natural seismicity of subduction earthquakes, the declustering process produces a Poisson distribution with only independent events. However, the correspondent earthquake loads might be revised when employing the whole catalog in a seismic hazard analysis.

Since all the IT analyses belong to the overall subduction zone, we expect that future research must separate interface and intraplate shocks to consider the change in the seismic activity in depth; it is clear that below 120 km, there is a decrease in the seismicity in the Cocos Plate (see **Figure 2**). The depth determinations contain a significant error in the Central America Isthmus that can make such differentiation cumbersome, especially when there is no reported focal mechanism for some events.

A *B* value of 1.0 retrieved from the Gutenberg–Richter recurrence relationship after removing dependent events validates the quality of the subduction catalog compiled in this study. Conditional probabilities that depend on the last event listed in the catalog for a certain magnitude are also given that are useful in time-dependent

seismic hazard assessments. The methodology provided in this chapter would improve the quality of the following seismic hazard assessment in the country.

Acknowledgements

Author details

Walter Salazar
Catholic University of El Salvador UNICAES, El Salvador

*Address all correspondence to: walter.salazar@catolica.edu.sv

IntechOpen

References

[1] Correa-Mora F, DeMets C, Alvarado D, Turner H, Mattioli G, Hernandez D, et al. GPS-derived coupling estimates for the Central America subduction zone and volcanic arc faults: El Salvador, Honduras and Nicaragua. Geophysical Journal International. 2009;**179**:1279-1291

[2] Salazar W, Seo K. Earthquake disasters of January 13th and February 13th 2001, El Salvador. Seismological Research Letters, Seismological Society of America. 2003;**74**(4):420-439

[3] White R, Ligorría J, Cifuentes I. Seismic history of the middle America subduction zone along El Salvador, Guatemala and Chiapas, Mexico: 1526-2000. Geological Society of America Papers. 2004;**375**:379-396

[4] Ambraseys N, Adams R. Large central American earthquakes 1898-1994. Geophysical Journal International. 1995;**127**:665-692

[5] Kanamori H, Kikuchi M. The 1992 Nicaragua earthquake: A slow tsunami earthquake associated with subducted sediments. Nature. 1993;**361**:714-716. DOI: 10.1038/361714a0

[6] Salazar W, Brown L, Hernández W, Guerra J. An Earthquake Catalogue for El Salvador and Neighboring Central American Countries (1528–2009) and its Implication in the Seismic Hazard. Journal of Civil Engineering and Architecture. 2013;**7**(8):1018-1045

[7] International Seismological Centre ISC. On-line Bulletin. 2020. DOI: 10.31905/D808B830

[8] Preliminary Determination of Epicenters PDE. Bulletin. 2020. Available from: https://earthquake.usgs.gov/data/pde.php

[9] Ekström G, Nettles M, Dziewonski AM. The global CMT project 2004-2010: Centroid-moment tensors for 13,017 earthquakes. Physics of the Earth and Planetary Interiors. 2012;**200–201**:1-9. DOI: 10.1016/j.pepi.2012.04.002

[10] Ambraseys N. Magnitudes of central American earthquakes 1898–1930. Geophysical Journal International. 1995;**121**:545-556

[11] Leeds D. Catalog of Nicaraguan earthquakes. Bulletin of the Seismological Society of America. 1974;**64**(1974):1135-1158

[12] Molnar P, Sykes L. Tectonics of the Caribbean and middle America regions from focal mechanism and seismicity. Geological Society of America Bulletin. 1969;**80**:1639-1684

[13] Hayes G, Moore G, Portner D, Hearne M, Flamme H, Furtney M, et al. Slab 2, a comprehensive subduction zone geometry model. Science. 2018;**362**:56-81

[14] Gardner JK, Knopoff L. Is the sequence of earthquakes in Southern California, with aftershocks removed, Poissonian? Bulletin of the Seismological Society of America. 1974;**64**:1363-1367

[15] Hidalgo-Leiva D, Linkimer L, Arroyo I, Arroyo-Solórzano M, Piedra R, Climent A, et al. The 2022 seismic Hazard model for Costa Rica. Bulletin of the Seismological Society of America. 2023;**113**(1):23-40

[16] Salazar W. Earthquake interoccurrence times and seismic hazard assessment for upper-crustal volcanic chain earthquakes in El Salvador, are they Poissonian distributed? Natural Hazards. 2021;**107**:

1443-1465. DOI: 10.1007/s11069-021-04640-w

[17] Bozzoni F, Corigliano M, Lai C, Salazar W, Scandella L, Zuccolo E, et al. Probabilistic seismic hazard assessment at the Eastern Caribbean Islands. Bulletin of the Seismological Society of America. 2011;**101**(5):2499-2521. DOI: 10.1785/0120100208

[18] Tinti S, Mulargia F. Completeness analysis of a seismic catalogue. Annali di Geofisica. 1985;**3**:407-414

[19] Abaimov S, Turcotte D, Shcerbakov R, Rundle J, Yakovlev G, Goltz C, et al. Earthquakes: Recurrence and interoccurrence times. Pure Applied Geophysics. 2008;**165**:777-795. DOI: 10.1007/s00024-008-0331-y

[20] Anagnos T, Kiremidjian S. Stochastic time-predictable model for earthquake occurrences. Bulletin of the Seismological Society of America. 1984;**74**(6):2593-2611

[21] Chen C, Wang J, Wu Y, Chan C, Chang C. A study of earthquake interoccurrence times distribution models in Taiwan. Natural Hazards. 2012. DOI: 10.1007/s1110 69-012-0496-7

[22] Hasumi TC, Chen TA, Aizawa Y. The Weibull-log Weibull transition of interoccurrence time for synthetic and natural earthquakes. Tectonophysics. 2010;**485**:9-16

[23] Tahernia N, Khodabin M, Mirzaei N, Eskandari-Ghadi M. Statistical models of interoccurrence times of Iranian earthquakes on the basis of information criteria. Journal of Earth System. 2012;**121**(2):463-474

[24] Walpole R, Myers R, Myers S, Ye K. Probability & Statistics. Eight ed. Upper Saddle River, New Jersey, USA: Pearson Prentice Hall; 2007. p. 816

[25] Bean S, Heuser M, Somerville P. A Fortran Program for Estimating Parameters in a Cumulative Distribution Function. Massachusetts, USA: Air Force Geophysical Laboratory; 1981. p. 15

[26] Anagnos T, Kiremidjian A. A review of earthquake occurrence models for seismic hazard analysis. Probabilistic Engineering Mechanics. 1988;**1**(3):3-11. DOI: 10.1016/0266-8920(88)90002-1

[27] Maeda K, Yoshida A. Probability of earthquake occurrence using Weibull distribution: An application of the seismic activity near Shizuoka city. Zisin. 1991;**44**:147-150

[28] Salazar W. Principles of Probabilistic Seismic Hazard Assessment (PSHA) and Site Effects Evaluation and Its Application for the Volcanic Environment in El Salvador. In: Svalova V, editor. Earthquakes - Forecast, Prognosis and Earthquake Resistant Construction. London: InTech Open Science; 2018. pp. 119-146. DOI: 10.5772/intechopen.75845

[29] Benito MB, Lindholm C, Camacho E, Climent Á, Marroquín G, Molina E, et al. A new evaluation of seismic hazard for the Central America region. Bulletin of the Seismological Society of America. 2012;**102**(2):504-523

[30] Global Earthquake Model (GEM). Caribbean and Central America (CCA) model. 2022. Available at https://hazard.openquake.org/gem/models/CCA/

[31] Salgado-Gálvez M, Ordaz M, Singh S, Pérez-Campos X, Huerta B, Bazurro P, et al. A Caribbean and Central America seismic Hazard model for sovereign parametric insurance coverage. Bulletin of the Seismological Society of America. 2023;**113**(1):1-22

Chapter 4

Locations of the 1982 Miramichi (Canada) Aftershocks: Implication of Two Rupture Regions Activated

Dariush Motazedian and Shutian Ma

Abstract

On 9 January 1982, in the Miramichi region of New Brunswick, Canada, an earthquake with mb 5.7 occurred. It was followed by extensive aftershocks and felt throughout eastern Canada and north-eastern USA. Since this earthquake occurred in an uninhabited region, the damage was minor. Due to an mb 5.7 event is rare in north-eastern America, investigating it and its aftershocks is important for understanding intraplate seismicity. Digital seismic stations were not yet common by 1982. Fortunately, four seismic phases at three stations could be used to locate larger aftershocks. A simplified master-event location method combined with regional depth-phase modeling was used to locate aftershocks. For each aftershock its focal depth was first determined using a depth phase; then, with the depth fixed, the epicenter was determined using the four arrival time readings measured at the same three stations. The located aftershocks were divided into three groups. In each group the earthquake numbers are similar, but the majority of the energy was released in one group. The epicenters formed two trends in the NE–SW direction, implying that the Miramichi earthquake sequence activated two rupture regions.

Keywords: Miramichi aftershocks, location, shallow focal depth, two rupture regions, depth phase sPg

1. Introduction

The 9 January 1982 Miramichi, New Brunswick, magnitude (mb) 5.7 earthquake was a rare case in North America (**Figure 1**). It was felt throughout eastern Canada and northeastern USA and intrigued scientists and the public as it was the largest one in eastern Canadian and eastern US in recent 100 years. The mainshock (mb 5.7; M_W 5.6) occurred at 12:53 UT on the 9th January, followed 3.5 hours later by a large mb 5.1 (M_W 4.9) aftershock. On the January 11th the largest aftershock (mb 5.4, M_W 5.0) followed, then on March 31st another large aftershock (mb 5.0, M_W 4.9) occurred. The above three large aftershocks were called principal aftershocks. The mb magnitude was used for the mainshock and the three principal aftershocks in the majority of the publications and the media for many years. The moment magnitudes can be found in the report by Bent [1].

IntechOpen
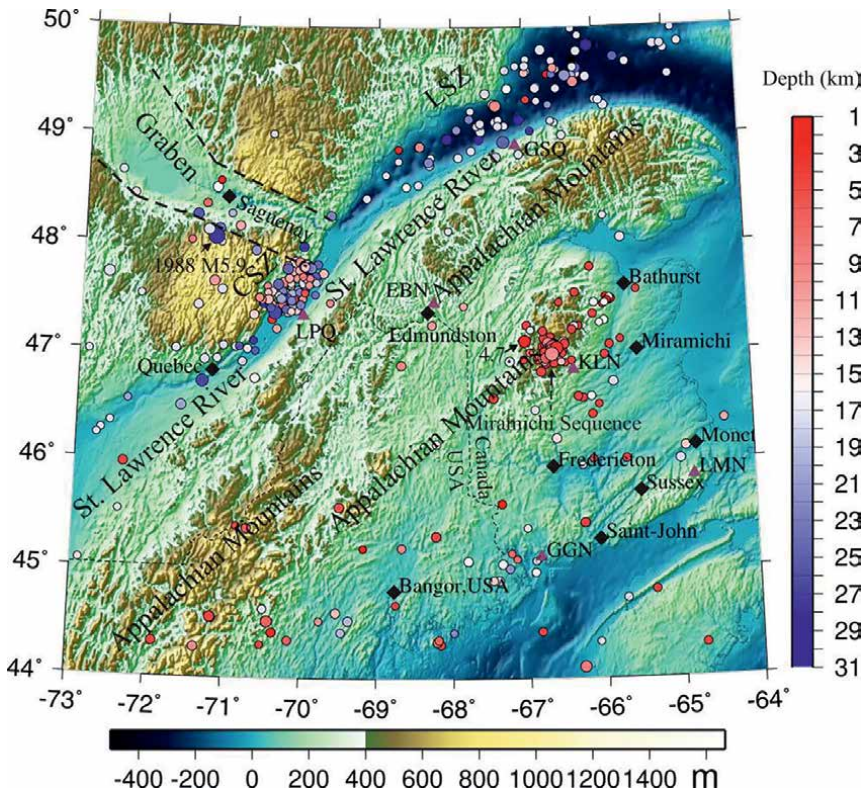
Figure 1.
*The location of the 1982 Miramichi earthquake sequence, the seismicity occurred from 1980 to March 2022, and the geological background in its surrounding regions. The triangles show the locations of seismic stations, KLN, EBN, GGN, LMN, LPQ, and GSQ. The diamonds show the locations of cities or towns. The symbols CSZ and LSZ are abbreviations for the Charlevoix seismic zone, and lower St. Lawrence seismic zone. A solid circle color coded with focal depth shows an earthquake epicenter, which were retrieved from the incorporated research institutions for seismology (IRIS). A focal depth value is indicated by the depth scale on the right. The color scale at the bottom shows the height of the topographic locations above the sea level. The St. Lawrence River runs through Quebec City, Charlevoix seismic zone, and lower St, Lawrence seismic zone. The St. Lawrence faults system also runs along this trend (e.g., [2]); for clarity it is not plotted. At the north of CSZ is the Saguenay Graben. The 1988 M_W 5.9 earthquake occurred along this Graben. **Figure 1** was plotted using the GMT program [3].*

Three field surveys were conducted in 1982 by the Geological Survey of Canada (GSC) to investigate the aftershock sequence. In the January survey (S1), the most detailed coverage of the aftershock activity was from 19 to 22 January (the temperatures were below -25C°) when aftershocks were recorded by analog MEQ-800 seismographs at four sites within 10 km of the active zone. The hypocenter of the mainshock was estimated using the hypocenters of the detected small aftershocks. The April survey (S2) was conducted in response to the 31 March mb 5.0 aftershock, whose hypocenter was also estimated using the hypocenters of the detected small aftershocks. The survey in June (S3) followed the 16 June mb 4.7 earthquake (**Figure 1**). As this event was located about 30 km west of the Miramichi mainshock (e. g. Wetmiller et al., [4]), it is not discussed in this article.

Responding to a request from Canada, the U.S. Geological Survey (USGS) installed a portable digital network. This network located about 40 aftershocks between the 15 and 22 January 1982 [5]. Among the 40 aftershocks, 4 larger ones were relocated and their focal mechanisms were studied by Saikia and Herrmann [6].
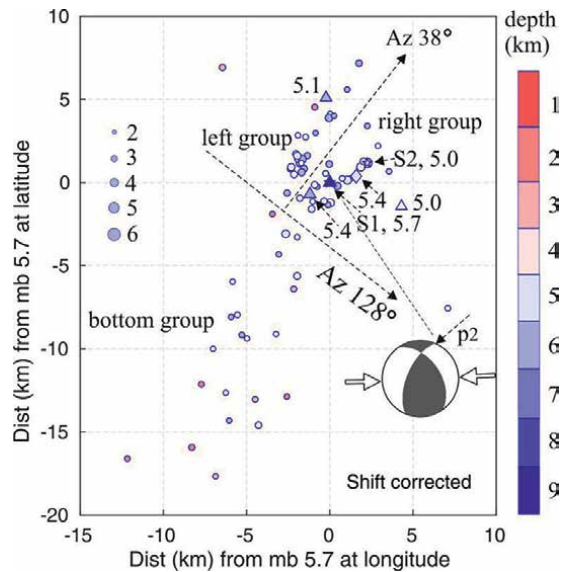
Figure 2.
The shift-corrected epicentral distribution of the located 68 aftershocks. The size of a solid circle is proportional to the magnitude, while the color matches the focal depth (see the depth scale on the right). Star S1 marks epicenter of the mainshock and star S2 marks the epicenter of the mb 5.0 aftershock, determined by Wetmiller et al. [4]. The coordinate point (0, 0) is at (47.0°N; 66.6°W). The aftershocks in the upper part of the figure were separated into two groups (the left and right groups) by a gap region indicated by a dashed-line with an arrow at Az 38°. The aftershocks in the lower part were included in the bottom group. The diamond shows the epicenter of the mb 5.4 aftershock, located using phase readings at stations EBN, GGN, LPQ, and GSQ. The triangles indicated with 5.7, 5.1, 5.4, and 5.0 show the epicenters of the mainshock and its three principal aftershocks, located by Choy et al. [8]. The epicenter of the mainshock was calibrated to that obtained by Wetmiller et al. [4]; accordingly, the epicenters of the 3 principal aftershocks were moved with the same amount of the distance and direction as those of the mainshock. The "beachball" shows focal mechanism of the mainshock calculated from the moment tensor solution (the global CMT project; globalcmt.org). The nodal plane indicated with p2 is the inferred the rupture plane. The two arrows pointed to the "beachball" show the compressive force direction in the source region.

The focal mechanism of the mainshock was a thrust type (e.g., [7]). The rupture was inferred to be updip on a west dipping NNE striking fault plane (Choy et al., [8]). The "beach-ball" is plotted using gCMT data (the global CMT project; globalcmt.org), and the inferred rupture plane is labeled p2 (see **Figure 2**).

As this earthquake sequence occurred in an almost completely uninhabited region, the damage was minor. However, investigating this mainshock and its aftershocks is important for understanding intraplate seismic activity, and assessing the seismic hazard in the source region and its vicinity for the future.

Since there was no close Canadian digital seismic station, a new station (KLN) was installed by GSC on 23 January 1982, 14 days after the mainshock, to better monitor the sequence. The station belonged to the Eastern Canadian Telemetered Network (ECTN). KLN recorded hundreds of aftershocks, and the waveform record quality was excellent. Two existing ECTN stations, EBN and GGN, also had clear records for the larger aftershocks ($m_N \geq 2.8$; the magnitude m_N was defined by Nuttli, [9]). **Figure 1** shows the locations of these three stations, as well as those of stations LPQ and GSQ.

Between latitudes 46.88° N – 47.16° N and longitudes 66.35° W–66.80° W, there were about 700 aftershocks (the smaller aftershocks detected in the field surveys are not included) in the Natural Resources Canada (NRCan) catalog database. Ma and Motazedian [10] determined the focal depths for more than 100 aftershocks with

$m_N \geq 2.8$, using depth phase sPmP recorded at EBN, but left the epicenters unchanged. Most of the aftershocks in the database were assigned the same epicenter (47.00° N, 66.60° W), which is the epicenter of the mainshock, determined by Wetmiller et al. [4].

For an earthquake with Pg and Sg arrival readings at KLN, Pg at EBN, and Pn at GGN, a conventional location method can in principle be used to determine its hypocenter. However, the value of an earthquake's focal depth is usually much smaller than those of the station distances; for a seismic phase recorded at a station, the depth typically has a much smaller contribution to the travel time than that from the station distance. As such, the error (uncertainty) in the depth is much larger than the uncertainties in the latitude and longitude of an epicenter. To reduce the error in an epicenter, a focal depth can be first determined using a depth phase; then, the epicenter is located at the depth determined.

Since the station coverage for the sequence was not good (**Figure 1**), and regional velocity models are not good either, it was not possible to determine an epicenter for an aftershock with small absolute errors. However, errors in the relative locations in a small aftershock group should be smaller and can be obtained using a master-event method (e.g., [11]).

Since the energy released by the mb 5.4 aftershock is of the same order as that of the mainshock, the Miramichi earthquake is also called a double-earthquake. The mainshock and its 3 principal aftershocks were relocated by Choy et al. [8]. The 4 focal depths were determined using a waveform modeling method [10]. The depth of mb 5.7 was 6.8 km, mb 5.1, 5.5 km, mb 5.4, 5.2 km, and mb 5.0, 2.0 km. The 4 depths were progressively shallower with occurrence times.

The durations of the surveys conducted by GSC or USGS were shorter than one week; the epicenters of the aftershocks available from IRIS database have large uncertainties. This implies that no clear patterns for the Miramichi earthquake sequence are available yet.

Our motivation was to obtain a reliable pattern of the hypocentral distribution by locating larger aftershocks. In the following sections we briefly introduce the seismicity and geological background in the vicinity of the Miramichi earthquakes; analyze the waveform data; briefly introduce the methods for locating aftershocks; present the hypocentral distribution features of the located aftershocks; display the time series and strength of the three earthquake groups obtained; analyze the errors in the relative locations between two adjacent aftershocks; and discuss some related issues.

2. Seismicity and geological background in the vicinity of the Miramichi earthquakes

The Miramichi earthquake sequence locates in the eastern part of the Appalachian Mountain range (**Figure 1**). The mountain range is mostly in the United States (US). It forms a zone from 160 to 480 km wide, running from the island of Newfoundland southwestward through New Brunswick, Canada to Central Alabama, US. In the north side, past the mountain range, is located the St. Lawrence River. Along this river, the St. Lawrence Faults system developed (e.g., [2]). In the northeast side of the Quebec City, about 100 km away is the Charlevoix seismic Zone (CSZ), which is the most active earthquake zone in eastern Canada. In the history, some destructive earthquakes occurred in the CSZ (seismescanada.rncan.gc.ca/historic-historique/events/18701020-en.php). Adjacent to the CSZ at the northern side is the Saguenay Graben. The 25 November 1988

M_W 5.9 earthquake occurred along this Graben (e.g., Ma et al., [12]). Downstream from the CSZ, is the Lower St. Lawrence Seismic Zone (LSZ). The largest earthquake detected is the 16 March 1999 m_N 5.1 earthquake (e.g., Lamontagne et al., [13]).

3. Waveform data analysis

Figure 1 shows the stations we used to locate the Miramichi aftershocks. The closest one to the sequence (about 25 km) was KLN. At this station clear Pg- and Sg-phase were recorded for almost all aftershocks. **Figure 3** shows 10 seismograms generated by 10 aftershocks, recorded at KLN. The top 5 traces were generated by the aftershocks
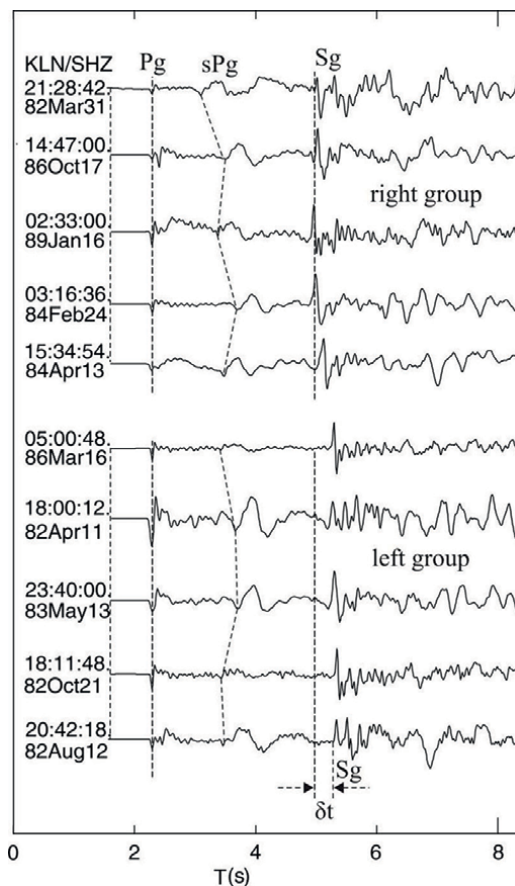
Figure 3.
*Vertical component short period displacement seismograms recorded at KLN (along a displacement trace, sPg phase is easier to identify than along a velocity trace), generated by 10 aftershocks in **Table 1**. All records are aligned at the Pg phase. The time on the left side of each record is the raw record start time. For each aftershock, the hypocentral distance to KLN is mainly constrained by the time difference $T_{Sg} - T_{Pg}$, while the focal depth is mainly constrained by $T_{sPg} - T_{Pg}$. The top 5 records were generated by the aftershocks in the right group, while the bottom 5 records by aftershocks in the left group (see **Figure 2**). The 10 aftershocks were selected along a line which is orthogonal to the located epicenter distribution trend (about Az 38°, see **Figure 2**). The $T_{Sg} - T_{Pg}$ times along the top 5 records are shorter than those along the bottom 5 records; due to those epicenters to KLN are shorter. The time difference δt corresponds to the spatial gap between the two groups.*

in the right group (see **Figure 2**), while the bottom 5 traces by aftershocks in the left group. The $T_{Sg} - T_{Pg}$ times along the top 5 traces are shorter than those along the bottom 5 traces; due to those epicenters to KLN are shorter (refer to **Figures 1** and **2**).

The second closest station was EBN (about 135 km from the sequence). At EBN, the onset of the Pg phase was usually clear on the seismograms generated by aftershocks with $m_N \geq 2.8$, so the arrival time of the Pg phase could be measured. **Figure 4** shows vertical displacement seismograms recorded at EBN. The trace indicated with mb 5.4 was generated by the mb 5.4 aftershock. The trace indicated with mb 5.0 was generated by the mb 5.0 aftershock. The other 4 traces in the top panel were generated by 4 aftershocks in the left group; the 5 traces in the bottom panel were generated by 5 aftershocks in the right group (see **Figure 2**). The $T_{Sg} - T_{Pg}$ times (about 16.54 s) along the traces 2, 3, 4, and 5 in the top panel, are shorter than those (about 17.04 s) along the bottom 5 traces; due to those aftershocks in the left group are closer to EBN. The $T_{Sg} - T_{Pg}$ times along the traces generated by the two principal aftershocks in the bottom panel are approximately equal; implying that they are in the same group.

The third closest station was GGN (station distance ~200 km). At this station, the Pn phase generated by aftershocks with $m_N \geq 2.8$, was clear (see **Figure 5**).

The waveforms at station LMN (station distance ~200 km; **Figure 1**) were also analyzed. The Pn phase, generated by aftershocks with $m_N \geq 2.8$, was clear when the
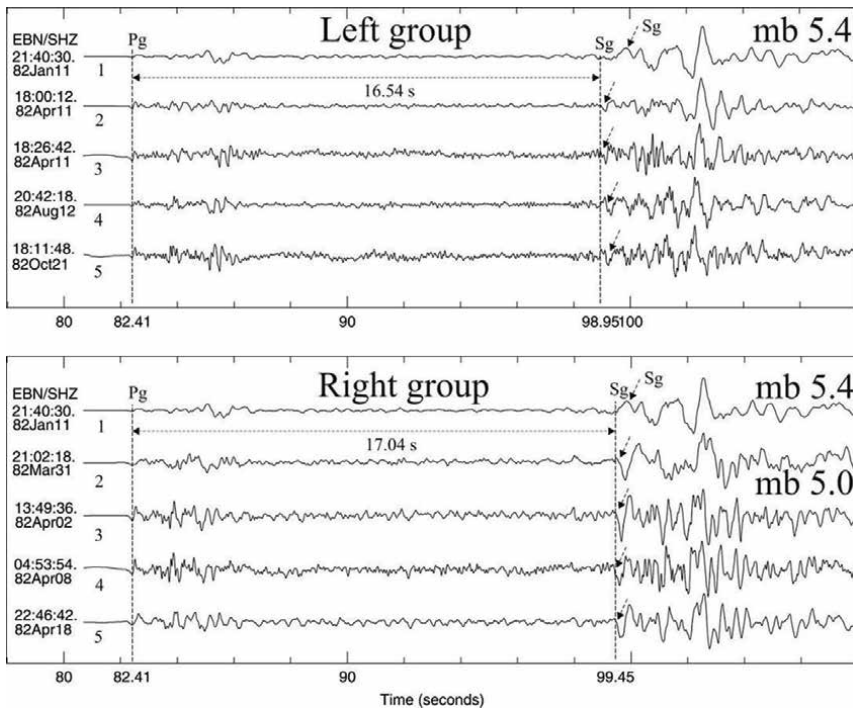
Figure 4.
Vertical component short period displacement seismograms recorded at EBN (station distance ~ 135 km) generated by 9 aftershocks in the Miramichi sequence. The trace indicated with mb 5.4 was generated by the mb 5.4 aftershock. The trace indicated with mb 5.0 by the mb 5.0 aftershock. The other 4 traces in the top panel were generated by 4 aftershocks in the left group; the other 3 traces in the bottom panel were generated by 3 aftershocks in the right group (see Figure 2). For each aftershock, the hypocentral distance to EBN is mainly constrained by the time difference $T_{Sg} - T_{Pg}$. The $T_{Sg} - T_{Pg}$ times (about 16.54 s) along the traces 2, 3, 4, and 5 in the top panel are shorter than those (about 17.04 s) along the bottom 5 traces; due to those epicenters to EBN are shorter.
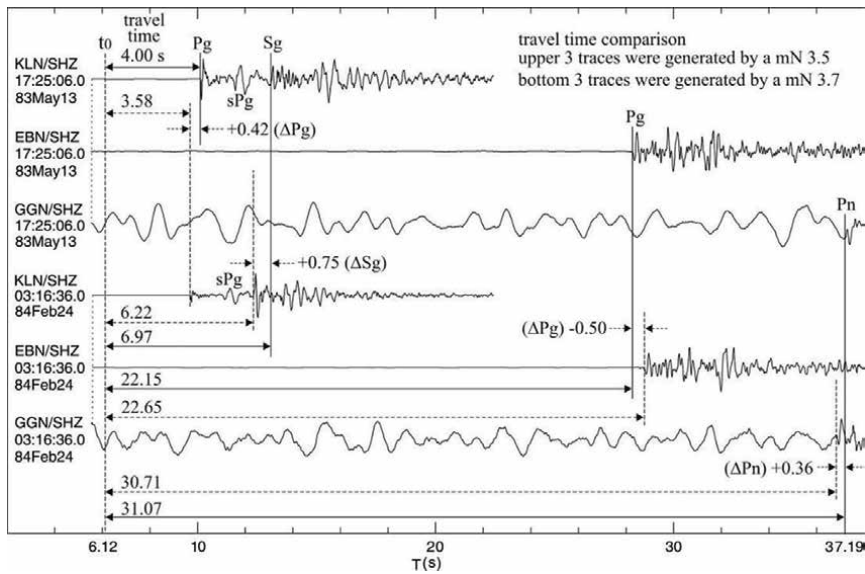
Figure 5.
*Travel time comparisons. The upper three traces were generated by the master event (ME, No. 36 in **Table 1**); the bottom three traces were generated by a secondary event (SE, No. 44 in **Table 1**). The time marked along the bottom axis is relative for conveniently aligning the traces. The symbol to means origin time; ΔPg, ΔSg, and ΔPn are travel time differences. The origin times of the ME and SE were aligned for comparison (the determined values of the two origin times are in **Table 1**; here they were calculated using Sg - Pg times). The travel times for the ME at KLN: Pg phase is 4.00 s and Sg phase is 6.97 s; at EBN: Pg is 22.15 s; at GGN: Pn is 31.07 s. the travel times for the SE at KLN: Pg phase is 3.58 s and Sg phase is 6.22 s; at EBN: Pg is 22.65 s; at GGN: Pn is 30.71 s. At KLN: ΔPg is + 0.42 s (4.00–3.58) and ΔSg is + 0.75 s (6.97–6.22); at EBN: ΔPg is − 0.50 s (22.15–22.65); at GGN: ΔPn is + 0.36 s (31.07–30.71). These differences determine the relative positions of the two aftershocks. These traces are vertically enlarged, horizontally expanded, and interpolated to 100 points/s, the arrival times could be measured with a precision of 0.01 s.*

seismograph at this station operated normally. Unfortunately, in 1982, the seismograms at LMN were often rectangular pulses with different amplitudes (probably due to instrument malfunction), so the Pn arrival times could only be measured for some aftershocks. As such, the waveform records were not used for the locations.

The Pn phase at stations LPQ and GSQ are also clear for aftershocks with magnitude $m_N \geq 3.5$. The Pn phase at these two stations and at GGN, as well as Pg and Sg at EBN were used to locate the mb 5.4 aftershock.

4. Methods

4.1 A simplified master-event relocation method

Master-event relocation methods have been studied and used by many scientists (e.g., [11, 14–16]). The steps in the master-event method described by Havskov and Ottemöller [11] are as follows: (1) Locate the master-event (ME) using a conventional location method; (2) Select stations and phases which are common to the ME and the slave-events (SEs); (3) Calculate the residuals at the selected stations for the ME; (4) Add the residual of a certain phase to the arrival time readings of the same phase for the ME and SEs; and (5) Relocate all events (the ME and the SEs) using a conventional event locating program.

The step (2) is necessary. We tested that once this necessary step was kept the uncertainty between two adjacent epicenters can be small, and the epicenter distribution pattern can be reliable, so we only kept this step in our work. We used the program in SEISAN (e.g., [17] to locate the aftershocks.

4.2 A depth phase modeling procedure to determine a focal depth

When the Pg- and Sg-phase arrival times at KLN, Pg at EBN, and Pn at GGN are available for an aftershock, theoretically the four source parameters (origin time, latitude, longitude, and focal depth) can be determined using the four time readings. However, the uncertainty in the four parameters could be large, especially that in focal depth. In practice, if only a few arrival time readings are available or station coverage is poor, the focal depth is assigned a nominal value to stabilize the location when locating an event.

To reduce uncertainties in epicenters due to uncertainty in focal depth, the time difference along a trace between depth phase sPg and its reference phase Pg (**Figure 3**) is used to first retrieve a reliable focal depth for the aftershock that generated the trace; then, the epicenter of the aftershock is located at the focal depth retrieved. In this way, the trade-off between the epicenter and the focal depth is removed, so the uncertainty in the epicenter can be dramatically reduced.

The crucial step in the procedure to retrieve a focal depth using a depth phase is the generation of the synthetic traces along which the depth phase appears. In generating synthetic waveforms, a crustal model, station distance, focal mechanism, and focal depth are needed input parameters. Since the crustal structures through which the waves travel are related to travel times, the crustal model is a key input parameter. The reflectivity method [18], the centroid moment tensor solution for the Miramichi mainshock from the gCMT Catalog (see data and resources section), and the crustal model introduced in next section were used to generate the synthetic traces. The details of the depth phase studies can be found in e.g., [19–22].

5. Crustal model

There are several studies on crustal models for eastern Canada (e.g., [23, 24]). Rayleigh-wave dispersion data from the 23 June 2010 M_W 5.2 earthquake about 60 km northeast of Ottawa, Ontario [25], were used to obtain 14 crustal velocity models around the epicenter [24]. The Rayleigh wave travel paths for model No. 8 ran approximately through the Miramichi region.

In recent years, some shallow, small earthquakes occurred in the Miramichi region. Those small earthquakes generated Rg–wave (Rayleigh waves traveling in the crust) records. Using the Rg–wave dispersion data, models for the shallow part of the crust (0–10 km) were obtained [26]. A velocity model was formed for the Miramichi region by replacing the shallow part of the model by Motazedian et al. [24] with the model reported by Ma [26]. The Vp/Vs ratio is assumed to be 1.74.

6. Aftershock locations

6.1 Location of the ME and the adjustment to the crustal model

We selected a m_N 3.5 aftershock (No. 36 in **Table 1**) as an ME. Its waveforms were presented in the upper three traces in **Figure 5**. This aftershock had very clear onsets

No	Date			Time			Lat. (°)	Long. (°)	H km	m_N	er_n km	er_e km	Dis km	Modu km	Perc
1	1982	02	24	04	43	01.0	46.977	−66.623	3.1	2.9	3.3	3.0	0.135	0.100	74
2	1982	02	27	17	34	57.6	47.033	−66.566	5.6	3.4	4.2	5.8	1.732	0.608	35
3	1982	03	01	09	33	57.1	46.955	−66.607	4.8	3.4	3.0	2.7	0.451	0.000	00
4	1982	03	03	00	28	32.7	46.996	−66.602	5.7	2.8	3.7	3.8	0.648	0.283	44
5	1982	03	04	06	06	31.1	47.019	−66.576	5.5	2.9	4.3	5.2	1.482	1.000	67
6	1982	03	13	11	38	13.0	46.995	−66.616	5.0	2.9	3.5	3.5	0.470	0.100	21
7	1982	03	13	23	27	51.6	46.974	−66.545	2.8	2.9	3.8	4.3	1.408	0.224	16
8	1982	03	16	11	14	01.8	46.919	−66.620	3.8	3.5	2.6	1.9	0.811	0.141	17
9	1982	03	26	05	36	39.6	46.988	−66.553	5.4	2.8	3.7	4.5	1.212	0.400	33
10	1982	03	26	13	38	07.3	47.006	−66.590	5.3	2.9	3.9	4.3	0.254	0.200	79
11	1982	03	31	21	02	21.2	46.979	−66.562	3.1	5.0	3.7	4.1	0.254	0.100	39
12	1982	03	31	21	29	19.3	46.971	−66.575	2.8	2.9	3.5	3.5	0.254	0.141	56
13	1982	04	02	13	50	12.3	46.977	−66.567	3.5	4.3	3.6	3.9	0.367	0.141	39
14	1982	04	02	19	49	35.4	46.912	−66.623	3.1	3.1	2.5	1.8	2.272	0.283	12
15	1982	04	08	04	54	33.9	46.980	−66.565	3.7	3.4	3.7	4.0	0.367	0.141	39
16	1982	04	11	18	00	53.4	46.980	−66.615	5.7	4.0	3.3	3.1	0.076	0.000	00
17	1982	04	11	18	27	19.3	46.984	−66.609	5.7	3.2	3.4	3.3	0.377	0.141	38
18	1982	04	11	20	07	00.1	46.898	−66.673	5.5	2.9	2.2	1.5	0.397	0.100	25
19	1982	04	18	22	47	21.3	46.958	−66.592	3.7	4.1	3.1	2.9	0.189	0.141	75
20	1982	05	02	23	31	36.9	46.961	−66.616	4.3	3.3	3.1	2.8	0.793	0.141	18
21	1982	05	06	16	28	07.7	46.942	−66.628	4.7	4.0	2.7	2.2	0.720	0.100	14
22	1982	06	16	11	43	30.5	47.001	−66.933	8.7	4.7	3.1	2.2	20.01	1.655	08

No	Date			Time			Lat. (°)	Long. (°)	H km	m_N	er_n km	er_e km	Dis km	Modu km	Perc
23	1982	06	18	11	24	36.0	46.899	−66.668	4.5	3.0	2.3	1.5	1.244	0.000	00
24	1982	06	25	06	47	10.3	46.931	−66.634	6.0	2.9	2.7	2.0	1.518	0.224	15
25	1982	07	18	15	01	04.8	46.940	−66.619	4.6	2.9	2.8	2.2	1.518	0.224	15
26	1982	08	12	20	43	18.2	46.982	−66.613	4.6	3.3	3.3	3.2	0.235	0.100	43
27	1982	09	19	01	37	17.5	46.957	−66.594	6.3	3.1	3.0	2.8	0.319	0.000	00
28	1982	10	18	04	37	48.9	46.967	−66.602	5.7	3.0	3.1	3.0	0.188	0.100	53
29	1982	10	21	18	12	47.6	46.982	−66.617	3.9	2.8	3.3	3.2	0.222	0.000	00
30	1982	10	26	15	31	33.0	46.985	−66.618	4.8	3.5	3.3	3.2	0.135	0.000	00
31	1982	10	28	06	35	10.9	46.842	−66.677	5.9	2.8	2.1	1.4	1.674	0.141	08
32	1982	10	31	12	44	41.4	46.999	−66.561	5.9	2.9	3.8	4.7	2.087	0.412	20
33	1982	12	22	12	53	26.4	46.994	−66.610	4.8	3.0	3.5	3.6	1.114	0.316	28
34	1983	02	12	18	00	25.8	46.886	−66.661	4.5	2.8	2.2	1.4	0.377	0.141	37
35	1983	05	12	20	42	25.4	46.853	−66.656	3.0	3.0	2.0	1.3	1.564	0.141	09
36	**1983**	**05**	**13**	**17**	**26**	**02.1**	**46.977**	**−66.612**	**5.9**	**3.5**	**3.2**	**3.1**	**0.269**	**0.100**	**37**
37	1983	05	13	23	40	57.4	46.982	−66.613	5.8	3.9	3.3	3.2	0.235	0.100	43
38	1983	06	10	04	22	39.2	46.964	−66.626	5.9	3.3	3.0	2.6	1.202	0.361	30
39	1983	06	11	13	47	58.6	46.979	−66.592	6.0	3.4	3.3	3.5	0.601	0.200	33
40	1983	06	28	08	05	49.3	47.033	−66.674	2.7	3.3	3.8	3.7	6.042	0.510	08
41	1983	11	02	06	02	00.4	46.857	−66.679	4.2	2.8	2.0	1.3	1.552	0.000	00
42	1983	11	17	15	32	18.2	46.975	−66.614	5.6	3.7	3.2	3.0	0.470	0.100	21
43	1983	11	18	10	28	39.5	46.862	−66.698	2.2	3.0	2.0	1.3	2.246	0.141	06
44	**1984**	**02**	**24**	**03**	**17**	**13.8**	**46.967**	**−66.586**	**5.9**	**3.7**	**3.2**	**3.2**	**0.539**	**0.283**	**52**

No	Date			Time			Lat.	Long.	H	m_N	er_n	er_e	Dis	Modu	Perc
							(°)	(°)	km		km	km	km	km	
45	1984	03	27	22	56	24.6	46.899	−66.502	3.9	3.0	2.8	2.4	9.261	0.539	06
46	1984	04	13	15	35	51.3	46.974	−66.595	4.7	3.1	3.3	3.3	0.956	0.316	33
47	1984	07	02	05	24	54.0	46.888	−66.665	5.9	3.0	2.3	1.5	1.918	0.224	12
48	1984	08	04	05	11	13.0	46.953	−66.638	2.0	2.9	2.9	2.4	1.526	0.224	15
49	1984	10	13	01	45	15.8	46.823	−66.758	2.0	3.0	1.8	1.2	3.931	0.000	00
50	1984	11	07	19	44	31.5	46.959	−66.606	4.7	2.8	3.0	2.7	0.685	0.100	15
51	1984	11	30	05	54	22.4	46.978	−66.622	5.0	3.8	3.2	3.0	0.470	0.100	21
52	1985	05	13	18	46	19.3	46.854	−66.631	2.0	2.8	2.0	1.3	2.420	0.141	06
53	1985	10	05	05	34	13.6	47.008	−66.587	6.0	3.9	3.7	4.4	0.334	0.100	30
54	1985	10	05	06	17	33.3	47.005	−66.587	6.0	2.8	3.7	4.3	0.334	0.100	30
55	1985	12	21	06	03	10.9	47.010	−66.602	2.3	3.1	3.9	4.2	1.162	0.283	24
56	1986	01	21	02	32	26.2	46.959	−66.597	5.2	3.4	3.0	2.8	0.685	0.100	15
57	1986	03	16	05	01	46.7	46.980	−66.614	4.1	2.8	3.3	3.1	0.235	0.100	43
58	1986	06	01	14	53	14.3	46.968	−66.604	4.3	3.4	3.2	3.0	0.956	0.316	33
59	1986	10	17	14	48	00.1	46.970	−66.578	4.5	4.1	3.4	3.4	0.324	0.000	00
60	1986	10	18	12	24	30.2	46.888	−66.638	4.6	2.8	2.2	1.5	2.058	0.100	05
61	1986	10	23	12	58	04.3	46.839	−66.654	4.4	3.4	2.1	1.4	2.420	0.141	06
62	1987	04	22	14	32	53.0	46.812	−66.689	3.3	2.8	1.8	1.3	2.247	0.100	04
63	1988	03	06	18	13	18.1	46.828	−66.707	2.0	3.2	1.8	1.2	3.841	0.224	06
64	1988	05	09	01	23	05.2	46.974	−66.620	4.4	3.5	3.2	2.9	0.470	0.100	21
65	1988	06	12	18	10	15.9	46.917	−66.671	5.4	2.8	2.4	1.7	3.219	0.424	13
66	1988	08	26	05	59	10.7	46.984	−66.617	4.6	3.8	3.3	3.2	0.377	0.000	00

No	Date			Time			Lat.	Long.	H	m_N	er_n	er_e	Dis	Modu	Perc
							(°)	(°)	km		km	km	km	km	km	%
67	1989	01	16	02	33	56.4	46.971	−66.582	4.2	3.0	3.4	3.4	0.539	0.283	52
68	1989	06	10	10	39	49.5	46.881	−66.688	4.6	2.8	2.1	1.4	2.246	0.141	06
average											3.0	2.8	1.233	0.183	24
69	1982	01	20	10	00		47.003	−66.619	5.4	2.8					
S1	1982	01	09	12	53	52.0	47.000	−66.600	7.0	5.7					
S2	1982	03	31	21	02	20.0	47.010	−66.570	2.5	5.0					
S3	1982	06	16	11	43	00.0	47.010	−66.970	7.0	4.7					
	1982	01	17	13	33	55.7	46.98	−66.61	4.9						
	1982	01	17	13	32	59.9	46.99	−66.63	2.4						
	1982	01	18	19	34	49.2	47.01	−66.61	3.5						
	1982	01	21	00	39	55.7	46.98	−66.60	4.8						

*Note: the epicenters and origin times are those outputs from computer program (no shift-correction yet); the magnitudes m_N came from the NRCan database. The magnitude type for No. 11 and No. 22 is mb. Column H lists the focal depths determined using the depth–phase method. Columns er_n and er_e are the errors in km for the N–S (latitude) and E–W (longitude), respectively. These error values are in the output files. Dis stands for the distance between an aftershock and its closest neighbor event; modu stands for the modular of a vector formed using the errors of one aftershock and those of its closest neighbor event; perc stands for percentage ($100 \times modu/dis$). No. 11 (mb 5.0) is indicated in **Figure 2**; No. 22 (mb 4.7) is indicated in **Figure 1**; No. 36 and No. 44 are used in the Section 6. The earthquake No. 69 is for a small aftershock, S1 for the mainshock, S2 and S3 for the two principal aftershocks [4]; and the last four are small aftershocks located by Saikia and Herrmann [6].*

Table 1.
Catalog of the located 68 aftershocks.
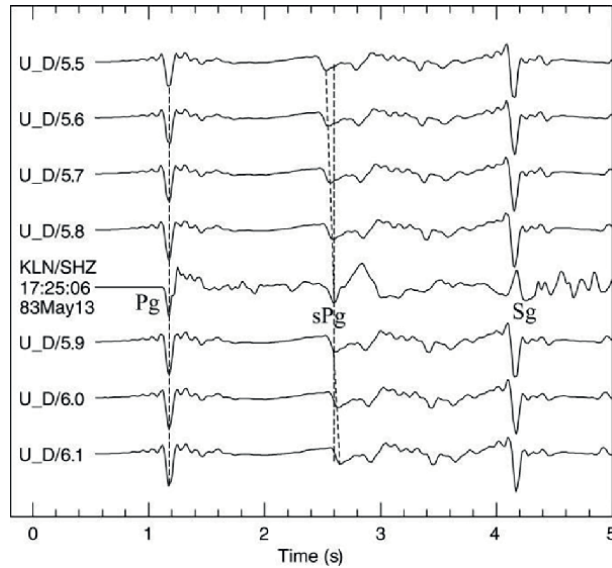
Figure 6.
Regional depth phase sPg modeling at KLN (distance 23.6 km) for the ME. The top synthetic vertical trace U_D/5.5 was generated using a depth of 5.5 km. Other synthetic traces were generated with a depth increment of 0.1 km. Trace KLN/SHZ is the observed vertical short period seismogram at KLN. The synthetic and the observed Pg are aligned. The time difference between sPg and Pg along trace U_D/5.9 and the time difference along the observed trace is approximately equal. Therefore, the modeled depth for the ME is 5.9 km.

of phases Pg, Sg, and Pn; the arrival time readings can be accurate. A focal depth of 4.5 km was previously estimated using the depth phase sPmP, recorded at EBN, and the epicenter (47.0°N, 66.6°W) of the mainshock [10]. However, the sPmP – PmP time could not be accurately measured at EBN (see **Figures 5** and **6** in [10]), resulting in an uncertainty of about 1.0 km in focal depth. In this article, we increased the depth accuracy by using the depth phase sPg at KLN. **Figure 6** demonstrates the depth phase sPg modeling for the ME. The top trace U_D/5.5 was generated using a depth of 5.5 km; other synthetic traces were generated with a depth increment of 0.1 km. The sPg - Pg time along trace U_D/5.9 and the time difference along the observed trace were approximately equal, so the modeled focal depth was 5.9 km. As the arrival times of Pg and sPg could be precisely compared, the uncertainty in the focal depth obtained using sPg was reduced.

After the focal depth for No. 36 was obtained, the SEISAN computer program was run at the newly obtained focal depth value. During the first trials of the epicentral location, the residuals between the arrival times of the observed and the calculated Pn phases at GGN were not small, so the P wave velocity value in the crustal model beneath the Moho was adjusted to reduce the residuals.

6.2 Location of the 68 aftershocks

The aftershocks with $m_N \geq 2.8$ that occurred after KLN installation usually had clear onsets of Pg and Sg phases at KLN, Pg at EBN, and Pn at GGN. Of the 113 aftershocks for which the focal depths were determined [10], 68 satisfied the requirements for using the ME relocation method. Therefore, 68 aftershocks were located at the focal depths determined using depth phase sPg. The epicenters of the 68 aftershocks are plotted in **Figure 2** and listed in **Table 1**.

6.3 Epicenter corrections

Since the station coverage was poor, the available arrival time readings were limited, and a 1-D crustal velocity model used, an epicentral shift relative to its true location was unavoidable. To obtain an epicentral distribution with absolute errors as small as possible, we performed an epicentral shift correction.

The star labeled S2 in **Figure 2** marks the epicenter of the mb 5.0 aftershock, determined by Wetmiller et al. [4] using the centre of the small aftershocks they detected. It was assumed that the epicenter had smaller absolute errors compared to the epicenter for the same aftershock we obtained. The reason is that Wetmiller et al. [4] used the arrival times at portable stations which were less than 10 km from the earthquake sequence the absolute errors in the small aftershocks they detected were small. Accordingly, the absolute errors in the epicenter of the mb 5.0 they obtained were smaller. The differences between the two epicenters for the same mb 5.0 earthquake were subtracted from the epicenters of all the 68 aftershocks in **Table 1**. **Figure 2** shows the corrected epicentral distribution.

6.4 Location of the mb 5.4 aftershock which did not have KLN record

Since the mb 5.4 aftershock was strong, it had clear Pg and Sg at EBN (**Figure 4**), clear Pn at GGN, LPQ, and GSQ, and it already had an accurate focal depth solution [10], so it can be located without a record at KLN. The aftershock mb 5.0 also had common phase arrival time reading as those of the mb 5.4, and had an accurate focal depth solution, so the mb 5.0 can also be located with the same precision as that of the mb 5.4. After the two epicenters were obtained using the arrival time readings at the above 4 stations, the epicenter of the mb 5.0 was corrected to that obtained by Wetmiller et al. [4]; accordingly, the epicenter of the mb 5.4 was moved the same amounts in latitude and longitude as did for the mb 5.0. The diamond symbol indicated with 5.4 in **Figure 2** shows the corrected epicenter for the mb 5.4 aftershock.

6.5 Distribution features of the located hypocenters

After the epicenter shift correction, the mainshock is located within the southern part of the located aftershock cluster (**Figure 2**). Most aftershocks occurred within a 5×5 km^2 area, with the remaining ones scattering to the southwest. Overall, the aftershocks trend in a northeasterly direction (about Az 38°). This trend is close to the strike of one of the nodal planes for the mainshock obtained by the CMT group (202°) and by Choy et al. ([8]; 195°). Within the overall trend, the located aftershocks appear to form a pair of northeast trends separated by a gap region indicated by a dashed-line at Az 38°.

To observe more distribution features, the epicenters were divided into three groups: the left group, right group, and the bottom group (**Figure 2**). The hypocenters in the left and right groups were projected onto a vertical plane at Az 128° (**Figure 7**). The gap region indicated by a vertical dashed line in the figure separates the aftershocks into clearly two groups. The hypocenters on the left side were clustered together, and most were in a depth range of 4 to 6 km. In this left group only one aftershock with magnitude $\geq$5.0, of which the epicenter (the triangle) was determined by Choy et al. [8]. This epicenter and its focal depth have been corrected for comparison. The hypocenters on the right side were distributed from about depth 7 km to about 2.5 km. In this right group the mainshock and aftershocks mb 5.4 and mb 5.0 located. The triangles show the projections of hypocenters determined by Choy et al. [8].
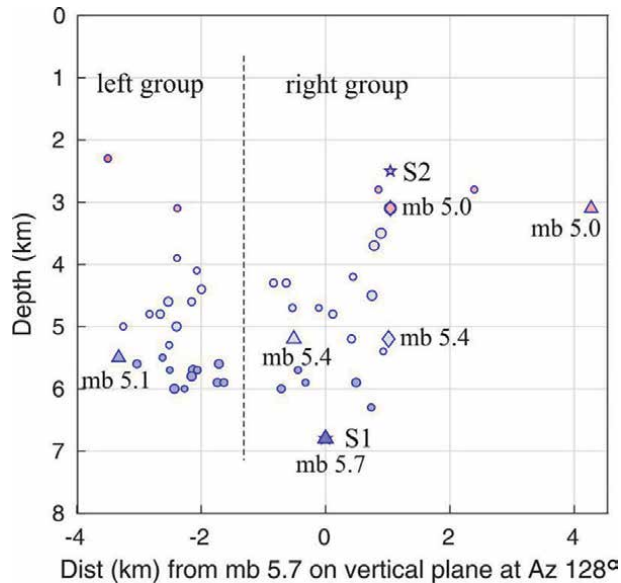
Figure 7.
Projections of the shift-corrected hypocenters in the left and right groups onto a vertical plane, striking at Az 128° (NW–SE) indicated in Figure 2. The diamond shows the projection of the hypocenter for the mb 5.4 aftershock, determined in this article. Most of the aftershocks occurred at depths between 3 km and 6 km. Stars S1 and S2 represent the hypocenter projections of the mainshock and the mb 5.0 aftershock, respectively, obtained by Wetmiller et al. [4]. The triangles indicated with 5.7, 5.1, 5.4, and 5.0 show the projections of the mainshock and its three principal aftershocks, located by Choy et al. [8]. The epicenter of the mainshock was calibrated to that obtained by Wetmiller et al. [4]; the epicenters of the 3 principal aftershocks were moved with the same amount of the distance and direction as those of the mainshock, accordingly. The 4 focal depths were calibrated to those obtained by Ma and Motazedian [10].
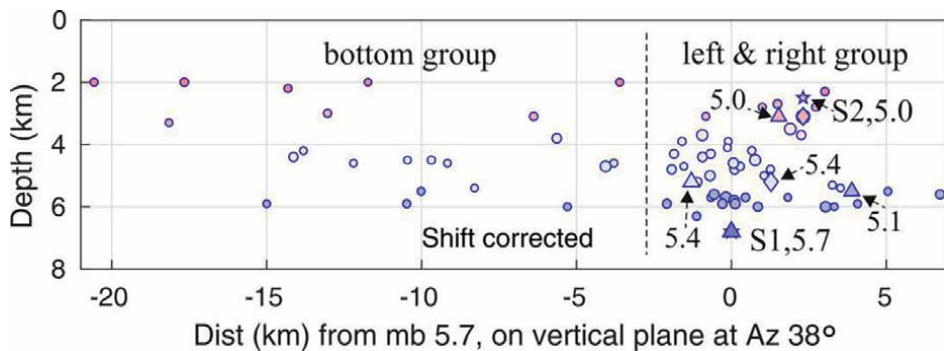
Figure 8.
*Projection of the located 68 hypocenters (the epicenters were shift-corrected) onto a vertical plane, striking at Az 38° (NE–SW), indicated by a dashed line with an arrow in **Figure 2**. Most of the aftershocks occurred at depths between 2 km and 6 km. Stars S1 and S2 represent the hypocenter projections of the mainshock and the mb 5.0 aftershock, obtained by Wetmiller et al., [4]. The triangles indicated with 5.7, 5.1, 5.4, and 5.0, show the hypocenter projections of the mainshock and its 3 principal aftershocks, relocated by Choy et al., [8]. The aftershocks were separated into two groups by a gap region indicated by a vertical dashed line. Most of the aftershocks occupy a region of around 5 × 5 km².*

We also projected all the corrected hypocenters onto a vertical plane at Az 38° (**Figure 8**). The aftershocks were separated into two groups by a gap region indicated by a vertical dashed line. The aftershocks at the left side of the vertical line are those

in the bottom group in **Figure 2**. The aftershocks at the right side are those in the left and right group. They occupied a region of around 5 × 5 km^2. Comparing to the region the left and right groups occupied in **Figure 2**, it can be inferred that the source volume formed by the left and right group is about 5 × 5 × 5 km^3.

7. Time series and strength of the three earthquake groups

In Section 6 the spatial features of the located aftershocks were analyzed. In this section the time series and the strength of the three earthquake groups are very briefly analyzed. After the events were sorted and plotted in **Figure 9**, we found in the upper panel (a), the right group (see **Figure 2**) there are 23 events, 6 of them with magnitude ≥4.0; in (b), the left group, 26 events, 2 of them with magnitude ≥4.0; and in (c), the bottom group, 22 events, only 1 of them with magnitude ≥4.0. Rough calculations show that the energy released in the right group is more 10 times than that in the left group; more 200 times than that in the bottom group. A common feature is that after 7 years since the mainshock, aftershocks still occurred in all groups.
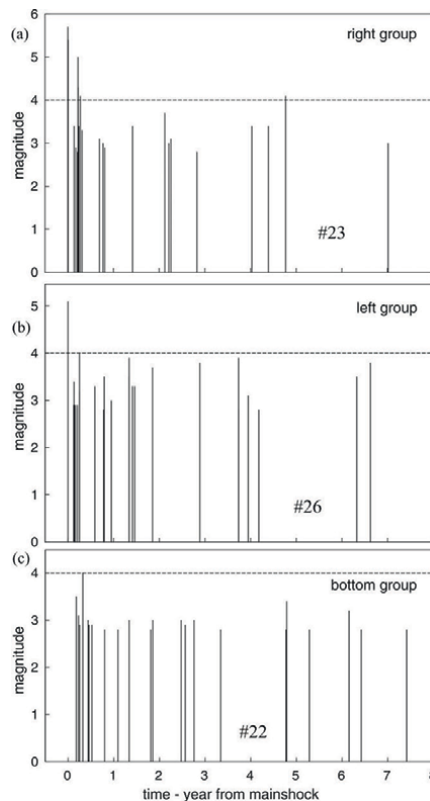
Figure 9.
*Time series and strength of the 3 earthquake groups. Each vertical line segment stands for an earthquake; the length shows the magnitude; the position along horizontal axis shows the origin time (the origin time of the mainshock was set to 0). (a) In the right group (see **Figure 2**) there are 23 events, 6 of them with magnitude ≥ 4.0. (b) In the left group, 26 events, 2 of them with magnitude ≥ 4.0. (c) In the bottom group, 22 events, 1 of them with magnitude ≥ 4.0. All the origin times of the earthquakes were converted into Unix epoch times, and the origin time of the mainshock was set to 0. The time duration is from 1982-0109 12:53 52 to 1989–0109 12:53 52.*

8. Error estimates in the relative locations of epicenters

When the azimuthal station coverage of an event is not good, the calculated location can move away from the true location because of the inaccuracy in the used velocity model [27]. **Figure 1** shows that the station coverage was not good, and the shifts were unavoidable in the epicenters we obtained. In this section, we examine the uncertainties (errors) in the relative locations between one epicenter and another. If the errors are small, the patterns of the epicentral distribution are reliable.

Errors in locations could be caused by inaccuracies in the used crustal model. To examine if the errors in the relative locations between two epicenters in a group were small, a location test for the ME and one SE was performed. We chose two aftershocks (the ME, No. 36, and an SE, No. 44, in **Table 1**; both have clear onsets, **Figure 5**). **Figure 10** shows the obtained epicenters of the two aftershocks using the same two data sets of arrival time readings but different crustal models and crustal thicknesses. The solid circle with mb 5.7 shows the location of the mainshock, determined by Wetmiller et al., [4]; the two solid squares show the locations of the ME and SE, obtained using our crustal model and a crustal thickness of 32 km. The two solid circles labeled 32, 34, 36, and 38 mark the epicenters of the same two aftershocks obtained using the GSC crustal model (Vp = 6.2 km/s) and crustal thicknesses of 32, 34, 36, and 38 km, respectively.
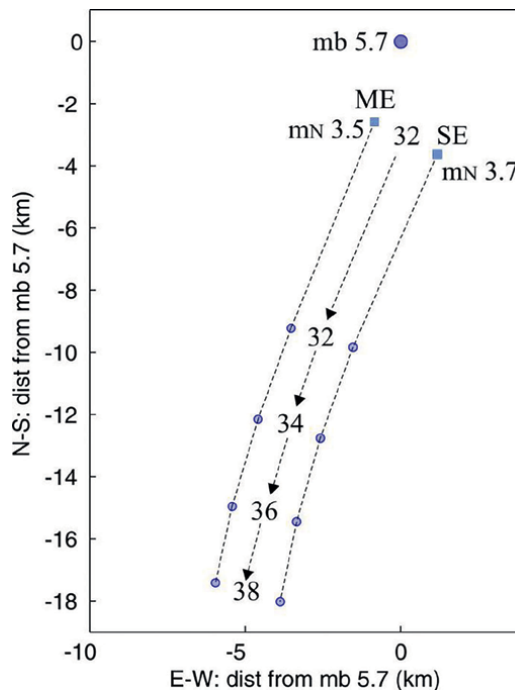
Figure 10.
The epicenters located using different crustal models for the same 2 aftershocks. The solid circle with mb 5.7 represents the epicenter of the mainshock, determined by Wetmiller et al., [4]; the two solid squares with ME and SE represent the located epicenters using our crustal model with thickness of 32 km. The 2 solid circles side by side show the same two aftershocks, located with the GSC crustal model (Vp = 6.2 km) and crustal thicknesses of 32, 34, 36, and 38 km, respectively. When the crustal thickness was changed, the 2 epicenters moved, but their relative positions were visually unchanged.

As shown in **Figure 10**, the epicenters of the two aftershocks mainly shifted southwards, and the relative locations of the two aftershocks were visually unchanged.

When the two epicenters were over plotted, only subtle changes in relative distances and relative azimuths between the two epicenters could be found. The absolute locations of two epicenters were determined using the calculated travel times, the same crustal model, and the same two sets of observed arrival times. When the parameters in the crustal model change, an increase or decrease in the calculated travel times causes the epicenter to move accordingly. Since the relative locations are mainly determined by the differences in the two sets of observed travel times (**Figure 5**), when the observed travel time readings were not changed, the relative distances and relative azimuths between the two epicenters could only have subtle changes, due to the change in used crustal model. Therefore, this test shows that errors in a crustal model cause systematic errors in the epicenters of an earthquake group, the errors in the relative locations in a group are very small.

Qualitatively speaking, two major types of errors -- errors in the crustal model and in the phase arrival time readings, cause the errors in the epicenters. The errors in the epicenters caused by arrival time reading errors may be roughly estimated. Along the top trace in **Figure 5**, the Sg – Pg time is δt = 6.97–4.00 = 2.97 s. If the P-wave traveled to station KLN with Vp = 6.2 km/s, and Vp/Vs = 1.74, the distance between the station and the epicenter is $\Delta = \delta t \times Vp / (1.74 - 1) = 24.88$ km. Since the precision of arrival time readings is to 2 decimal places, the reading error in δt is ±0.02 s, and the error in the station distance is $\delta\Delta = \pm 0.02 \times Vp / (1.74 - 1) = \pm 0.17$ km. If the error in the crustal model causes a +3.5 km error in the latitude of an aftershock, the total error (caused by the error in the crustal model and the error in arrival time readings) is +3.5 ±0.17 = +3.67 or +3.33 km.

Since the same crustal model and arrival time readings of the common phases at the common stations were used to locate the aftershocks, the signs for the absolute errors in the output files should be same. For example, the epicenter of aftershock *a* is (46.977° ±3.2 km, −66.612 ±3.1 km; #36 in **Table 1**), and the epicenter of aftershock *b* is (46.982° ±3.3 km, −66.613 ±3.2 km; #37). For aftershock *a*, if we take (46.977° +3.2 km, −66.612-3.1 km), then *b* is (46.982° +3.3 km, −66.613-3.2 km). In other words, for all aftershocks, the same sign of the errors (+ or -) needs to be assigned because the same crustal model was used. The error caused by the crustal model dominates the total error in an epicenter in the output files of the location program.

The errors in the relative locations of two adjacent aftershocks may be mathematically estimated using the absolute errors in their epicenters. Assume that the epicenters of any two adjacent earthquakes *a* and *b* are (latitude_a, longitude_a) with errors (err_na, err_ea) and (latitude_b, longitude_b) with errors (err_nb, err_eb). If vectors **A** = **A0** + **ΔA** = (latitude_a, longitude_a) + (err_na, err_ea) and **B** = **B0** + **ΔB** = (latitude_b, longitude_b) + (err_nb, err_eb), then the vector difference is **C** = **B** - **A** = (**B0** – **A0**) + (**ΔB** – **ΔA**) = **C0** + **ΔC**. Then we obtain **C0** = (latitude_b - latitude_a, longitude_b - longitude_a) and **ΔC** = (err_nb – err_na, err_eb - err_ea). Vector **C0** shows the location of *b* relative to that of *a*, while vector **ΔC** shows the errors in the location of *b* relative to *a*. Assume aftershock No. 8 in **Table 1** is *a* and one of its adjacent aftershocks, No. 14, is *b*, the errors in the location of No. 14 relative to that of No. 8 are −0.1 km (2.5–2.6) in latitude and − 0.1 km (1.8–1.9) in longitude. No. 13 and No. 15 are adjacent, and the errors in their relative location are (−0.1 km, −0.1 km).

For any given aftershock in **Table 1**, its neighbor events can be found by comparing its distances to other aftershocks. For a given aftershock the distance from its closest neighbor event, the module of its **ΔC** with its closest neighbor, and the ratio of this module over this distance are listed in **Table 1**. The average of the modules is 0.183 km, which is much smaller than the gap indicated by the line with an arrow at Az 38° in **Figure 2** or that indicated by the vertical line in **Figure** 7; therefore, the pattern of the obtained hypocenters is reliable.

9. Discussion and conclusion

More than 40 years ago, on 9 January 1982 in the Miramichi region of north-central New Brunswick, an earthquake with magnitude mb 5.7 occurred. Since the digital seismographs had not been widely deployed at that time, the source parameters of the mainshock and its aftershocks were not well determined. We analyzed the seismograms and found that at station KLN, there were very clear onsets of Pg- and Sg-waves, at EBN, clear onsets of Pg-waves, and at GGN, clear onsets of Pn phase for the larger aftershocks. We also unexpectedly found that the depth phase sPg was well developed and recorded at KLN. Once the velocity records were converted into displacement records, the onsets of the depth phase could be read correctly and accurately. The depth phase information can be used to determine focal depth accurately, and the Pg, Sg, and Pn arrival time readings at the three stations can be used to stably determine epicenters and the origin times at fixed focal depth using a conventional location method. To obtain a reliable epicentral distribution pattern, the uncertainties (errors) in the relative locations of the epicenters need to be small. To reduce errors in the relative locations, we used a simplified master-event method; specifically, we used the elite part in the master-event method. By using arrival time readings of the common four phases at the same three stations, the errors in the relative locations of adjacent aftershocks can be small.

In our study on the locations of larger aftershocks in the Miramichi sequence, we made a great effort to reduce the errors in the relative hypocenters. The errors in the relative locations between an epicenter and its closest neighbor event are listed in **Table 1**. Most of the values in the modu column are less than or equal to 0.3 km, which is smaller than the narrowest part of the gap indicated by the dashed vertical line in **Figure** 7. In another word if any epicenter in the left group is moved by 0.3 km in any direction, it cannot go into the right group. This implies that the pattern of two groups is reliable.

The left and right group phenomenon could be observed by arranging the waveform records at stations KLN and EBN. **Figure 3** shows the vertical component seismograms recorded at KLN, generated by aftershocks along a line approximately running through KLN at about Az 128°. The top 5 records were generated by the aftershocks in the right group, while the bottom 5 records by aftershocks in the left group (see **Figure 2**). The $T_{Sg} - T_{Pg}$ times along the top 5 records are shorter than those along the bottom 5 records; due to those epicenters to KLN are shorter. The time δt indicated along the bottom trace in **Figure 3** corresponds to the spatial gap between the left and right group. Similarly **Figure 4** shows vertical component seismograms recorded at EBN generated by 9 aftershocks, occurred along a line running through EBN at about Az 128°. The $T_{Sg} - T_{Pg}$ times (about 16.54 s) along the traces 2, 3, 4, and 5 in the top panel (left group) are shorter than those (about 17.04 s) along the bottom 5 traces (right group). The time difference 0.5 s (17.04–16.54) also corresponds to the spatial gap between the left and right group in **Figures** 2 or 7.

In **Figure 2** the located aftershocks were divided into three groups. The mainshock, its largest (mb 5.4), and the mb 5.0 aftershocks are in the right group. In the left group only one principal aftershock (the mb 5.1) occurred there. The total energy released in the right group is more 10 times than that released in the left group. The fault in the right group is larger than that in the left group. However, the located aftershock number is 26 in the left group, more than that (No. 23) in the right group (**Figure 9**). The left group looks like an earthquake swarm.

The aftershocks we located were in about 8 years when KLN station was operated. Since the mainshock occurrence more than 40 years has past, the aftershock activity in the source region still continues. The mystery related to the Miramichi earthquake sequence, such as why there are so many aftershocks, and several principal aftershocks followed the mainshock, is still waiting for being explored.

Based on the analyses of the located aftershocks in previous sections, the following can be concluded: (1) the major source volume was about $5 \times 5 \times 5$ km^3; (2) the focal depths ranged from about 2 km to 7 km; (3) two separate fault systems (the left and right group in **Figure 2**) were activated; the right one, activated by the mainshock and its two principal aftershocks, was large, and most energy was released there; the left one was small; (4) the trend in the aftershock epicenters was close to the northeast strike of the nodal plane for the mainshock; (5) the epicenter distribution trend was parallel to the trend of the Appalachian Mountain range (NE–SW); and (6) for more than 40 years the aftershocks have been occurring in the mainshock source region.

The procedure used to locate the Miramichi aftershocks has been successfully used for other earthquakes (e.g., [28, 29]). It is applicable for any earthquake sequence that has depth phase records.

The reliable epicentral distribution trends we obtained are crucial information for the seismic hazard assessment in the source region and its vicinity.

Acknowledgements

Data and resources

The seismograms used in this study were collected from the Natural Resources Canada (NRCan) at earthquakescanada.nrcan.gc.ca (last accessed in November 2016). The *SEISAN program tutorial* by Havskov, Ottemöller, and Voss (2014) was downloaded from seisan.info/seisan-tutorial.pdf. The Global CMT Catalog is available at globalcmt.org/CMTsearch.html.

Author details

Dariush Motazedian and Shutian Ma*
Department of Earth Sciences, Carleton University, Ottawa, Canada

*Address all correspondence to: Shutian33@yahoo.ca

IntechOpen

References

[1] Bent AL. A moment magnitude catalog for the 150 largest eastern Canadian earthquakes. Geological Survey of Canada: Open File. 2009;**6080**:23

[2] Kumarapeli PS, Saull VA. The St. Lawrence valley system: A north American equivalent of the east African rift valley system. Canadian Journal of Earth Sciences. 1996;**3**:639-658

[3] Wessel P, Smith WHF. Free software helps map and display data. EOS Earth and Space Science News. 1991;**72**:441-444

[4] Wetmiller RJ, Adams J, Anglin FM, Hasegawa HS, Stevens AE. Aftershock sequence of the 1982 Miramichi, New Brunswick, earthquake. Bulletin of Seismological Society of America. 1984;**74**:621-653

[5] Cranswick E, Mueller C, Wetmiller R, Sembera E. Local Multi-Station Digital Recordings of Aftershocks of the January 9th, 1982 New Brunswick earthquake. USGS, Open-File Report;**1982**:82-777

[6] Saikia CK, Herrmann RB. Application of waveform modeling to determine focal mechanisms of four 1982 Miramichi aftershocks. Bulletin of Seismological Society of America. 1985;**75**(4):1021-1040

[7] Basham PW, Adams J. The Miramichi, New Brunswick Earthquakes: Near-surface thrust faulting in the Northern Appalachians. Geoscience Canada. 1984;**11**(3):115-121

[8] Choy GL, Boatwright J, Dewey JW, Sipkin SA. A teleseismic analysis of the New Brunswick earthquake of January 9, 1982. Journal of Geophysical Research. 1983;**88**:2199-2212

[9] Nuttli OW. Seismic wave attenuation and magnitude relations for eastern North America. Journal of Geophysical Research. 1973;**78**:876-885

[10] Ma S, Motazedian D. Focal depth distribution of the 1982 Miramichi earthquake sequence determined by modelling depth phases. Canadian Journal of Earth Sciences. 2017;**54**:359-369

[11] Havskov J, Ottemöller L. Routine Data Processing in Earthquake Seismology, with Sample Data, Exercises and Software. New York: Springer Dordrecht Heidelberg London; 2010. p. 347

[12] Ma S, Motazedian D, Lamontagne M. Further studies on the 1988 Mw 5.9 Saguenay, Quebec, earthquake sequence. Canadian Journal of Earth Sciences. 2018;**55**:1115-1128

[13] Lamontagne M, Keating P, Perreault S. Seismotectonic characteristics of the lower St. Lawrence seismic zone, Quebec: Insights from geology, magnetics, gravity, and seismic. Canadian Journal of Earth Sciences. 2003;**40**:317-336

[14] Stoddard PR, Woods MT. Master event relocation of Gorda block earthquakes - implications for deformation. Geophysical Research Letters. 1990;**17**(7):961-964

[15] Zollo A, De Matteis R, Capuano P, Ferulano F, Iannaccone G. Constraints on the shallow crustal model of the Northern Apennines (Italy) from the analysis of microearthquake seismic records. Geophys Journal International. 1995;**120**:646-662

[16] Bouchaala F, Vavryčuk V, Fischer TJ. Accuracy of the master-event and double-difference locations:

Synthetic tests and application to seismicity in West Bohemia. Czech Republic. Journal of Seismology. 2013;**17**(3):841-859

[17] Havskov J, Ottemöller L. SEISAN earthquake analysis software. Seismological Research Letters. 1999;**70**:5

[18] Randall G. Efficient calculation of complete differential seismograms for laterally homogeneous earth models. Geophysical Journal International. 1994;**118**:245-254

[19] Langston C. Depth of faulting during the 1968 Meckering, Australia, earthquake sequence determined from waveform analysis of local seismograms. Journal of Geophysical Research. 1987;**92**(B11):11561-11574

[20] Uski M, Hyvonen T, Korja A, Airo M. Focal mechanisms of three earthquakes in Finland and their relation to surface faults. Tectonophysics. 2003;**363**:141-157

[21] Ma S, Atkinson GM. Focal depth distribution for earthquakes with m_N ≥ 2.8 in western Quebec, southern Ontario and northern New York. Bulletin of Seismological Society of America. 2006;**96**:609-623

[22] Ma S. Focal depth determination for moderate and small earthquakes by modeling regional depth phases sPg, sPmP, and sPn. Bulletin of Seismological Society of America. 2010;**100**:1073-1088

[23] Mereu R, Wang D, Kuhn O, Forsyth D, Green A, Morel P, et al. The 1982 COCRUST seismic experiment across the Ottawa–Bonnechere Graben and Grenville front in Ontario and Quebec. Geophysical Journal of the Royal Astronomical Society. 1986;**84**:491-514

[24] Motazedian D, Ma S, Crane S. Crustal shear-wave velocity models obtained from *Rayleigh* wave dispersion data in North-Eastern America. Bulletin of Seismological Society of America. 2013;**104**(4):1976-1988

[25] Ma S, Motazedian D. Studies on the June 23, 2010 North Ottawa M_W 5.2 earthquake and vicinity seismicity. Journal of Seismology. 2012;**16**:513-534

[26] Ma S. S-wave velocity models obtained using Rg wave dispersion data at shallow parts of the crust in the southern New Brunswick region. Report to: Natural Resources Canada, Ottawa, ON, Canada (2015: contract No. 3000565835)

[27] Lienert BRE, Havskov J. A computer program for locating earthquakes both locally and globally. Seismological Research Letters. 1995;**66**:26-36

[28] Motazedian D, Ma S. Source parameter studies on the 8 January 2017 mw 6.1 resolute, Nunavut, Canada, earthquake. Seismological Research Letters. 2018;**89**(3):1030-1039

[29] Motazedian D, Ma S. Studies on the source parameters of the 23 June 2014 Rat Islands, Alaska, Mw 7.9 earthquake sequence. In: Salazar W, editor. Earthquake–Recent Advances, New Perspectives and Applications. London, UK: INTECHOPEN; 2022

Section 2

Earthquake Forecasting

Chapter 5

The Possibility of Earthquake Forecasting, a Few Days before the Earthquake Using GNSS Satellites

Nikola Solarić and Miljenko Solarić

Abstract

Today, large lengths and compressions of the Earth's crust can be measured with great precision using GNSS satellites. This makes it possible to accurately determine how much the distances were shortened in 1 day under the action of compression, every day, 24 hours a day. If most of the distances were shortened in 1 day, compression of the Earth's crust has occurred, and it can be expected that an earthquake will occur in 2 to 3 days. An earthquake occurred in Skopje after 3 days of compression. We have also analyzed several other earthquakes that occurred after 2 days of compression: the Kraljevo earthquake of 2010, the Drežnica earthquake of 2013, and the Zagreb earthquake of 2020. Based on the conclusions of our analyses of all of these earthquakes, we propose that the Zagreb office for crisis management organize a department that would use satellite monitoring in the vicinity of faults under compression every day.

Keywords: earthquake, forecasting, GNSS satellite

1. Introduction

Today, large distances and compressions of terrain can be measured very precisely using satellites of the GNSS (global navigation satellite system). GNSS consists of GPS (American), GLONASS (Russian), GALILEO (European), and COMPAS (Chinese). GPS (global positioning system) satellites orbit the Earth at an altitude of 20,200 km from the Earth's surface in six orbital planes, so that the GPS receiver on Earth can always receive signals from at least four satellites.

Satellites send signals to Earth, which contain the time of the satellite's atomic clock at the moment the signal is sent from the satellite. The receiver on the Earth's surface records the arrival time of the antenna signal according to its electronic clock. The satellite distance is calculated based on the difference in the time of transmission and the reception of the signal. In a similar way, satellite coordinates are measured from stations on the Earth's surface whose coordinates have previously been established. To make the calculation easier, a positioning system on the Earth's surface was installed in Macedonia. For this purpose, a system of permanent reference stations called MAKPOS (English abbreviation for Macedonian positional system) was set up in North Macedonia to determine the position of points on the ground. Similar

terrestrial positioning systems have also been developed in Croatia (CROPOS), Slovenia (SIGNAL), Serbia (AGROS), Montenegro (MONTEPOS), and Bosnia and Herzegovina (BHPOS and RSPOS) [1, 2].

In order to measure compression in the Earth's crust, four reference stations near the epicenter of the earthquake are selected and measured by GNSS satellites 24 hours a day for several days before and after the earthquake. If almost all the distances are shortened in 1 day, compression has occurred in the Earth's crust, after which an earthquake occurs 3 or 2 days later. In 2016, an earthquake occurred in Skopje, 3 days after compression, while the aforementioned earthquakes in Kraljevo, Drežnica, and Zagreb occurred after 2 days of compression. This phenomenon can be used to predict earthquakes in the vicinity of the fault under compression.

2. Analysis of the deformations of the Earth's crust before and after the Skopje earthquake in September 2016

In order to see the daily changes in the distances between reference stations, we obtained the coordinates of referent stations Skopje, Tetovo, Kumanovo, and Veles from the cadaster in Skopje (**Figure 1**).
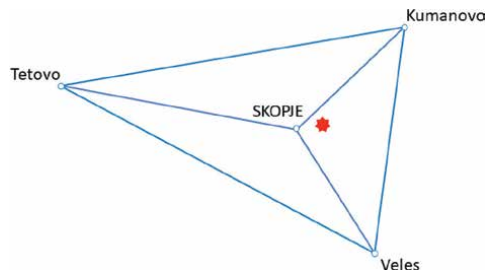
Figure 1.
Reference stations near Skopje.
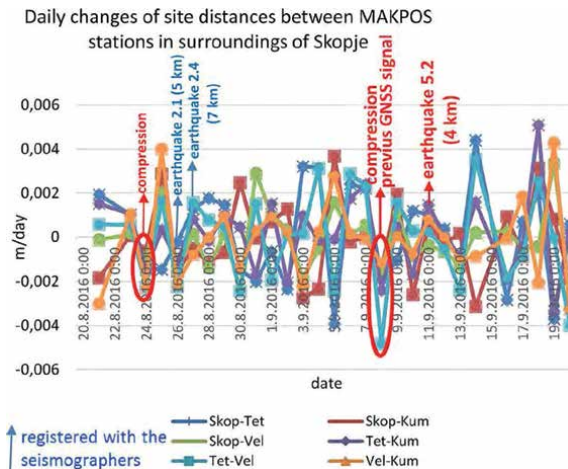
Figure 2.
Daily changes of distances between the observed MAKPOS GNSS stations around Skopje.

We calculated the daily distance changes between reference stations in the vicinity of Skopje and presented the changes graphically in **Figure 2** [3].

Figure 2 shows the decrease in all the distances between the stations on the 8th of September 2016 (i.e., the terrain has compressed), and the strongest earthquake in this area with a magnitude of 5.2 according to the Richter scale occurred 3 days later.

3. The Kraljevo earthquake

The earthquake occurred on November 3, 2010, near Kraljevo. It had a magnitude of 5.4, according to the Richter scale. We received a yearbook from our Sarajevo colleagues and at the end of the yearbook, under the foreign works cited, we found a paper in which the results of measurements after the Kraljevo earthquake were published. Later, we also received standardized measurements published in foreign literature.
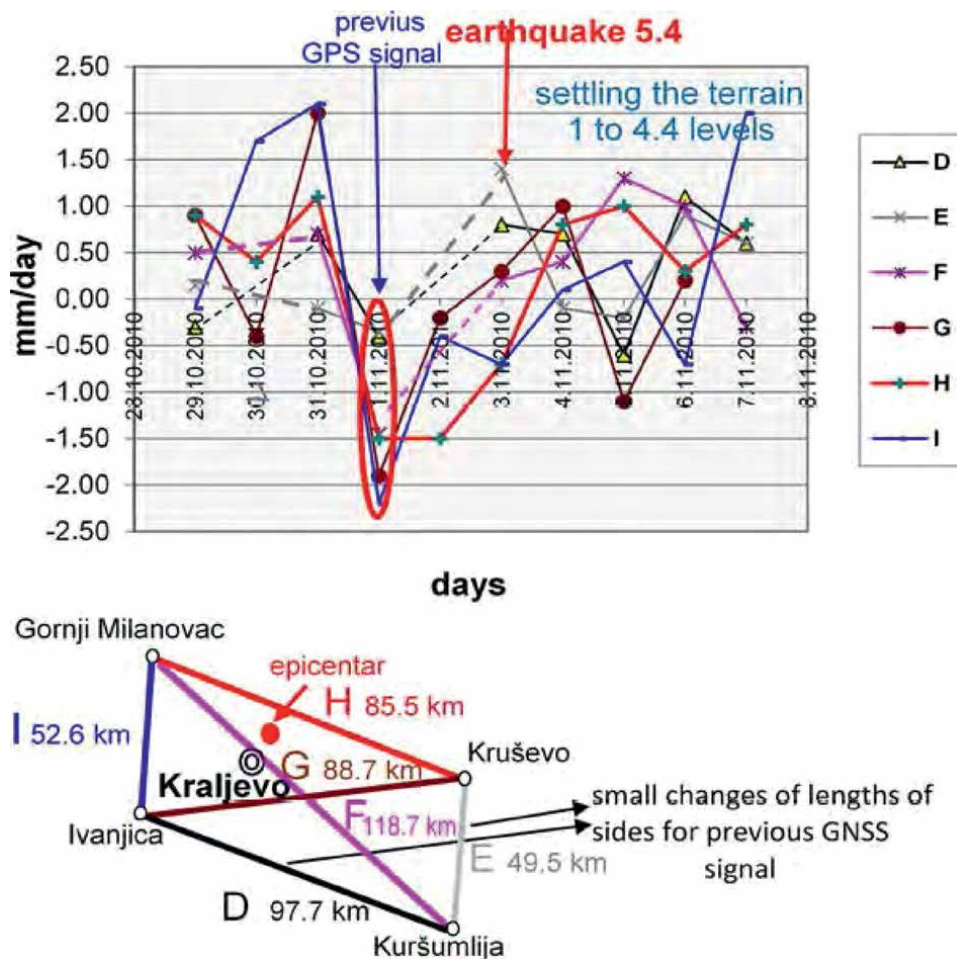
Figure 3.
Daily changes in the side distance between the AGROS permanent stations are presented in quadrangle with diagonals around Kraljevo. Almost all the sides were slightly decreased 2 days before the earthquake, while the sides E, D, and I on the quadrangle, which were further away from what was to be the epicenter of the earthquake shows no significant daily changes in distances [4].

In our analysis of Kraljevo earthquake, we used an elongated quadrangle with diagonals with reference stations in the AGROS network (**Figure 3**).

We calculated the lengths of the sides and the daily changes of lengths and diagonals in Excel and graphically presented them in **Figure 3**.

4. The 2013 Drežnica earthquake

On the 30th of July 2013, at 14:58 local time, a minor earthquake occurred in Croatia with an epicenter in Drežnica, 15 kilometres northeast of Senj [5]. The earthquake had a magnitude of 4.6, according to the Richter scale and its hypocenter was at a depth of 20 km. The intensity in the earthquake epicenter was VI-VII on the Mercalli-Cancan-Selberg (MCS) scale.

The earthquake was felt in the Ogulin, Karlovac, and Zagreb areas, as well as in southern and central Slovenia. The county emergency communications centre in Karlovac received only two reports of damage. Given the low intensity of the earthquake, only minor damage was possible in the epicenter area.

We calculated the daily changes in distances and pressure and presented them graphically in **Figure 4**. From the graph, it can be seen where the compression was.
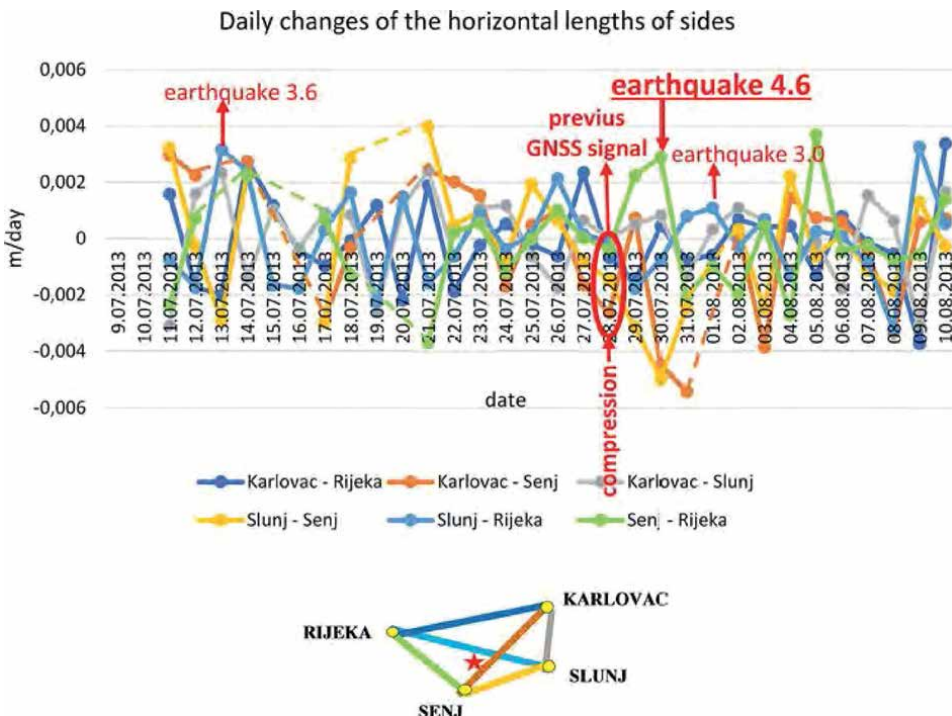
Figure 4.
For our analysis, we chose four crops reference stations in Karlovac, Rijeka, Senj, and Slunj, calculated the daily distance changes and presented them graphically. We saw that almost all distances were shortened on the 28th of July 2013 and 2 days later, on the 30th of July 2013, there was an earthquake [6].

5. The 2020 Zagreb earthquake

The Croatian geodesy journal *Geodetski list* [7] provides a brief overview of the earthquakes that occurred in Zagreb and its surroundings in the past, as well as of the latest earthquakes, which occurred on the 22nd of March 2022, and had magnitudes of 5.4 and 5.0, respectively. These earthquakes, which caused extensive damage to more than 25,000 buildings, occurred 140 years after the great earthquake that devastated Zagreb in 1880.

We chose four reference stations (**Figure 5**) from which GNSS satellite signals were received 24 hours a day. The signals were processed in the Geodetic Administration with the Bernise program package. With the help of these measurements, the daily changes in length were determined. We presented them graphically in **Figure 6**.
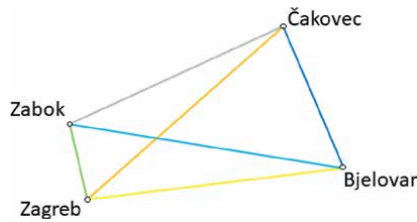
Figure 5.
Crops reference stations for the analysis of daily distance changes before and after the earthquake the Zagreb earthquake on March 22, 2020.
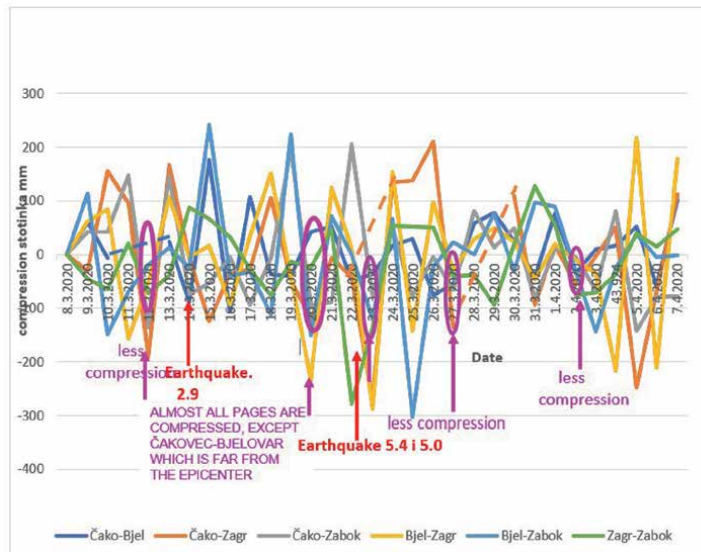
Figure 6.
Daily changes in distances (the Zagreb earthquake on March 22, 2020) [7].

	Earthquake magnitude according to the Richter scale	Pre-earthquake compression (days)	Pre-earthquake compression if calculation time is deduced (days)
Kraljevo, 2010	5.4	2	1.5
Drežnica (Senj), 2013	4.6	2	1.5
Skopje, 2017	5.2	3	2.5
Zagreb, 2020	5.5	2	1.5

Table 1.
A list of earthquakes that have been analyzed.

Figure 6 shows that the Earth's crust was compressed on March 20th, 2020, which meant the earthquake would occur in 2 days. Since approximately half a day is spent on the calculation, this means that an earthquake could be announced one and a half days before.

A similar elongated quadrangle with diagonals was used in the analysis of the Kraljevo [4], Drežnica [5], and Zagreb [7] earthquakes (**Table 1**).

6. Analysis of terrain deformations using daily distance changes in the MAKPOS network before and after the main earthquake, that is, from the 1st of January 2016 to the 30th of October 2016, around Skopje

In order to investigate whether there was previous compression of the terrain before the main earthquake on September 11, 2016, we analyzed the daily changes in the distance between GNSS stations in the vicinity of Skopje since the beginning of the year (i.e., 7 months before the main earthquake).
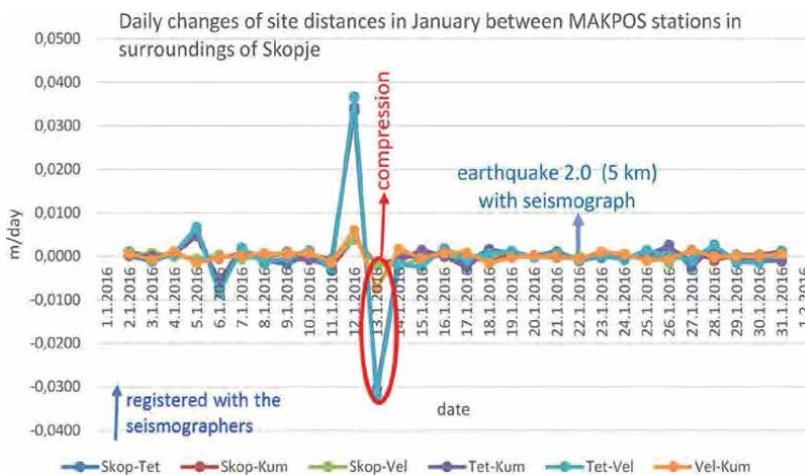
Figure 7.
We also examined the daily changes in longitude from the beginning of 2016 until the main earthquake. For January 2016, we got the daily length changes shown in Figure 7. We can see that there was one small earthquake in January, which was preceded by a small compression. We can see that the two lengths became longer at the beginning of the year. This is typical for such situations because at that time the distance between the plates was large. After the collision, their direction changes, and they become shorter. When it happens later it is usually a sign that the earthquake will be weak. The same thing happened several other months before the earthquake. Graphs for other months in which minor earthquakes occurred can be found in source [8].

Several minor earthquakes occurred in Macedonia in the vicinity of Skopje on September 11, 2016. The third and largest of them occurred at 15:10 (local time) and had a moderate magnitude of 5.2 on the Richter scale. The epicentre of the earthquake was located at latitude $\varphi = 41.98°$ and longitude $\lambda = 21.50°$, and its hypocentre was at a depth of 4 km. It was felt in Kosovska Mitrovica, Niš, Vranje, and Belgrade.

A similar quadrilateral with diagonals was used in the analysis of earthquakes in Kraljevo [4], Drežnica [5], and Zagreb [7].

We also calculated daily changes in the distance between MAKPOS reference stations in the vicinity of Skopje for the months of February, March, April, May, June, July, August, September, and October of 2016. They are graphically shown in Figures 7–15 in our paper [8].

7. Conclusion

This analysis shows that compression of terrain happened before each earthquake. Two to nine days after compression, an earthquake occurred. Only once, on the 29th of July 2016, was there no earthquake after compaction of soil, because the soil layers did not crack.

We determined the daily changes in the distance between GNSS stations in the vicinity of Skopje for January 2016. The graph of the daily changes for January is shown in **Figure** 7. This graph shows that on the 12th of January 2016, there was a relatively large extension of Skoplje-Tetovo and Tetovo-Kumanovo distances. These shifts were about 3.5 cm in length. The spaces between the plates were large, but after the collision of the plates, the direction of the plates' motion changed. Nine days after the compression in January, a smaller earthquake with a magnitude of 2.0 on the Richter scale occurred (**Figure** 7).

8. Proposal

Based on our analysis of the four earthquakes, my brother and I can confidently propose that a department be established at the Geodetic Administration and the Faculty of Geodesy that will monitor the daily changes in the length of the Earth's crust using our method with GNSS measurements. The department would initially act in the Zagreb area, where the population is largest, and it would move on to other seismically active areas of Croatia once it has proved to be effective. That department of the Geodetic Administration would have almost all the instrumentation necessary for such analyses. There would be no great need for additional funding for the instruments. Furthermore, the Geodetic Administration already has an excellent expert, who would be ideal for the task of processing our geodetic measurements. All measurements and calculations should be automated. All of this should be included in the annual financial plan of the Geodetic Administration and the Faculty of Geodesy. Also, the geodetic expert from the Geodetic Administration should invite colleagues from the Faculty of Geodesy and the Seismology Department of the Faculty of Science to work with them. The Zagreb office for crisis management should financially support this initiative. In addition, the project could be EU-funded. We would be overjoyed if my friends, as well as all inhabitants of Zagreb and Croatia, become safer from, and more prepared for, earthquakes.

Acknowledgements

Author details

Nikola Solarić* and Miljenko Solarić
Faculty of Geodesy, University of Zagreb, Zagreb, Croatia

*Address all correspondence to: nikola.solaric@geof.hr

IntechOpen

References

[1] Dimeski S, Burovski D, Tasevski S. National Report – Republic of Macedonia EUREF 2012 Symposium, 6-18. 2012

[2] Trpeski S, Dimeski S, Lekoski Z. MAKPOS – Network of Permanent GNSS Stations in Republic of Macedonia, Proceedings, 3rd CROPOS Conference, 24-25 October 2013, Opatija. 2013. pp. 77-81

[3] Solaric M, Solaric N, Bogdanovski Z, Dimeski S. Određivanje pomicanja Zemljine kore u okolici Skopja s pomoću MAKPOS-ovih referentnih GNSS-postaja. (Determining the movement of the Earth's crust in the vicinity of Skopje using MAKPOS reference GNSS stations). Geodetski list. 2017;**71** (94) (4):277-290

[4] Solaric N, Solaric M. Prijedlog da se u Zagrebu i okolici uz CROPOS-ove stanice postavi i nekoliko GPS (GNSS)-permanentnih stanica za geodinamiku i moguću najavu većeg potresa u sljedećem vremenskom razdoblju. (Proposal that in Zagreb and its surroundings, in addition to CROPOS stations and several GPS (GNSS) permanent stations for geodynamics and the possible announcement of a major earthquake in the next period of time). Geodetski list. 2012;**66** (89)(3):149-164

[5] Solaric N, Solaric M, Pejakovic M. Dva dana prije potresa u Drežnici 2013. godine došlo je do kompresije terena. (Two days before the earthquake in Drežnica in 2013 there was a compression of the terrain). Geodetski list. 2017;**71** (94)(3):203-214

[6] Solaric N, Solaric M, Marjanovic M, Bogdanovski Z, Dimeski S. Reference GNSS stations for warning on possibility of upcoming earthquake in Zagreb. Earth Science. 2020;**9**(3):100-107. DOI: 10.11648/j.earth.20200903.12

[7] Solaric N, Solaric M. Kompresija Zemljine kore dva dana prije potresa 22. ožujka 2020. u Zagrebu. (Compression of the Earth's crust two days before the earthquake 03/22/2020. in Zagreb). Geodetski list. 2021;**75** (98)(1):1-8

[8] Solaric N, Solaric M, Bogdanovski Z, Dimeski S. Tri dana prije potresa u Skopju došlo je do kompresije Zemljine kore. (Three days before the earthquake in Skopje, compression of the Earth's crust occurred). Geodetski list, 72 (95). 2018;**1**:15-35

Section 3

Geotechnical Engineering

Plasticity Model Required to Prevent Geotechnical Failures in Tectonic Earthquakes

Tse-Shan Hsu

Abstract

Although geotechnical engineering design must meet seismic design specifications, many geotechnical failures, including foundations, retaining walls, and slopes, have nevertheless occurred during tectonic earthquakes. The evaluation of the ultimate bearing capacity of the foundation, the active and passive earth pressure of the retaining wall, and the safety factor of the slope all need to use the shear failure band and soil plasticity models at the same time. In view of this, it is first proven that shear failure bands can only appear in the strain softening model. Secondly, it is shown through case studies that traditional evaluation methods for determining the foundation ultimate bearing capacity, the active earth pressure of the retaining wall, and the safety factor of slope stability all adopt both the shear failure band and the perfectly plastic soil model. Since the perfectly plastic soil model is incompatible with shear failure bands, this results in a large number of foundations, retaining walls, and slopes failing during tectonic earthquakes. Based on the research results, it is suggested that a soil strain softening model compatible with shear failure bands be adopted in the analysis of geotechnical engineering projects so as to ensure safety during tectonic earthquakes.

Keywords: tectonic earthquake, geotechnical failure, shear band, foundation, retaining wall, slope

1. Introduction

According to the generalized soil stress–strain diagram shown in **Figure 1**, after the strain in firm or dense soil exceeds the point of maximum stress, the stress decreases with increasing strain (known as strain softening) and finally approaches the residual stress.

The deformation of various structures under the action of external loads has previously been determined under Drucker stability postulates [1, 2], *i.e.*, $d\boldsymbol{\sigma}$: $d\boldsymbol{\varepsilon}_p \geq 0$, where $d\boldsymbol{\sigma}$ is the stress increment tensor and $d\boldsymbol{\varepsilon}_p$ is the incremental plastic strain tensor. For this reason, limit analysis methods have been proposed for analysis
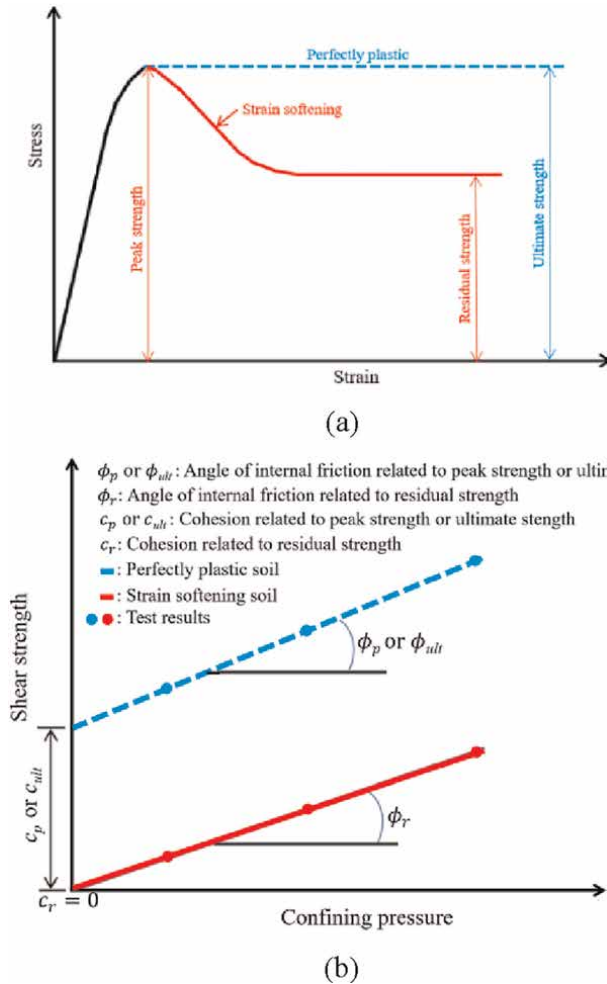
Figure 1.
Results of a typical triaxial compression test for strain softening soil and perfectly plastic soil. (a) Stress-strain relationships for a confining pressure. (b) Shear strength-confining pressure relationships for three different confining pressures.

of foundation ultimate bearing capacity, the active earth pressure of retaining walls, and slope stability. Based on the requirements of limit analysis, the strain softening behavior of soil has been ignored and been replaced with a perfectly plastic model. **Figure 1a** is the stress–strain relationships of soil obtained from a typical triaxial compression test. **Figure 1a** shows that when the strain is greater than the strain corresponding to the peak strength, the soil strength should decrease with the increase of the strain, so the phenomenon of strain softening occurs. However, since the traditional analyses of soil mechanics and foundation engineering are carried out under the conditions of Drucker stability postulates, the experimental result of strain softening is modified to be perfectly plastic.

When foundations, retaining walls, and slopes are designed using limit analysis and safety factors are used in accordance with seismic design codes, geotechnical failures such as those shown in **Figures 2–4** should not be prevalent during tectonic

Figure 2.
Tilting failure of a new building [3] after the Meinong earthquake in 2016 (Tainan, Taiwan).

Figure 3.
Failure of retaining walls under different conditions [4]: (a) during no rain and no earthquake (Formosa expressway 3.1 K, Keelung, Taiwan); (b) during the rainy season (Lincoln County in New Taipei City, Taiwan); (c) during an earthquake (Quanjiafu Community in Taichung, Taiwan).
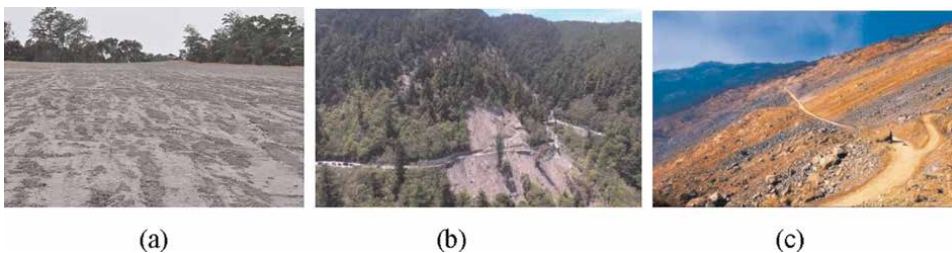
Figure 4.
Shear failure of slopes under different conditions: (a) normal conditions [5] (Formosa expressway 3.1 K, Keelung, Taiwan); (b) during the rainy season (Tai-8 route 109 K, Taichung, Taiwan); (c) during an earthquake (Jiufen-Ershan, Nantou, Taiwan).

earthquakes. Therefore, it is necessary to further explore the suitability of the perfectly plastic model as used in limit analysis.

2. Numerical simulation analysis

2.1 The elastic: plastic model

The yield function adopted is given in Eq. 1 [6]:

$$F = \sqrt{J_{2D}} - \left(\kappa + H\gamma_{oct}^P\right) = 0 \tag{1}$$

where J_{2D} is the second invariant of deviatoric stress; κ is the size of the initial yield surface; γ_{oct}^p is the plastic octahedral shear strain; and H is the strain-hardening (or strain-softening) parameter. Differentiating Eq. 1 leads to:

$$dF = \left(\frac{\partial F}{\partial \boldsymbol{\sigma}}\right)^T d\boldsymbol{\sigma} + \left(\frac{\partial F}{\partial \gamma_{oct}^p}\right)^T d\gamma_{oct}^p = \left(\frac{\partial F}{\partial \boldsymbol{\sigma}}\right)^T d\boldsymbol{\sigma} - H d\gamma_{oct}^p = 0 \qquad (2)$$

where $d\boldsymbol{\sigma}$ is the incremental stress vector; the transpose of vector $\frac{\partial F}{\partial \boldsymbol{\sigma}}$ is $\left(\frac{\partial F}{\partial \boldsymbol{\sigma}}\right)^T$; the transpose of vector $\frac{\partial F}{\partial \gamma_{oct}^p}$ is $\left(\frac{\partial F}{\partial \gamma_{oct}^p}\right)^T$; and $d\gamma_{oct}^p$ is the incremental plastic octahedral shear strain. The flow rule is:

$$d\boldsymbol{\varepsilon}^p = \lambda \frac{\partial F}{\partial \boldsymbol{\sigma}} \qquad (3)$$

where $d\boldsymbol{\varepsilon}^p$ is the incremental plastic strain vector. Therefore, the elastic–plastic stress–strain matrix $\boldsymbol{D}^{ep}$ can be expressed as follows:

$$\boldsymbol{D}^{ep} = \boldsymbol{D}^e - \boldsymbol{D}^p = \boldsymbol{D}^e - \boldsymbol{D}^e \left(\frac{\partial F}{\partial \boldsymbol{\sigma}}\right)^T \frac{\partial F}{\partial \boldsymbol{\sigma}} \boldsymbol{D}^e \left[\frac{1}{\sqrt{6}}H + \left(\frac{\partial F}{\partial \boldsymbol{\sigma}}\right)^T \boldsymbol{D}^e \frac{\partial F}{\partial \boldsymbol{\sigma}}\right]^{-1} \qquad (4)$$

where super indexes e and p mean elastic and plastic, respectively.

2.2 Conditions of stability

For strain-softening materials, under the action of external force, when the strain goes deep into the plastic range, to obtain the stable incremental finite-element solutions, Prevost [7] used the variational approach based on the internal strain energy due to the stresses of the existing state and the stress increments, thereby obtaining the failure mechanism; then, define "A failure mechanism develops when the incremental external work put into the system, plus the incremental work reduced by the plastic, strain-softening zone, equals or exceeds the work that may be absorbed by the surrounding unyielded and/or strain-hardening material." The total volume of the body, V, can be divided into V_{ps} and V- V_{ps}, where V_{ps} is the total volume of the strain-softening regions. Under this consideration, the uniqueness of the incremental solutions is proved.

For physical materials, if the total external incremental applied energy is positive, the total induced internal incremental strain energy must be positive. On the other hand, if the total external incremental applied energy is negative, the total induced internal incremental strain energy must be negative. All stable numerical solutions must obey such a law; otherwise, the numerical solution will be unstable.

If π_p, is the total potential energy in static analyses under a variational approach, then the total incremental potential energy, $d\pi_p$ is:

$$d\pi_p = \frac{1}{2} \int_V d\boldsymbol{\sigma}^T d\boldsymbol{\varepsilon} dV - \sum d\boldsymbol{u}^T d\boldsymbol{F} \qquad (5)$$

where $d\boldsymbol{\sigma}^T$ is the transpose of the incremental stress vector, $d\boldsymbol{\varepsilon}$ is the incremental strain vector, $d\boldsymbol{u}^T$ is the transpose of the incremental displacement vector, and $d\boldsymbol{F}$ is the incremental force vector.

In the finite-element approximation, Eq. 5 can be expressed as

$$d\pi_p = \frac{1}{2}\int_V \left(d\boldsymbol{u}^T\boldsymbol{B}^T\boldsymbol{D}^{ep}\boldsymbol{B}d\boldsymbol{u}\right)dV - \sum\left(d\boldsymbol{u}^T d\boldsymbol{F}\right) \tag{6}$$

where $\boldsymbol{B}^T$ is the transpose of the strain–displacement matrix. The global stiffness matrix $\boldsymbol{K}$ is:

$$\boldsymbol{K} = \int_V \left(\boldsymbol{B}^T\boldsymbol{D}^{ep}\boldsymbol{B}\right)dV \tag{7}$$

Substitution of Eq. 7 into 6 leads to:

$$d\pi_p = \frac{1}{2}d\boldsymbol{u}^T\boldsymbol{K}d\boldsymbol{u} - d\boldsymbol{u}^T d\boldsymbol{F} \tag{8}$$

It can be seen from Eq. 8 that, for the condition of the prescribed displacements and since all of the forces are induced, both terms on the right-hand side of Eq. 8 will always have the same sign. This means that the condition of stability for the incremental solutions for the prescribed displacement case is guaranteed. When the forces are prescribed and if the total external incremental energy is positive, the stability of the incremental solutions is guaranteed only when the global stiffness matrix is positive definite. When the global stiffness matrix is negative definite, the solution will be unstable [6].

2.3 Conditions of uniqueness

For a strain-hardening material or perfectly plastic material, since these types of materials meet the Drucker stability postulates, the solution is unique because the two potential energy increments on the right-hand side of Eq. 8 are both positive.

Based on the need to prove a unique solution, first let us assume two sets of solutions, $d\boldsymbol{u}_1$ and $d\boldsymbol{u}_2$, satisfy the equilibrium condition at the same time. Under this assumption, both $d\boldsymbol{u}_1$ and $d\boldsymbol{u}_2$ should provide the same minimum total incremental potential energy. By substituting $d\boldsymbol{u}_1$ and $d\boldsymbol{u}_2$ into Eq. 8 and minimizing the total incremental potential energy with respect to $d\boldsymbol{u}_1$ and $d\boldsymbol{u}_2$, one obtains:

$$\boldsymbol{K}d\boldsymbol{u}_1 = d\boldsymbol{F} \tag{9}$$

$$\boldsymbol{K}d\boldsymbol{u}_2 = d\boldsymbol{F} \tag{10}$$

Eq. 9 minus Eq. 10 equals:

$$\boldsymbol{K}(d\boldsymbol{u}_1 - d\boldsymbol{u}_2) = \boldsymbol{0} \tag{11}$$

Therefore, one of the following two conditions must be true:

$$d\boldsymbol{u_1} = d\boldsymbol{u_2} \tag{12}$$

(when the determinant of $\boldsymbol{K}$ is not equal to zero) or

$$\det(\boldsymbol{K}) = \boldsymbol{0}(\text{when } d\boldsymbol{u_1} \neq d\boldsymbol{u_2}) \tag{13}$$
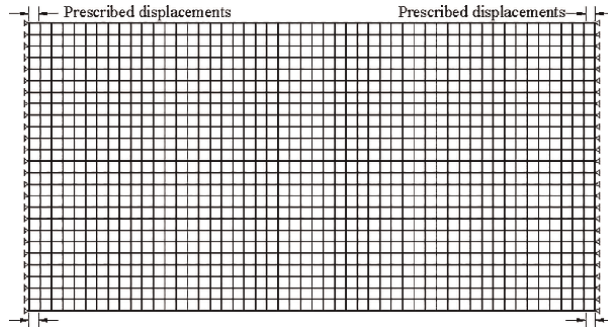
Figure 5.
*Finite element mesh, boundary conditions, and prescribed lateral displacements.*

2.4 Finite element solutions

For the 5.08 cm × 2.54 cm plate shown in **Figure 5** under plane strain conditions loaded at both ends and where the movement in the direction perpendicular to the loading is constrained, a uniform 50 × 25 mesh was used to analyze its behavior under uniformly prescribed loading conditions. The material properties used were: (1) the initial size of the yield surface, κ, was equal to 24 kPa, (2) Young's modulus, E, was equal to 1200 kPa, (3) Poisson's ratio, ν, was equal to 0.3, (4) the shear modulus, G, was equal to 462 kPa, and (5) the strain softening parameter, $H/2G$, was equal to 0.0 to model perfectly plastic behavior and equal to -0.05 to model strain softening behavior. To obtain shear bands in a numerical solution close to 45 degrees, it will be better to use square with the five-node elements. For the plate problem analyzed, the sequence for the application of the uniform prescribed displacements in the main load steps are 0.1143 cm, 0.0635 cm, 0.0635 cm, 0.0635 cm, 0.0635 cm, and 0.0635 cm, respectively. Each main load step is further subdivided into five sub-steps of load. Therefore, after applying all the load, the width of the plate remains unchanged at 2.54 cm, and the length is shortened to 4.6482 cm.

For elastic–perfectly plastic materials, when the determinant of the structural stiffness matrix $\boldsymbol{K}$ is not equal to zero, then $d\boldsymbol{u}_1 = d\boldsymbol{u}_2$. In this case, the results of finite element analysis including the deformed mesh, velocity vector distribution map, and contour lines of incremental strain energy density (see **Figure 6**) do not include shear failure bands and maintain the original symmetry because Drucker stability postulates continue to be satisfied.

(a)   (b)   (c)
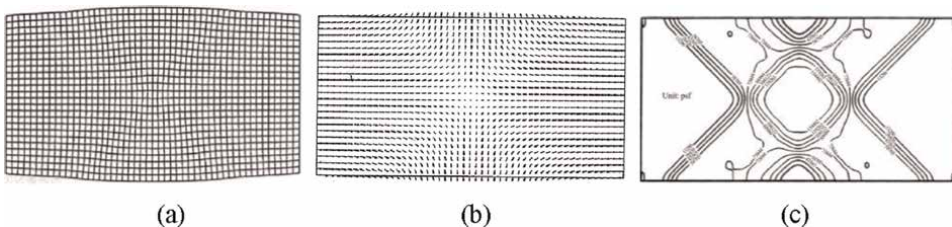
Figure 6.
Results of the finite-element analysis of a plate using an elastic–perfectly plastic model [6]: (a) deformed mesh; (b) velocity vector distribution map; (c) contours of incremental strain energy density. Note: Dimensions for the plates shown in Figure 6b and c are 5.08 cm × 2.54 cm.
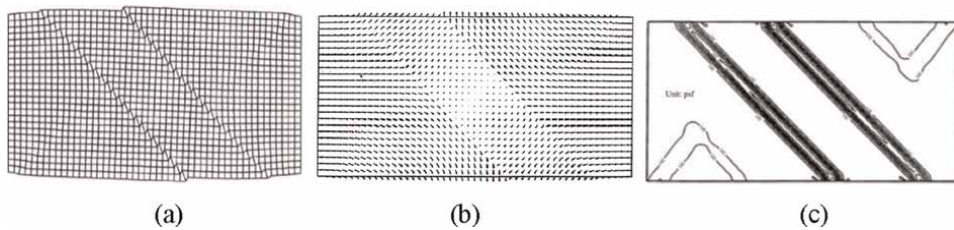
Figure 7.
Results of the finite-element analysis of a plate using an elastic–plastic strain softening model [6]: (a) deformed mesh; (b) velocity vector distribution map; (c) contours of incremental strain energy density. Note: Dimensions for the plates shown in Figure 7b and c are 5.08 cm × 2.54 cm.

For elastic–plastic strain-softening materials, the determinant of the structural stiffness matrix K is equal to zero. In this case, external agencies must be applied as specified displacements instead of specified loads to obtain the results of the finite element analysis, including the deformed mesh, velocity vector distribution map, and contour lines of incremental strain energy density (see **Figure 7**), such that they do include asymmetric shear failure bands.

2.5 Loss of symmetry

It can be seen from **Figure 7** that the condition for the loss of symmetry of the foundation soil or the soil specimen is the appearance of shear failure bands induced by plastic strain softening.

As far as the structural stiffness matrix K is concerned, its determinant will be equal to zero because of the plastic strain softening, which will induce shear failure bands under prescribed displacements. In the elastic range, the entries of the structural stiffness matrix K have a symmetric condition, that is $k_{ij} = k_{ji}$, and in the plastic strain-softening range, the condition for the determinant of K to be equal to zero is that the entries in the two adjacent rows of the structural stiffness matrix K correspond, that is $k_{mi} = k_{nj}$ for $n = m+1$. The structure matrix is therefore asymmetric [3].

3. The ultimate bearing capacity of the strip foundation

3.1 Equation derivation

Before deriving the ultimate bearing capacity of a strip foundation, Terzaghi [8] assumed symmetric general shear failure bands in the foundation soil under the ultimate load (see **Figure 8**). The required foundation soil properties include the cohesion c, angle of internal friction ϕ, and unit weight γ. The cohesion $c = c_{ult}$ and internal friction angle $\phi = \phi_{ult}$ were obtained from the perfectly plastic curve shown in **Figure 1b**. **Figure 8** shows that Terzaghi [8] divided the whole area enclosed by the general shear failure bands into active zone I, radial shear zones II and II1, and passive zones III and III1. The ultimate bearing capacity Q_{ult} of the foundation was equal to twice the passive earth pressures P_p that act on the shear failure bands $\overline{ad}$ and $\overline{bd}$. The passive earth pressure P_p included the passive earth pressure P_{p1} generated by the soil cohesion c, the passive earth pressure P_{p2} was generated by the overburden pressure γD_f (*i.e.*, q), and the passive earth pressure P_{p3} was generated by the weight of the soil
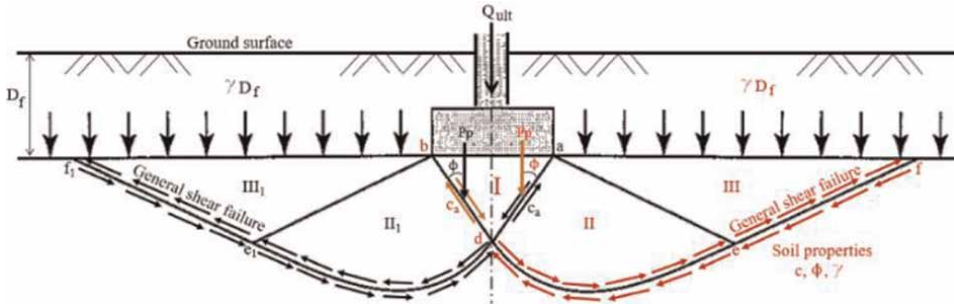
Figure 8.
The general shear failure bands set before deriving the ultimate bearing capacity equation of the strip foundation (reproduced from Terzaghi [8]).

enclosed by the shear failure band $\overline{adef}$. Based on the balance of the vertical components of all forces, Terzaghi obtained the ultimate bearing capacity of the foundation as:

$$q_{ult} = 2\left(P_{p1} + P_{p2} + P_{p3} + \frac{1}{2}Bc\tan\phi\right)/B = cN_c + qN_q + \frac{1}{2}B\gamma N_\gamma \tag{14}$$

where N_c, N_q, and N_γ are bearing-capacity factors: $N_q = \frac{a^2}{2\cos^2\left(45°+\phi/2\right)}$; $N_c = \left(N_q - 1\right)\cot\phi$; $N_\gamma = \frac{\tan\phi}{2}\left(\frac{K_{p\gamma}}{\cos^2\phi} - 1\right)$; $a = \exp\left[\left(0.75\pi - \frac{\phi}{2}\right)\tan\phi\right]$; $K_{p\gamma}$ =10.8, 14.7, 25.0, 52.0, and 141.0 when ϕ is equal to $0°$, $10°$, $20°$, $30°$, and $40°$, respectively.

3.2 The overestimation problems

3.2.1 Problems arising from adopting symmetric general shear failure band

When plastic strain softening induces structural instability, the asymmetric structural matrix results in asymmetric general shear failure bands (detailed in **Figure 9**). Thus, the adoption of symmetric general failure bands by Terzaghi before deriving the ultimate bearing capacity equation of the strip foundation should be improved by the asymmetric shear failure pattern. In this case, when the ultimate bearing capacity of the strip foundation is evaluated by Eq. 14, the evaluation result will be overestimated twice.
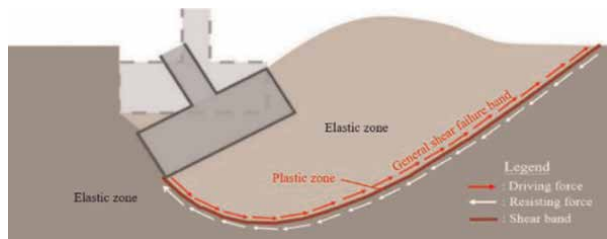
Figure 9.
Schematic diagram of the asymmetric general shear failure band of a strip foundation (reproduced from [3]).

3.2.2 Problems arising from adopting perfectly plastic model

When the perfectly plastic model is adopted, the shear strength parameters used are obtained from the experimental results of the ultimate shear strength shown in **Figure 1**, but the asymmetric general shear failure band is induced by the plastic strain softening effect; therefore, the shear strength will decrease from the peak value to the residual value as the strain softens. In other words, the cohesion c will be reduced from the peak value c_p to the residual value c_r, $c_r \approx 0$, and the angle of internal friction ϕ will also be reduced from the peak value ϕ_p to the residual value ϕ_r. Therefore, when calculating the ultimate bearing capacity Q_{ult} using the ultimate shear strength parameter, there will also be an overestimation problem [3].

4. The active Coulomb's earth pressure of retaining wall

4.1 The adopted perfectly plastic model

In **Figure 1a**, the red solid line represents the stress–strain curve of real soil obtained from laboratory triaxial compression tests. It shows the transition from peak strength to residual strength due to plastic strain softening. However, the plastic strain softening curve of soil has generally been simplified as a perfectly plastic curve in the retaining wall literature, as shown in **Figure 1a**.

4.2 Numerical simulation for the formation of shear failure bands

Coulomb [9] proposed the theory of active earth pressure as applied to retaining walls using both a shear failure band and a perfectly plastic model. At that time Coulomb did not know whether the use of the perfectly plastic model could induce shear failure bands.

For perfectly plastic and strain softening models, the numerical simulation analysis results using the finite element method are presented in **Figures 6** and 7, respectively. The results show that in the perfectly plastic model, the plate does not develop a shear failure band when the strain of the lateral compression of the plate goes deep into the plastic range. Only in the plastic strain softening model does the plate show the induced shear failure bands.

Figure 7 shows that the formation of the shear failure bands has two requirements: strain deep into the plastic range and strain softening. The strain softening originates from the volume expansion of the sliding failure block. In other words, the negative incremental strain energy in strain softening is the motivating force for inducing the shear failure band.

4.3 Case study of when Coulomb's active earth pressure of retaining walls is not a maximum

In **Figure 10**, ΔABC is the potential active sliding failure block for a retaining wall, as proposed by Coulomb [9]. Here, H is the height of the retaining wall, γ is the unit weight of the soil, W is the weight per unit length of ΔABC, β is the inclination angle of $\overline{AC}$, θ is the inclination angle of $\overline{AB}$, ρ is the inclination angle of the potential active shear failure band $\overline{BC}$, $\rho - \beta$ is the angle between $\overline{CA}$ and $\overline{CB}$, R is the resultant shear
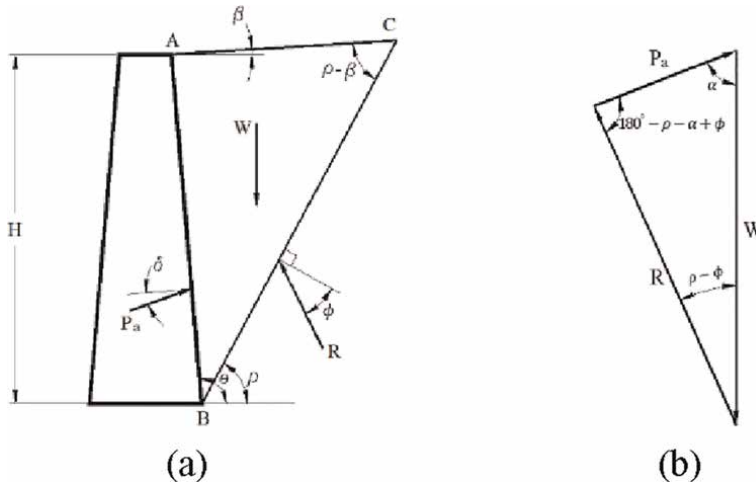
Figure 10.
Various forces acting on a retaining wall as proposed by Coulomb [9]: (a) Coulomb's potential sliding failure block under active conditions; (b) the closed force polygon of W, R, and P_a.

resisting force acting on $\overline{BC}$, internal friction angle ɸ is the intersection angle of R and the normal to $\overline{BC}$, P_a is the active earth pressure acting on $\overline{AB}$, and wall friction angle δ is the angle of intersection between P_a and the normal to $\overline{AB}$. From **Figure 10**, it can be seen that the Coulomb's active earth pressure P_a of retaining walls does not consider the effects of strain softening and shear banding.

We used a retaining wall height of H = 6 m, soil unit weight $\gamma = 22\,\text{kN/m}^3$, internal friction angle $= 50°$, cohesion c = 0 kPa, wall friction angle δ = 33.3°, $\overline{AC}$ inclination angle $\beta = 0°$, and $\overline{AB}$ inclination angle θ = 105°. When adopting the elastic-perfectly plastic model, the result of the analysis shows that the sliding failure plane inclination angle was $\rho = 72.83°$, the failure block weight was W = 228.46 kN, and the traditional Coulomb active earth pressure was $P_a = 98.19$ kN.

4.3.1 Increase in the Coulomb's active earth pressure of retaining walls from the strain softening effect

Coulomb's active earth pressure of retaining walls is the maximum lateral earth pressure. **Figure 11a** shows that during the 921 Jiji earthquake, the shear-banding zone on the left bank of the downstream Shigang Weir caused the sandy gravel layer on the back of the retaining wall to change from its original dense state to a loose state after shear banding. **Figure 11b** shows that after shear banding, the sand and gravel separated and the retaining wall slid into the riverbed.

As the failure block continued to slide along the same shear failure band, it continued to undergo brittle fracture and strain softening during the sliding process. Further, the angle of internal friction ɸ decreased from a peak value of 50° to a residual value of 33°, and the wall friction angle δ decreased from 33.3° to 22°. When the inclination angle β of $\overline{AC}$, the inclination angle θ of $\overline{AB}$, the internal friction angle ɸ, the wall friction angle δ, and the angle α shown in **Figure 10b** are all known, the inclination angle ρ of the potential active shear failure band $\overline{BC}$ can be calculated using

(a)

(b)

Figure 11.
Collapse of the retaining wall induced by shear banding during the 921 Jiji earthquake [10]: (a) different sandy gravel conditions on both sides of the failure plan; (b) the separated sandy gravel and retaining wall slipped to the riverbed.

$\phi_p \rightarrow \phi_r$	δ	P_a(kN)	ΔP_a(kN)
$50^{\circ} \rightarrow 33^{\circ}$	$33.3^{\circ} \rightarrow 22^{\circ}$	$98.19 \rightarrow 146.51$ ($100\% \rightarrow 149.2\%$)	48.32

Table 1.
Analysis results of the increase of the Coulomb's active earth pressure of the retaining wall induced by soil strain softening [10].

Eq. 15. Then the Coulomb's active earth pressure P_a of the retaining wall shown in **Table 1** can be calculated using Eq. 16 [10]:

$$cot\,(\theta - \rho) + cot\,(\rho - \beta) = cot\,(\rho - \phi) - cot\,(\rho + \alpha - \phi) \qquad (15)$$

$$P_a = W\,\frac{sin\,(\rho - \phi)}{sin\,(180° - \rho - \alpha + \phi)} = \frac{1}{2}\gamma H^2\,\frac{sin\,(\theta - \beta)}{sin^{\,2}\theta}\cdot\frac{sin\,(\theta - \rho)}{sin\,(\rho - \beta)}\cdot\frac{sin\,(\rho - \phi)}{sin\,(\rho + \alpha - \phi)}$$
$$(16)$$

According to **Table 1**, the Coulomb's active earth pressure of the retaining wall increased from 98.19 kN to 146.51 kN due to soil strain softening; therefore, the increment of the Coulomb's active earth pressure of the retaining wall, ΔP_a, was 48.32 kN.
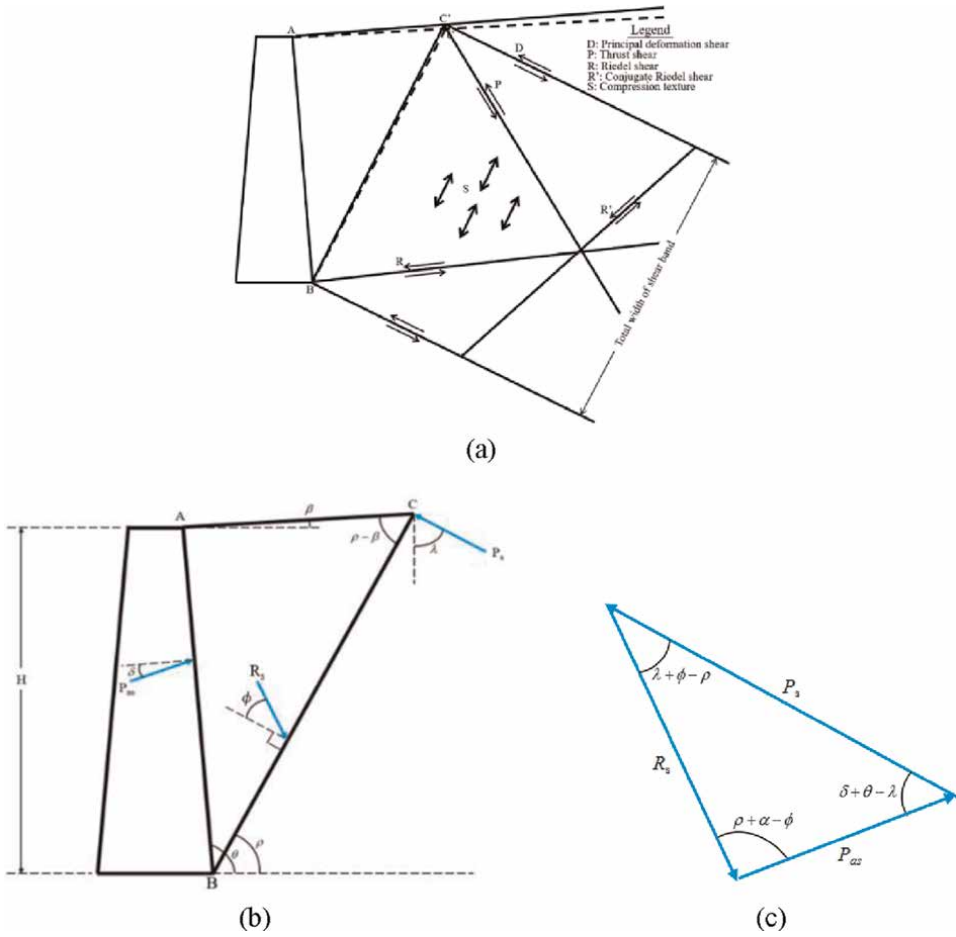
Figure 12.
The mechanism of the shear-band tilting effect inducing an increment in the Coulomb's active earth pressure of the retaining wall [10]: (a) shear-band tilting effect; (b) the action positions of P_s, R_s, and P_{as} on the retaining wall and the soil behind the wall; (c) the closed force polygon of P_s, R_s, and P_{as}.

4.3.2 Increase in the Coulomb's active earth pressure of retaining walls from the shear band tilting effect

Without the constraint of vertical pressure on the ground surface, a tectonic plate induces a shear-band tilting effect under lateral compression. **Figure 12a** shows the shear-band tilting effect of the shear band on the back of the retaining wall. **Figure 12b** shows the shear-band tilting force P_s caused by shear banding shown in **Figure 12a**, the resultant force R_s of the resistance on the shear failure band of the retaining wall, and the increment of the Coulomb's active earth pressure of the retaining wall P_{as} [10].

According to the closed force polygon shown in **Figure 12c** and the sine law, Eq. 17 can be used to calculate P_{as} [10]:

$$P_{as} = P_s \frac{\sin (\lambda + \phi - \rho)}{\sin (\rho + \alpha - \phi)} \tag{17}$$

Following the case study of the retaining wall discussed in Section 4.3.1, when the elastic-perfectly plastic model was adopted, the calculated inclination angle of the sliding failure plane was $\rho = 72.83°$., the failure block weight was $W = 228.46$ kN, and the Coulomb's active earth pressure was $P_a = 98.19$ kN.

When one side of the failure block at the back of the retaining wall was uplifted by the shear-band tilting force P_s, if $P_s = 0.5W$, the increment in the Coulomb's active earth pressure of the retaining wall P_{as} can be calculated as 48.81 kN. Thus, the increment rate of Coulomb's active earth pressure caused by the shear-band tilting effect was 49.7% [10].

5. The shear-band slope stability analysis method

Considering the lateral compression of tectonic plates, Hsu [3] simulated the formation of shear failure bands, as shown in **Figure 7**. **Figure 7a** and **b** demonstrate that when the strain goes deep into plastic range, the localization of deformations of the tectonic plate will appear due to the loss of ellipticity caused by strain softening and further develop shear failure bands and shear-band tilting slopes.

Since the amount of shear banding accumulates from all previous tectonic earthquakes, the degree of brittle fracture in rocks of multi-step shear-band tilting slopes (**Figure 13**) will increase and large-scale shear failure of slopes will occur.

The Tsaoling area had three shear failures before the 1999 Jiji earthquake, in 1861, 1941, and 1979 [13]. Given that slope shear failure continued to occur at the same location, it can be deduced that the existing slope stability analysis methods did not consider the shear banding effect. Therefore, the Tsaoling landslide area had a total length of 2324.5 m and an average thickness of 24 m as shown in **Figure 13**. Although Hung et al. [14] obtained the shear strength parameters for the sliding plane, since the shear failure plane shown in **Figure 13** is the interface between silty sandstone and shale, the shear strength parameters they obtained were low because only the horizontal ground vibration was considered. To improve this, a new shear-band slope stability analysis method is provided below.

Figure 13.
Five-steps appeared in the Tsaoling shear failure planes during the Jiji earthquake [11, 12].
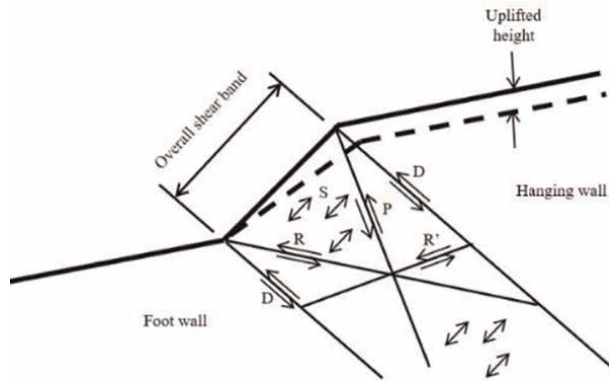
Figure 14.
Shear banding that causes the hanging wall to rise [12].

5.1 The shear-band slope stability analysis method

Figure 14 shows a sliding block with two sliding surfaces, the lower sliding surface has a relatively gentle slope and the upper sliding surface has a relatively steep slope. Since the relatively steep sliding surface is caused by the uplifting action of shear banding, **Figure 14** shows that the shear textures within an overall shear band include principal displacement shear D, thrust shear P, Riedel shear R, conjugate Riedel shear R', and compression textures S. Thus, the hanging wall shown in **Figure 14** will continue to be lifted during the shear banding of tectonic earthquakes, whereas the foot wall will remain stationary [12].

First, based on the consideration of the shear banding and ground vibration effects of tectonic earthquakes, a new slope stability analysis model as shown in **Figure 15** is presented; in which a shear banding force, P_s, is acting on the top of the upper sliding
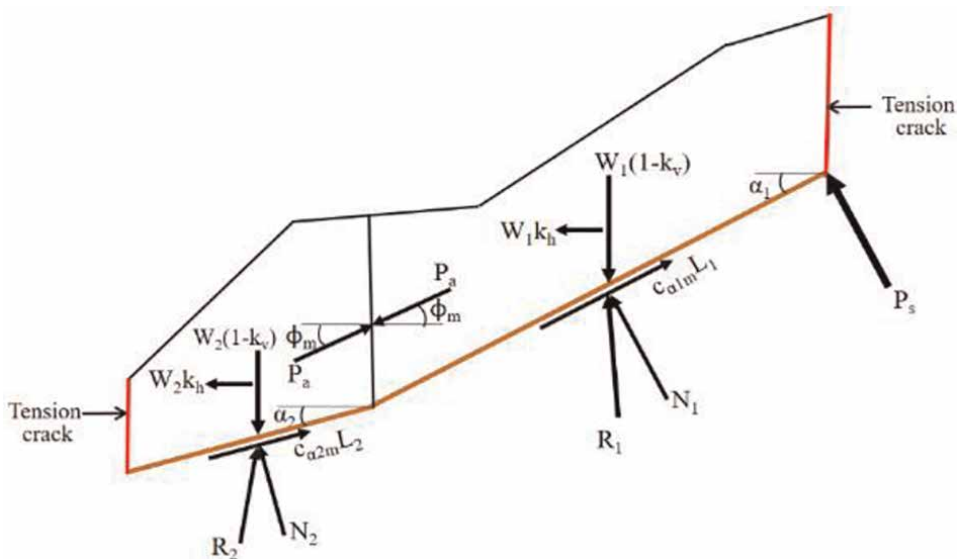
Figure 15.
The proposed slope stability analysis model with dual shear failure planes [12].

surface and is perpendicular to it. The horizontal and vertical ground vibration forces acting on the upper sliding block are $k_h W_1$ and $- k_v W_1$, respectively, and the horizontal and vertical ground vibration forces acting on the lower sliding block are $k_h W_2$ and $-k_v W_2$, respectively.

As for the shear-band tilting force P_s, due to the shear banding effect, it is assumed that tension cracks exist at both ends of the right side of the upper sliding block and the left side of the lower sliding block, and the relatively steep upper sliding surface was caused by the uplifting effect of shear banding from previous tectonic earthquakes. Under these conditions, the shear-band tilting force P_s will be approximately equal to half of the upper sliding block weight $W_1/2$ [12].

Next, since the groundwater table is lower than the sliding surface when the Tsaoling landslide occurs, it will not affect the slope stability analysis results. Therefore, as shown in **Figure 13**, the required parameters or material properties for the slope stability analysis of the Tsaoling landslide area include:

For the upper sliding block, the sliding surface length L_1., inclination angle α_1, weight W_1, normal component of W_1 on the upper sliding surface N_1, adhesion $c_{\alpha 1}$, friction angle δ_1, the resultant force from the friction and adhesion resistances R_1, and shear banding force P_s.

For the lower sliding block, the sliding surface length L_2., inclination angle α_2, weight W_2, normal component of W_2 on the lower sliding surface N_2, adhesion $c_{\alpha 2}$, friction angle δ_2, and the resultant from the friction and adhesion resistances R_2

As for the vertical interface between the upper and lower sliding blocks, under static equilibrium the active earth pressure of the upper sliding block P_{a1} and its angle of intersection with the horizontal plane ϕ_1 need to equal the active earth pressure of the lower sliding block P_{a2} and its angle of intersection with the horizontal plane ϕ_2, respectively; therefore, the factor of safety that satisfies the relationships of $P_{a1} = P_{a2} = P_a$ and $\phi_1 = \phi_2 = \phi$ is the factor of safety FS desired in the analysis.

For the forces acting on the upper and lower sliding blocks shown in **Figure 16** under static equilibrium, the closed force polygons of all forces acting on the upper sliding block and lower sliding block are presented in **Figure 16a** and **b**, respectively.

(a) Upper sliding block

(b) Lower sliding block
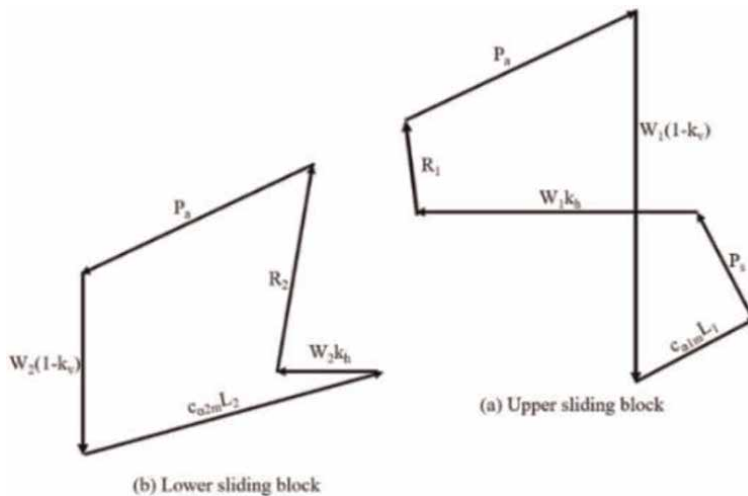
Figure 16.
The closed force polygons for the upper and the lower sliding blocks [12].

For the upper sliding block, the closed force polygon shown in **Figure 16a** can be used as supplemented by the horizontal and vertical force balances (*i.e.*, $\sum F_h = 0$ and $\sum F_v = 0$). The active earth pressure for the upper sliding block P_{a1} is thus given in Eq. 18 as:

$$P_{a1} = A^* / [cos\, \phi_m + sin\, \phi_m\, tan\, (\alpha_1 - \delta_{1m})] \qquad (18)$$

where

$$A^* = [W_1(1 - k_v) - P_s\, cos\, \alpha_1 - c_{\alpha 1m}L_1\, sin\, \alpha_1]\, tan\, (\alpha_1 - \delta_{1m}) + W_1 k_h + P_s\, sin\, \alpha_1 \quad (19)$$
$$- c_{\alpha 1m}L_1\, cos\, \alpha_1$$

Next, for the lower sliding block, the closed force polygon shown in **Figure 16b** can be used as supplemented by the horizontal and vertical force balances of $\sum F_h = 0$ and $\sum F_v = 0$, respectively. The active earth pressure of the lower sliding block P_{a2} is given by Eq. 20 as:

$$P_{a2} = B^* / [cos\, \phi_m + sin\, \phi_m\, tan\, (\alpha_2 - \delta_{2m})] \qquad (20)$$

where

$$B^* = -[W_2(1 - k_v) - c_{\alpha 2m}L_2\, sin\, \alpha_2]\, tan\, (\alpha_2 - \delta_{2m}) - W_2 k_h + c_{\alpha 2m}L_2\, cos\, \alpha_2 \qquad (21)$$

Since the force balance conditions for the upper and lower sliding blocks need to be met at the same time, a trial-and-error method can be used by first assuming a factor of safety FS_a. Subsequently, Eq. 18 can be used to calculate the active earth pressure acting on the upper sliding block P_{a1}, and then Eq. 20 can be used to calculate the active earth pressure acting on the lower sliding block P_{a2}. Finally, after the calculated value of $P_{a1} - P_{a2}$ becomes less than the error tolerance ε, the slope stability factor of safety FS is then set equal to FS_a. Based on this trial-and-error method [12], a calculation procedure was used to obtain the slope stability factor of safety FS.

5.2 Case study

The large-scale Tsaoling landslide induced by the 1999 Jiji earthquake was selected as a case study for the slope stability analysis. The back analyses of the slope stability were conducted under the following two conditions:

Condition 1: Considering the effects of shear banding and the horizontal and vertical ground vibration of the tectonic earthquake [12].

Condition 2: Only considering the effect of the horizontal ground vibration of the tectonic earthquake [14].

From **Figure 13**, points A to K can be roughly divided into five shear-band tilting slope steps: ABC, CDE, EFG, GHI, and IJK [12]. Each step in the shear-band tilting slope has a relatively gentle slope segment, AB, CD, EF, GH, and IJ, and a relatively steep slope segment, BC, DE, FG, HI, and JK. Using the sliding failure mechanism of multi-step shear-band tilting slopes, it was found that after sliding failure of the first step, each of the following steps would have a sliding failure in succession.

For the slope stability analysis of the Tsaoling landslide area, the coordinates, horizontal distance, elevation difference, and inclination angle of each line segment shown in **Figure 13** were first recorded. Then, for the shear failure planes of the five non-shear banding zones AB, CD, EF, GH, and IJ shown in **Figure 13**, the unit weight

Sliding block	PGA (g)	k_h	k_v
1st step	0.5	0.16	0.08
2nd step	0.8	0.24	0.12
3rd step	>0.8	0.24	0.12
4th step	>0.8	0.24	0.12
5th step	>0.8	0.24	0.12

Table 2.
The adopted k_h and k_v corresponding to each PGA for the five step sliding blocks [12].

for the corresponding sliding blocks was 24.52 kN/m³, whereas for the five shear banding zones BC, DE, FG, HI, and JK it was 20.60 kN/m³. From the distribution map of peak acceleration for the landslide area in Tsaoling, the peak ground acceleration (PGA) for the five step shear failure blocks in the Tsaoling landslide area can be obtained from PGA distribution map of the 921 Jiji earthquake reported by Earthquake Prediction Center, Central Weather Bureau, Taiwan [15]. The corresponding relationship between the PGA and seismic acceleration coefficients was provided by the Ministry of Economic Affairs [16]. The adopted horizontal seismic acceleration coefficient k_h and vertical seismic acceleration coefficient k_v corresponding to each PGA are given in **Table 2**.

In the slope stability analysis for the five stepped shear-band tilting slopes, the shear banding forces P_s, the horizontal ground vibration forces of the upper sliding block, the vertical ground vibration forces of the upper sliding block, the horizontal ground vibration forces of the lower sliding block, and the vertical ground vibration forces of the lower sliding block are given in **Table 3**.

The shear resistance strength parameters obtained through back-calculation under Condition 1 are given in **Table 4**.

The shear resistance strength parameters obtained through back-calculation under Condition 2 are given in **Table 5**.

The obtained safety factors using the shear resistance strength parameters of the sliding surface obtained from the back analysis under different conditions for the shear-band slope stability analysis are given in **Table 6**.

Shear banding tilting slopes	Shear banding forces	Ground vibration forces			
		Upper sliding block		Lower sliding block	
	P_s (kN)	$W_1 k_h$ (kN)	$-W_1 k_v$ (kN)	$W_2 k_h$ (kN)	$-W_2 k_v$ (kN)
1st Step: ABC	44,485	14,235	−7118	11,204	−5601
2nd Step: CDE	51,652	24,793	−12,396	67,785	−33,892
3rd Step: EFG	30,151	14,472	−7236	37,706	−18,853
4th Step: GHI	69,198	33,215	−16,608	51,546	−25,773
5th Step: IJK	33,116	15,896	−7948	29,656	−14,828

Table 3.
The shear banding forces and ground vibration forces used in the case study for the shear-band tilting slopes [12].

	Upper sliding plane		Lower sliding plane 2	
	Adhesion $c_{\alpha 1}$ (kPa)	Friction angle δ_1 (degree)	Adhesion $c_{\alpha 2}$ (kPa)	Friction angle δ_2 (degree)
1st Step: ABC	0	30.0	38.89	31.0
2nd Step: CDE	0	30.0	42.69	31.5
3rd Step: EFG	0	30.0	40.63	31.3
4th Step: GHI	0	32.0	123.36	36.0
5th Step: IJK	0	31.8	90.39	35.0

Table 4.
Shear resistance strength parameters obtained through back analyses under condition 1 [12].

	Upper sliding plane		Lower sliding plane 2	
	Adhesion $c_{\alpha 1}$ (kPa)	Friction angle δ_1 (degree)	Adhesion $c_{\alpha 2}$ (kPa)	Friction angle δ_2 (degree)
1st Step: ABC	0	20.0	0	20.0
2nd Step: CDE	0	20.0	0	20.0
3rd Step: EFG	0	20.0	0	20.0
4th Step: GHI	0	20.0	0	20.0
5th Step: IJK	0	20.0	0	20.0

Table 5.
Shear resistance strength parameters obtained through back analyses under condition 2 [14].

Shear banding tilting slope	*FS*	
	The condition 1	The condition 2
1st Step: ABC	1.000 (100%)	0.120 (12.0%)
2nd Step: CDE	1.000 (100%)	0.134 (13.4%)
3rd Step: EFG	1.000 (100%)	0.136 (13.6%)
4th Step: GHI	1.000 (100%)	0.130 (13.0%)
5th Step: IJK	1.000 (100%)	0.131 (13.1%)

Table 6.
Shear-band slope stability analyses as obtained from the back-calculation results under conditions 1 and 2 [12].

For multi-step slope failure induced by the effects of shear banding and ground vibration of a tectonic earthquake, when the shear banding effect is ignored and only the horizontal ground vibration effect is considered, low shear strength parameters of the sliding plane are obtained by back analysis. When the shear-band slope stability analysis is carried out using the shear strength parameters obtained from the back analysis, only the back analysis results that consider the effects of the shear banding and the horizontal and vertical ground vibrations can obtain a factor of safety that meets the actual requirements.

For the Tsaoling landslide that occurred during the 921 Jiji earthquake, when the back analysis considered the effects of the shear banding and the horizontal and vertical ground vibration effects, **Table 6** shows that the shear strength parameters obtained from the back analysis of the five-step shear-band slopes resulted in the calculated safety factors being consistent with the actual safety factor of 1.0; however, when the back analysis only considered the horizontal ground vibration effect, **Table 6** shows that the shear strength parameters obtained from the back analysis of the five-step shear-band slopes resulted in the calculated safety factors being much lower than the actual safety factor of 1.0 [12].

6. Conclusions

1. The finite element simulation results of the plate under lateral compression show that only in the elastic–plastic strain softening model can the shear band be induced.

2. For the general shear failure plane proposed by Terzaghi, since the strain-softening model is replaced by the perfectly plastic model, the foundation soil will remain perfectly plastic when it should be strain softened, and then it will still maintain symmetry when it should be lost. Thus, the problem of overestimating the ultimate bearing capacity of foundations arises.

3. Both the strain softening effect and the tilting effect make the maximum lateral earth pressure of the retaining wall increase from the traditional Coulomb active earth pressure. The case study results show that the maximum lateral earth pressure of the retaining wall induced by strain softening can increase up to 49.2%, and the maximum lateral earth pressure of the retaining wall induced by the tilting effect can increase up to 99.4%. When the strain softening effect and the tilting effect are superimposed, the increase in the maximum lateral earth pressure of the retaining wall can be as high as 148.6%.

4. For tectonic earthquakes induced large-scale landslides, the case study results show that either through back- or forward-calculation, only when the shear banding effect (i.e., the primary effect) and the horizontal and vertical ground vibration effects (i.e., secondary effects) of tectonic earthquakes are considered, can the slope stability analysis results conform to the actual situation on site.

Author details

Tse-Shan Hsu
Institute of Mitigation for Earthquake Shear Banding Disasters, Feng-Chia University, Taichung, Taiwan

*Address all correspondence to: tshsu@fcu.edu.tw

IntechOpen

References

[1] Drucker DC. A definition of a stable inelastic material. Journal of Applied Mechanics. 1959;**26**:101-195. DOI: 10.1115/1.4011929

[2] Drucker DC. Some implications of work hardening and ideal plasticity. Quarterly of Applied Mathematics. 1950; **7**(4):411-418

[3] Hsu TS, Lin DJ, Chuang TF, Huang YM. Influence of shear-banding effects on the ultimate bearing capacity. International Journal of Organizational Innovation. 2022;**14**(3):205-233

[4] Hsu TS, Chen YJ, Wu ZL, Hsieh YL, Yang JC, Huang YM. Influence of strain softening and shear-band tilting effect on the maximum earth pressure of retaining walls. International Journal of Organizational Innovation. 2021;**14**(1):45-86

[5] Hsu TS, Wu ZL, Lin CT, Huang YM. The major cause of anchor block slope failures. International Journal of Organizational Innovation. 2018;**11**(2):175-198

[6] Hsu TS. Capturing Localizations in Geotechnical Failures [Thesis]. USA: Civil Engineering in the School of Advanced Studies of Illinois of Technology; 1987

[7] Prevost JH. Soil Stress-Strain-Strength Models Based on Plasticity Theory. University Microfilms International; 1977. Available from: https://books.google.com. tw/books/about/Soil_Stress_strain_streng th_Models_Based.html?id=LUIUnQEA CAAJ&redir_esc=y

[8] Terzaghi K. Theoretical Soil Mechanics. New York: John Wiley & Sons Inc.; 1943. pp. 257-262. DOI: 10.4236/jmp.2012.32022

[9] Coulomb CA. Essai sur une application des regles des maximis et minimis a quelques problemes de statique relatifs a l'Architecture. In: Memoires de Mathematique et de Physique. Vol. 7. Paris: Presentes a l'Academie Royale des Sciences, par divers Savans, et lus dans ses Assemblees; 1776. pp. 343-382

[10] Hsu TS, Chen YJ, Wu ZL, Hsieh YL, Yang JC, Huang YM. Influence of strain softening and shear-band tilting effects on the active earth pressure on retaining walls. International Journal of Organizational Innovation. 2021;**14**(1):45-86

[11] Google Earth. 2020. Available from: https://www.google.com.tw/intl/zh-TW/earth/download/gep/agree.html

[12] Hsu TS, Wang LY, Tsao CC, Chang HC, Chuang TF. A new slope stability method considering the tectonic earthquake effects. International Journal of Organizational Innovation. 2021; **13**(3):220-247

[13] Hung JJ. A study on Tsaoling rockslides, Taiwan. Journal of Engineering Environment. 1980;**1**:29-39

[14] Hung JJ, Lee CT, Lin ML, Lin ML, Jeng FS, Chen CH. A flying mountain and dam-up lake: Tsaoling rockslides. Sino-Geotechenics. 2000;**77**:5-18

[15] Earthquake Prediction Center, Central Weather Bureau, Taiwan: PGA distribution map of free-field strong earthquake stations of the 921 earthquake. 1999. Available from: https://scweb.cwb.g ov.tw/zh-tw/page/iframe?txtUrl=/special/ 19990921/921pga-map.htm

[16] Ministry of Economic Affairs, ROC. Derivation of Seismic Coefficient. Technical Directions for Hydraulic Structures Inspection and Safety Evaluation, Reservoir and Water-Conveying Structures. 2008. Available from: https://law.moea.gov.tw/ LawContent.aspx?id=FL045951

Section 4

Buildings Structures

Morphology of the Vernacular Masonry Structure in Adana City and Its Qualitative Analysis According to the Rule of Art

Kerimcan Apak

Abstract

Adana city has a significant risk for seismicity in the past, today, and in the future. Therefore, traditional unreinforced masonry houses in Adana city and their structural qualifications are essential to provide information on these buildings, which will be of value to researchers and practitioners, policymakers, and disaster managers. Therefore, one of the traditional houses was examined by identifying the construction details, damage, and collapse analysis in the Tepebağ settlement. At the end of the study, the construction details and their description could be added to the literature. In addition, the rule of art was used for interpreting the crack, damage, and predicted structure collapse scenario. Working on the rule of art was not enough separately to identify the collapsed analysis of the building. Besides, engineering applications and calculations are the other critical scientific aspects for determining the collapsed scenario. However, the rule of art is efficient for architects to predict the damage and collapsed analyses of the old structures.

1. Introduction

This paper's subject is the determination of the morphology of the Adana Tepebağ traditional house structures with their crack, degradation, and predicted collapsed analysis using the rule of art. The traditional houses in Tepebağ are a part of the significant architectural heritage in Turkey. Understanding the primary structural system and its qualifications is essential for sufficient restoration work to conserve those structures. There is always a gap in data for traditional houses' structure and construction details in restoration work. Moreover, the architects need a practical method for predicting damage and collapse analyses of those structures.

Many researchers work on Tepebağ houses, but a few work on the details of the structures and construction. In addition, the prediction of the collapse scenario of those structures is a gap for research. Therefore, this paper is an improved study of the construction, degradation, damage, and prediction of collapse analysis of the traditional load-bearing structures in the Tepebağ settlement.

The rule of art is used to answer the questions and gaps in research areas. After the analysis, the data show that the construction type and condition of the Traditional houses in Adana-Tepebağ are critical against the seismicity. In addition, their construction details are not very effective for seismic loads. There are some precautions for providing extra strength for horizontal loads. But they are not very sufficient. This paper provides valuable data and analyses for future restoration works and research.

2. Seismicity in the Adana region

Adana is located in the southeastern part of Anatolia, close to the border of the Mediterranean Sea, which was one of the historical cities of Turkey. So many civilizations were placed in this city. In a chronologic order, Adana was a settlement of the Hittite Kingdom (B.C. 1900–1200), Assyria Kingdom (B.C. 713–663), Persian Satrapy (B.C. 612–333), Seleukos Empire (B.C. 312–133), and Roman Empire (B.C. 112–A.C. 395), before being a part of Ramazonoğlu seigniority (sixteenth century) and following Turkish civilizations.

Tepebağ was the oldest historical settlement in Adana. According to the bibliographic sources, this area is the first placement of the Hittite Kingdom. The new neighborhoods such as Kayalıbağ, Ulucami, Sarıyakup, and similar regions were developed when the city was expanded from the Tepebağ through the south. The traditional houses in Adana were built in the seventeenth century in those settlements. With the city's trade progression, people's wealth increased; therefore, the typology of the traditional houses changed and got bigger. Those big houses were designed as two or three-story, called "konak" [1]. Mostly those houses belonging to the tradespeople were more prominent than the city's other houses.

The traditional houses of Adana are authentic and essential heritage in this region. However, from the past to the present, they were at risk of damage from environmental aspects. One of those aspects was seismicity. Therefore, identifying the seismic risk of this region, the tectonic faults, and their location with the historical seismicity of the area was examined. As seen in the below figure, the land had a complex tectonic regime. The location of the Adana was between the Göksu and Ecemiş faults. Besides those faults, the Eastern Anatolian fault and its extension faults are passing on this land. The African, Anatolian, and Arabian plates intersect in this area. The Eastern Anatolian fault is the most effective and causes many seismic events (**Figure 1**).

Historical seismic activities in Adana city and its surroundings are shown below in **Figures 2** and **3**. In **Figure 2**, the marked locations on the map were signed according to the estimated and calculated historical seismic location and time. It brought an idea about the historical seismicity of this area. In **Figure 3**, all the marked areas were the locations of seismic activity after 1951.

One of the most significant historical seismic activities in this area happened in 1114 near Ceyhan Adana, with a magnitude of 7. In the recent past, the most important seismic activities happened in Adana city in 1945, 1952, and 1998 with a magnitude of 6.1, 5.2, and 6.3, respectively [3].

The magnitude of the Adana earthquake in 1998 was 6.3, which caused various damages to more than 4000 buildings [4]. Although the historical structures essentially in the Tepebağ region and its surroundings were affected by this earthquake, most of them collapsed. Today, few numbers of registered buildings remained in this region. Most of those structures were in bad condition [5].
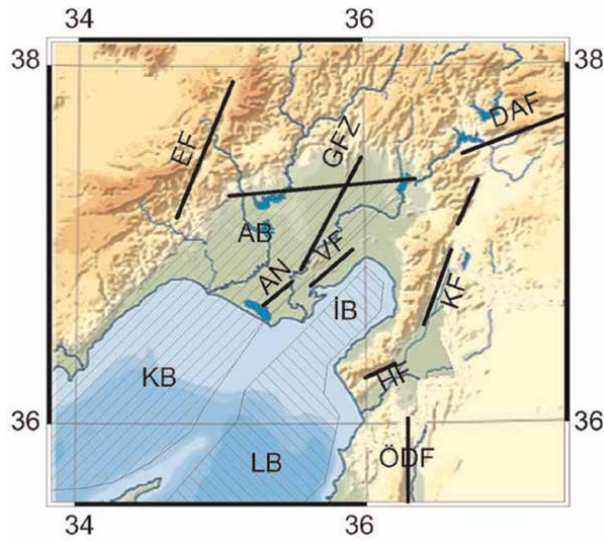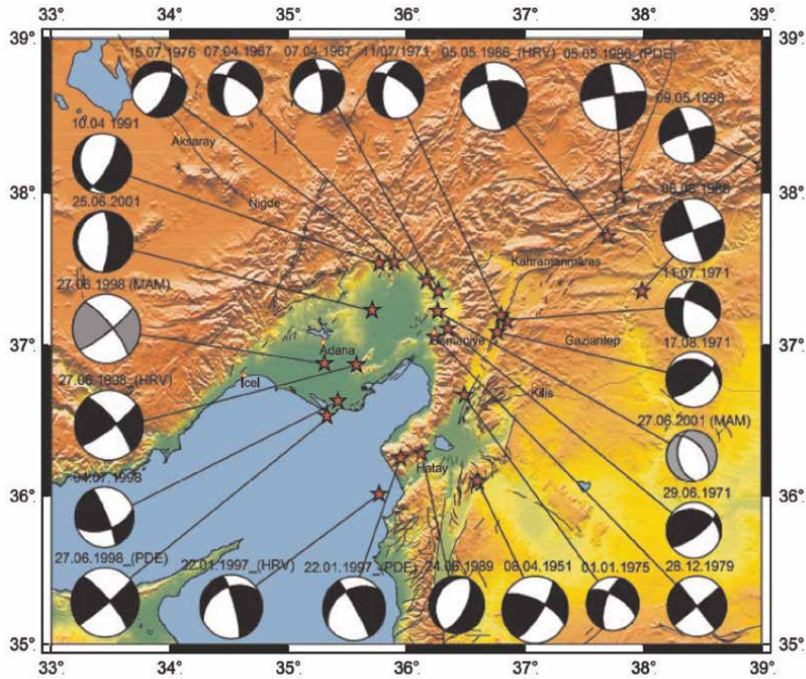
Figure 1.
Faults on the Klikya area; AB: Adana Basin, AN: Andırın, DAF: Eastern Anatolian fault, E.F.: Ecemiş fault, GFZ: Göksu fault, G.S.: Girne ridge fault, H.F.: Hatay fault, İB: İskenderun basin, K.B.: Klikya basin, K.F.: Karasu fault, L.B.: Latakia basin, MS: Misis ridge, ÖDF: Ölü Deniz fault, Y.F.: Yumurtalık fault [2].
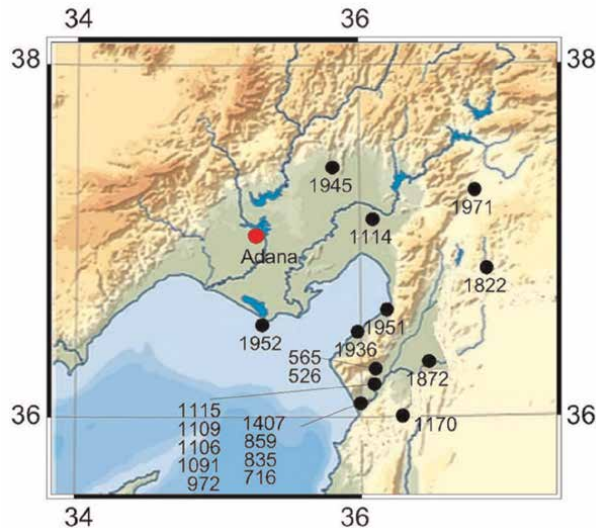
Figure 2.
The historical seismic activity of the Klikya region with marked location and time [2].

In site analysis, it was observed that the structural systems of the historical houses in Adana-Tepebağ region were damaged. Those damages could be occurred from the seismic activities or other environmental effects.

The morphology of Vernacular masonry wall structures in the Adana-Tepebağ traditional houses clarifies the key concepts of masonry construction techniques against seismicity.

Figure 3.
"Beach balls" represent the focal mechanism in the region, mainly strike-slip and normal faulting [2].

3. Morphology of Vernacular masonry structures in Adana-Tepebağ traditional houses

In general, the traditional houses in Adana-Tepebağ were built in the nineteenth century up to two to three floors. The load bearing and timber frame system were used on the structures of those houses. Oriels and eaves were the architectural units of those houses.

In this chapter, the construction materials and construction techniques that were used in Adana-Tepebağ traditional house structures were examined.

3.1 Building materials

In the Adana-Tepebağ region, dry soil, stone, and timber were the primary construction materials in traditional buildings. The building materials were an essential step for getting the historical texture. Mainly timber was used in a vast area.

Stone, brick, and adobe were widely used as masonry wall materials and infill materials in historical structures in Adana.

The construction materials and their application areas were varied in historical buildings. The dry soil is used in flat roof structures to provide extra heat to the interior spaces. Stone material was used in basement wall structures identically used in Turkish house construction. And the timber was used on the upper floors as a frame system with infill of brick, stone, and adobe blocks for keeping the temperature in the interior space and providing a light structure for the upper floors against the seismic action. Besides this specification, the timber frame wall with infill materials provides airflow and prevents humidity inside the wall [4, 6].

3.2 Building techniques

Three primary structural systems were used in traditional houses in the Adana region. The load-bearing system with stone or brick was widely used in these buildings (**Figure 4**). The second technique was timber frame with stone, brick, and adobe infill. Generally, brick was used for the infill material around the Tepebeğ region. The corners of the building were strengthened with timber bracing for the seismic actions. Besides, timber beams were passed inside the stone masonry walls to provide horizontal strength for the masonry structure. In last, "Bağdadi" was a construction system with a timber frame covered with timber lath and finished with plaster.

The traditional houses in Tepebağ were raised from the underground water with stone masonry, and after, brick masonry was knitted on a stone base. The brick masonry structures were supported with 80–90 cm timber beams on the outer walls. The timber lintels were placed on upper and lower parts of the window and the door openings. The masonry wall thickness of the ground floor was 60–65 cm (**Figure 5**).

The space between timber studs was 120, 200–250 cm, which was used to build timber frame walls with infill materials to support timber beams on the first and above floors of traditional Tepebağ house structures. The timber bracings were used on the corners of the timber walls to prevent collapse under seismic effects.

The timber beams inside the brick masonry walls were placed with a checker pattern. The general use of the timber beams was 8–10 cm. The dimension of the timber studs was 20–25 cm. The corner studs of the walls are thicker than others.
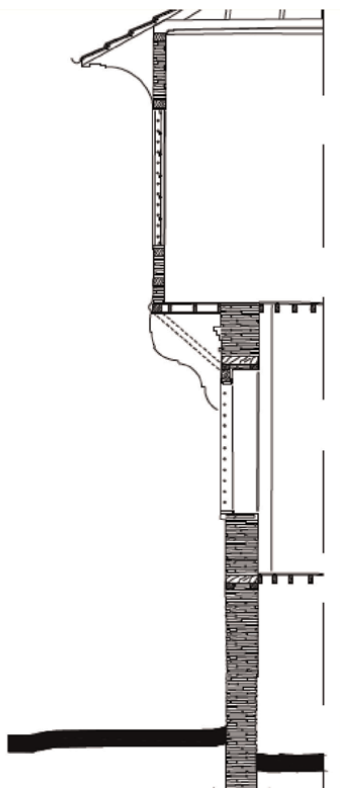
Figure 4.
The elevation of the traditional Adana-Tepebağ house [7].

Figure 5.
The cross section of the traditional Adana-Tepebağ house [6].

The roofs were designed as flat or hipped roofs with the use of dry soil or timber [4, 6]. The oriels were supported with 15–15 cm timber bracings, which were repeated with 80–100 cm space horizontal. The balconies were designed in half cantilevers with 100–150 cm lengths.

4. The rule of art

The rule of the art was to define brick masonry walls and timber frame structural deficiencies with their mechanical behavior. The following steps were identified according to the rule of art.

• Interpretation of quality through the walls of the crack.

• The behavior of the masonry wall according to the horizontal and vertical actions.

4.1 Interpretation of quality through the crack walls

The picture of the lesions is highly indicative of detecting the quality of the walls. Irregular cracks or degradation on the wall layer, which are spread everywhere, indicate that the wall is not properly connected with its unit element brick or could be a sign of separation of masonry layers. Therefore, masonry walls could be at risk of getting damaged or collapsed.

The masonry wall has a monolithic behavior, and the wall is composed of two or more layers. The layers of the masonry walls were attached to retain their shape and

form under horizontal and vertical forces. But lesions on the layers could decrease the connection and overall functioning of the masonry wall.

The purpose of the survey of the masonry is to define the degradation and failures of the materials and structure. By these definitions, the damage mechanism of the masonry structure is identified. In the analysis of typical vulnerabilities of the structure, defining degradation and disruption of the structure is to be determined.

The figures in **Tables 1–3** are the proposal symbolism for the representation of the crack and degradation of the masonry wall structures (**Tables 1–3**), [8–11].

4.2 Behavior of the masonry wall according to the actions

The behavior of the masonry wall structures is under the effect of three actions.

- Vertical actions

- Horizontal loads in-plane action

- Horizontal loads out-of-plane action
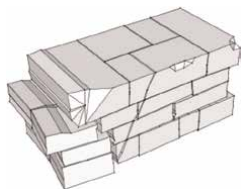
	Deterioration of brick elements with identification of breakup, detachment, erosion, exfoliation, fracturing, and spalling.
	Loss of binder between the joints.
	Inflection of timber elements.
	Decompose the head of the timber elements.
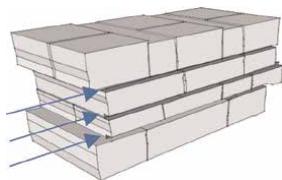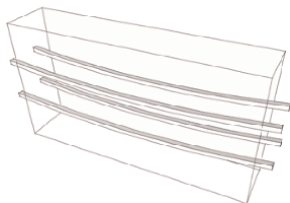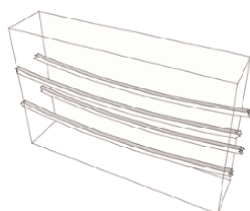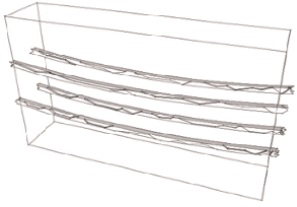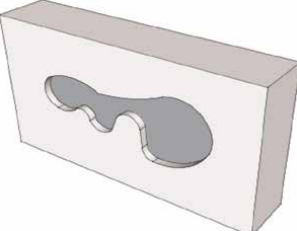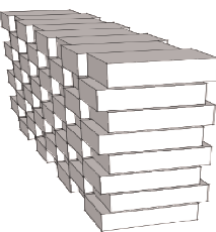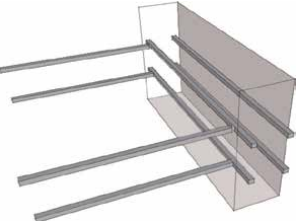
Table 1.
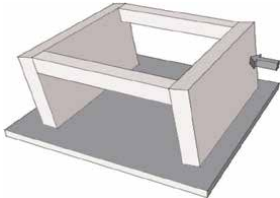*Crack and degradation of the masonry; A [8–11].*
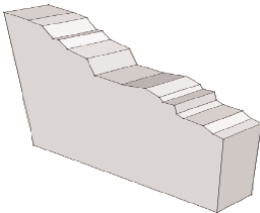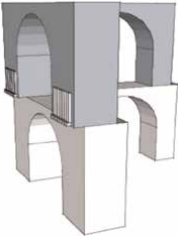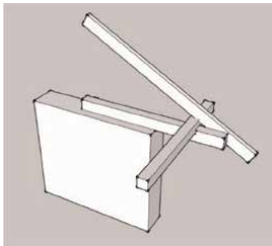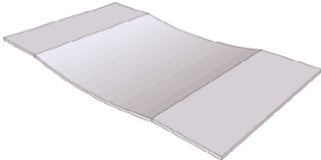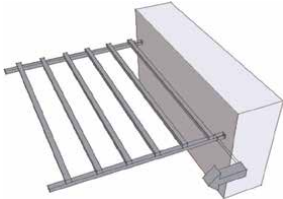
	General deterioration of wooden elements such as decay and biological attacks.
	Major cracks on the surface of the masonry wall.
	Major cracks are diffused and formed branched cracks.
	Fracture concentrating, loss of adhesion between mortar and bricks, localized with or without expulsion parts, plaster corrugations.
	Delamination spread of masonry (loss of adhesion between mortar and supports), crazing, and widespread lesions close together cannot be described graphically, and disconnection of scaffolding terracotta.
	Extraction (from the place of a wooden element in the wall), slipping, or sliding closed joint (between parts of stone or masonry blocks) in millimetric displacement.

Table 2.
Crack and degradation of the masonry; B [8–11].

	Collapse parts and drop items.
	Relief of the deviation from verticality (outside/inside lead) or the horizontality (bulging), with dimensions in mm, the deviation of the points noted by the vertical or horizontal line of reference.
	The main beams are not resting on the supports. Or the walls are inefficient to support.
	Deflection of the slab.
	Disconnection of the floor from the wall.
	Loss of a square, out of shape of the opening, or deformation.

Table 3.
Crack and degradation of the masonry; C [8–11].

4.2.1 Vertical actions

The masonry wall structures are under risk of vertical action, which means vertical loads are subjected to the state of compression. The wall under the state of compression determines different situations depending on the stress, such as gravity loads besides and various magnitudes of seismic actions escalated the amount of vertical loads on the structure.

The masonry walls are composed of a varied number of vertical leaves and quality of materials, which determined its behavior under compression. In the following table, the effect of vertical loads on masonry as a result of cracks, possible sector of rotation, and single wall failure mechanism is symbolized (**Table 4**), [8–11].

	The compressive force pushed away two masonry leaves from each other. The masonry wall gets into the formation of symmetric bulging.
	Outer vertical deflection. Inside the leaf of the masonry wall under pressure. Therefore, the outside of the leaf is pushed away from the wall.
	Vertical cracks on the masonry wall tend to collapse the structure.
	A typical mode of failure of the masonry wall is due to the applied forces that trigger the thickness of the masonry with orthogonal seismic action. Thinner bricks have lower diffusion; therefore, there is higher stress, and cracks could be in this area.

Table 4.
Vertical actions [8–11].

4.2.2 Horizontal loads in-plane actions

In-plane action, the mechanism of the masonry wall can be triggered by various seismic intensities. The wall's quality and ductility level allow for avoiding collapse even for earthquakes of high intensity.
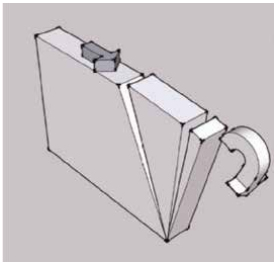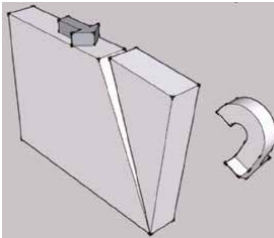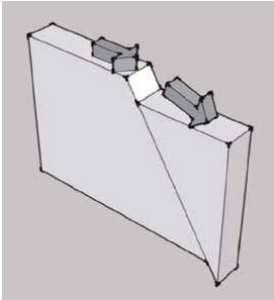
The quality of the connections between masonry walls, the type of masonry, and the characteristics of the laying materials determine the behavior of the masonry under the effect of in-plane action.

In the following table, the effect of in-plane action on masonry occurs cracks, possible sector of rotation, sliding, and single wall failure mechanisms, which are symbolized (**Table 5**), [8–11].

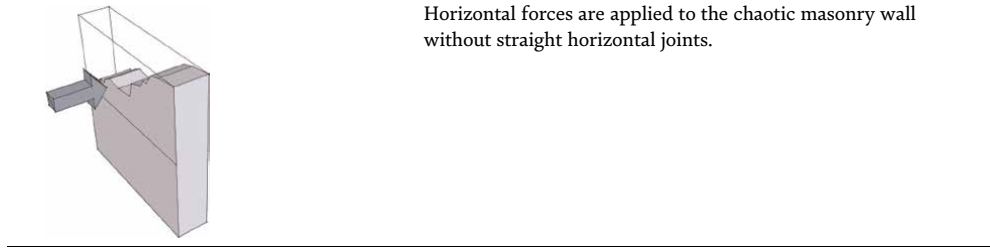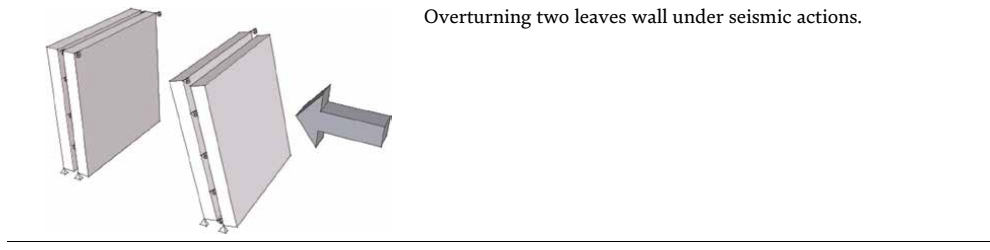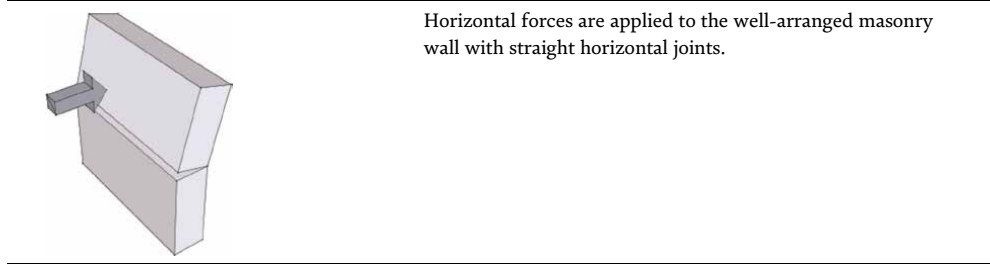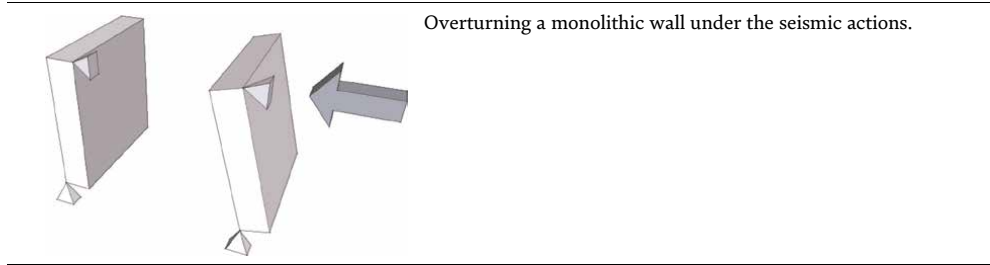### 4.2.3 Horizontal loads in out-of-plane actions

In out-of-plane action, the masonry wall is under the effects of perpendicular loads, categorized as seismic and wind loads. The presence of connections between two leaves of a masonry wall is crucial for its behavior for out-of-plane actions. The
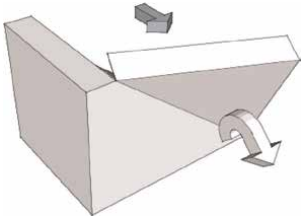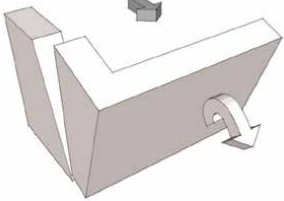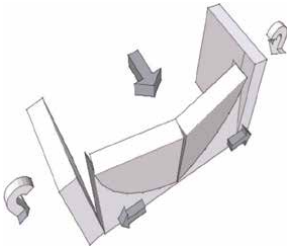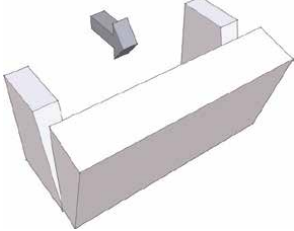
	In a sector of rotations, the horizontal kinematic mechanism occurs in higher values of the seismic effects on the structure.
	In a sector of rotations, it emphasizes the main effect of the kinematic mechanism, which essentially consists of a rigid rotation of the broken part.
	It is a critical line in a sector of rotations; seismic actions divert static compression and can be transferred to the foundation.

Table 5.
Horizontal loads in-plane actions [8–11].

	Overturning a monolithic wall under the seismic actions.
	Horizontal forces are applied to the well-arranged masonry wall with straight horizontal joints.
	Overturning two leaves wall under seismic actions.
	Horizontal forces are applied to the chaotic masonry wall without straight horizontal joints.
	Overturning a monolithic wall.
	Reversal of the outer leaves.

	Mechanism of diagonal damage.
	The mechanism of damage and crack starts from the corner of the wall.
	The mechanism of damage on a masonry cell wall structure under horizontal forces.
	The tilt mechanism is composed of double corner cracks.

Table 6.
Horizontal loads in out-of-plane actions [8–11].

type and tied connections between masonry leaves are determined by the failure mechanism of the wall structure.

In the following table, the effect of out-of-plane action on masonry occurs in cracks, possible sectors of rotation, and single wall failure mechanisms are symbolized (**Table 6**), [8–11].

5. Case study

The rule of art applies to the case study to identify the building's damage analyses and possible collapse scenarios. The case study is selected from the Adana-Tepebağ region, which is under risk of seismicity.

5.1 Traditional Tepebağ house with inventory number 63

The house is located in Adana-Tepebağ, with inventory number 63. It is assumed that it was constructed in the nineteenth century. The house is built on two floors with load-bearing structural system. Brick material was primarily used in masonry walls. Timber material was used in different parts of the structure; in floor-roof slabs and beams inside the brick masonry walls. Besides, the oriel was constructed with timber materials. And dry soil with timber beams was used for building the flat roof (**Table 7**), [12].

According to the rule of art, crack and degradation analysis and possible collapse scenario were determined for the traditional Tepebağ house with inventory number 63. In the following pictures (**Figures 6–9**), cracks and damaged areas of the house are identified with arrows, lines, and instructions.

On the north side of the building facade, there was a significant loss of brick materials because of the low bonding strength of the bricks and the detachment of the masonry leaves. The second clue of the detachment of the masonry leaves was one crack on the upper corner of the roof, which was under the stress of vertical loads (**Table 8**).

Table 7.
Traditional Tepebağ houses with inventory number 63 [12].

Figure 6.
Traditional Tepebağ house with inventory number 63, north-east view.

Figure 7.
Traditional Tepebağ house with inventory number 63, east view.

The timber beams and lintel were at risk of deterioration and were not continuing through the entire wall length. The load-bearing walls are insufficient to support the dead load of the flat dry soil roof. Therefore, there was a detachment and outpour
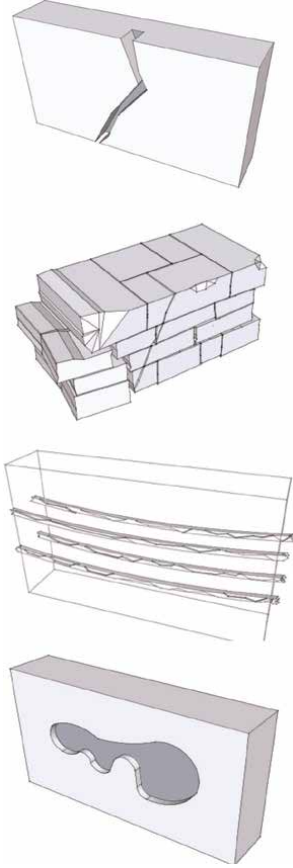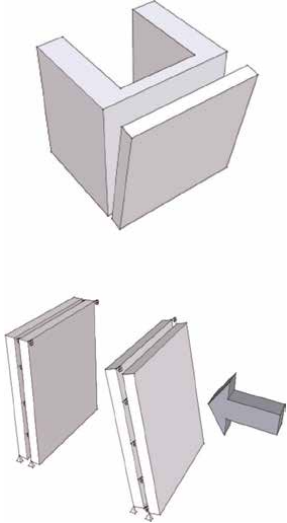
Figure 8.
Traditional Tepebağ house with inventory number 63, south-west view.
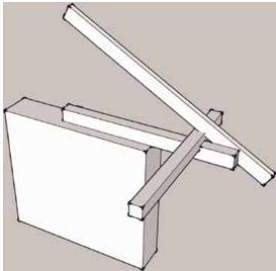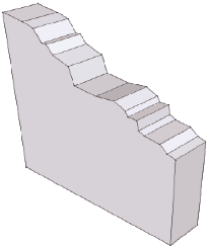

Figure 9.
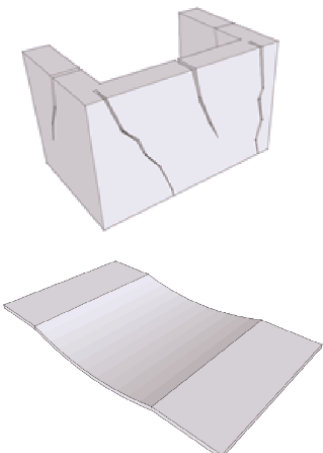*Traditional Tepebağ house with inventory number 63, west view.*

within the joint parts of the masonry and the roof beams. The stone arch was supported with thick masonry brick walls. However, one side of the arch wall was standing on the opening of the brick masonry, which caused cracks and deflection (**Table 9**).

Crack and degradation of the masonry	Descriptions	The assumed failure mechanism of the wall structure
	Deep cracks on the upper width part of the brick masonry wall. Besides detachment and outpour of bricks on the outer leaf of the masonry. In addition, the deterioration of wooden elements such as decay and biological attacks. It indicated that part of the outer leaf could be detached from the masonry wall structure. It will cause a reversal of the outer leaves failure mechanism onto the structure.	

Table 8.
The rule of art, crack, and degradation analysis and possible collapse scenario for the traditional Tepebağ house with inventory number 63, A.

Crack and degradation of the masonry	Descriptions	The assumed failure mechanism of the wall structure
	The main timber beams supporting the roof are not resting on the supports, or it is inefficient. Therefore, the collapse of parts and dropped items of the masonry occurred.	

Crack and degradation of the masonry	Descriptions	The assumed failure mechanism of the wall structure
	Deflection of the masonry wall and deep vertical crack on the surface of it.	The masonry wall was under the effect of vertical load, and if any precautions were not taken, it tended to collapse.

Table 9.
The rule of art, crack, and degradation analysis and possible collapse scenario for the traditional Tepebağ house with inventory number 63, B.

6. Conclusion

With the use of methodological progress and analysis, with bibliographic research, it will be understood that traditional houses in the Adana Tepebağ settlement are at risk of deflection and collapse against seismic activities because of their uncared and damaged structures. Moreover, it was understood that the rule of art was an efficient tool for predicting the collapse scenario of those structures. For improving the bibliographic research, the construction materials and the exact historical construction techniques were identified for future conservation works and research studies. For future research, the possible conservation ideas and applications of those buildings could be studied to provide a bibliographic source for restoration works.

Author details

Kerimcan Apak
Adana Alparslan Türkeş Science and Technology University, Adana, Turkey

*Address all correspondence to: kerimcanapak@atu.edu.tr

IntechOpen

References

[1] Saban D. Adana'nın Kentsel Gelişimi-Urban Development of Adana. In: Karaman F, Saban D, Erman O, Baş Yanarateş D, Ramazanoğlu G, editors. Adana Kentsel Kültür Envanteri. Adana Valiliği İl Özel İdaresi; 2012. pp. 17-25/85-86. ISBN: 975-487-130-2

[2] Ökeler A. Recent Seismicity and Stress Analysis of the Cilician Region. İstanbul: İstanbul Technical University; 2003

[3] Mehmet İ, Hayri BÖ, Hüseyin B. Earthquake damages in turkey and the evaluation of building stock. In: Proceedings of the Sixth National Conference Earthquake Engineering; İstanbul. 16-20 October 2007. p. 250

[4] Saygün D. The Construction Techniques of the Traditional Buildings in the Historical City Adana. Adana: Çukurova University; 2003

[5] Umar N. Adana Tepebağ-Kayalıbağ Urban and Archaelogical Site Conservation Project. İstanbul: İstanbul Technical University; 2010

[6] Apak K. Historical timber structures in Adana-Tepebağ settlement and consolidation approach with modern timber prefabricated systems. In: Proceedings of 12th International Conference on Structural Analysis of Historical Constructions; 29-30 September 2021; Online

[7] Adana Municipality. Ascertainment report for seismicity guidelines of number; 152 inventory historical building report; 2012

[8] Apak K. Construction Techniques of Ottoman Bath's from the 13th to 16th century in seismic areas. Milano: Politecnico di Milano; 2015

[9] Baila A, Binda L, Borri A, Cangi G, Cardani G, Castori G, et al. Manuale Delle Murature Storiche. In: Analisi E Valutazione Del Comportamento Strutturale. Vol. 1. Roma: Tipografia Del Genio Civile; 2011. p. 471

[10] Baila A, Binda L, Borri A, Cangi G, Cardani G, Castori G, et al. Manuale Delle Murature Storiche. In: Analisi E Valutazione Del Comportamento Strutturale. Vol. 2. Roma: Tipografia Del Genio Civile; 2011. p. 348

[11] Doglioni F. Codice di Practica (Linee Guida). Venezia: Istituto Universitario di Architettura di Venezia D. S. A; 2011

[12] Adana Municipality. Ascertainment report for seismicity guidelines of number; 63 inventory historical building report. 2012

Chapter 8

Some Risky Practices in Earthquake Engineering That Need More Research and Evaluation

Jamal Alomari

Abstract

Every building is designed according to its own structural system. Needs of making modifications to the structural systems of buildings may arise after the buildings are constructed. Any change in the structural components of the building by addition or omission will necessarily produce a change in its dynamic properties such as its stiffness, mass, and damping matrices, and modes of vibration. During earthquake actions, the new structural system will have different seismic responses than the original system. The new seismic responses such as shear, torsion, moment, and displacement may be reduced, or increased. Safety provisions require that before any changes in the structural system are carried out, a thorough seismic structural analysis of the new system be carried out. Linking two adjacent buildings with rigid or semi-rigid sky bridges is one example of such changes. Theoretical investigation of linking two buildings together by damping devices to mitigate seismic risks is finding its way into the literature. There have been numerous studies addressing the effects of connecting two buildings by rigid sky bridges on the seismic response of the new structural complex which comprises the two buildings and the linking beams and slabs. Dramatic changes in the seismic response of buildings are noted in most cases studied.

Keywords: structural system, seismic, dynamic properties, response, mode of vibration, damping device

1. Introduction

The structural design of buildings is meant to resist the anticipated loads likely to act on a structure. The structural designer chooses the structural system to resist gravity and lateral loads. There is a variety of simple and complex structural systems used to resist combinations of vertical gravity loads and earthquake actions. The techniques available nowadays to alleviate seismic actions are numerous. The requirements of continuous load paths in the vertical and horizontal directions, stiffness and strength, and ductility are well-known requirements for the proper seismic design of structures [1].

Structural systems employing shear walls, bracing and moment-resisting frames, and combinations of them are now widely used by designers. Analysis and design

of structures are guided by design codes and cover the most encountered needs and requirements of typical buildings. However, sometimes, building owners wish to make changes to their properties after the completed buildings are finished and occupied due to some unforeseen needs arising later on. Structural engineers are then consulted to execute the desired changes in the building. Some of the desired changes could produce changes to the overall structural behavior of the building. The designers are required to investigate thoroughly the new configuration of the building based on criteria and requirements of design codes originally used during the initial analysis and design stages. However, in many cases, such investigation is not performed, and a decision is finally taken to execute the desired changes without examining the structural safety of the new configuration of the buildings. The changes take many forms according to the needs arising. In one example, a new multi-story building is built beside an old and similar one and the owner decided to connect the two buildings by a corridor bridge for easy and fast circulation. In another example, a multi-story building is connected to a nearby high retaining wall in order to brace the retaining wall and provide it with ample lateral support against rotation and sliding. Other examples of adding or removing walls, partitions, beams, or even, columns, in order to suit the spaces of buildings to some new business needs are also encountered in practice. Partial or complete fatal collapses of buildings were reported due to arbitrary, non-engineered changes.

Many previous studies investigated the effects of connecting buildings together by sky bridges, sky pools, and sky gardens built of reinforced concrete or steel [2–10].

On the other hand, numerous theoretical studies on twin buildings linked by damping devices striving for mitigating seismic effects on the linked buildings have been conducted [11–14].

In this chapter, the following cases of changes to the dynamic properties of buildings are investigated. This chapter is organized into four parts.

First: Two or more adjacent buildings connected together by bridges after the buildings are completed and occupied for the purpose of easy circulation and saving of time and effort.

Second: Buildings connected by reinforced concrete beams to nearby high retaining walls in order to provide strong lateral support to the retaining walls.

Third: Theoretical investigation and structural analysis of connecting two or more buildings together by rigidly linked sky bridges and the effects of this linking on the seismic performance of the connected buildings.

Fourth: Theoretical investigation and structural analysis of connecting two or more buildings with special devices that are designed to mitigate seismic response and reduce earthquake effects on the connected buildings.

These parts are discussed in the next paragraphs.

2. Buildings rigidly connected together long after completion without being designed as such

A need to connect two adjacent buildings together by a bridge or corridor arises sometimes long after the buildings are constructed and occupied. Fast and easy circulation of occupants and goods is a clear benefit of linking the buildings. There are uncountable examples of buildings linked together by a bridge for similar purposes. **Figure 1** shows two hospital buildings connected by a steel sky bridge over a street with a span of around 22 m. The steel bridge is partly supported by the stone walls,
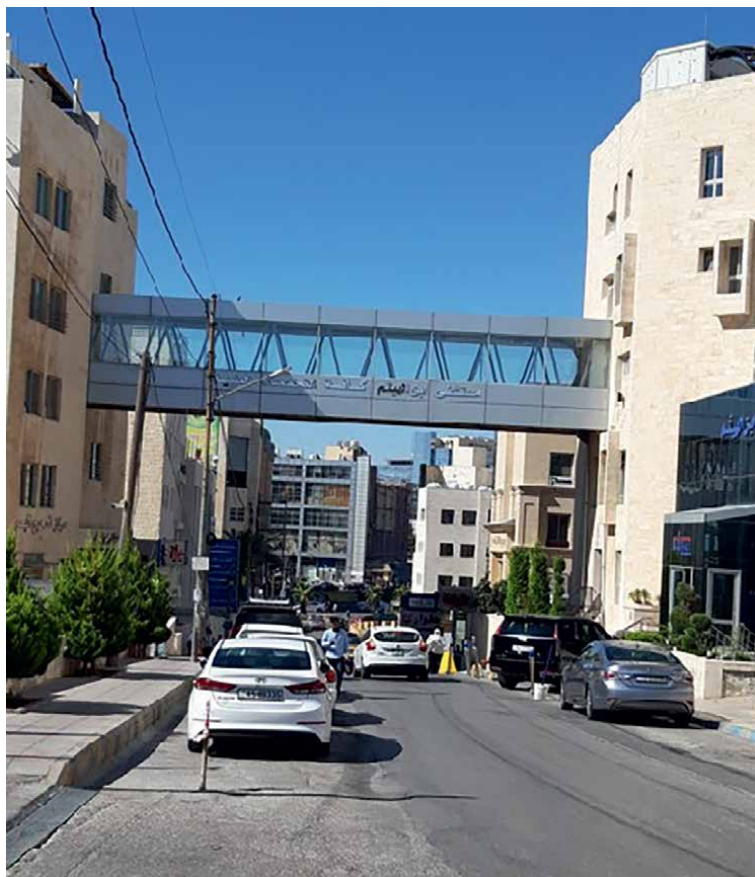
Figure 1.
Steel sky-bridge connecting two parts of a multistory hospital building in Amman, Jordan.

and partly fixed to the walls using steel plates and bolts, **Figure 2**. The sky bridge was erected long after the two buildings were constructed when the need to use the two buildings as one hospital came into existence. Often, in such cases, a thorough seismic structural investigation of the linked buildings is not carried out.

The connecting bridges are usually built of reinforced concrete or steel. The link may be supported directly on the beams' or slabs' tops of the two buildings. The concrete of the beam or slab tops may be removed and the steel bars exposed in order to splice or weld the steel bars of the linking bridge to the steel of the beams or slabs of the buildings. Steel sections (for example, Section I) may protrude into the beam or slab concrete, or be connected by plates and bolts. In all such cases of connections, the linking bridge becomes rigidly connected to the two buildings. A new complex building is, therefore, created, which comprises the two buildings and the linking bridge. The stiffness, mass, and damping matrices of this complex replace the individual matrices of the two buildings during analysis. Seismic analysis of this complex proves that its structural behavior is completely different from that of the isolated individual buildings.

In order to obtain some insight into this case, a seismic analysis of two buildings connected by sky bridges is carried out by the author. The two buildings are 18 and 13 floors in height, with different plan configurations. Sky bridges are modeled as beam columns, and hence it is a rigid connection. The buildings are connected together by

Figure 2.
*The connecting steel sky bridge from below.*

one, two or three sky bridges, and seismic investigations are carried out for different cases. El Centro earthquake time- acceleration recording is utilized [15]. SAP2000 analysis results revealed that the modes of vibration of the connected buildings are quite different from those of the individual buildings. The following **Figures 3–5** are the results of SAP200 analysis of two linked buildings. One of the outputs of the analysis shows that the modes of vibration are out of phase, **Figure 3**, and they depart from each other [15]. For example, in the structure with one sky-bridge, horizontal displacements in the right building frame U1 in **Figure 3** for the two
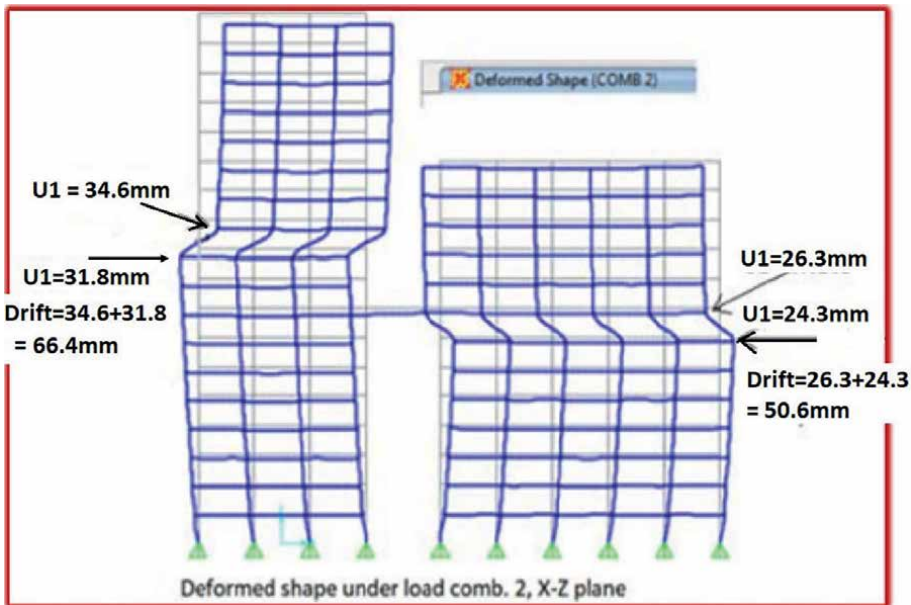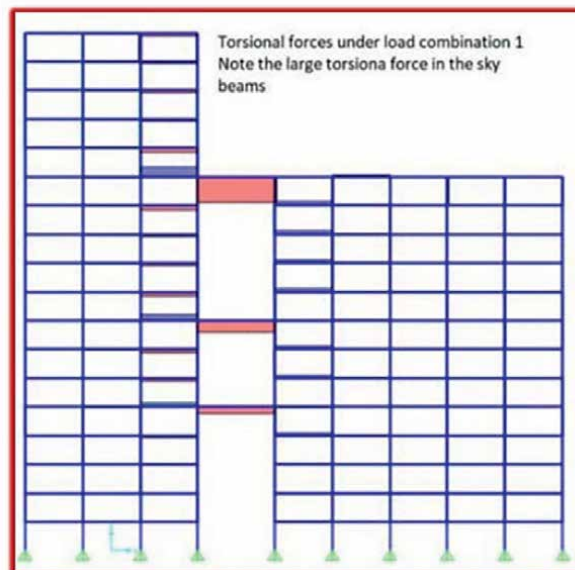

Figure 3.
Out-of-phase mode of vibration and deformation of two connected buildings, a case of 1 sky bridge, with permission of the author [15].

joints shown, being one to the left and the other to the right, produce a story drift of 263 + 243 = 50.6 mm. Similarly, for the left building frame, it is 66.4 mm. Some code limitations require that inter-story drift not exceed 0.015–0.02 h where h = story height. 0.015x3000 = 45 mm. These values of inter-story drift could be detrimental
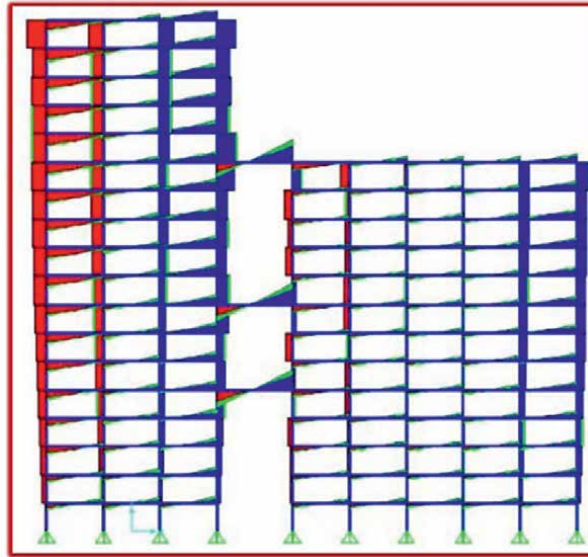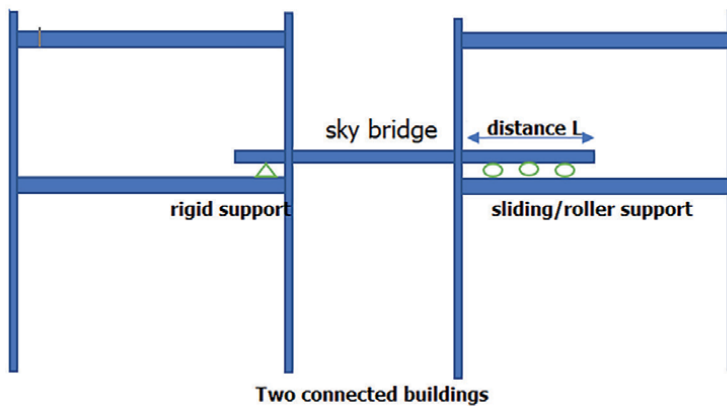

Figure 4.
Shear forces in beams and columns and the sky bridges under seismic excitation, a case of three sky bridges, with permission of the author [15].

Figure 5.
Torsional forces in beams and columns and the sky bridges under seismic excitation, a case of three sky bridges, with permission of the author [15].

to the whole structure unless they are designed for such high values [15]. The linking bridge or bridges as well as some of the beams and columns of the two buildings may attract very large torsional, shear and moments values, which may well exceed their design capacities, and might render the buildings unsafe, **Figures 4** and **5**, [15]. For example, in the structure with three sky bridges, **Figures 4** and **5**, the bending moment in columns 269–270 is 93.2 kN.m as compared to 35.4, 51.6, and 60.6 kN.m for other columns in the same floor in the same plane. The same column has a shear force of 51.7 kN as compared to 25.3, 31.2, and 38.1 kN for other columns on the same floor in the same plane (see **Figure 4**).

Another note-worthy example is for a column in the top short tower which shows a moment of 67.4 kN.m when it is part of the twin towers and connected to the sky

Figure 6.
Suggested method of connecting two building by a sky bridge.

Figure 7.
A. Car park building connected to a nearby college building. B. Apparent details of the connection.

beam, but it shows a reversed moment of 63.7 kN.m when it is in the unconnected single short tower under the same load combination. Similarly, some of the linking beams may attract large torsional forces that exceed their design capacities. The same note can be observed in the beams closest to the sky beams, **Figure 5**.

Code and safety requirements warrant that seismic analysis and redesign of the complex should be considered by the designer before connecting the two buildings.

The author suggests the connection of the two buildings be designed by having the linking bridge rigidly connected to one building while the other end has a sliding support to allow some movements during earthquake excitations, **Figure 6**. One important requirement for this type of connection is that the distance of the linking bridge resting on the building floors (distance L in **Figure 6**) should be larger than the expected maximum sum of the two displacements of the two connected floors during the design earthquake by a suitable factor of safety. The two displacements comprising the distance L should be obtained from inelastic dynamic analysis of the buildings where nonlinear plastic properties of the materials are utilized. **Figure 7** shows another example of a multistory building linked to a car park building by steel I section long after the two buildings were constructed.

3. Buildings connected to nearby walls at deep cuts

Often in mountainous terrains, a building is constructed at the foot of an excavated hill, and a high "facing wall" is constructed to support the excavation. The idea of connecting the building, at floor levels, to the "facing wall" by reinforced concrete beams attracts the designer. The author prefers to call it a facing wall rather than a retaining wall because, in fact, the wall is never designed as a retaining wall. The fact is that it is usually a reinforced concrete thin wall with constant thickness and very narrow base. Connecting such a wall to the highly stiff diaphragms of the building by beams seems to convince designers that the wall is provided with a high factor of safety against sliding and overturning. According to the geometry of the excavated hill, the building slabs may be connected to the "facing wall" in two directions (see **Figures 8–10**).

The structural seismic analysis of a complex a multistory building connected to a wall as described has in general a completely different structural response than the bare building alone. Shear, moment, and torsional forces prove through seismic analysis to be different from the values of the isolated building. The number of the linking beams as well as their distribution on the facades of the building have a great effect on the response. The choice of the number and distribution of linking beams at the level of each floor, that is to say, their configuration on the building elevation is in fact more arbitrary than studied by practicing engineers. As such, the response of the structural complex of the building, linking beams, and facing wall may reveal a non-safe seismic performance. Ground shaking may be imparted to the building at the base level and at all floor levels, which are connected to the wall **Figure 8**.

This will be more evident and may be very unsafe when the building is connected to the wall in two directions.

Time history seismic analysis of a 10-story 3-D building connected to a nearby facing wall 0.35 m thick, is carried out using the well-known El Centro acceleration recording in two directions, **Figures 9** and **10**. The X direction is that of the linking beams, and Y direction is perpendicular to it. The analyzed model includes the foundation soil below the building and the soil behind the facing wall attempting
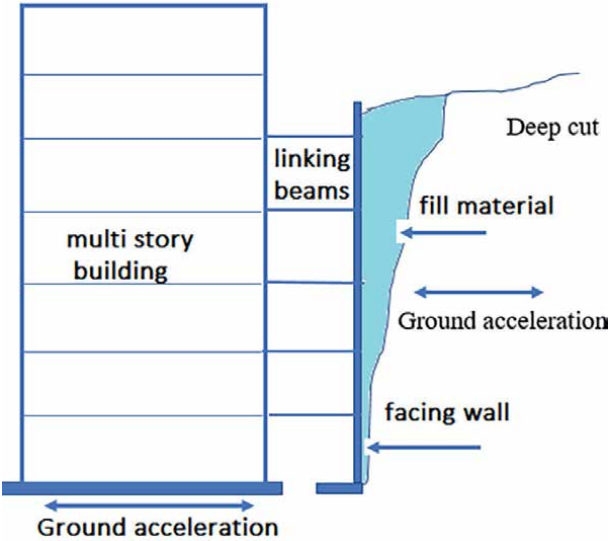
Figure 8.
Section of a multi-story building connected to an adjacent wall by beams.

Figure 9.
A multi-story building connected to the nearby wall by beams at several floor levels, Amman, Jordan.
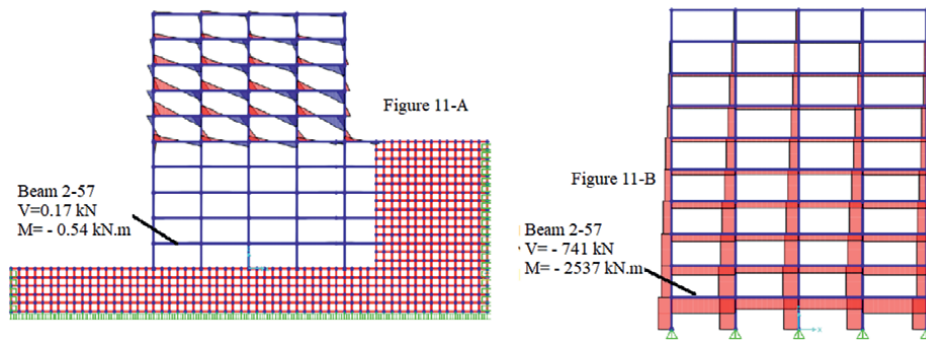
Figure 10.
A building connected to a nearby wall by several beams at different floor levels, Amman, Jordan.

to include soil-structure interaction. Below foundation soil and the deep-cut soil are modeled as solid elements in SAP200. Soil properties are modulus of elasticity E = 2x10^5 MPa, Poissons ratio = 0.2, and shear modulus G = 77 MPa. The facing wall or beams can be connected to the cut soil by Gap links according to SAP 200 modeling techniques. While the foundation of the column can be connected to the underlying soil by springs with suitable spring constants depending on the soil stiffness. The analysis results show that the behavior of the connected building with the linking beams is completely different from that of the isolated building. Behavior differences are evident in displacements, member response forces, periods of vibration, and mode shapes. **Figures 11a** and **12a** show analysis plots of SAP2000 output for the shear, moment and torsional forces of the building with the linking beams and soil, while **Figures 11b** and **12b** show the output of the isolated building. The differences between the results can not be overstressed. These are only examples to show the complete change of the structure behavior when the building is linked to a nearby wall.

Based on the analysis results, the following general notes can be drawn:

1. Linking a multistory building to a retaining wall or a facing wall by reinforced concrete beams at floor levels can provide lateral support to the walls.

2. The structural behavior of the connected building under seismic actions is completely different from that of the isolated building. Behaviors are manifested in the structure's periods of vibration, mode shapes, displacements, and member forces.

3. The number of linking beams, their stiffness, and their distribution on the elevation of the building have unpredictable effects on the seismic response of the building. A complete analysis is required.

Figure 11.
Comparison between shear and moment values of the isolated building B, and the building connected with linking beams to the wall and soil masses below and adjacent to the wall a. values are taken at 1.0 second from the application of El Centro excitation in the direction perpendicular to the linking beams.
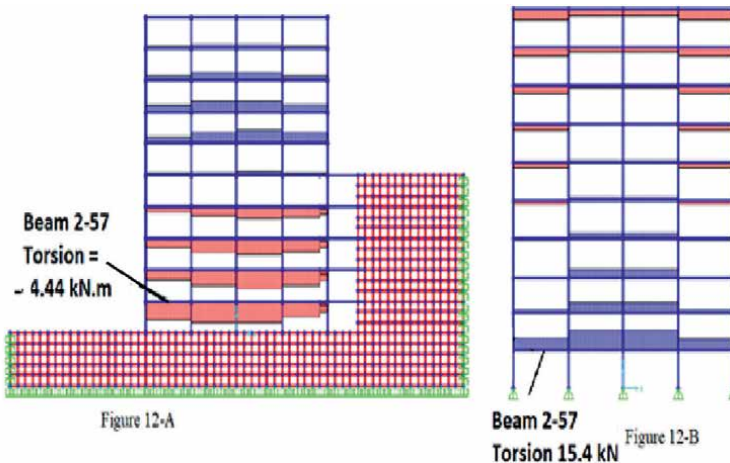
Figure 12.
Comparison between torsional force values of the isolated building (12-B), and the building connected with linking beams to the wall and soil masses below and adjacent to the wall (12-a). Values are taken at 1.0 seconds from the application of El Centro excitation in the direction perpendicular to the linking beams.

4. The shear, torsional forces, and moments in the building beams and columns as well as the linking beams and the "facing" wall may have excessive values beyond their original design capacities and could be unsafe.

4. Theoretical studies of buildings rigidly connected by sky bridges

There has been a lot of theoretical research on nearby buildings linked together by steel or reinforced concrete sky bridges. Numerous adjacent world skyscrapers are connected by sky bridges. The Petronas Twin Towers in Malaysia is a typical example (**Figure 13**).

Esthetic and grand appearance of similar connected towers is one architectural purpose of the connection. The sky bridges can serve as fire escape routes in addition to ease of circulation and time-saving purposes [3]. Theoretical studies of the effects

Figure 13.
Petronas twin towers in Malaysia connected together by a sky bridge. Petronas twin towers | buildings, Kuala Lumpur, Malaysia | Britannica.

of inking on the seismic performance of connected buildings have been addressed by many authors [2–10]. The problem of buildings linked together by sky bridges has not found its way into building design codes due to the extreme complexity of the issue. Research has shown, in general, cases of increased seismic response of the buildings, and cases of reduced seismic performance. The heights of the connected buildings varied from few floors up to more than 250 m of height. The connection was, usually, modeled as rigid beams or slabs made up of reinforced concrete or steel. The position of linking sky bridges, as they are called by researchers, was shifted from floor to floor to investigate the effects of such positions on the performance of the buildings. In general, the findings of most of those theoretical studies indicated that such rigid connections of the two buildings often resulted in dramatic changes in the seismic performance of the two isolated buildings. The seismic response (mode shapes, frequency, shear, torsion, moment) of the complex of linked buildings and sky bridges are much different for each isolated building before connection. A summary of some theoretical work is presented next.

Sayed, M [2] studied 30-floor twin buildings with sky bridges connecting them at different heights utilizing ETABS software. The sky bridge connecting the towers is 33.6 m long built of reinforced concrete and resting on the buildings' columns on either side. As such, the connection to the towers is a rigid connection. The study did not aim at alleviating the buildings of any earthquake actions. The study conclusions described the effect of changing the height of the position of the sky bridge on the seismic response of the buildings. None of the findings of the research mentioned anything about reducing the forces or seismic responses of the buildings.

Abbood et al. [3] conducted a study on 40-floor twin buildings connected rigidly by 3 reinforced concrete links at the upper two stories. The links were 15 m long and modeled as a beam and slab. The results of the study showed that the seismic response of the two connected buildings increased or decreased compared to the single tower's response. The study did not aim at reducing the effect of earthquake actions on the structures.

Tse et al. [4] investigated the 3-D theoretical model of two 40-floor buildings with the links connecting them modeled as rigid beams with 3 degrees of freedom at each end. The study examined the effect of changing the location of the links on the periods of vibrations.

Sayed et al. [5] carried out a 3-D dynamic (time history) analysis of the Petronas Twin Towers in Malaysia connected with a linking reinforced concrete sky bridge. The analysis used an earthquake string record scaled to 0.15 g ground acceleration in the direction of the sky bridge as well as in the orthogonal; direction. The sky bridge was positioned at the following floor heights to investigate the effect of its position on the seismic response of the connected twin towers: 22nd, 44th, 66th, and 88th floors. The analysis results were compared to the results of the bare towers, which revealed that the seismic response in the sky bridge was amplified. It was also found that the location of the sky bridge on the upper floors had a detrimental effect on the seismic response of the twin towers when the earthquake excitation was in the direction of the sky bridge.

Hu et al. [7] theoretically investigated two linked buildings for the wind-induced response. The effects of the mass, stiffness, and location of the links on the acceleration of the linked buildings revealed that the torsional acceleration of the linked buildings was always larger than that of the unlinked buildings. This is in agreement with other research [15]. The author concluded that designers should be careful of this fact when designing linked buildings [7].

Based on the general findings of previous research, the following notes can be drawn:

1. Many studies were interested in the effect of changing the location and height of the linking sky bridges on the structural behavior of the connected buildings. The sky bridges, built of reinforced concrete, were rigidly connected to the buildings. All studies had the evident conclusion that the connected buildings showed different seismic responses than the isolated buildings. Some studies revealed detrimental effects or amplified response on the buildings during seismic analysis.

2. These studies were not aimed at relieving the buildings of earthquake actions by linking them by sky bridges.

3. The door is wide open for re-considering those same studies searching for solutions of relieving the connected buildings of any risks caused the connections during earthquake excitations.

5. Theoretical studies of buildings connected together by damping devices

The three previous parts of this chapter show cases of connecting building together or to adjacent walls. The purposes of such connections are to make easy and fast circulation between connected buildings in the former case and produce strong lateral support for the walls in the latter case. Previous studies of those cases have not tried to investigate means of mitigating earthquake effects on the new structural complexes produced by the connections. Numerous new studies have been carried out adopting newly invented technical devices to control and alleviate seismic effects on buildings. These techniques could be suitable methods of balancing the risks arising from connecting buildings to each other or to nearby walls. The door is open for more theoretical and experimental research in this regard.

Newly developed techniques for changing the dynamic properties of buildings are linking two nearby buildings by damping devices. Previous sections of this chapter considered buildings rigidly connected to each other or to walls, without aiming at reducing seismic responses during earthquake excitations. This section considers previous theoretical studies conducted to enhance buildings' performance during seismic actions. The purpose was to reduce story drifts, member moments, shear, and torsional forces. This is done by connecting two adjacent buildings with damping devices to dissipate energy imparted to the buildings by ground acceleration.

The buildings were considered a few stories to more than 50 floors in height. Many types of damping devices were used. Friction pendulum bearings are seismic isolators used usually between the structure and its foundation. In one study [12], they are used between the sky bridge and the buildings on both sides of the sky bridge. Viscous, viscoelastic, and friction dampers were also used in another theoretical study [12] to connect two buildings at different heights to reduce the effects of earthquake actions. Viscous damper reduces the vibrations induced by earthquakes, while viscoelastic dampers dissipate the building's mechanical energy by converting it into heat. Friction dampers operate by dissipating kinetic energy through friction. Friction dampers are installed diagonally between floors to reduce the story drifts. In one study, they were used between two buildings to reduce the earthquake effects by dissipating energy through frictional forces as shown in **Figure 14**. A summary of these studies is included here.

Bhaskararao et al. [11] conducted a theoretical investigation of two adjacent buildings connected with various types of dampers namely *viscous, viscoelastic, and friction dampers*. With all types of dampers used, it was concluded that the earthquake response of the two buildings was reduced. It was also concluded that it was not necessary to connect the buildings at all floor levels to achieve such a reduction. Optimum location of dampers at specific floor heights can be obtained.

Xiaohan et al. [12] considered four similar towers, around 240 m high, connected with a sky corridor bridge 300 m long at the rooftop. SAP200 software was used in
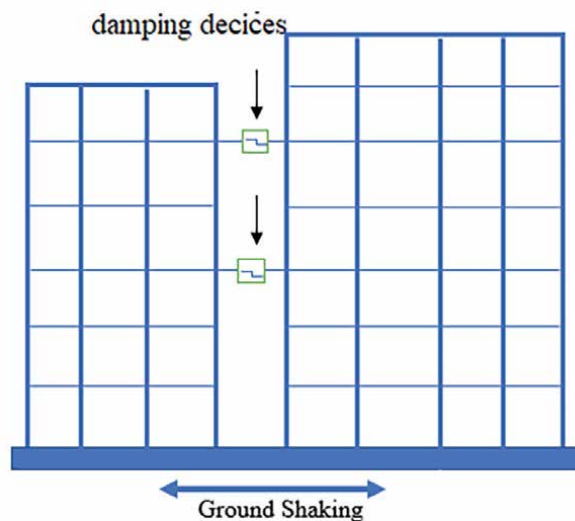
Figure 14.
*Friction dampers used to connect two buildings at floor levels.*
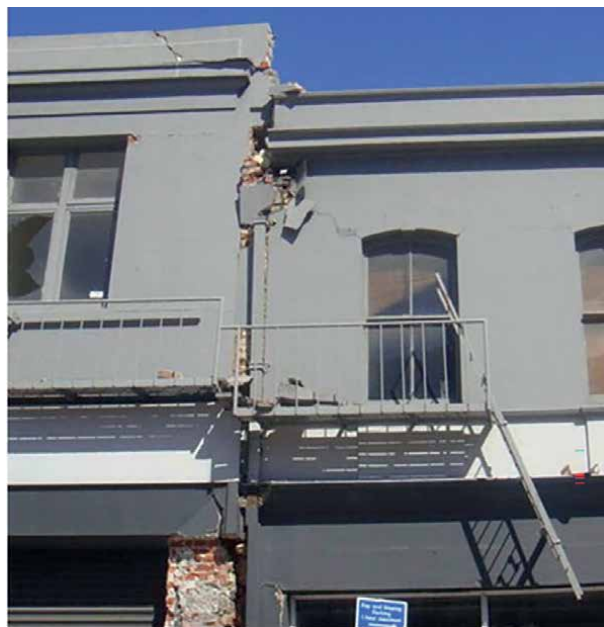
Figure 15.
Pounding of two adjacent buildings and damage produced. Full article: Effects of pounding on adjacent buildings of varying heights during earthquake in Pakistan (tandfonline.com).

the analysis. *Friction pendulum bearings* are installed on the buildings' tops to support the sky corridor bridge. Several damping devices connected the towers and the sky bridge. The purpose of the study is to reduce the earthquake response and the member forces using the used devices. The authors concluded that connecting towers with friction pendulums with tuned mass dampers reduced effectively the structure seismic responses. Best seismic reduction was obtained when the frequency of the dampers is close to the frequency of the primary structure. On the other hand, larger interaction forces between sky bridges and towers were noted when towers and bridges were rigidly connected, a finding consistent with other research conclusions [15].

Rouzbeh et al. presented a state-of-the-art review of buildings connected together by various types of links. The authors classified the buildings coupling as rigid, passive, semi-active, active, and hybrid connections. These coupling links proved to be effective in preventing the pounding of adjacent buildings and reducing their seismic response. Damage to buildings due to pounding is very common between nearby or adjacent buildings during earthquakes, **Figure 15**.

Uz et al. [14] used fluid viscous dampers to connect two buildings and concluded that they improve the response of buildings to earthquakes, **Figure 16**.

Huaxiao et al. [16] carried out a theoretical study of two unequal buildings connected together by varying number of passive control devices at different floor levels. These devices can be metal friction dampers or fluid viscous dampers. The buildings are 59 stories (268 m height) and 55 stories (210.2 m height). The buildings are connected by a corridor with rigid support at one terminal and sliding support at the other terminal, the same way as suggested by the writer. The study considered wind forces and earthquake excitation at the same time. Tuned Liquid Column Damper Inerter (TLCDI) and tuned mass damper with an inerter (TMDI) are used to connect the two buildings to mitigate the wind and earthquake responses. The authors
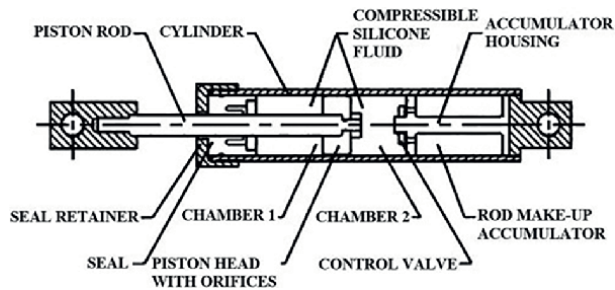
Figure 16.
Typical fluid viscous dampers. Viscous damper - an overview | ScienceDirect topics.

concluded that these devices are effective in reducing the wind and earthquake responses, and they are more effective in the wind case than in the earthquake case.

Based on these and other studies concerning the earthquake mitigating devices linking two buildings, the flowing can be concluded:
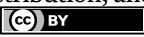
1. Friction pendulum bearings, viscous, viscoelastic, and friction dampers are control devices used in theoretical studies to connect two adjacent buildings in order to mitigate earthquake responses. They proved through dynamic analysis of the linked buildings to be effective in reducing earthquake responses.

2. Linking two buildings by a rigid connection on one building and sliding connection on the other is considered effective in avoiding the transfer of building response to the other building.

3. Pounding of adjacent buildings can be prevented by using suitable linking devices, and more effective developments are finding their way into the smart building industry.

Author details

Jamal Alomari
Khawarizmi University Technical College, Amman, Jordan

*Address all correspondence to: tomsunny54@gmail.com

IntechOpen

References

[1] Shashikant K. Duggal, Earthquake-Resistant Design of Structures. 2nd ed. Oxford University Press; 2013. Retrieved from: www.knovel.com. ISBN: 978-0-19-808352-8

[2] Sayed M. Horizontally connected high-rise buildings under earthquake loadings. Ain Shams Engineering Journal. 2019;**10**:227-241

[3] Abbood IS, Mahmod M, Hanoon AN, Jaafar MS, Mussa MH. Seismic response analysis of linked twin tall buildings with structural coupling. International Journal of Civil Engineering and Technology. 2018;**9**(11):208-219

[4] Tse KT, Jie S. Modal properties of twin buildings with structural coupling at various locations. In: The Eighth Asia-Pacific Conference on Wind Engineering. Chennai, India: CSIR-Structural Engineering Research Centre (SERC); 2013. pp. 862-869

[5] Mahmoud S, Abdallah W, Hanna N, Abdelaal A. Seismic response evaluation of connected super-tall structures. Proceedings of the Institution of Civil Engineers. Structures and Buildings. 2016;**169**(SB11):840-852

[6] Sun HS, Liu MH, Zhu HP. Connecting parameters optimization on unsymmetrical twin-tower structure linked by sky-bridge. Journal of Central South University. 2014;**21**:2460-2468

[7] Hu G, Tse KT, Song J, Liang S. Performance of wind-excited linked building systems considering the link-induced structural coupling. Engineering Structures. 2017;**138**:91-104

[8] Yuan W, Wang L. Influence of connection location on dynamic characteristics of three-towers-connected high-rise building. Advanced Materials Research. 2011;**243-249**:419-425

[9] Shi S. Complicated high-rise structure Design of Ning Bo-Liansheng Commercial Plaza. The Open Civil Engineering Journal. 2015;**9**:799-804

[10] Luong A, Kwok M. Finding structural solutions by connecting towers. Council on Tall Buildings and Habitat. 2012;**3**:26-31

[11] Bhaskararao AV, Jangid RS. Seismic response of adjacent buildings connected with dampers. In: Proceedings of the 13th World Conference on Earthquake Engineering. Paper No. 3143. Vancouver, B.C., Canada; 2006

[12] Xiaohan W. Seismic performance analysis of a connected multi-tower structure with FPS and viscous damper. Shock and Vibrations, Hindawi, Vol. 2018, Article ID, 1865761, 19 pages. https://doi.org/10.1155/2018/1865761

[13] Rouzbeh D, Seyed HHL. Connection of coupled buildings, a state of the art review. Journal home page: www.elsevier.com/locate/structures, Structures. 2021;**33**:1299-1326

[14] Uz ME, Hadi MNS. Dynamic analysis of adjacent buildings connected by viscous fluid dampers. Earthquake Resistant Engineering Structures. 2009;**VII**:139

[15] Alomari J. Conceptual seismic analysis of two R.C. adjacent buildings with different dynamic properties connected horizontally by sky bridges. Journal of Engineering Science and Technology. 2021;**16**(3):2610-2628

[16] Huaxiao W, Qinhua W, Nayan DT. and Dario DD. Comparison of Dynamic Responses of Parallel-Placed Adjacent High-Rise Buildings under Wind and Earthquake Excitations. 2021. Vol. 2021. Article ID 6644158. DOI:10.1155/2021/6644158. available from: https://www.hindawi.com/journals/sv/2021/6644158/ [Accessed: August 10, 2022]

Chapter 9

On the Nonlinear Transient Analysis of Structures

Miroslav Trcala, Ivan Němec and Adéla Gálová

Abstract

This chapter consists of four sub-chapters the first of them is the introduction. The second sub-chapter discusses the suitability of the explicit and implicit methods for seismic analysis of buildings exposed to a substantially nonlinear response. Taking into account a duration typical for earthquakes from several seconds to about twenty seconds, it seems that the implicit method is more suitable. Because of the shape of accelerograms, it is needed to use quite short time steps. Both methods were compared for a heavily nonlinear response, typical for seismicity. The third subchapter discusses the analysis of the time-dependent behavior of concrete using nonlinear time-dependent material models during fast dynamic actions. Huge plastic yielding or damage of the material is reached. The fourth sub-chapter discusses sources of dynamical damping that are needed in earthquake analysis. This subchapter aims to take into account the influence of different kinds of damping in the dynamic analysis of structures. More advanced analysis taking into account the various sources of damping, i.e., material viscosity, plasticity/damage, and friction in connections and supports is strongly recommended in the earthquake analysis.

Keywords: earthquakes, seismicity, dynamics, transient, implicit, explicit, finite element method, plasticity, damage, viscosity, damping

1. Introduction

In the last decades, a big development in the field of nonlinear and time-dependent material models, including those that are suitable for seismic analysis, were achieved. But to take advantage of these developments, the use of spectral analysis must be abandoned and a method of direct integration of the equation of motion must be used (also called the transient or time history analysis). Several aspects of this area, including the comparison of the explicit and implicit method in seismic analysis [1, 2], suitable material models, and sources of dynamic damping are discussed in this chapter. Subchapter 2 deal with several aspects of the transient dynamic approach in seismic analysis. Subchapter 3 compared the response to seismic loading of various material models, specifically the Drucker-Prager plasticity model [3] and Mazars damage model [4]. Subchapter 4 showed different types of dynamic damping in structural analysis which should not be neglected in transient analyses.

2. Numerical methods of direct integration of equation of motion and their application in seismic analysis

This subchapter aims to compare the suitability of the explicit and implicit methods in the nonlinear earthquake analysis from the point of view of computational time and accuracy. We implemented these methods in RFEM [5] software and we used Ansys software [6] to compare and validate the results. In the following text let us introduce the numerical methods used in the study. The equation of motion of a discrete model of a structure subjected to a dynamic load can be written

$$\mathbf{M}\ddot{\mathbf{u}}(t) + \mathbf{C}\dot{\mathbf{u}}(t) + \mathbf{f}^{\text{int}}(t) = \mathbf{M}a(t) + \mathbf{C}v(t) + \mathbf{f}^{\text{int}}(t) = \mathbf{f}^{ext}(t) \qquad (1)$$

where $\mathbf{M},\mathbf{C}$ are matrices of mass and damping respectively, $\mathbf{f}^{ext}$ and $\mathbf{f}^{\text{int}}$ are the vectors of the external and internal forces respectively and $\mathbf{u}$, $\mathbf{v} = \dot{\mathbf{u}}$, $\mathbf{a} = \ddot{\mathbf{u}}$ are displacement, velocity, and acceleration, respectively.

The numerical process of direct integration of the equation of motion (1) in a time interval $t \in \langle t_0, t_m \rangle$ is called transient analysis. Time is discretized to finite number of time instants $t_0, t_1, \dots, t_m$. The distance between individual time instants $\Delta t_i = t_i - t_{i-1}$ is called the time step. The lengths of time steps Δt_i influences the accuracy, stability and speed of the numerical solution. At the time $t = 0$ an initial conditions $\mathbf{u}(t_0) = \mathbf{u}_0$, $\mathbf{v}(t_0) = \mathbf{v}_0$ have to be defined. Eq. (1) then can be read as follows:

$$\mathbf{M}\ddot{\mathbf{u}}_i + \mathbf{C}\dot{\mathbf{u}}_i + \mathbf{f}_i^{\text{int}} = \mathbf{M}a_i + \mathbf{C}v_i + \mathbf{f}_i^{\text{int}} = \mathbf{f}_i^{ext} \qquad (2)$$

2.1 Explicit method: Central differences

In explicit methods, we introduce explicit assumption about the course of displacement in interval $\langle t_i, t_{i+1} \rangle$ and the knowledge of the displacement vector $\mathbf{u}_i$ at time instant t_i, and we calculate vectors $\mathbf{u}_{i+1}$, $\mathbf{v}_{i+1}$, $\mathbf{a}_{i+1}$ from (2).

The numerical integration of differential equations uses the substitution of the derivative of the displacement with respect to time. in (2) by

$$\mathbf{v}_i = \frac{1}{2\Delta t_i}(\mathbf{u}_{i+1} - \mathbf{u}_{i-1}) \qquad (3)$$

$$\mathbf{a}_i = \frac{1}{\Delta t_i^2}(\mathbf{u}_{i+1} - 2\mathbf{u}_i + \mathbf{u}_{i-1}) \qquad (4)$$

we obtain a recurrent formula for $\mathbf{u}_i$

$$\left(\frac{1}{\Delta t_i^2}\mathbf{M} + \frac{1}{2\Delta t_i}\mathbf{C}\right)\mathbf{u}_{i+1} = \mathbf{f}_i^{ext} - \mathbf{f}_i^{\text{int}} + \frac{2}{\Delta t_i^2}\mathbf{M}\mathbf{u}_i - \left(\frac{1}{\Delta t_i^2}\mathbf{M} - \frac{1}{2\Delta t_i}\mathbf{C}\right)\mathbf{u}_{i-1} \qquad (5)$$

The method has all the advantages of explicit methods as long as $[\mathbf{C}] = [\mathbf{0}]$ or $[\mathbf{C}] = \alpha[\mathbf{M}]$, where α is the mass coefficient of the Rayleigh damping. The most effectivity is achieved when the mass matrix $\mathbf{M}$ is diagonal. The explicit methods are conditionally stable. The time steps must satisfy the following condition:

$$\Delta t_i \leq \frac{T_n}{\pi} \qquad (6)$$

where T_n is the smallest vibration period.

2.2 Implicit method: Newmark

Implicit methods in transient dynamics are based on the equation of motion (2) at the time instant t_i. The numerical solution of the system is performed step by step by the following text.

$$\mathbf{a}_i = f(t_i, \ \mathbf{f}_i, \ \mathbf{u}_{i-1}, \ \mathbf{v}_{i-1}, \ \mathbf{a}_{i-1}) \tag{7}$$

with the necessity to evaluate the acceleration at the start of the motion at time t_0 from the equation of motion (2)

$$\mathbf{M}\mathbf{a}_0 + \mathbf{C}\mathbf{v}_0 + \mathbf{K}\mathbf{u}_0 = \mathbf{f}_0 \tag{8}$$

The basic formula of the Newmark method that specifies the relations between displacement, velocity, and acceleration vectors have the following form:

$$\mathbf{u}_i = \mathbf{u}_{i-1} + \Delta t_i \mathbf{v}_{i-1} + \left(\frac{1}{2} - \beta\right)\Delta t_i^2 \mathbf{a}_{i-1} + \beta \Delta t_i^2 \mathbf{a}_i \tag{9}$$

$$\mathbf{v}_i = \mathbf{v}_{i-1} + (1 - \gamma)\Delta t_i \mathbf{a}_{i-1} + \gamma \Delta t_i \mathbf{a}_i \tag{10}$$

where β and γ are what is termed Newmark's parameters. As formulas.
$\mathbf{u}_i = \mathbf{u}_{i-1} + \Delta \mathbf{u}_i, \mathbf{v}_i = \mathbf{v}_{i-1} + \Delta \mathbf{v}_i, \mathbf{a}_i = \mathbf{a}_{i-1} + \Delta \mathbf{a}_i$ (11)
holds we can write the following formula for the vector of acceleration increments and velocity increments:
$\Delta \mathbf{a}_i = \Delta \bar{\mathbf{a}}_i + \frac{1}{\beta h^2}\Delta \mathbf{u}_i, \Delta \mathbf{v}_i = \Delta \bar{\mathbf{v}}_i + \frac{\gamma}{\beta h}\Delta \mathbf{u}_i$ (12)where.
$\Delta \bar{\mathbf{a}}_i = \left(-\frac{1}{\beta \Delta t_i}\mathbf{v}_{i-1} - \frac{1}{2\beta}\mathbf{a}_{i-1}\right), \Delta \bar{\mathbf{v}}_i = \left(1 - \frac{\gamma}{2\beta}\right)\Delta t_i \mathbf{a}_{i-1} - \frac{\gamma}{\beta}\mathbf{v}_{i-1}$ (13)
The total increments of the vector of displacement can be written as:

$$\Delta \mathbf{u}_i = \sum_{k=1}^{n_{ITER}} {}^k \Delta \Delta \mathbf{u}_i \tag{11}$$

By substitution according to formulas above into the equation of motion (2) and modifying the obtained relation, we get:

$$\left(\frac{1}{\beta \Delta t_i^2}\mathbf{M} + \frac{\gamma}{\beta \Delta t_i}\mathbf{C} + {}^k\mathbf{K}_{T,i}\right) \cdot {}^k\Delta \mathbf{u}_i = {}^k\Delta \mathbf{f}_i - \mathbf{M}\Delta \bar{\mathbf{a}}_i - \mathbf{C}\Delta \bar{\mathbf{v}}_i \tag{12}$$

where ${}^k\mathbf{K}_{T,i}$ is the tangent stiffness matrix for the kth iteration of the ith time step.
The bracket on the left-hand side of (15) represents what is termed a modified stiffness matrix, which can be denoted $\hat{\mathbf{K}}_i$. The presented formula can be written in a similar form as:

$$
{}^k\Delta\Delta\mathbf{u}_i : \begin{cases} \hat{\mathbf{K}}_i {}^k\Delta\Delta\mathbf{u}_i = {}^k\Delta\Delta\mathbf{f}_i - \mathbf{M}\Delta\bar{\mathbf{a}}_i - \mathbf{C}\Delta\bar{\mathbf{v}}_i \ ; \text{for } k = 1 \\ \hat{\mathbf{K}}_i {}^k\Delta\Delta\mathbf{u}_i = {}^k\Delta\Delta\mathbf{f_i} \ ; \text{for } k > 1 \end{cases} \tag{13}
$$

Eq. (16) enable us to calculate partial increments of displacement.

2.3 Comparison of the explicit and implicit method in seismic analysis

For this numerical study, a wall of six-floor building was used. The structure was subjected to seismic load due to the accelerogram from Umbro-Marchigiana, Italy.

This sub-chapter aims to decide what numerical method of the transient analysis of buildings exposed to earthquake is most suitable from the point of view of accuracy and processing time. The earthquake should be strong enough to cause a highly nonlinear response of the analyzed building so the modal analysis cannot be used and the usage of a numerical method for direct time integration of the equation of motion is justified.

It is widely known that the explicit method (see [7–9]) is proper for analyzing processes with very short duration, such as explosions or the collisions of vehicles, i.e., processes generally studied via transient dynamic analysis.

Because the explicit method is conditionally stable, the time step must fulfill the inequality (6). Only in this case is it possible to use the diagonal form of matrices **M,C,K** to enable conditions for maximal performance. Small time steps imposed by the relation (6) are not a substantial disadvantage in the case of earthquake analysis as the earthquake accelerograms also require very short time steps.

Implicit methods of solving a set of differential equations (see [7, 10–12]) are characterized by the fact that a system of linear equations must be solved at each time step. These methods do not require such a short time step as is needed in an explicit method. Therefore, the implicit methods are mostly used for the solution of dynamical analyses of a duration longer than several seconds.

To choose what numerical method is the most suitable for transient seismic analysis of a typical building structure (see **Figure 1**), a real accelerogram from Italy (see **Figure 2**) was used along with the Drucker-Prager material model. The accelerogram of quite strong earthquake was chosen to be strong enough to cause huge nonlinear behavior with damage and plastic yielding, where spectral analysis cannot be applied and a transient analysis using the direct integration of the equation of motion has to be used. The comparison of the explicit and implicit methods method was focused on accuracy and computational performance. A time step of 0.0001 s was used for the explicit method due to stability requirements. The same time step was also chosen for the implicit method to compare the time of processing of both methods. Another reason was to obtain a very accurate reference solution for accuracy comparisons.

The following graphs (**Figures 3–6**) show the time course of the horizontal displacement of the upper right corner of the building. The graphs show very good concordance between the explicit and implicit method. It can be also seen that RFEM and ANSYS programs provide practically identical results.

The calculation performed by the implicit method for the same time step was approximately five times slower than the explicit method. Increasing the time step for the implicit method showed that this method is accurate enough until the time step was twenty times greater than that for the explicit method.

The implicit method provides good results for a computational time four times lower than that of the explicit method. But because of the difficulty to estimate the highest acceptable time step from the point of view of accuracy, it can be concluded that explicit and implicit methods are comparable for seismic analysis, but the implicit Newmark's method is slightly preferred.

An interesting partial observation of this study is the finding that both basic numerical methods for the transient analysis, namely the explicit method and Newmark's implicit method, are competitive for seismic analyses.
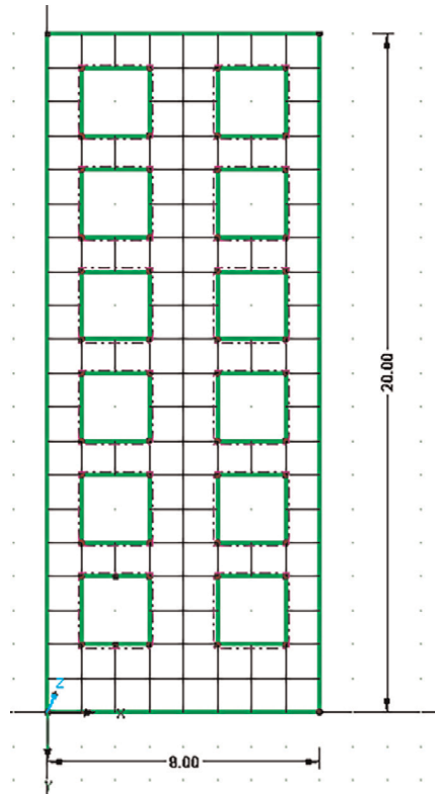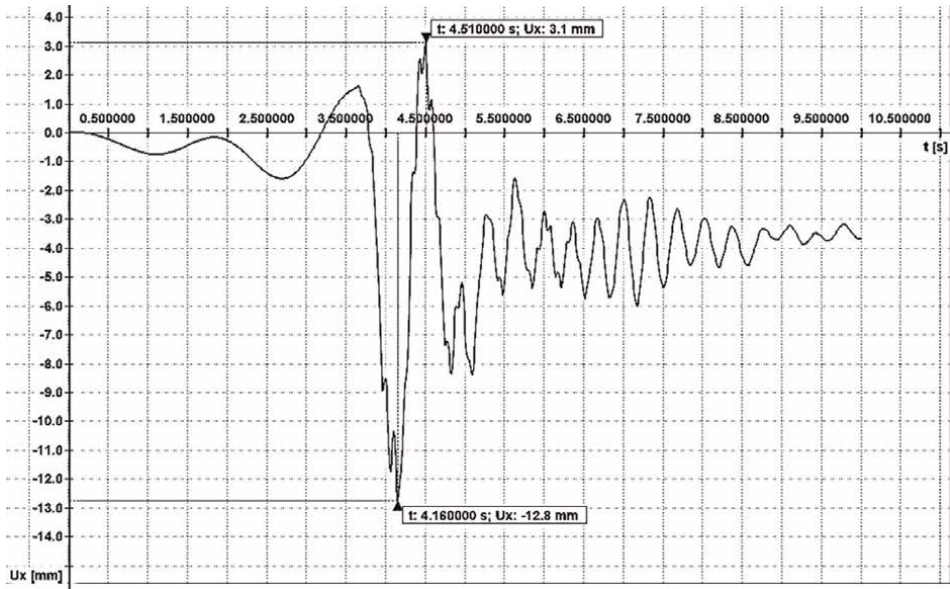
Figure 1.
The analyzed concrete wall with 21 GPa of initial elasticity modulus, elements size of 1 meter, thickness of 0.2 meters [2].
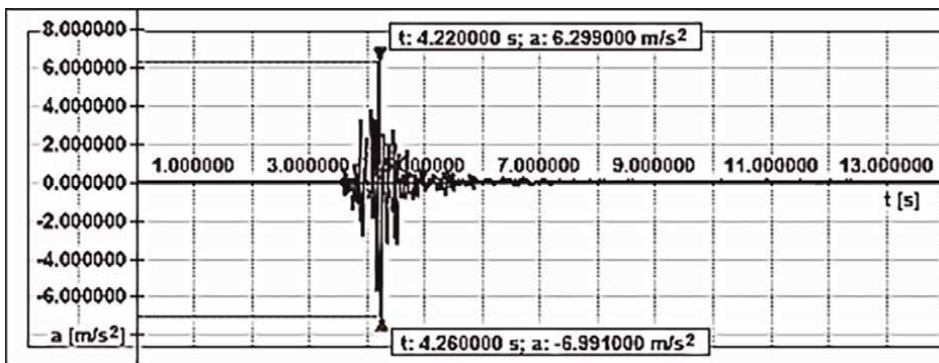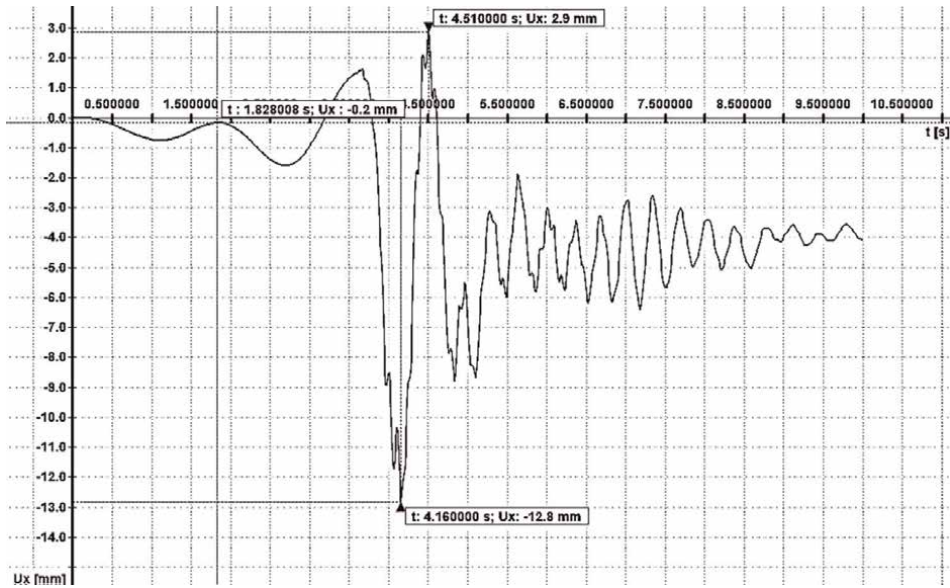

Figure 2.
Accelerograms Umbro-Marchigiana, station Colfiorita-Casermette [2].

Results of the numerical analysis showed excellent concordance between the results of the ANSYS and RFEM programs for the implicit method. The comparison in explicit methods showed a bit worse concordance between the above-mentioned programs. The RFEM program gives more accurate results than ANSYS.
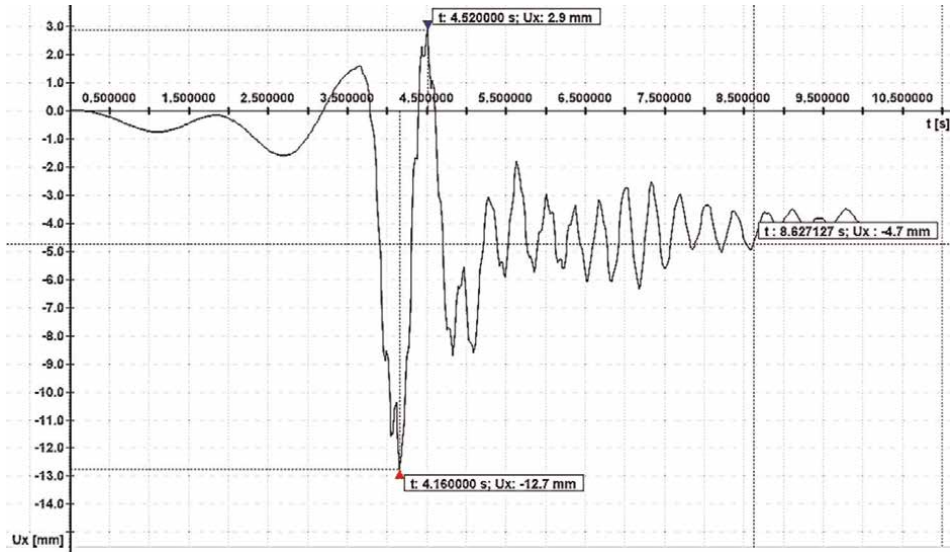
Figure 3.
Explicit method—The time course of the horizontal displacement of the upper right corner for the time step 0.0001 s [2].
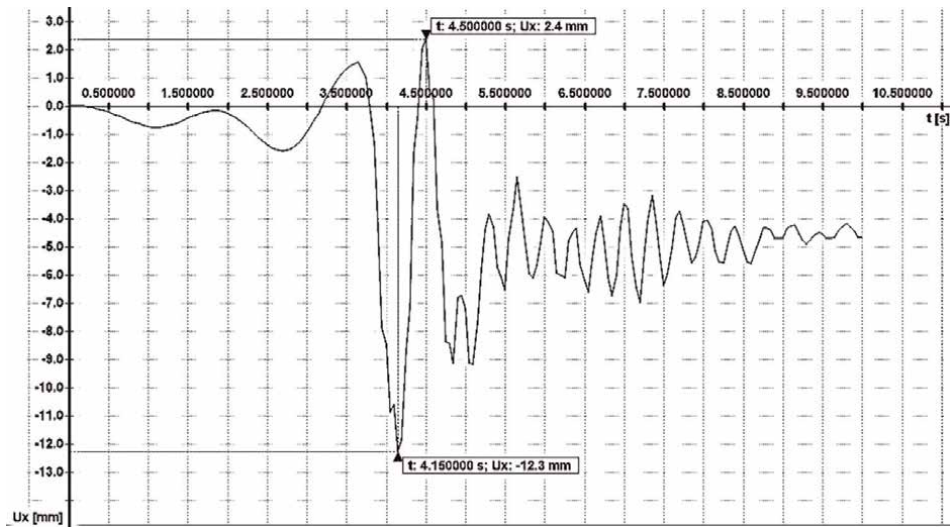

Figure 4.
Implicit method—The time course of the horizontal displacement of the upper right corner for the time step 0.0001 s [2].

3. Plasticity and damage response of structure

The aim of the article is to compare responses of a building structure for two different nonlinear material models. A wall of a six-story building (see **Figure 1**)

Figure 5.
Implicit method—The time course of the horizontal displacement of the upper right corner for the time step 0.002 s [2].

Figure 6.
Implicit method—The time course of the horizontal displacement of the upper right corner for the time step 0.005 s [2].

exposed to seismic load according to an accelerogram from Umbro-Marchigiana, Italy, was used to compare the two material models.

Three different material models were used: the linear elastic model, the Drucker-Prager plasticity model, and the Mazars continuous damage model [4]. Geometric nonlinearity was used for all the calculations but its influence is fairly small due to the relatively small displacement and rotation values involved.

3.1 Elasto-plastic material model

The Drucker-Prager model with isotropic hardening was executed to include different behavior of material in tension and compression which is necessary for concrete. The yield surface has the following form [3]:

$$\Phi(\boldsymbol{\sigma}, \bar{\varepsilon}^p) = \sqrt{J_2(\boldsymbol{\sigma})} + c_1 \frac{1}{3} I_1(\boldsymbol{\sigma}) - c_2 coh(\bar{\varepsilon}^p) \tag{14}$$

where J_2 is the second deviatoric stress invariant, I_1 is the first stress invariant, *coh* is the cohesion that is dependent on accumulated plastic strain $\bar{\varepsilon}^p$, and the relevant coefficients c_1, c_2 are chosen according to the required approximation to the Mohr-Coulomb criterion or can be calculated using the stress–strain diagram for uniaxial stress state and determining two conditions for the relevant yield points in tension and compression.

A standard procedure for elastic prediction and plastic correction with an implicit algorithm was used for the analysis of this elasto-plastic model. After the iterative calculation (general return-mapping update formula) of the plastic multiplicator $\Delta\gamma$, the resultant stress tensor can be calculated [3]:

$$\boldsymbol{\sigma}_{n+1} = \boldsymbol{\sigma}_{n+1}^{trial} - \Delta\gamma \mathbf{D}^e : \mathbf{N}_{n+1} \tag{15}$$

In this case, the updated stress, $\boldsymbol{\sigma}_{n+1}$, obtained by the implicit return mapping is the projection of the trial stress $\boldsymbol{\sigma}_{n+1}^{trial}$ onto the updated yield surface along the direction of the tensor $\mathbf{D}^e : \mathbf{N}_{n+1}$. Note that, since the definition of the flow vector in the smooth portion of the cone differs from that at the apex singularity, two possible explicit forms exist for the return-mapping algorithm.

3.2 Elasto-damage material model

To account for the different nonlinear performances of concrete under tension and compression, and to explicitly reproduce the dissimilar effects of the tensile and shear damage mechanisms, a decomposition of the effective stress tensor into positive and negative components with the fourth-order projection tensors $\mathbf{P}^t$ and $\mathbf{P}^c$. The Mazars isotropic damage model is modified to consider the various tensile and compressive behaviors of concrete in a more effective manner. The calculation of the resultant stress tensor is carried out with the aid of linear elastic stress estimates $\boldsymbol{\sigma}^{trial}$ and the damage parameters d^t and d^c in the following way [4]:

$$\begin{aligned} \boldsymbol{\sigma} &= (1-d^t)\boldsymbol{\sigma}^t + (1-d^c)\boldsymbol{\sigma}^c = (1-d^t)\mathbf{P}^t : \boldsymbol{\sigma}^{trial} + (1-d^c)\mathbf{P}^c : \boldsymbol{\sigma}^{trial} \\ &= [(1-d^t)\mathbf{P}^t + (1-d^c)\mathbf{P}^c] : \boldsymbol{\sigma}^{trial} \end{aligned} \tag{16}$$

where $\boldsymbol{\sigma}^{trial} = \mathbf{D}^e : \boldsymbol{\varepsilon}$.

Damage parameters are derived from the stress–strain diagram where equivalent strains calculated according to [4] are used:

$$\varepsilon_t = \frac{I_\varepsilon}{2(1-2\nu)} + \frac{\sqrt{J_\varepsilon}}{2(1+\nu)}, \tag{17}$$

$$\varepsilon_c = \frac{I_\varepsilon}{5(1-2\nu)} + \frac{6\sqrt{J_\varepsilon}}{5(1+\nu)} \tag{18}$$

### 3.3 Comparison of the material models

The Drucker-Prager plasticity model parameters were selected so as to ensure that there is an adequate level of plasticization in the most exposed areas of the structure for the given accelerogram. The aim of the investigation is not to execute the calculations required for a real building, but merely to compare the suitability for use of various numerical methods, as well as the behavior of various material models. While the earthquake was taking place, plasticization occurred in some parts of the structure. This demonstrated itself through increased damping and a change in the distribution of tension with regard to the linear material. It can be seen from the results that at a time of 10 s (i.e., practically straight after seismicity ended) the shape of the building had undergone permanent deformation. This was in accordance with expectations. There was an overall increase in the height of the building, as well as in its width in the plasticized area. On higher floors, where plasticization did not occur, the width of the building remained the same. The increase in height and the partial expansion in terms of width might seem surprising at first sight, but these phenomena can be explained by the fact that only plasticization in tension occurred, and that the rocking of the building from one side to the other caused plasticization to take place on both sides of the structure. This increased the height of the whole building, and not only in its tilting. It also became wider for similar reasons.

The Mazars damage model expects the structure to fail due to micro cracks. The cracks are not localized but it is expected that they occur continuously (smeared cracking model). According to the Mazars model, it can be concluded from the stress–strain curve for the material that micro-cracks close after stress disappears, and that deformation also disappears in a similar way, as took place in the case of the linear elastic model. However, failure did occur. It demonstrated itself via the fact that the stress–strain curve followed a different trajectory during unloading and thus energy dissipation occurred, which resulted in a damping in oscillation. After the end of seismicity, no permanent deformation or strain remained, unlike in the case of plastic material, but there was a permanent decrease in the stiffness of the material and a change in the response of the structure to loading as a result (in this case, the loading was from continuing seismic effects). The decrease in stiffness will have an impact on dynamics in terms of a decrease in natural oscillation frequencies. The following images show the differences in the response of the structure to the same seismic loads for various material models. The corresponding results of both material models have been placed next to each other, e.g., resultant deformations and strain, with the same being shown for the time of maximum displacement (see **Figure 7**).

The main aim of the study was to compare the response to seismic loading of various material models, specifically the Drucker-Prager plasticity model and Mazars damage model. At first sight, the results appeared somewhat surprising but on closer investigation, it became clear that they are correct, and that they correspond to the relevant material models. In the case of Drucker-Prager, the building remained slightly tilted after the end of the earthquake (see **Figure 8**, which was expected) and was also higher and wider as a whole (which was surprising at first). This somewhat remarkable result was obtained because plasticization took place only in tension and, because of the oscillation of the building from one side to the other, plasticization due
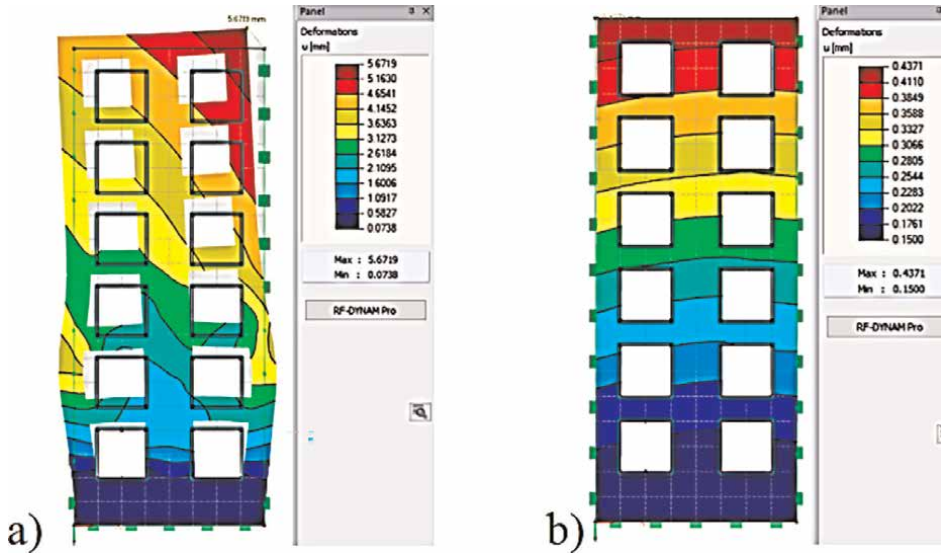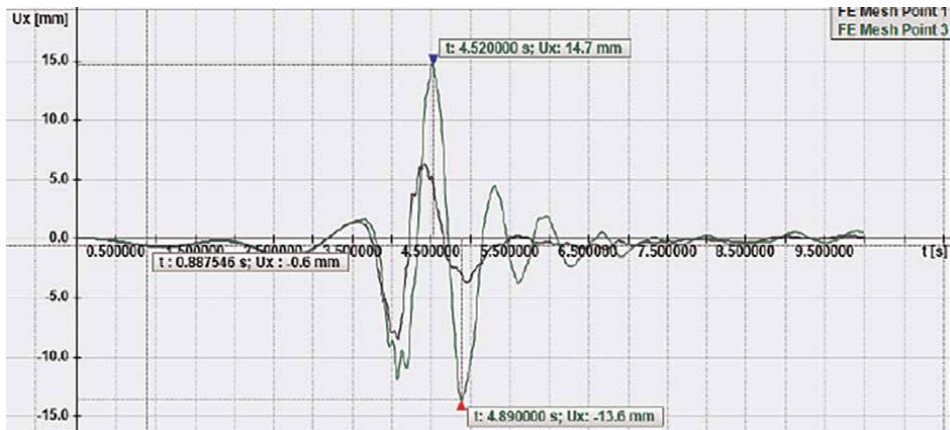
Figure 7.
The resulting shapes of the building a) Drucker-Prager plasticity model and b) the Mazars damage model.
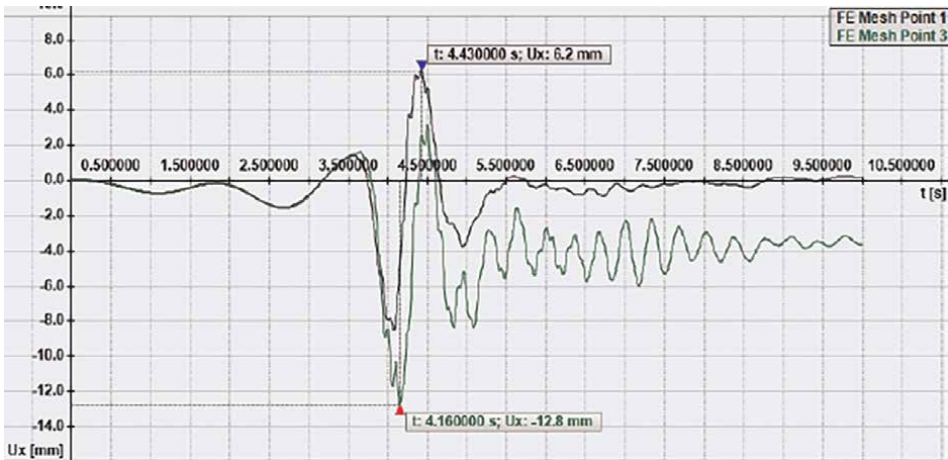
Figure 8.
Drucker-Prager plasticity model—Time diagram of the horizontal displacement of the highest and the lowest nodes.

to tension gradually occurred on both sides of the building. The result was an overall increase in the height of the building. For similar reasons, the building was also wider after the earthquake. In the case of the Mazars model, the geometry of the building remained the same after the end of the earthquake even though material failure occurred. However, the building was damaged. The micro-cracks did close after loading, though, and the deformation and stress from seismicity remained zero. The damage only demonstrated itself through lowered stiffness of the material in the damaged areas, which is also demonstrated in **Figure 9** by the decreasing frequency. The energy loss in the form of warmth appeared as increased damping in the numerical solution.

Figure 9.
Mazars damage model—Time diagram of the horizontal displacement of the highest and the lowest nodes.

4. Dynamic damping—Comparison of different concepts from the point of view of their physical nature and effects on civil engineering structures

There are a variety of sources of dynamical damping of vibration in civil engineering structures. Generally, damping can be caused either by the external environment or by energy dissipation due to structural deformation. The most common way to account for the damping in the motion equation is Rayleigh damping (see [13–15]). The Rayleigh damping is proportional to a linear combination of the stiffness and mass matrix.

This subchapter deals with the justification for the use of Rayleigh damping and discusses another solution because there is no direct physical interpretation of the mass damping parameter and the stiffness damping parameter. The damping given by internal resistance of structure occurs in the case of using inelastic materials when the loading and unloading parts of the strain–stress diagram differ, and therefore dissipation occurs in loading cycles, as described in [1–3, 5, 6, 10–12, 16–20]. Another source of damping is friction in structural connections.

4.1 Finite element analysis of the equation of motion

The virtual work of external forces has to be equal to the virtual work of internal forces. For one element with the volume Ω_e and the surface boundary Γ_e we can write this equilibrium of virtual work as follows:

$$\int_{\Omega_e} \delta \mathbf{u}^T \mathbf{b} d\Omega_e + \int_{\Gamma_e} \delta \mathbf{u}^T \mathbf{t} d\Gamma_e + \sum_{i=1}^{n} \delta \mathbf{u}_i^T \mathbf{f}_i = \int_{\Omega_e} (\delta \mathbf{u}^T \rho \ddot{\mathbf{u}} + \delta \mathbf{u}^T c \dot{\mathbf{u}} + \delta \boldsymbol{\varepsilon}^T \boldsymbol{\sigma}) d\Omega_e \qquad (19)$$

where $\delta \mathbf{u}$ and $\delta \boldsymbol{\varepsilon}$ represent the virtual displacement and pertinent strain, respectively, ρ is the material density, c is the viscous damping parameter, $\mathbf{b}$ and $\mathbf{t}$ are the volume and surface forces respectively, $\mathbf{f}_i$ and $\delta \mathbf{u}_i$ represent the concentrated forces and pertinent generalized displacement, respectively. The damping parameter c does not take into account material (internal) or external resistance. The material viscosity is not taken into account because it has an impact only in the case of a nonzero rate of

deformation in the given mass point (strain of the body). The influence of the external environment is not taken into account because the stress vector $c\dot{\mathbf{u}}$, which acts against the motion $\mathbf{u}$, arises even in the internal points of the bodies.

When discretizing for the finite element method we obtain the following relations:

$$\mathbf{u} = \mathbf{Nd} \qquad \dot{\mathbf{u}} = \mathbf{N}\dot{\mathbf{d}} \qquad \ddot{\mathbf{u}} = \mathbf{N}\ddot{\mathbf{d}} \qquad \boldsymbol{\varepsilon} = \mathbf{Bd} \tag{20}$$

Combining eqs. (22) and (23) we obtain:

$$\delta\mathbf{d}^T \left(\int_{\Omega_e} \rho\mathbf{N}^T\mathbf{N}d\Omega_e\ddot{\mathbf{d}} + \int_{\Omega_e} c\mathbf{N}^T\mathbf{N}d\Omega_e\dot{\mathbf{d}} + \int_{\Omega_e} \mathbf{B}^T\boldsymbol{\sigma}d\Omega_e - \int_{\Omega_e} \mathbf{N}^T\mathbf{b}d\Omega_e - \int_{\Gamma_e} \mathbf{N}^T\mathbf{t}d\Gamma_e - \sum_{i=1}^{n} \mathbf{f}_i \right) = 0 \tag{21}$$

where it is assumed that the concentrated forces $\mathbf{f}_i$ act in nodes. Let us denote the first two integrals in the equation as the consistent mass matrix and the damping matrix.

$$\mathbf{M}_e = \int_{\Omega_e} \rho\mathbf{N}^T\mathbf{N}d\Omega_e \tag{22}$$

$$\mathbf{C}_e = \int_{\Omega_e} c\mathbf{N}^T\mathbf{N}d\Omega_e \tag{23}$$

The word consistent means that the matrix follows directly from the discretization of a finite element with corresponding shape functions $\mathbf{N}$. Let us define the vectors of the internal and external nodal forces:

$$\mathbf{f}_e^{int} = \int_{\Omega_e} \mathbf{B}^T\boldsymbol{\sigma}d\Omega_e \tag{24}$$

$$\mathbf{f}_e^{ext} = \int_{\Omega_e} \mathbf{N}^T\mathbf{b}d\Omega_e + \int_{\Gamma_e} \mathbf{N}^T\mathbf{t}d\Gamma_e + \sum_{i=1}^{n} \mathbf{f}_i \tag{25}$$

Substituting from eqs. (25), (26), (27), and (28) into eq. (24), and taking into account the fact that variation $\delta\mathbf{d}$ can be arbitrary, and hence the second form of the product must be equal to zero, we obtain:

$$\mathbf{M}_e\ddot{\mathbf{d}} + \mathbf{C}_e\dot{\mathbf{d}} + \mathbf{f}_e^{int} = \mathbf{f}_e^{ext} \tag{26}$$

For a linear elastic material without viscosity, we can write the following relation for the internal nodal forces:

$$\mathbf{f}_e^{int} = \mathbf{K}_e\mathbf{d} \tag{27}$$

where

$$\mathbf{K}_e = \int_{\Omega_e} \mathbf{B}^T\mathbf{DB}d\Omega_e \tag{28}$$

is the stiffness matrix of the element, with $\mathbf{D}$ being the constitutive matrix of the material. Then eq. (29) can be rewritten as:

$$\mathbf{M}_e\ddot{\mathbf{d}} + \mathbf{C}_e\dot{\mathbf{d}} + \mathbf{K}_e\mathbf{d} = \mathbf{f}_e^{ext} \tag{29}$$

Eqs. (30) and (32) express in discretized form Newton's second law, or, more generally, the law of conservation of momentum. When writing these equations in the global form, i.e., for all degrees of freedom of the analyzed structure, we obtain the following equation:

$$\mathbf{M}\ddot{\mathbf{d}} + \mathbf{C}\dot{\mathbf{d}} + \mathbf{f}^{int} = \mathbf{f}^{ext} \tag{30}$$

$$\mathbf{M}\ddot{\mathbf{d}} + \mathbf{C}\dot{\mathbf{d}} + \mathbf{K}\mathbf{d} = \mathbf{f}^{ext} \tag{31}$$

4.2 Rayleigh damping

For Rayleigh damping, the damping matrix $\mathbf{C}_e^R$ is defined as the linear combination of the consistent mass matrix $\mathbf{M}_e$ and the stiffness matrix $\mathbf{K}_e$.

$$\mathbf{C}_e^R = \alpha\mathbf{M}_e + \beta\mathbf{K}_e \tag{32}$$

When substituting to eq. (35) $\mathbf{M}_e$ from eq. (25) and $\mathbf{K}_e$ from (31), we obtain the relation for the damping matrix in the following form:

$$\mathbf{C}_e^R = \alpha\int_{\Omega_e}\rho\mathbf{N}^T\mathbf{N}d\Omega_e + \beta\int_{\Omega_e}\mathbf{B}^T\mathbf{D}\mathbf{B}d\Omega_e \tag{33}$$

The damping matrix has two parts and the first one is identical with $\mathbf{C}_e$ as defined in (26), where $c = \alpha\rho$ and its physical nature is unclear. The second part of the expression does not correspond with relation (26) but is proportional to the stiffness matrix. The damping for $\alpha = 0$ and $\beta > 0$ is thus proportional to the rate of deformation of the body. The internal nodal forces arise only when the body deforms over time and no internal forces arise when an element moves as a rigid body.

### 4.2.1 Damping caused by material viscosity

As we mentioned before the internal damping caused by material arises only when a body is strained and is proportional to the strain rate. We have chosen the three most well-known viscoelastic models for this article for the damping caused by material viscosity and they are described below.

4.2.2 The Maxwell material model

For the Maxwell (see **Figure 10**) model the following relations are valid:

$$\sigma(t) = \sigma^e(t) = \sigma^v(t), \ \varepsilon(t) = \varepsilon^e(t) + \varepsilon^v(t), \ \varepsilon^e(t) = \frac{\sigma(t)}{E}, \ \dot{\varepsilon}^v(t) = \frac{\sigma(t)}{\eta} \tag{34}$$

As a result, we obtain the following linear nonhomogenous ordinary differential equation which describes the constitutive relation between stress and strain:
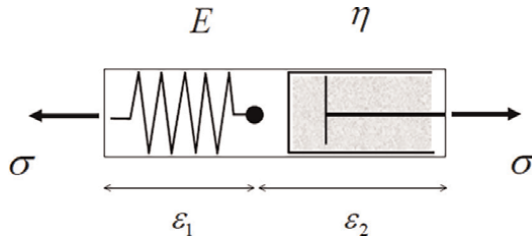
Figure 10.
Scheme of the Maxwell model.

$$\sigma(t) + \frac{\eta}{E}\dot{\sigma}(t) = \eta\dot{\varepsilon}(t) \tag{35}$$

4.2.3 The kelvin-Voigt material model

The Kelvin-Voigt model (see **Figure 11**) is based on the following relations:

$$\varepsilon(t) = \varepsilon^e(t) = \varepsilon^v(t), \ \ \sigma(t) = \sigma^e(t) + \sigma^v(t), \ \ \varepsilon^e(t) = \frac{\sigma(t)}{E}, \ \ \dot{\varepsilon}^v(t) = \frac{\sigma(t)}{\eta} \tag{36}$$

Using these relations, we obtain as a result the following linear non-homogenous ordinary differential equation which describes the constitutive relation between stress and strain:
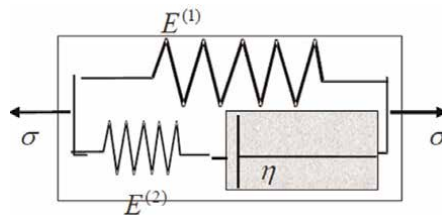
$$\sigma(t) = E\varepsilon(t) + \eta\dot{\varepsilon}(t) \tag{37}$$

4.2.4 The standard linear solid (SLS) material model

For the SLS model (see **Figure 12**) the following relations are valid:
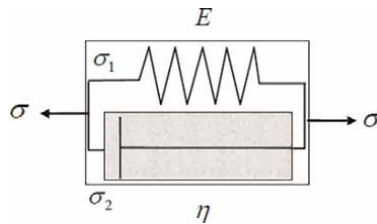
Figure 11.
Scheme of the kelvin-Voigt model.

Figure 12.
Scheme of the standard linear solid model.

176

$$\varepsilon(t) = \varepsilon_1(t) = \varepsilon_2(t), \ \varepsilon_1(t) = \varepsilon_1^e(t) = \frac{\sigma(t)}{E_1}, \ \varepsilon_2(t) = \varepsilon_2^e(t) + \varepsilon_2^v(t), \ \sigma(t) = \sigma_1(t) + \sigma_2(t),$$

$$\sigma_1(t) = E_1\varepsilon(t) \text{ and } \sigma_2(t) = E_2\big(\varepsilon(t) - \varepsilon_2^v(t)\big) \tag{38}$$

Then, for the resulting stress the following relations can be written:

$$\sigma(t) = E_1\varepsilon(t) + E_2\big(\varepsilon(t) - \varepsilon_2^v(t)\big) \tag{39}$$

After several modifications, we obtain the final relation for expressing strain rate as a function of stress rate, stress, and actual strain (it is a differential equation describing the constitutive relation between stress and strain).

$$\sigma(t) + \frac{\eta}{E_2}\dot{\sigma}(t) = \frac{\eta(E_1 + E_2)}{E_2}\dot{\varepsilon}(t) + E_1\varepsilon(t) \tag{40}$$

4.2.5 Damping caused by the kelvin-Voigt model

Let us now demonstrate how the damping caused by the Kelvin-Voigt model will manifest itself in the equation of motion. Let us substitute for $\boldsymbol{\sigma}(t)$ from (41) into eq. (27). For the vector of internal nodal forces, we obtain:

$$\mathbf{f}_e^{\text{int}} = \int_{\Omega_e}\mathbf{B}^T(\boldsymbol{\sigma}^e + \eta\dot{\boldsymbol{\varepsilon}})d\Omega_e = \int_{\Omega_e}\mathbf{B}^T\big(\boldsymbol{\sigma}^e + \eta\mathbf{B}\dot{\mathbf{d}}\big) = \int_{\Omega_e}\mathbf{B}^T\boldsymbol{\sigma}^e + \eta\int_{\Omega_e}\mathbf{B}^T\mathbf{B}\dot{\mathbf{d}} \tag{41}$$

Taking into consideration the fact that the damping will be caused by the material, we will not expect damping to take place with the help of the matrix $\mathbf{C}$ here. The equation of motion shall then read:

$$\mathbf{M}_e\ddot{\mathbf{d}} + \int_{\Omega_e}\mathbf{B}^T\boldsymbol{\sigma}^e + \eta\int_{\Omega_e}\mathbf{B}^T\mathbf{B}\dot{\mathbf{d}} = \mathbf{f}_e^{ext} \tag{42}$$

The equation can then be rewritten for a linear elastic material as:

$$\mathbf{f}_e^{\text{int}} = \mathbf{K}_e\mathbf{d} + \eta\int_{\Omega_e}\mathbf{B}^T\mathbf{B}\dot{\mathbf{d}}d\Omega_e \tag{43}$$

$$\mathbf{M}_e\ddot{\mathbf{d}} + \mathbf{f}_e^{\text{int}} = \mathbf{f}_e^{ext} \tag{44}$$

and after the substitution for $\mathbf{f}_e^{\text{int}}$, we can rewrite the equation of motion in the form

$$\mathbf{M}_e\ddot{\mathbf{d}} + \mathbf{K}_e\mathbf{d} + \eta\int_{\Omega_e}\mathbf{B}^T\mathbf{B}\dot{\mathbf{d}}d\Omega_e = \mathbf{f}_e^{ext} \tag{45}$$

4.3 Comparison of Rayleigh damping with the damping of the kelvin-Voigt material

The Rayleigh damping depends only on the velocities of mass points in space, and that damping also arises in the case of the movement of a rigid body due to coefficient

α. To compare the Rayleigh damping and damping caused by the Kelvin-Voigt material model let us assume $\alpha = 0$. The equation of motion then will read as:

$$\mathbf{M}_e\ddot{\mathbf{d}} + \beta \int_{\Omega_e} \mathbf{B}^T\mathbf{D}\mathbf{B}d\Omega_e\dot{\mathbf{d}} + \int_{\Omega_e} \mathbf{B}^T\boldsymbol{\sigma}d\Omega_e = \mathbf{f}_e^{ext} \tag{46}$$

If we compare the equation with the Kelvin-Voigt material model (45) with this eq. (49), one can see that the difference between them lies only in the term with the first derivative of the deformation parameters by time, i.e., the velocities $\dot{\mathbf{d}}$. If we simplify (reduce) these equations to 1D tasks, substituting Young's modulus E for the constitutive matrix $\mathbf{D}$ and comparing the terms with $\dot{\mathbf{d}}$ from the equations we obtain the relation

$$\beta E \int_{\Omega_e} \mathbf{B}^T\mathbf{B}d\Omega_e\dot{\mathbf{d}} = \eta \int_{\Omega_e} \mathbf{B}^T\mathbf{B}d\Omega_e\dot{\mathbf{d}} \tag{47}$$

and subsequently simple relation between the parameters β and η of both models.
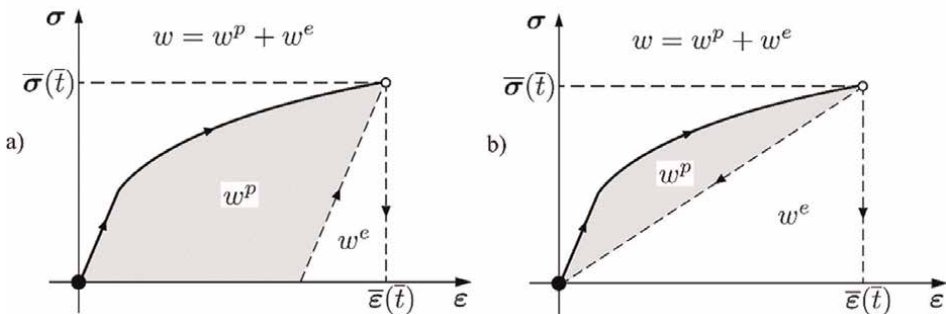
$$\boxed{\beta E = \eta} \tag{48}$$

It is clear that the Rayleigh damping and the damping caused by Kelvin-Voight material model are identical for 1D problems.

### 4.4 Damping caused by the plasticizing, or damaging of material

Figure 13 shows a loading and unloading diagram for a) elasto-plastic b) elasto-damage material for the 1D stress and strain state.

$$\text{a) } w^p(\bar{t}) = \int_0^{\bar{t}} \boldsymbol{\sigma}(t) : \dot{\boldsymbol{\varepsilon}}^p(t)dt = \int_0^{\bar{t}} \boldsymbol{\sigma}(t) : \dot{\boldsymbol{\varepsilon}}(t)dt - \frac{1}{2}\mathbf{C}^{-1} : \overline{\boldsymbol{\sigma}}(\bar{t}) : \overline{\boldsymbol{\sigma}}(\bar{t}) \tag{49}$$

$$\text{b) } w^p(\bar{t}) = \int_0^{\bar{t}} \boldsymbol{\sigma}(t) : \dot{\boldsymbol{\varepsilon}}^p(t)dt = \int_0^{\bar{t}} \boldsymbol{\sigma}(t) : \dot{\boldsymbol{\varepsilon}}(t)dt - \frac{1}{2}\overline{\boldsymbol{\varepsilon}}(\bar{t}) : \overline{\boldsymbol{\sigma}}(\bar{t}) \tag{50}$$

Figure 13.
Loading and unloading diagram for elasto-plastic (a) and elasto-damage (b) materials, with division of energy into elastic and dissipative.
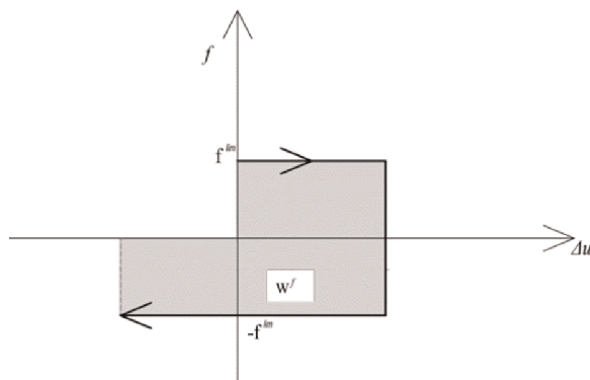
Figure 14.
Friction diagram [1].

This dissipation energy is lost from the mechanical system in the form of heat and this process manifests itself in dynamics as damping. The sum of this dissipation energy w^p plus the elastic energy w^e is equal to the total energy used for the deformation work.

In the case of plasticizing the damping occurs at the time when a plastic deformation, arises, and later vibration is no longer damped unless the maximum strain achieved so far is overcome once again. Plasticizing does not affect the natural frequency of the structure.

In the case of damage, the damping occurs at the time when a material damage arises, and later vibration is no longer damped unless the maximum strain achieved so far is overcome once again. Damage causes material softening, so the Eigen frequencies will be decreased.

4.5 Damping caused by friction

The Coulomb friction (see the diagram in **Figure 14**) is also a significant part of internal damping of structures. It occurs in connections of structural elements and most often comes about in screw or rivet connections in steel structures. Mechanical work and pertinent dissipation arise in the case of any relative motion in the connections. In contrast to plastic or damage behavior, mechanical work is performed with each relative forward and backward motion, and the pertinent damping is then permanent during vibration. The friction force is usually proportional to the pressure force in connections (Coulomb friction).

5. Conclusions

The conclusion is that for accurate nonlinear seismic analysis we cannot use spectral methods but we have to use the methods of direct integration of the motion equation. We can use both methods (explicit and implicit) with a slight advantage of the explicit method with respect to time consumption. Another important conclusion is that the mathematical model of the concrete has a significant influence on the nonlinear transient response of structure (earthquake analysis) and reality is somewhere between analyzed elasto-plastic and elasto-damage behavior and thus we recommend using combination of plasticity and damage models simultaneously.

The analysis of different sources of damping showed that it is needed to use not only external damping but also (and mainly) internal damping using material inelasticity models (viscosity, plasticity/damage, friction) instead of simple Rayleigh damping which is insufficient for the huge nonlinear time-dependent response of structure on earthquake loading.

Acknowledgements

Author details

Miroslav Trcala[1*], Ivan Němec[2] and Adéla Gálová[2]

1 Faculty of Civil Engineering, Institute of Mathematics and Descriptive Geometry, Brno University of Technology, Brno, Czech Republic

2 Institute of Structural Mechanics, Brno University of Technology, Brno, Czech Republic

*Address all correspondence to: nemec.i@fce.vutbr.cz

IntechOpen

References

[1] Němec I, Trcala M, Vaněčková A, Rek V. Dynamic damping – Comparison of different concepts from the point of view of their physical nature and effects on civil engineering structures. In: Programs and Algorithms of Numerical Mathematics 19. Proceedings of Seminar, Hejnice, June 24–29, 2018. Prague: Institute of Mathematics CAS; 2019. pp. 107-118

[2] Němec I, Štekbauer H, Vaněčková A, Vlk Z. Explicit and implicit method in nonlinear seismic analysis. In: Dynamics of Civil Engineering and Transport Structures and Wind Engineering - DYN-WIND 2017. MATEC Web of Conferences. EDP Sciences; 2017

[3] de Souza, Neto EA, Periæ D, Owen DRJ. Computational Methods for Plasticity, Theory and Applications. John Wiley & Sons; 2008

[4] Mazars J, Hamon F, Grange S. A New 3D Damage Model for Concrete under Monotonic, Cyclic and Dynamic Loadings, Material and Structures. Springer; 2014

[5] RFEM-FEM, Structural Analysys Software, Available from: https://www.dlubal.com/en/products/rfem-fea-software/what-is-rfem

[6] Ansys® Engineering Simulation Software, Available from: https://www.ansys.com/

[7] Němec I, Kolář V, Ševčík I, Vlk Z, Blaauwendraat J, Buček J, et al. Finite Element Analysis of Structures, Principles and Praxis. Shaker Verlag; 2010

[8] Shen RW, Gu L. Introduction to the Explicit Finite Element Method for Nonlinear Transient Dynamics. John Wiley & Sons; 2012

[9] Rodriguez J, Rio G, Cadou JM, Troufflard J. Numerical study of dynamic relaxation with kinetic damping applied to inflatable fabric structures with extensions for 3D solid element and non-linear behavior. Thin-Walled Structures. 2011;**49**(11):1468-1474, Elsevier

[10] Brio M. Numerical Time-Dependent Partial Differential Equations for Scientists and Engineers. Academic Press; 2010

[11] Bathe KJ. Finite element procedures. New Jersey: Prentice Hall; 1996

[12] Belytschko T, Hughes TJR. Computational Methods for Transient Analysis. Elsevier science publishers B.V; 1983

[13] Timoshenko S., Young D.H., Weaver JR. (1974) Vibration Problems in Engineering, John Wiley & Sons, New York.

[14] Sondipon A. Damping Models for Structural Vibration [Thesis]. Cambridge: Trinity College, Cambridge, Trinity College; 2000

[15] Mesquita AD, Coda HB. Alternative kelvin viscoelastic procedure for finite elements. Applied Mathematical Modelling. 2002;**26**(4):501-516

[16] Simo JC, Hughes TJR. Computational Inelasticity. New York: Springer; 2008. p. 392

[17] Němec I, Trcala M, Rek V. Nelineární mechanika. Brno: VUTIUM; 2018

[18] Courant R, Fredrichs KO, Lewy H. On the partial difference equations of

mathematical physics. IBM Journal of Research and Development. 1967;**11**(2): 215-234

[19] Alamatian J. A new formulation for fictitious mass of the dynamic relaxation method with kinetic damping. Computers & Structures. 2012;**90-91**:42-54, Elsevier

[20] Oller S. Nonlinear Dynamics of Structures (Lecture Notes on Numerical Methods in Engineering and Sciences). Springer; 2014

Edited by Walter Salazar

Earthquakes - Recent Advances, New Perspectives and Applications is a compilation of nine chapters covering aspects of tectonics, seismicity, earthquake forecasting, geotechnical engineering, and buildings. It presents state-of-the-art techniques for calculating moment tensors, rupture inversions, and hypocentral locations. It also presents methodologies to test probabilistic earthquake distributions on clustered and declustered catalogs and improves on classical methodologies to estimate bearing capacity and slope stability analysis. The final section discusses the structural behavior of vernacular and modern structures in the nonlinear range and the consequences of modifying the original structural system of a building.